On the Origin of Transport Non-Universality and Piezoresistivity in Segregated Conductor-Insulator Composites and Application to Thick-Film Resistors

THÈSE N^{O} 4351 (2009)

PRÉSENTÉE LE 27 MARS 2009

À LA FACULTÉ SCIENCES ET TECHNIQUES DE L'INGÉNIEUR
LABORATOIRE DE PRODUCTION MICROTECHNIQUE 2
PROGRAMME DOCTORAL EN SYSTÈMES DE PRODUCTION ET ROBOTIQUE

ÉCOLE POLYTECHNIQUE FÉDÉRALE DE LAUSANNE

POUR L'OBTENTION DU GRADE DE DOCTEUR ÈS SCIENCES

PAR

Niklaus JOHNER

acceptée sur proposition du jury:

Prof. M.-O. Hongler, président du jury
Prof. P. Ryser, directeur de thèse
Dr A. Danani, rapporteur
Prof. P. De Los Rios, rapporteur
Dr E. Grivei, rapporteur

ÉCOLE POLYTECHNIQUE
FÉDÉRALE DE LAUSANNE

Suisse
2009

Abstract

In this thesis we address the description of electrical transport properties of disordered conductor-insulator composites, mostly by numerical Monte Carlo simulations and analytical study of realistic tunnelling-percolation models. Such composites are basically constituted by conducting particles dispersed in an insulating matrix and present a conductor-insulator phase transition, with critical exponent t, as the volume concentration of the conducting phase x is decreased towards a critical concentration x_c. Percolation theory shows that close to this phase transition the conductivity Σ of the composite follows a simple power-law

$$\Sigma = \Sigma_0 (x - x_c)^t, \tag{1}$$

with a universal transport exponent $t = t_0 \simeq 2$, independent of the detailed characteristics of the system.

Two representative examples of such composite materials are conducting polymers, used for example for anti-static purposes, electromagnetic interference shielding or current-limiting switches and thick-film resistors (TFRs) used as resistors in electronic applications where high thermal, chemical, mechanical and aging stability are needed and as sensing elements for force and pressure sensors. This work focuses mostly on TFRs, composed of a glassy phase embedding small conducting grains, which are, from our point of view, ideal model systems. They present a complex microstructure, due to segregation of the conducting phase in the spaces left over in between the large glassy regions, unusually large piezoresitive responses and are an important class among the composite materials presenting universality-breakdown of the critical transport exponent, showing values of $t > t_0$, and as large as 10. Experimentally, non-universal transport exponents have been repeatedly observed, but we lack a theory accounting satisfactorily for this phenomenon. A better understanding of this transport non-universality is the main issue addressed in this thesis.

We formulate a lattice and a continuum model, aimed at describing the transport properties of disordered conductor-insulator composites, presenting or not a segregated microstructure. Our main assumptions are that the transport properties, close to the phase transition, are governed by the formation of a percolating cluster of conducting particles and that the electrical transport between the conducting particles is mainly governed by simple tunnelling. We also introduce segregation in the continuum model, which is the

main interaction between the conducting and insulating phases considered in this work.

In this framework, we present a complete study of segregation and its influence on the critical concentration x_c. We show how the relative size of the conducting and insulating particles changes the effectiveness of segregation. Moreover we show that the critical concentration x_c is not a monotonically decreasing function of segregation, but presents a minimum, well before maximal segregation is reached, which is a result of broad technological interest.

Now, the main outcome of this work is a new interpretation of the experimentally observed non-universality of the direct current transport exponent. We show that realistic tunnelling-percolation models, although not presenting true non-universality of transport, lead to a transport exponent t strongly depending on the concentration of the conducting phase x, so that the conductivity does, indeed, not follow a simple power-law. As t is experimentally extracted by fitting the concentration dependence of the conductivity with the simple power law of equation 1, apparent non-universal transport exponents will be obtained. This is what we call apparent non-universality, which might be experimentally very difficult to distinguish from true non-universality. We propose an analytical formula, containing only few parameters of our model, replacing the power-law of equation 1, which fits very nicely some experimental measurements of the conductivity of conductor-insulator composites.

Our models also account for the large increase of the piezoresistivity experimentally observed in conductor-insulator composites close to the percolation threshold. But contrary to classical tunnelling-percolation predictions, we show that more realistic models lead to a saturation of the piezoresistivity close enough to the percolation threshold. This feature has not been observed yet, but would be a direct confirmation of the scenario proposed in this work for the appearance of transport non-universality.

Keywords: Percolation, thick-film resistors, conductor-insulator composites,transport properties, DC conductivity, criticality, non-universality, segregation, high-voltage trimming.

Résumé

Nous abordons, dans ce travail, la description des propriétés de transport électrique de matériaux composites conducteur-isolant. Nos résultats proviennent principalement de simulation Monte Carlo ainsi que d'études analytiques de modèles réalistes de percolation avec conduction par effet tunnel (tunnelling-percolation). Ces matériaux composites sont constitués principalement par des particules conductrices dispersées dans une matrice isolante et présentent, lorsque l'on diminue la concentration volumique x de la phase conductrice vers une valeur critique x_c, une transition de phase conducteur-isolant, avec exposant critique t. La théorie de la percolation stipule que, près de cette transition de phase, la conductivité du composite, Σ, suit une loi de puissance de la forme

$$\Sigma = \Sigma_0 (x - x_c)^t, \tag{2}$$

avec un exposant critique $t = t_0 \simeq 2$ universel, c'est-à-dire qui ne dépend pas des caractéristiques détaillées du système.

Deux exemples types de tels matériaux composites sont les polymères conducteurs et les résistances en couche épaisse (TFRs). Les premiers servent, entre autres, comme protection antistatique, boucliers électromagnétiques et limitateurs de courant, alors que les seconds sont utilisés en électronique, lorsqu'une grande stabilité thermique, chimique, mécanique ou de vieillissement sont requises, ainsi que comme éléments actifs dans des senseurs de force ou de pression. Dans ce travail nous nous intéressons particulièrement aux TFRs, formés par une dispersion de fines particules conductrices dans une phase vitreuse, qui nous semblent être un système modèle idéal. Ils présentent en effet une microstructure complexe, de par la ségrégation de la phase conductrice dans les interstices vides entre les grandes particules isolantes, une piézorésistivité inhabituellement grande et forment une classe importante parmi les matériaux composites présentant la rupture de l'universalité, avec des exposants critiques $t > t_0$ allant jusqu'a $t = 10$. Alors que la non-universalité a été expérimentalement obtenue à maintes reprises, il n'y a toujours pas une théorie satisfaisante pour l'expliquer. Mieux comprendre l'origine de cette non-universalité est le problème central traité dans cette thèse.

Pour ce faire nous développons un modèle sur réseau et un modèle dans le continu, visant la description des propriétés de transport électrique dans les matériaux conducteur-isolant désordonnés, avec ou sans ségrégation. Les

hypothèses de base de ce travail sont que, près de la transition de phase, les propriétés électriques sont dominées par la formation d'un cluster de particules conductrices qui percolent au travers de la phase isolante, et que la conduction entre les particules conductrices est essentiellement dominée par l'effet tunnel. Nous introduisons également la ségrégation dans le modèle continu, qui est l'interaction principale entre les phases isolante et conductrice que nous traitons dans ce travail.

Nous présentons, dans ce cadre, une étude complète de la ségrégation et de son influence sur la concentration critique x_c. Nous montrons comment le rapport de taille entre les particules conductrices et isolantes change l'efficacité de la ségrégation. Nous montrons également que la concentration critique x_c ne diminue pas de façon monotone avec la ségrégation, mais possède un minimum nettement avant la ségrégation maximale, un résultat d'un intérêt technologique certain.

La contribution la plus importante de ce travail est une nouvelle interprétation de la non-universalité observée expérimentalement. Nous montrons qu'un modèle réaliste de tunnelling-percolation, même s'il ne permet pas d'obtenir une réelle non-universalité du transport, entraine un exposant critique t qui dépend fortement de la concentration de la phase conductrice x. Ainsi, la conductivité n'obéit en réalité pas à une simple loi de puissance. Mais comme, expérimentalement, t est obtenu en ajustant l'équation 2 aux mesures de la conductivité en fonction de la fraction volumique x, des exposants critiques apparemment non-universels peuvent être obtenus. C'est ce que nous avons appelé la non-universalité apparente, qu'il pourrait être très difficile de distinguer expérimentalement de la non-universalité réelle. Nous obtenons également une formule analytique, ne contenant que quelques paramètres de notre modèle, qui remplace la loi de puissance de l'équation 2 et qui décrit parfaitement certaines mesures expérimentales de la conductivité de composites conducteur-isolant.

La forte augmentation de la piézorésistivité, observée expérimentalement près du seuil de percolation des composites conducteur-isolant, est également expliquée par nos modèles. Nous montrons néanmoins que, contrairement aux prédictions du modèle classique de tunnelling-percolation, des modèles plus réalistes impliquent une saturation de la piézorésistivité pour des concentrations x suffisamment proches de x_c. Cette saturation, qui n'a encore jamais été observée, serait une confirmation directe du scénario que nous proposons dans cette thèse pour expliquer l'apparition de la non-universalité.

Keywords : Percolation, résistances en couche-épaisse, Composites conducteur-isolant, propriétés de transport, conductivité DC, criticalité, non-universalité, ségrégation, trimming à haute tension.

Remerciements

Une thèse de doctorat n'est évidemment pas un travail qui s'effectue seul et je tiens à remercier sincèrement toutes les personnes qui m'ont encadré, fait confiance et soutenu durant ces 4 dernières années.

Tout d'abord un grand merci au Prof. Peter Ryser qui m'a permis d'effectuer mon doctorat au LPM à l'EPFL et qui m'a accordé une grande liberté de travail ainsi qu'au Dr Claudio Grimaldi qui m'a encadré et sans qui ce travail n'aurait pas été possible. J'ai particulièrement apprécié sa modestie, sa disponibilité, la clarté de ses explications et sa manière de simplifier les problèmes pour n'en garder que l'essentiel. Je lui dois beaucoup pour l'accomplissement de ce travail et notamment pour toutes les parties analytiques auxquelles il a largement contribué ainsi que pour les nombreuses idées et interprétations qu'il a apportées. Ma gratitude va également au Dr Thomas Maeder, mon autre chef de projet, qui aurait sans doute aimé que ce travail soit moins théorique, mais qui a néanmoins toujours été présent lorsque j'avais une question ou un doute quelconque, partageant volontiers son très large savoir. Merci également à Gianluca Ambrosetti pour notre collaboration et nos sorties durant ces deux dernières années. Ce sont également ces quatre là qui ont relu, corrigé et commenté ma thèse, me permettant de rendre ce texte bien plus complet et équilibré.

J'aimerais également exprimer ma gratitude aux membres du jury, le Dr Eusebiu Grivei, le Dr Andrea Danani et le Prof. Paolo De Los Rios, ainsi qu'au président du jury le Prof. Max-Olivier Hongler, pour le temps qu'ils ont consacré à lire et évaluer mon travail, ainsi que pour leur présence, commentaires et discussions soulevées lors de mon examen de doctorat.

Il ne faut pas oublier qu'une thèse de doctorat ce n'est pas seulement un travail long (et parfois difficile), mais que c'est également une assez grande tranche de vie. J'ai passé quatre années dans un laboratoire où l'ambiance de travail était exceptionnelle. Un tout grand merci donc à tous les membres du LPM pour les innombrables moments de détente passés ensemble, que ce soient les pauses cafés, les repas, les soupers de Noël et autres sorties de labo ou les nombreux apéros sauvages, et particulièrement à Frank, mon collègue de bureau, pour nos heures passées à faire musique commune et à toutes sortes de gamineries. Un grand merci également à Simon, Antoine, Caro et Karine avec qui j'ai passé le plus clair de mes quatre ans au LPM, ainsi qu'aux nouveaux arrivés, Sandra, Zoltan, Lucas et Giuseppe, qui ont largement contribué à la bonne ambiance dans ma dernière année de thèse.

Finalement une pensée toute particulière pour Nathalie qui a occupé une grande part de mon esprit et finalement pris une place importante dans ma vie durant cette dernière année.

Pour finir, je n'oublie pas non plus tous ceux que je côtoie en-dehors du travail. Merci à Stéphanie d'être toujours là, à Céline pour son soutien et ses histoires, à Thamani pour nos discussions nocturnes, à Valentin pharmacien pour notre sport du lundi, à Laura pour son amitié, à Estelle de me faire rire, à Mathias pour notre voyage, à Yannick pour sa présence, à Isabelle, Ismaël, Robert, Matthieu, Aprili et tous les autres.

Enfin un tout grand merci à ma famille, à Brigitte d'être simplement ma grande soeur, à mon frère Stéphane pour le temps qu'on passe ensemble, à mon père pour nous avoir toujours encouragés à aller de l'avant dans la vie et à ma mère pour être toujours présente pour moi avec tout l'amour d'une maman.

Contents

List of Figures

Chapter 1

Introduction

Composite materials (or composites) are nowadays of common use in many industrial products. A composite is constituted of at least two different materials, a matrix and one or several fillers, remaining distinct, on a microscopic length scale, in the final product. The aim of a composite is to benefit from some physical or chemical properties of the different constituents to obtain new materials with enhanced properties.

Wood or bones are examples of natural composites where the filler is a fiber enhancing the material's mechanical properties. Construction is maybe the area where composites have been longest and most widely used. Indeed bricks, concrete, cements and more recently carbon or glass fiber reinforced materials are all composites. From a broader perspective also magnetic recording media (tapes and disks), porous materials, foams, gels and emulsions are diphasic composites.

Another important class of diphasic composite materials are conductor-insulator composites, consisting of conducting particles embedded in an insulating matrix. Conducting polymers are a very current example of such composites, which combine relatively good electrical conductivity with the ease of processing of the polymer matrix. Poorly conducting polymers can be used for anti-static purposes, whereas good enough conductivity for applications such as electromagnetic interference shielding [1] can also be obtained. The difference in thermal expansion of the conductive filler and the insulating polymer matrix can lead to very large positive temperature coefficients of resistance (PTC) of the composite [2], used for current-limiting switches [3], where local heating above the melting temperature of the matrix induces a large increase in resistance.

There is another type of commonly used conductive composites, the so-called thick-film-resistors (TFRs), composed of a glassy phase embedding small conducting grains, usually ruthenium oxide (RuO_2) or ruthenates such as $Pb_2Ru_2O_7$. TFRs are used as resistors in electronic applications where high thermal, chemical and aging stability is needed. They also present a high piezoresistive response and are therefore widely used as force and

pressure sensors.

Although those materials can seem quite different, they have one thing in common: they all undergo a phase transition when the filler concentration x is raised above some critical value x_c, corresponding to global connectivity of the filler in the system. This phase transition is described by percolation theory and characterized by a sudden change of some physical properties of the composite, for example the insulator-metal transition in conductor-insulator composites. Above this concentration, the current flows through chains of neighbouring conducting particles, forming geometrically complex paths connecting the edges of the system. For concentrations close but above this threshold, the conductivity Σ follows a power-law of the form

$$\Sigma = \Sigma_0 (x - x_c)^t, \tag{1.1}$$

where t is the critical direct-current (DC) transport exponent and Σ_0 a constant prefactor. Classical percolation theory shows that this exponent is universal, meaning that its value is independent of the microscopic details of the system and takes the value $t = t_0 \approx 2$ [4] for three-dimensional systems. Fortunately for this thesis, this is not the whole story. Experimental determination of this exponent for many different conductor-insulator composites has shown that there are cases where the universality is broken, leading to transport exponents different from the universal t_0. A collection of such exponents is shown in figure 1.1, where you can see that around half the exponents measured are relatively close to t_0, but that the remaining exponents take values mostly above 2 and as high as 10. Though some results of this thesis are quite general, explaining the origin of this non-universality of the DC transport exponent in conductor-insulator composites is its main aim. There are already theories accounting for the appearance of non-universality in conductor-insulator composites, but none agreeing satisfactorily with the experimentally obtained exponents.

This thesis is also concerned with the particular microstructure of TFRs, which appear in figure 1.1 as an important class of composites displaying non-universal behaviour. Indeed TFRs consist of a mixture of a coarse glassy powder (typical particle sizes of a few micrometers) with fine conducting particles ($10 - 100\ nm$ in diameter), fired at around $850°C$, leading to the sintering of the glassy phase (softening of the glass, wetting and binding the conducting particles together). The final composite nevertheless basically conserves its initial geometrical structure, where the small conducting grains are forced to occupy the empty spaces left between the much larger glass particles. This phenomenon, called segregation, leads to a large decrease in the critical concentration x_c and is studied quite in detail in this thesis. This is of particular technological interest as a low percolation threshold usually diminishes the composite's cost, but also helps preserving the initial mechanical characteristics of the matrix.

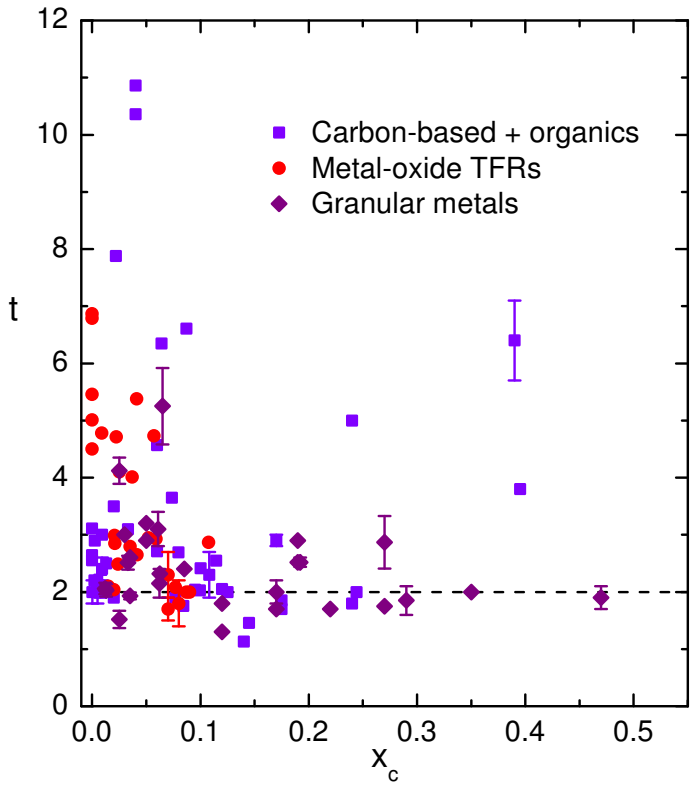

Figure 1.1: Collection of critical transport exponents t and corresponding critical concentrations x_c for various disordered conductor-insulator composites. The dashed line denotes the universal value $t_0 = 2$. This figure is taken from Ref. [5].

1.1 Thesis overview

In the next chapter, I will introduce the basics of percolation theory, phase transition and theoretical background of universality breakdown. I will also rapidly present the pre-existing models of conduction in conductor-insulator systems.

Then we will turn, in chapter 3 to a description of the thick-film resistors, which are the composites guiding the theoretical work of this thesis. We will examine their fabrication process, microstructure and transport properties. We will discuss their mechanical, thermal and chemical properties and stability. We will also present in this chapter a study of the sensitivity of TFRs to voltage pulses and discuss their use as model systems for our upcoming

theoretical studies.

In chapter 4, I will present a tunnelling-percolation model on a square lattice and show that tunnelling conduction does not lead to a true universality breakdown, but to apparent non-universality. This apparent non-universality reconciles semi-quantitatively the experimental and theoretical DC transport exponents. Then in the second part of that chapter, the piezoresistivity of the system will be examined for this same lattice model. We show in this chapter how the piezoresistivity is a much more sensitive tool than conductivity measurements to verify the true critical behaviour of a system, which is masked by apparent non-universality when looking at the conductivity. Indeed, it is shown that the piezoresistivity undergoes a clearly visible crossover between non-universal and universal behaviour as the percolation threshold is approached from above.

At this point of the thesis, I leave simple lattice models behind to treat more realistic continuum percolation models of conductor-insulator composites in the following two chapters. Chapter 5 is dedicated to the transport properties in a semi-permeable concentric shell model, with tunnelling between the conducting particles as conduction mechanism, representing typically a dispersion of conducting particles in a polymer matrix. It is shown that the transport exponent t is in fact dependent on the conducting phase concentration, leading again to apparent non-universality. We propose here an analytical expression for the conductivity in such systems, replacing the classical power law of equation 1.1 and leading to a new interpretation of non-universality. This expression is used to fit the conductivity data of a carbon-black/polymer composite, leading to values of the parameters in very good accord with the expected ones. Then, towards the end of this chapter, the piezoresistivity of this continuum tunnelling-percolation model is studied, showing similar results to those obtained for the lattice model of chapter 4.

In the last chapter before the conclusion, we turn to a closer description of thick-film resistors. We introduce a model of segregated tunnelling-percolation in the continuum, specially designed to represent the conduction in TFRs. To this aim, we reformulate the concentric-shell model of the preceding chapter, introducing large insulating spheres forcing the conducting particles into the remaining voids. We study the influence of segregation on the percolation threshold and show that there exists an optimal insulating sphere volume fraction, minimizing the percolation threshold of the conducting phase. We then study the transport properties of this model, and find that they remain basically unchanged compared to the non-segregated systems. We are indeed able to map the conductivity of the segregated systems onto that of the non-segregated ones, simply by shifting the critical concentration x_c and using an appropriate renormalization of the conductivity. This allows us to apply the theoretical results of the preceding chapter to obtain a simple expression for the conductivity in segregated tunnelling-percolation

systems. This expression is applied to experimental measurements of the conductivity of TFRs, leading to values of the parameters of the model completely consistent with the theoretical expectations.

The last chapter is of course devoted to the conclusions drawn from this work.

1.2 List of symbols

We give hereafter in table 1.1 a list of most symbols used in this thesis aimed at simplifying the reading of this work.

Table 1.1: This table contains the list and corresponding definition of most symbols used in this thesis

Symbols from the Latin alphabet	
Symbol	Definition
a	Mean nearest-neighbour distance, from center to center
d	$d/2$ is the thickness of the penetrable shell of the conducting particles
D	Dimensionality of the system
$h(g)$	Distribution function of the local conductances g
g	Local conductance between two adjacent nodes
G	Conductance of the system between two opposite edges
k	Number of neighbouring nodes (degree)
L	Linear size of the system
N	Number of particles or nodes in the system or in the one-dimensional channels (chapter 4)
N_s	Number of realizations of the system in numerical simulations
p	Probability of a bond (or site) to be occupied
t	DC transport critical exponent
$t(x)$	local transport exponent such that $\Sigma \propto (x - x_c)^{t(x)}$
$t^*(x)$	$t^*(x) = d\ln(\Sigma)/d\ln(x - x_c)$, same definition for $t^*(p)$
t^*	value of t extracted by fitting the conductivity with the simple power-law
x	Hard-core volume fraction of conductor particles
Symbols from the Greek alphabet	
Symbol	Definition
$\delta(x)$	Dirac delta function
η	$\eta = \eta_1 = \frac{\pi}{6}\rho\,(\sigma_1 + d)^3$, the volume occupied by the conducting particles, including the penetrable shell, $\eta_2 = \frac{\pi}{6}\rho_2{\sigma_2}^3$
γ	Microscopic piezoresistivity
Γ	Macroscopic piezoresistive factor of the system
λ	$\lambda = \sigma_1/(\sigma_1 + d)$, the penetrability coefficient of the conducting particles
ν	Correlation length critical exponent
$\Pi(p)$	Probability to have a percolating cluster at bond concentration p
ϕ_1	Volume fraction of conducting particles with penetrable shell
ϕ_2	Volume fraction of insulating spheres
ρ	$\rho = N/L^3$, number density of conducting particles (ρ_2 for the insulating ones)
ς	Microscopic conductance between two adjacent particles in the one-dimensional channels of chapter 4
Σ	Conductivity of the system
σ_1	Diameter of the conducting particles
σ_2	Diameter of the insulating particles
$\Theta(x)$	Heaviside step function
ξ	Tunnelling decay length
ζ	Correlation length

Chapter 2

Percolation basics

As outlined in the introduction, the conductor-insulator phase transition in composite materials is described using percolation theory. This chapter is aimed at giving the basic ideas needed to understand the remainder of this thesis. Fortunately, although percolation theory is a very complex subject, with very few analytical results, the basic ideas are simple. The reader interested in the field may start his readings with Stauffer and Aharony's "introduction to percolation theory" [4] containing also an extensive bibliography on the subject and from which this second chapter is largely inspired.

2.1 Graph theory

Before turning to percolation theory, I first need to say a few words about graphs. In 1736 Euler used graph theory to solve the problem nowadays known as "the seven bridges of Königsberg". The city of Königsberg lay in Prussia on two islands and both riversides of the Pregel river. Seven bridges were connecting the four parts of the city. The problem was to know whether it was possible to walk around the city, crossing each bridge once but only once. The map of the city drawn in Euler's paper is shown in figure 2.1(a).

To solve this problem, Euler simplified it, keeping only its essential abstract structure. He replaced each part of the city by a node (also called vertex or site), shown as red discs in panel (b) of figure 2.1 and the bridges linking the different parts of the city by edges (or bonds), shown as lines connecting the vertices, mapping the problem into a graph. The position of the nodes and the shape of the edges are completely irrelevant in a graph, the only information left is connectivity between the vertices, so by this mapping, Euler discarded all irrelevant information about the problem. A graph is said to be *connected* if there is a path from any vertex to any other one in the graph and the number of edges connected to a vertex is called its *degree*. Euler showed that there was no solution to this problem, there is no Eulerian path on this graph. In fact he showed that an Eulerian path exists

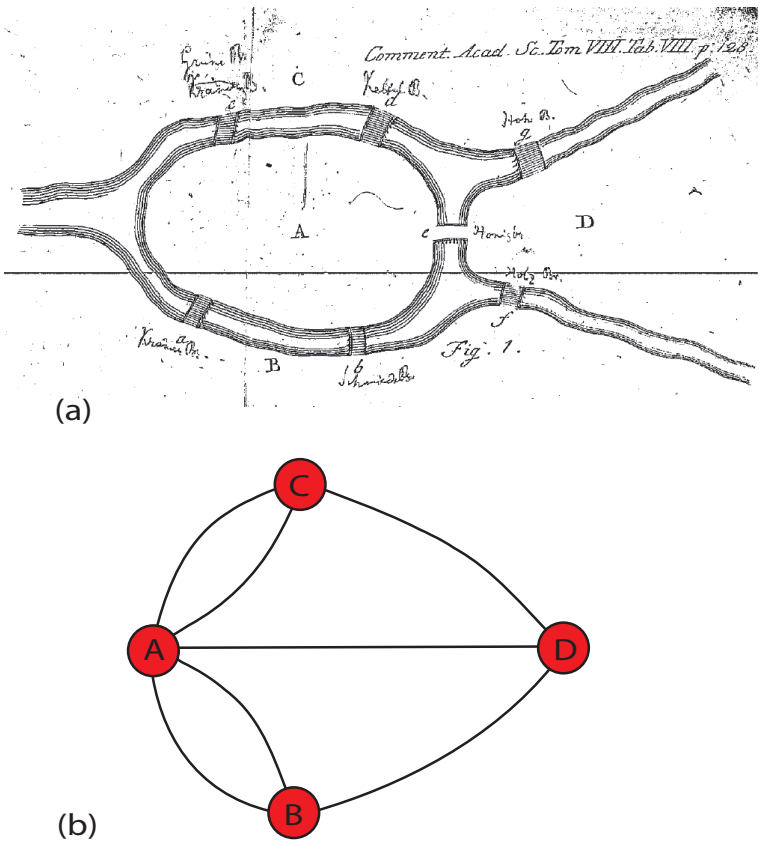

Figure 2.1: (a) Drawing of the city of Königsberg taken from Euler's paper [6]. (b) Graph representation of the problem.

only if the graph is connected and if all nodes, except maximum two, have an even degree. If there are nodes with an odd degree, they are the starting and ending point of any Eulerian path. In Königsberg's graph, all five nodes have an odd degree, and therefore the walk around the city is impossible. This is the first use of graph theory for a demonstration. Let's keep in mind here that it shows that some properties of the system are completely determined just by the connectivity information about the graph.

We call a *cluster*, a set of nodes forming a connected subgraph, meaning that all nodes accessible from one certain vertex belong to the same cluster. Two vertices are said to be *adjacent* (or *neighbours* in this work) if there is an edge connecting them. As pointed out just above, a graph represents only the geometrical connectivity pattern and can therefore be represented by an N by N matrix A, called the *adjacency matrix*, where N is the number of

nodes and

$$A(i,j) = \begin{cases} 1 & \text{if there is an edge between vertices } i \text{ and } j \\ 0 & \text{if there is no edge between vertices } i \text{ and } j \end{cases} .$$

A graph can also be represented by an *adjacency list*, a vector of size N by M, where M is the highest degree of the graph. In this representation the line i contains a list of the vertices adjacent to node i. This representation requires less storage space but is not practical for matricial calculations. In our simulation codes we make use of both representations, depending on which one is most appropriate.

2.2 Percolation theory

The basic ideas in percolation theory were born from a study of polymerization reactions, where, at a certain extent of reaction, gelation occurs. The gel point is a phase transition from liquid to gel, accompanied by an abrupt change in physical properties of the polymer. How do we explain this, as polymerization is a continuous phenomenon? Indeed, at the beginning of the reaction we have only monomers, starting to bond together and form dimers, trimers and larger polymers. As the average number of chemical bonds for each monomer increases, large polymers link together and, at a certain point, we will have formation of a giant molecule spanning the whole system. Gelation was first attributed to the formation of an infinite polymer network by Flory [7], and this sudden apparition of an infinitely large molecule of course drastically changes the properties of the system, which loses its ability to flow. Similarly, a classical problem in percolation theory is the flow of a liquid through a porous material. In that case there is again a phase transition at a certain pore volume fraction, below which no infinite network of pores exists and the liquid is blocked, whereas above it, the liquid can flow from hole to hole and make its way from one edge of the system to the opposite. We see that in both cases the appearance of an infinite cluster in the system leads to a phase transition. Percolation theory deals with the number and properties of clusters on a graph, the appearance of a giant cluster spanning the whole system when the density of edges is increased and the macroscopic properties of the system close to this phase transition.

2.2.1 Bethe Lattice

It is easiest to enter into percolation theory by looking at a lattice model. We can think here for example of the nodes as representing the monomers of our above polymerization problem, and the edges being the chemical bonds between them. In that case we would consider all nodes as being occupied and monitor the state of the system with the bond concentration p, the

probability that two neighbouring nodes are linked together by an edge. This is called *bond-percolation*. There is a second class of lattice models, called *site-percolation*, in which the nodes are occupied with probability p, and an edge is present between any pair of occupied neighbouring nodes.

To get a good feeling with the basic mechanisms of percolation we will first look at a very special lattice, called the Bethe lattice (or Cayley tree) which is, to my knowledge, the only lattice, apart from the less interesting one-dimensional case, on which the percolation problem is analytically solvable in a simple way [4]. Though bond and site percolation are very similar on the Bethe lattice we will start by studying site percolation because it is a little less ambiguous, notably when talking about cluster sizes.

A Cayley tree has, as its name indicates, a tree-like structure, with no closed loops, and is constructed as follows. One starts with a central node, from which k edges lead to its k neighbouring nodes (first generation). Then again, k edges emanate from each node, one leading back to the central node and the $k-1$ others to new sites belonging to the second generation. This branching process is repeated to infinity. Therefore all nodes in this structure are equivalent and there are no closed loops because each time we reach a node we can only go backwards or to new sites. This structure is presented in figure 2.2 for $k = 3$.

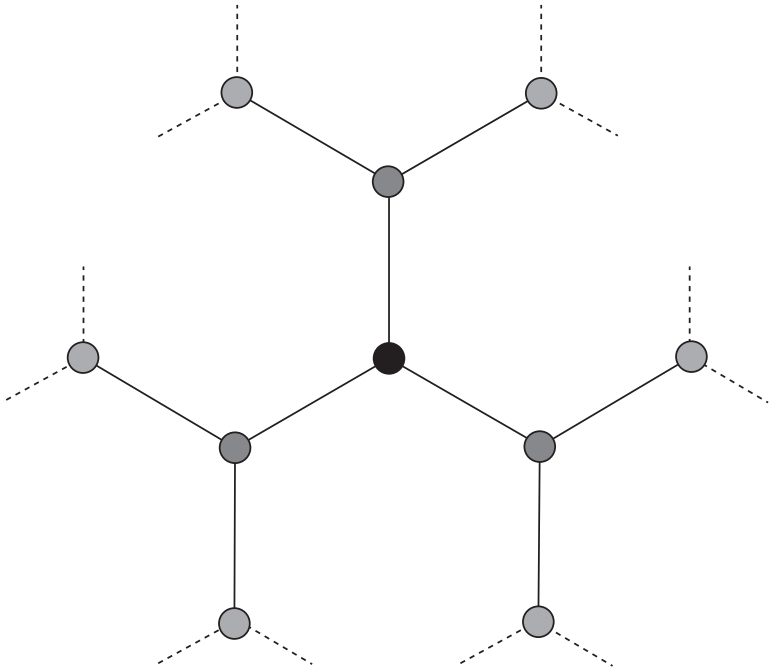

Figure 2.2: Illustration of the structure of a Cayley tree with $k = 3$ neighbours

We are now interested in calculating the critical concentration p_c at which

an infinite cluster first appears. If I arrive at a node, the chance that I can find a path to go on, or equivalently the mean number of paths leading from there to the next generation of nodes is $p(k-1)$. At the next node I have again the same situation, and therefore the mean number of paths leading n steps further is $[p(k-1)]^n$. From this it is clear that if $p(k-1) < 1$ the probability to find a path leading to infinity ($n \to \infty$) will be 0, whereas the number of paths I can follow if $p(k-1) > 1$ increases at each step, and an infinite network will exist. We have therefore derived

$$p_c = \frac{1}{k-1}$$

But of course not all occupied sites are part of the infinite cluster. Let's calculate the strength P of the infinite cluster, being the probability that any site belongs to the infinite cluster. We will do this in the special case when $k = 3$ because it is easiest to solve and sufficient to show the behaviour of P. Lets call Q the probability that a site is not connected to infinity through one fixed neighbour. If this neighbour is occupied, then it is itself not connected to infinity through one of its neighbours with probability Q (because all sites are equivalent in the Cayley tree) and as it has 2 neighbours it is not connected to infinity by any of them with probability Q^2. On the other hand this neighbouring site can also not lead to infinity because it is empty, with probability $1-p$. We therefore obtain $Q = 1-p+pQ^2$, having two solutions: $Q = 1$ corresponding to the absence of infinite network in the system, and therefore associated with $p < p_c$, and $Q = (1-p)/p$, corresponding to the more interesting situation $p > p_c$. Now the strength P of the infinite network is obtained by substracting the probability that a site is occupied but not connected to infinity by any of its neighbours, pQ^3, from the probability, p, of a site to be occupied. Therefore we obtain:

$$P = p - pQ^3 = p\left[1 - \left(\frac{1-p}{p}\right)^3\right]. \tag{2.1}$$

If we now define the size s of a cluster by the number of nodes it contains, we can obtain, by a calculation very similar to the above, the mean cluster size S below the percolation threshold ($p < p_c$),

$$S = \frac{1+p}{1-2p}$$

Above p_c we have to be a little more careful because of the presence of the infinite cluster, which is not done here. We now introduce the correlation function $\widetilde{g}(r)$, the 'probability that a site at distance r from an occupied site is also occupied and belongs to the same cluster' and the *correlation length* ζ, a measure of the average distance between two sites belonging to the same

cluster:

$$\zeta^2 = \frac{\sum_r r^2 \widetilde{g}(r)}{\sum_r \widetilde{g}(r)}, \tag{2.2}$$

where r runs over all lattice sites. From the above definition of $\widetilde{g}(r)$ we see that $\sum_r \widetilde{g}(r) = S$, the average number of sites in a cluster. Equation 2.2 defining ζ is valid for $p < p_c$ and can be generalized to $p > p_c$ by substracting the contribution of the infinite cluster, replacing $\widetilde{g}(r)$ with $\widetilde{g}(r) - P^2$ (the same remark holds for the mean cluster size S defined above the percolation threshold as the mean size of the finite clusters). The correlation function is straightforward in the Cayley tree, again because there are no closed loops. Now if a node is i generations away from the central node, the probability that they belong to the same cluster is p^i, and there are $k(k-1)^{i-1}$ such nodes, except for $i = 0$ where there is just one node. We therefore obtain

$$\sum_r \widetilde{g}(r) = 1 + \sum_{i=1}^{\infty} k(k-1)^{i-1} p^i = \frac{1+p}{1-p/p_c} = S, \tag{2.3}$$

which generalizes the above result for S to any k. We now have to introduce a notion of Euclidean distance on the Cayley tree. Indeed a Cayley tree can be represented in an infinite-dimensional Euclidean space, where each new generation of edges leads to an unexplored direction in space. Therefore if each edge is of length 1, then the distance r between two nodes i generations apart is calculated using the general Pythagoras' theorem, holding $r = \sqrt{i}$ (see Ref. [8]), so that

$$\sum_r r^2 \widetilde{g}(r) = \sum_{i=1}^{\infty} k(k-1)^{i-1} i p^i = p \frac{d}{dp} \sum_r \widetilde{g}(r) = \frac{p + p/p_c}{(1-p/p_c)^2}$$

$$\Rightarrow \zeta^2 = \frac{p + p/p_c}{(1-p/p_c)(1+p)}. \tag{2.4}$$

We can now extract from equations 2.1, 2.3 and 2.4 the asymptotic behaviours (close to the percolation threshold) of the infinite cluster strength, mean cluster size and correlation length :

$$P \propto (p - p_c)^{\beta} \tag{2.5}$$
$$S \propto |p_c - p|^{-\widetilde{\gamma}} \tag{2.6}$$
$$\zeta \propto |p_c - p|^{-\nu}, \tag{2.7}$$

with $\beta = 1$, $\widetilde{\gamma} = 1$ and $\nu = 1/2$ (for the Cayley tree with any k), called the critical exponents. We see here a very general feature of percolation and phase transitions in general, namely that most properties of interest, close to

the phase transition, behave as simple power laws. Equation 2.5 is true only above the percolation threshold, whereas equations 2.6 and 2.7 are valid on both sides of the phase transition, with the same critical exponents. Here we arrive at a fundamental observation: although the critical concentration p_c depends on k, the critical exponents are independent of the details of the system considered and are therefore said to be *universal*. The exponents usually depend solely on the dimensionality of the system, although it has been shown that the exponents obtained for the Cayley tree are exact for any system with dimension $D \geq 6$ (in such high dimensions, the loops in the system become unimportant so that the geometry of the percolating cluster not very different from that on the Cayley tree).

2.2.2 Scaling

We have now seen that close to the percolation threshold, quantities of interest of an infinite system behave as power laws. In fact we can rewrite this for a general property X as

$$X \propto (p - p_c)^{-\chi} \propto \zeta^{\chi/\nu}. \tag{2.8}$$

I have evidenced here that all properties behave as powers of the correlation length, close to the percolation threshold. Why is this so? Well, we have seen above that close to the percolation threshold, the properties are insensitive to the details of the system. This is because they are dominated by the geometry of the clusters. The geometry is itself controlled by ζ, which is a measure of the mean cluster radius, the size of the inhomogeneities in the system. This is why we expect the properties to depend solely on the length scale ζ.

Now, what happens if we study the properties of a large but finite system of linear size L? If $L \gg \zeta$ we can subdivide the system in $(L/\zeta)^D$ boxes of linear size ζ (D being the dimensionality of the system). In each of those boxes the geometry of the system is the same as in an infinite system, because the size of the box is as large as the typical size of the inhomogeneities given by ζ. Therefore in each box we will have $X \propto \zeta^{\chi/\nu}$, but X might also depend on the number of such boxes, giving $X(L, \zeta) = \zeta^{\chi/\nu} f_1(L/\zeta)$.

On the other hand, when $L \ll \zeta$, the size of the inhomogeneities in the system will be limited by the system size, and therefore we expect to have the same dependence as above, but with L instead of ζ so that we obtain $X(L, \zeta) = L^{\chi/\nu}$.

Those considerations can be summarized in a general scaling law

$$X(L, \zeta) = \zeta^{\chi/\nu} f(L/\zeta), \tag{2.9}$$

When $L \gg \zeta$, all boxes of linear size ζ are similar and therefore we expect a property X to depend on the number of boxes as it would depend on the

volume in a homogeneous system. We expect some properties, such as the strength of the infinite cluster P or the mean cluster size S, to be independent of the number of boxes $(L/\zeta)^D$ when $L \gg \zeta$, so that $f(x \gg 1) \simeq constant$. Now, properties such as the mass of the infinite cluster (number of nodes in the infinite cluster) are expected to scale as the number of boxes $(L/\zeta)^D$, whereas the length of the shortest path leading from one end of the system to the other l_{min} should depend linearly on L/ζ. From this we finally obtain that

$$\begin{aligned} f(L/\zeta \gg 1) &\propto \left(\frac{L}{\zeta}\right)^{D_X} \\ f(L/\zeta \ll 1) &\propto \left(\frac{L}{\zeta}\right)^{\chi/\nu} \end{aligned} \tag{2.10}$$

with D_X a dimension between 0 and D determining how a property would depend on the size of the system if it were homogeneous. Using $\zeta \propto (p-p_c)^{-\nu}$ and the equations 2.10 for f, we can rewrite equation 2.9 as

$$X(L,\zeta) = \begin{cases} (p-p_c)^{-\chi+\nu D_X} L^{D_X} & L \gg \zeta \\ L^{\chi/\nu} & L \ll \zeta \end{cases} . \tag{2.11}$$

This scaling form has no formal demonstration, but agrees with all analytical and numerical results obtained so far. We see in this equation that the correlation length is of particular interest, as it gives a crossover length between two distinct behaviours. The determination of the critical exponent ν is very important as the use of finite size scaling (studying the behaviour of a quantity X on the percolation threshold as a function of the system size) permits usually more accurate determination of the ratio χ/ν than separate studies of the two exponents. In two-dimensional systems the correlation length exponent is exactly known to be $\nu = 4/3$ and in three dimensions, numerous estimates agree on the value $\nu \simeq 0.88$ [9, 10]. Estimates of ν in two to five dimensions can also be found in Ref. [11].

2.2.3 Square lattice

To get a better feeling about the scaling laws derived above, we will now look at some more properties in lattice percolation, but this time in a two-dimensional square lattice. We consider the bond percolation problem on a square lattice of size L (taking the distance between two adjacent nodes to be normalized to 1), as illustrated in figure 2.5. Each site has $k = 4$ neighbours, and more generally in a D-dimensional hypercubic lattice $k = 2D$. In two dimensions the percolation threshold is $p_c = 0.5$. In figures 2.3 and 2.4 I have plotted some examples of bond percolation on the square lattice and drawn the largest cluster in red, whereas all other clusters of size $s \geq 2$

are shown in blue, isolated sites are not shown. In figure 2.3 I show three different realizations of the bond percolation problem on a lattice of size $L = 30$ and at three different concentrations $p = 0.4$, $p = p_c$ and $p = 0.6$. The aim here is to show the influence of the correlation length ζ on the fluctuations. We see that at $p = 0.4$ the three realizations are very similar to one another, with a largest cluster of approximately the same size in all three cases. The same is true above the percolation threshold, at $p = 0.6$, where the largest cluster percolates the system and occupies almost the whole lattice with some holes of typically a few sites (corresponding to the length scale ζ). Now at p_c the situation is quite different: the three realizations show very different behaviours. In the left panel the largest cluster percolates the system, whereas in the two others it does not. Considering its mass, we can see that it is also very variable at this length scale (in a system of size $L = 30$). This is of course due to the divergence of ζ, so that here the system size $L \ll \zeta$, so that we are unable to get a correct image of the geometry of the percolating cluster. In fact, as shown in figure 2.4, the percolating cluster at p_c has inhomogeneities at all length scales. Its surface and interior contains holes of all sizes, ranging up to the system size L, regardless of L. It therefore presents a fractal geometry. Indeed, if we look at the strength P of the percolating cluster we know from the above equations 2.5 and 2.10 that at p_c

$$P \propto L^{-\beta}, \tag{2.12}$$

and $\beta = 5/36$ in two dimensions, showing that the percolating cluster is fractal. On the contrary if we look at the three panels of figure 2.4 for $p = 0.6$, we see that the sizes of the inhomogeneities in the infinite cluster are not changing with the system size, because $L \gg \zeta$, at least for the $L = 30$ and $L = 60$ cases. Therefore we have a constant strength of the infinite cluster (P is independent of the system size in that case).

If we looked at the mass $M = L^d P$ of the system, we would find that $M \propto L^{D_m}$. From the above results on P we immediately deduce that above p_c, $D_m = D$, whereas at p_c

$$D_m = D - \beta/\nu. \tag{2.13}$$

Equation 2.13 is called a hyper-scaling relation because it links several critical exponents and the dimensionality D of the system.

This change of the characteristics of the percolating cluster close to the percolation threshold, and our inability to capture correctly its geometry in a system of finite size, will lead to the increase of the intrinsic variability of any property X measured in a system of finite size as p_c is approached. This remark makes it evident that the error on the value of any parameter extracted from several realizations of a system of finite size will steadily increase as $p \to p_c$.

Indeed if X_i is the value of the property X measured for a certain realization of a system of finite size, we estimate X from the mean value $\bar{X}$ over N_s realizations:

$$X \simeq \bar{X} = \frac{1}{N_s} \sum_{i=1}^{N_s} X_i. \tag{2.14}$$

The standard deviation of the distribution of X_i is then given by

$$\sigma(X) = \sqrt{\frac{1}{N_s - 1} \sum_{i=1}^{N_s} \left(X_i - \bar{X}\right)^2} \tag{2.15}$$

and the standard deviation of the mean value $\bar{X}$ is then obtained from

$$\sigma(\bar{X}) = \frac{\sigma(X)}{\sqrt{N_s}}. \tag{2.16}$$

As close to p_c the variability, given by $\sigma(X)$ will increase, so will the error on the average for which we used twice the standard deviation $\sigma(\bar{X})$. This increase of the error bars will be repeatedly observed in our numerical simulation data of the conductivity and piezoresistivity of percolating systems, obtained from mean values over several realizations of systems of finite size.

2.3 Random resistor networks

Now that we have some basics in percolation theory, we can turn to models of the conductivity in heterogeneous disordered materials. We start again on the square lattice, but we superimpose a conduction mechanism on the bond-percolation problem. We now imagine that a bond between site i and j has conductivity $g_{ij} = 1$ with probability p (occupied bond) and is otherwise insulating (bond empty with probability $(1 - p)$). This problem can be rewritten as choosing the conductance between any pairs of neighbouring nodes from the distribution function

$$\psi(g) = (1 - p)\delta(g) + ph(g) \tag{2.17}$$

with $h(g) = \delta(g-1)$ and δ the Dirac delta function. We measure the conductance G of this system by applying a unit voltage between two opposite edges (or surfaces in 3D) of the lattice and measuring the current flowing through the lattice. This system, called a random resistor network (RRN), was studied numerically for the first time by Kirkpatrick in 1973 [12] and is illustrated in figure 2.5. To avoid the geometrical dependence of the conductance we use here the conductivity $\Sigma = GL^{D-2}$. It is obvious that this random resistor network will also undergo a percolation transition at $p_c = 0.5$, where the conductivity of the system will vanish, as there will be no more infinite

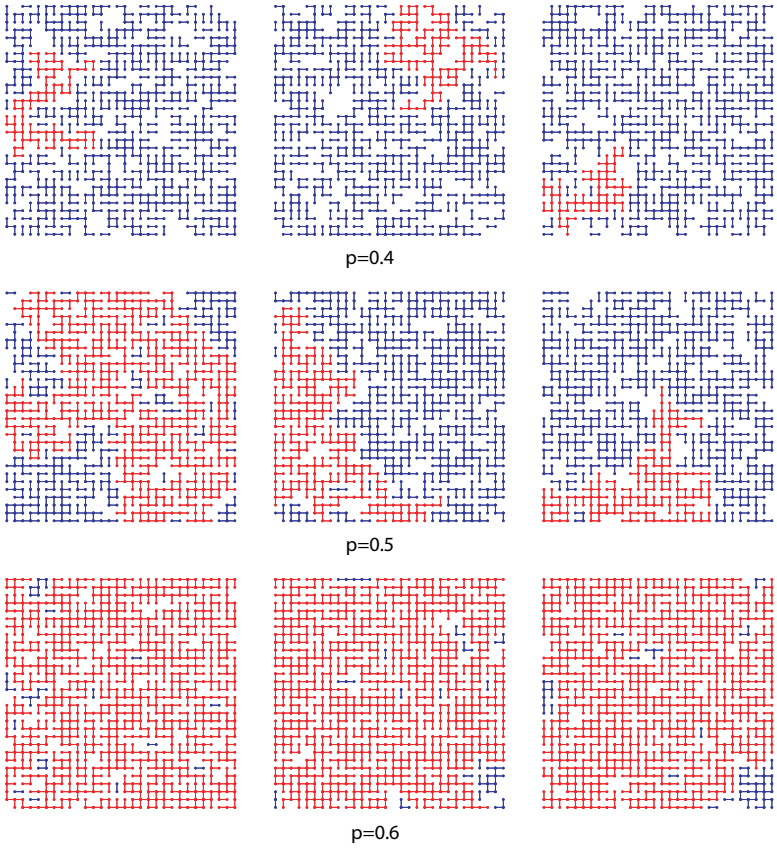

Figure 2.3: Bond-percolation on a square lattice of size $L = 30$. The largest cluster in the system is shown in red, whereas the other clusters containing at least two nodes are shown in blue. Three different realizations are shown for three different concentrations, one above, one on and one below the percolation threshold $p_c = 0.5$.

cluster percolating the system for $p < p_c$. We can write from what we have learned in section 2.2.2

$$\Sigma = \Sigma_0 (p - p_c)^t \tag{2.18}$$

for an infinite system. t is the direct current (DC) transport critical exponent. In his paper Kirkpatrick found that $t = 1.6 \pm 0.2$ in three-dimensional systems and between 1 and 1.3 in two dimensions. More recent numerical studies have refined those estimates and we now currently admit that $t \simeq 2$ in three dimensions and $t \simeq 1.3$ in two dimensions. For example

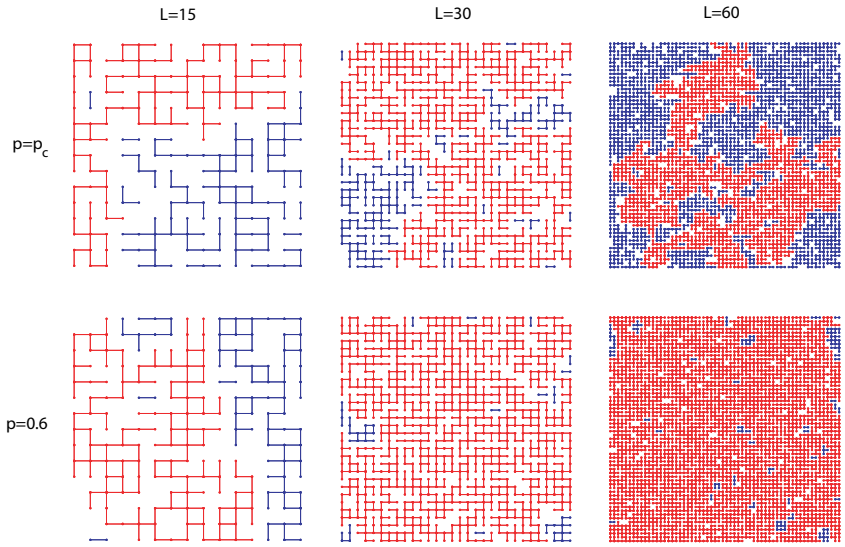

Figure 2.4: Bond-percolation on a square lattice. The largest cluster in the system is shown in red, whereas the other clusters containing at least two nodes are shown in blue. Three different system sizes $L = 15$, 30 and 45 are shown for two concentrations, one above and one on the percolation threshold $p_c = 0.5$.

Gingold [13] obtained $t = 2.003 \pm 0.047$ on a cubic lattice and Derrida found $t/\nu = 0.95 \pm 0.01$ [14] and $t/\nu = 2.2 \pm 0.1$ [15], in respectively two and three dimensions, using a transfer matrix approach. Normand found $t/\nu = 0.9745 \pm 0.0015$ [16] for the square lattice. In the four last estimates cited here it is t/ν and not t that was obtained, as finite size scaling was used. The values $t \simeq 2\,(\text{or } 1.3)$ can be extracted using $\nu = 0.88\,(\text{or } 4/3)$ in three (or two) dimensions.

We can note here that the conductivity increases much slower than the strength of the percolating cluster. Indeed $P \simeq (p - p_c)^\beta$ with $\beta = 5/36$ and $\beta = 0.41$ in two and three dimensions respectively, compared to the exponents for the conductivity that are much larger. In fact we even see that P approaches p_c with an infinite slope, whereas Σ with zero slope. This is due to two reasons. First, close to p_c only a tiny part of the percolating network participates to the conductivity, as most of its mass is in so-called dead ends, branches that lead nowhere. The current carrying part of the infinite cluster is called the backbone and scales with a critical exponent $\nu(D - D_b) = 0.53\,(1.14)$ [11,17] in two (respectively three) dimensions, which are larger than β, showing that the mass of the backbone becomes negligible compared to the mass of the percolation cluster as the percolation threshold is approached. Second, the shortest path l_{min}, leading through the system

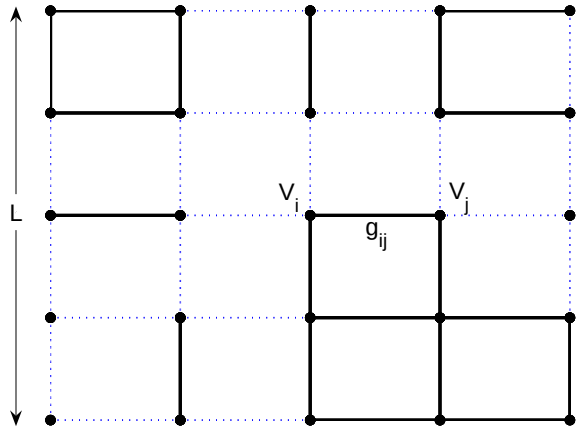

Figure 2.5: Illustration of a random resistor network on a square lattice. The empty bonds are shown as dashed lines and the occupied ones as plain lines.

on the percolating cluster, becomes very tortuous close to p_c and scales as $(p - p_c)^{\nu(1-D_{min})}$, with $\nu(1 - D_{min}) = -0.173\,(-0.33)$ in two (three) dimensions [18], therefore diverging as p_c is approached.

As any critical exponent, t is universal, depending solely on the dimensionality of the system, and not on its details such as the type of lattice (square, triangular, honeycomb) or the conductances distribution function $h(g)$. It should even stay the same for non lattice (continuum) systems that we will consider in section 2.4. To better understand where this universality comes from and why it is sometimes broken, as was shown in figure 1.1, we need to introduce some suitable tools to study analytically the conductivity of percolating systems.

2.3.1 Effective medium theory

The effective medium theory (EMT) was introduced for random resistor networks by Kirkpatrick [12] and provides a simple tool to obtain approximate solutions for the conductivity equations on a RRN which can be written as

$$\sum_{j=1}^{k} g_{ij}\Big(V(i) - V(j)\Big) = 0, \tag{2.19}$$

where the sum runs over the k neighbours of node i, and V_i is the voltage at node i, as shown in figure 2.5. Those equations are simply the conservation equations for the current at each node. The effective medium theory equation is obtained by replacing the influence of the RRN on the current flowing

through one particular g_{ij} by an effective medium consisting of a network of identical conductances having the mean conductance of the network G. The condition that the fluctuations average out over a large region in the system gives the EMT equation

$$\int_0^\infty dg\, \psi(g) \frac{G-g}{g+(k/2-1)G} = 0, \tag{2.20}$$

where $\psi(g)$ is the distribution function of the conductances in the system, as defined in equation 2.17. This equation gives the best first order approximation of the fluctuations stemming from the fact that not all links in the network have the same conductance, $\psi(g) \neq \delta(G)$. The derivation of those equations can be found in [12]. Using $\psi(g) = (1-p)\delta(g) + ph(g)$ equation 2.20 is easily transformed into

$$\int_0^\infty dg\, h(g) \frac{g-G}{g+(k/2-1)G} = \frac{1-p}{p(k/2-1)} \tag{2.21}$$

This equation is valid for the bond-percolation problem, but it can also be derived in other cases, notably for site-percolation and continuum percolation. Those generalizations can be found for example in the book of Sahimi [19], containing a lot of applications of the effective medium theory.

2.3.1.A Solutions of the EMT and universality

Equation 2.21 can be exactly solved in some cases, starting with the RRN considered in section 2.3 characterized by $h(g) = \delta(g-g_0)$, all occupied links having the same conductance g_0. It is straightforward to obtain the solution for G

$$G = g_0 \frac{p-2/k}{1-2/k} \tag{2.22}$$

showing that the critical exponent of the EMT is $t = t_0 = 1$ and the critical concentration $p_c = 2/k$. Though this result doesn't yield the correct exponent t for the conductivity of the original system ($t = 1.3$ or $t = 2$), it nevertheless holds a solution qualitatively in agreement with percolation theory. This solution again also yields the concept of universality, as p_c is dependent on the underlying lattice, but t is not. Moreover, close enough to the percolation threshold, this equation leads to the same $p - p_c$ dependence with $t = 1$ for any well-enough behaved $h(g)$. Indeed we can rewrite equation 2.21 as follows:

$$\begin{aligned} \frac{1-p}{p(k/2-1)} &= \int_0^\infty dg\, h(g) \frac{g+(k/2-1)G-(k/2-1)G-G}{g+(k/2-1)G} \\ &= \int_0^\infty dg\, h(g) - \int_0^\infty dg\, h(g) \frac{k/2G}{g+(k/2-1)G} \end{aligned} \tag{2.23}$$

As the distribution function $h(g)$ has to be normalized, we obtain

$$p_c \frac{p-p_c}{p(1-p_c)} = G \int_0^\infty dg \, \frac{h(g)}{g + (k/2-1)G} \simeq G \int_0^\infty dg \, \frac{h(g)}{g} \tag{2.24}$$

where the last equality holds close to p_c, when $G \simeq 0$. Now if $\int dg\, h(g)/g$ is finite the above equation will yield again $G \propto (p-p_c)^1$, so that we obtain the universal behaviour of the conductance as long as $h(g)$ decreases fast enough for small values of g.

2.3.1.B Distribution-induced non-universality

Kogut and Straley were the first ones to propose that non-universality could be induced by the distribution function $h(g)$ [20]. Indeed as we saw above universality is obtained as long as $\int dg\, h(g)/g$ is finite. Let's see now what happens if we take

$$h(g) = (1-\alpha) g^{-\alpha} \Theta(1-g) \tag{2.25}$$

with Θ the heaviside step function defined as $\Theta(x) = 1$ for $x > 0$ and $\Theta(x) = 0$ for $x < 0$. This distribution function is normalized for all $\alpha < 1$ and the parameter α controls the behaviour for $\lim_{g\to 0} h(g)$. We now study the critical behaviour of the conductance G, when $p \to p_c$, using equation 2.24.

$$\int_0^\infty dg \, \frac{h(g)}{g} = \int_0^1 dg \, (1-\alpha) g^{-(\alpha+1)} = \begin{cases} -\frac{1-\alpha}{\alpha} & \text{for } \alpha \leq 0 \\ \infty & \text{for } \alpha > 0 \end{cases} \tag{2.26}$$

We therefore obtain again the universal behaviour for $\alpha \leq 0$, but we have a problem for $\alpha > 0$, in which case we have to be a little more cautious to obtain the behaviour of G. We start again from equation 2.24 but without simplifying the denominator in the integral, which cannot be done if $\int h(g)/g dg$ does not exist. To solve this, we separate the integral into two parts, in which one of the terms in the denominator is dominant. Using $w = (k/2-1)$ we have

$$\begin{aligned} \frac{p_c(p-p_c)}{Gp(1-p_c)} &= \int_0^{wG} dg \, \frac{h(g)}{g+wG} + \int_{wG}^\infty dg \, \frac{h(g)}{g+wG} \\ &\simeq \int_0^{wG} dg \, \frac{h(g)}{wG} + \int_{wG}^\infty dg \, \frac{h(g)}{g} \\ &= \frac{(wG)^{-\alpha}}{\alpha} - \frac{1-\alpha}{\alpha} \\ &\simeq \frac{(wG)^{-\alpha}}{\alpha} \end{aligned} \tag{2.27}$$

where the last equality is obtained for small G and $\alpha > 0$, so that we can finally write

$$G \propto \begin{cases} (p - p_c) & \text{for} \quad \alpha \leq 0 \\ (p - p_c)^{\frac{1}{1-\alpha}} & \text{for} \quad \alpha > 0 \end{cases} \tag{2.28}$$

We see here the appearance of non-universality, induced by the anomalous behaviour of the distribution function $h(g)$ diverging for $g \to 0$. This situation can be fairly well understood by noting that in equation 2.27 the non universal behaviour can be obtained by looking solely at the second integral in the first line, which is of the form

$$\int_G^\infty \frac{h(g)}{g} dg = \langle g^{-1} \rangle_{\{g>G\}}.$$

This integral is the mean value of the microscopic conductances with $g > G$, noted here as $\langle g \rangle_{\{g>G\}}$, so that we can obtain from equation 2.27

$$G \propto (p - p_c)^{t_0} \langle g^{-1} \rangle^{-1}_{\{g>G\}}. \tag{2.29}$$

We see here that the non-universality stems from the divergence of the mean local conductivity, superimposed on top of the normal divergence of $G \propto (p - p_c)^{t_0}$ (which has a geometrical origin). This can be understood as follows: far above p_c the conducting path is made of lots of parallel routes, so that the current can avoid the very low local conductances. When p_c is approached, there are more and more singly connected bonds, through which the whole current has to flow, so that $h(g)$ will be probed for lower values of g. Therefore the non-universal behaviour is induced by the fact that the mean value of the conductance the current has to flow through in the system diverges as p_c is approached.

This result has since been refined outside the frame of the EMT and it was shown that the critical exponent t of a D-dimensional system with a distribution function $h(g)$ behaving as in equation 2.25, is given by [21, 22]

$$t = \begin{cases} t_0 & \text{if} \quad (D-2)\nu + \frac{1}{1-\alpha} < t_0 \\ (D-2)\nu + \frac{1}{1-\alpha} & \text{if} \quad (D-2)\nu + \frac{1}{1-\alpha} > t_0 \end{cases} \tag{2.30}$$

2.4 Continuum percolation

The random resistor network model allowed us to understand the power-law dependencies of the properties on the system size and phase concentrations. It also allowed us to understand how non-universality could stem from a very broad distribution function of the microscopic conductances in the network, $h(g)$. Now, in order to justify the observed non-universality in real systems, we have to show why RRN can be used as realistic models of disordered

conductor-insulators and how diverging $h(g)$ can be obtained in this framework. In this section we will look at several models of continuum percolation and try to answer those questions, and finally justifying our particular choice of the tunnelling-percolation model as basis for this thesis.

2.4.1 Swiss cheese model

The first experimental measurement of the conductivity of a percolating system was made by Last and Thouless in 1971 [23]. They measured the conductivity of a colloidal graphite sheet with holes randomly punched in it. In this experiment they showed that the conductivity indeed behaved as $(p - p_c)^t$ with $1 < t < 2$. In fact, as it is a two-dimensional system, the exponent is $t = 1.3$, but their results were not good enough to allow a precise estimation of t. Anyway, it is clear that the results obtained for the RRN apply to this particular percolation material. The Swiss cheese (or random void) model depicts this situation, but also the flow of a liquid in a sedimentary rock. We note here that even though electrical conductivity and liquid flow are similar, they are not completely identical phenomena. Indeed the volume flowing through a cylinder of radius R is proportional to R^4, whereas the electrical current flow is proportional to the section $\propto R^2$. This can lead, as stated below, to different critical exponents for those two phenomena.

We consider a continuous conducting phase with randomly placed spherical insulating inclusions. The insulating spheres are penetrable and can therefore overlap and conduction takes place in the remaining free space. Kerstein [24] showed that this continuum percolation problem was equivalent to a bond percolation problem on the edges of the Voronoi tessellation of the sphere centers. A tessellation is a decomposition of space into regions that fill the whole space with no gaps and no overlaps and the Voronoi tessellation considered here is formed by such regions consisting of all points closer to the center of one sphere than to any other. The construction of the model and its associated network is shown in figure 2.6 for two dimensions. A similar construction can be done in three dimensions, where the cells of the Voronoi tessellation are polyhedra, and the percolation problem is defined on the edges of those polyhedra. As this problem can be mapped on a network, it has the same geometrical critical exponents as a lattice percolation problem (such as ν, β, D_m, *etc.*).

Now regarding the electrical transport, each bond of the tessellation network has a conductivity depending on the width of the channel passing between the insulating spheres. Close to the percolation threshold, the conductivity is governed by very thin such paths, bottlenecks. It was shown that the distribution function of those conductivities is precisely of the form of equation 2.25, with $\alpha = -1$ and $\alpha = 1/3$ in two and three dimensions respectively [25]. This model therefore leads to a universal behaviour of

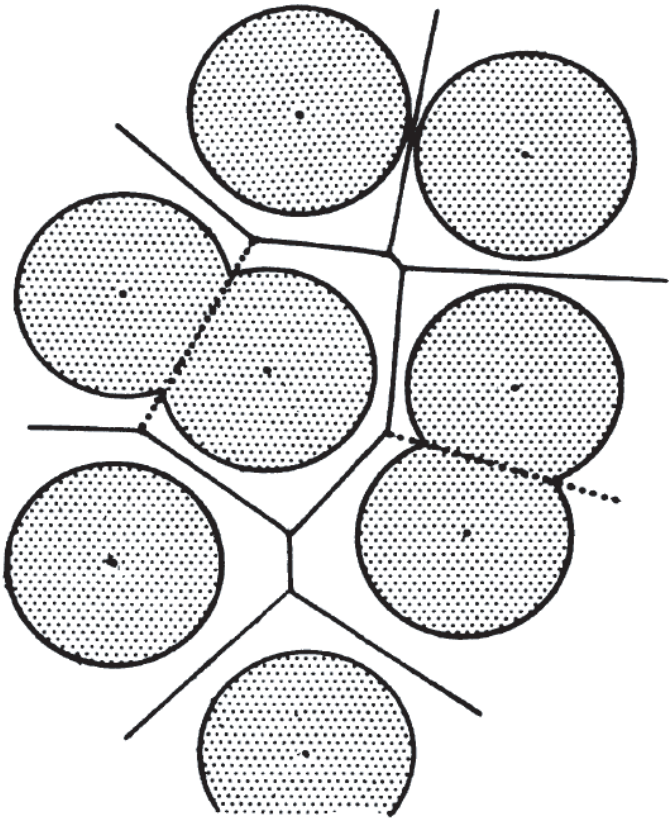

Figure 2.6: Illustration of the Swiss-cheese model in two dimensions. The straight lines show the bonds of the associated network, dotted lines are missing bonds. This figure is taken from Ref. [25]

the conductivity Σ in two dimensions, but to non-universality in three dimensions, giving $t = 2.38$. In this same article it is also shown that this model gives non-universal exponents for the flow of viscous fluids through the system $t = 2.5$ ($t = 4.38$) for a two-(three-)dimensional system.

In the framework of conductive composites, this model applies in principle only to composites where the size of the conducting particles is much smaller than the typical insulating grain size, so that the conducting phase can be safely approximated by a continuum. This model has been generalized to yield even larger t exponents, but with no strong physical background [26]. Anyway, non-universality has been reported also for composites whose microstructure cannot be described by a random-void construction, as for the case of some carbon-black/polymer composites displaying t values much larger than t_0 (see figure 1.1).

2.4.2 Inverted random void model

The inverted random void model is the same model as above, but with the phases being exchanged. The current now flows through the spherical inclusions and the remaining space is insulating. The mapping on a network is now very simple. The nodes are the center of the spheres, and the edges connect neighbouring overlapping spheres. The conductance of the bonds is now affected by the range of overlap of neighbouring spheres. If the spheres barely overlap, the resistance will be increased as the current has to flow through a very thin region. This model again gives rise to a distribution function of the form $h(g) \propto g^{-\alpha}$, but with values of α too small to break the universality of electrical transport [25].

This model could be a fairly good approximation for electrical conduction in composite materials consisting of an insulating matrix filled with conducting particles, where transport would occur through contact. But as we have seen, this model predicts a universal behaviour and is therefore unable the account for the experimentally-observed non-universal transport exponents. On the other hand the Swiss cheese model can lead to non-universality, but to just one class of non-universality, with a fixed value for the transport exponent, $t = 2.38$, again not accounting for the very broad range of observed t values.

2.5 Tunnelling-percolation model

The tunnelling-percolation (TP) model was introduced by Balberg [27] to explain non-universality in conductor-insulator composites. He proposed that the mechanism governing electrical conduction in most disordered conductor-insulator composites was tunnelling. This model is somewhat similar to the inverted random void except that the conduction between overlapping spheres is by tunnelling, giving an exponential dependency of the conductivity on the distance between the particles. Indeed the tunnelling conductance between two particles separated by a distance r is given by

$$g = g_0 \exp\left(-\frac{2r}{\xi}\right) \tag{2.31}$$

where g_0 is a constant prefactor and ξ the tunnelling decay factor, being typically of the order of a few nanometers. In such a model, all particles are electrically connected to all others, but because of the very rapid decay of the tunnelling conductance with r, we consider that conduction is dominated by nearest-neighbour tunnelling. Here we suppose that the conducting particles are point-like (with diameter $\sigma_1 = 0$), therefore the distribution function of the distance between nearest neighbouring particles is given by the Hertz-

distribution [27, 28]

$$P(r) = \frac{3r^2}{a^3} \exp\left(-\frac{r^3}{a^3}\right) \tag{2.32}$$

where a is the mean nearest-neighbour inter-particle distance. Balberg then simplified this distribution function into its "one-dimensional form", still carrying the essence of the problem $P(r) = (1/a)\exp(-r/a)$. Combining this with equation 2.31 we can obtain

$$h(g) = \frac{1-\alpha}{g_0}\left(\frac{g}{g_0}\right)^{-\alpha} \quad \text{with} \quad \alpha = 1 - \frac{\xi}{2a} \tag{2.33}$$

leading to non-universality for sufficiently small ξ/a values. The corresponding transport exponent is $t = \nu + 2a/\xi$ which can take any value $t \geq t_0$ and therefore account for all experimental t values.

2.5.1 Why tunnelling transport mechanism?

The choice of tunnelling as dominating conduction mechanism to model disordered conductor-insulator composites is motivated by several studies. It has been shown that the thermal and voltage [29, 30] and ac stress [31] dependencies of carbon-based disordered composites were well reproduced by fluctuation-induced tunnelling. Also the piezoresistivity in ruthenium-based metal-insulator composites supports a tunnelling conduction mechanism [32]. A study of field, temperature and stress dependence of graphite based conducting polymers also leads to the conclusion that tunnelling processes are of major importance above but close to the percolation threshold [33, 34]. Now in thick-film resistors, an extensive experimental study of their electrical properties (thermal, field and frequency dependence of the conductivity, dielectric constant, Hall mobility and Seebeck coefficient) was done by Pike and Seager [35] and lead to tunnelling conduction as the only choice explaining their experimental results.

A last important result supporting the tunnelling-percolation picture in thick-film resistors is a study of piezoresistivity. Indeed, as we have seen, the transport exponent, obtained from the tunnelling-percolation model, when non-universal, depends on the mean nearest neighbour distance a. It can therefore be changed by an applied external strain, leading to a characteristic behaviour of the piezoresistivity Γ as the percolation threshold is approached [5]. It is easy to show (and we will come back to this later on, in section 4.4.2) that

$$\Gamma = \begin{cases} \Gamma_0, & t = t_0 \\ \Gamma_0 - \dfrac{dt}{d\epsilon}\ln(x - x_c), & t > t_0 \end{cases} \tag{2.34}$$

which has been experimentally well confirmed and is a feature unique to the tunnelling-percolation model [5]. All those experimental results therefore comfort our choice to study models in which tunnelling is the dominating transport mechanism.

Nevertheless there are still open questions with this tunnelling-percolation model. First of all, in many composites, this model would predict values of $t \approx 50$, taking reasonable values for $a = 50$ nm and $\xi = 1$ nm, whereas the largest t values experimentally observed are of the order of $t \simeq 10$ [36]. The second issue is the one-dimensional form of the Hertz distribution function that is used in the model. As we will see in more detail in chapter 4, this was physically justified for the case of segregated conductor-insulator composites [37], but has no physical origin in the non-segregated ones. Moreover, even in the segregated composites, a more careful analysis of the situation shows that this one-dimensional distribution function cannot be obtained in real systems. Therefore we will study in this thesis the tunnelling-percolation with more realistic nearest-neighbour distribution functions, on lattice and in the continuum, trying to lift the weaknesses of the original tunnelling-percolation model.

Chapter 3

Thick-Film Resistors

In this chapter we will examine the principal experimental results obtained for the electrical transport properties of Thick-Film Resistors (TFRs), which are the materials guiding the theoretical work of this thesis. We will present an experimental study of high-voltage trimming of TFRs and we will also discuss their fabrication process and use as model systems for our upcoming theoretical studies. These composites are of particular interest because they are both widely used in applications and have several interesting theoretical features. Indeed, they have a complex microstructure, due to segregation of the conducting phase, and complex transport properties, dominated by inter-grain tunnelling. They present non-universal transport exponents, large piezoresistive responses and unusual thermal coefficients of resistance, properties that need to be better accounted for by theoretical models.

3.1 Composition and fabrication process

Thick-film technology is mainly used in hybrid electronic circuits. One of its main characteristics is the method used for the film deposition, namely screen printing. Screen printing was traditionally used in art reproduction, but was modernized to allow a more precise film deposition and is illustrated in figure 3.1. This process is very simple: the paste is forced through a screen onto the substrate by a squeegee. The screen is usually made of finely woven stainless steel wires, with an UV-sensitive emulsion on top. The desired pattern is obtained by positive or negative exposition of the screen and development to remove the emulsion in the pattern regions. The standard substrate is aluminum oxide, a very stable and chemically quite unreactive compound. Several successive layers can be deposited and co-fired, as long as the pastes are dried before a new deposition step.

There are mainly three different paste types: conductive, insulating and resistive. In this work we study the characteristics of the resistive pastes, which serve as passive resistors in hybrid circuits, but also as strain-sensing

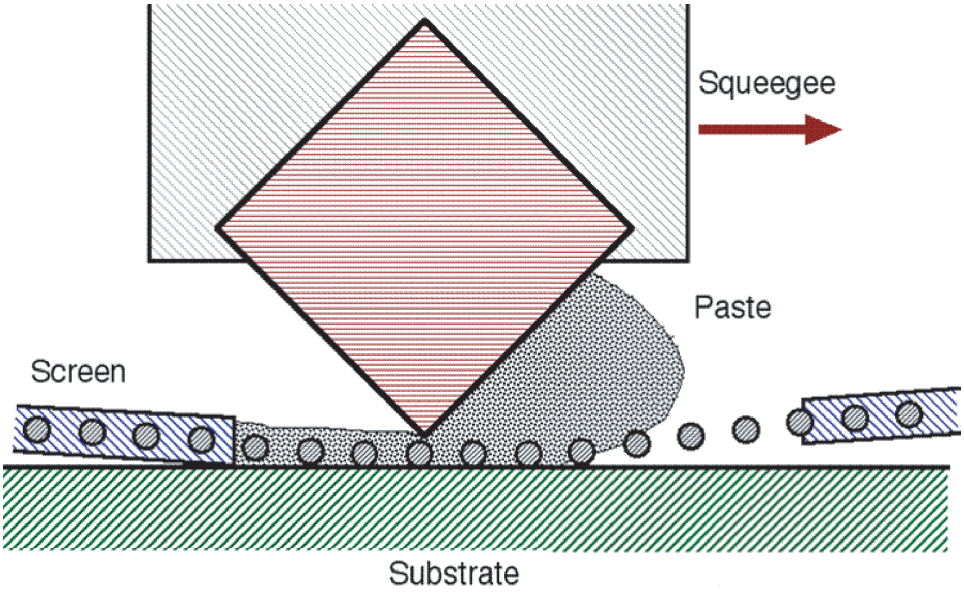

Figure 3.1: Illustration of the screen-printing process

elements, mainly due to their large piezoresistance. Modern resistive pastes, usually of resistivity around 10 mΩ·m and above, consist basically of a mix of two powders: a fine-grained ($20 - 100$ nm in diameter) conductive phase (RuO_2 or ruthenate) and a lead borosilicate glass frit ($1 - 3$ μm). A temporary organic vehicle (solvent and binder) is added in order to control the viscosity and allow screen-printing.

After screen-printing, the pastes have to be dried and fired. This can be done in one single firing cycle [38], constituted of a heating step, slowly increasing the temperature (100 K/min) up to the peak temperature (typically 850°C, attained in 10 minutes), a high temperature plateau and a cooling stage. The drying is done at temperatures below 150°C leading to the evaporation of the volatile organic vehicle. After this first drying step, the remaining (polymer) binder gives the dried film moderate mechanical stability, so that the screen-printed film can be manipulated for other printing steps. Then between 150 and 450°C, the remaining organics are essentially removed. Finally, towards the end of the heating ramp (from about 400 to 700°C) and during the high temperature dwell (typically around 10 minutes), the glass frit softens and sinters. Various chemical and physical reactions may also take place at this temperature. At last the system is cooled down to ambient temperature, again in typically ten minutes [38].

3.2 Microstructure of TFRs

As pointed out in the preceding section, a TFR is made of a mixture of large insulating grains and a finer conducting powder. Because of the size difference, the conducting grains are forced into the spaces left over between the large insulating ones. During the firing step, the glassy phase softens and sinters, wetting and enclosing the conducting grains, but the final compound basically conserves its initial geometrical structure. This particular microstructure, with large insulating regions surrounded by small conducting grains, is called a segregated structure. A scanning electron microscopy image of an RuO_2-based thick-film resistor is shown in figure 3.2, where this segregated microstructure is clearly seen. We see that there are extended insulating regions of several μm. The conducting grains form both large conducting regions of sizes up to a few μm and one-dimensional like chains.

What is interesting about segregation is that it lowers the percolation threshold, allowing to obtain electrical conduction at lower filler concentrations (around a few percent volume fraction). This is a valuable effect, since the conducting powders are usually very expensive. In other composite systems the lowering of the percolation threshold can also be desired to benefit from the properties of the charge, without degrading too much those of the matrix. For example low filler contents in conducting polymers allow to maintain the mechanical properties and ease of process of the initial insulating phase, also not increasing too much its density, which can be of importance for example in aerospatial applications. The segregated structure of TFRs is also interesting from the theoretical point of view, as it adds some geometrical inhomogeneity to the system. This will be studied in chapter 6 using a model specially designed to represent the structure of TFRs.

3.3 Transport properties and piezoresistivity

We now turn to the transport properties of the TFRs. As we have seen in figure 1.1, the TFRs are an important class of the composites presenting transport non-universality. Measurements of the conductivity of four series of RuO_2-based TFRs, fabricated by our group, are presented in figure 3.3. Our samples were prepared starting with a glass frit with the following basic composition: PbO (75% weight), B_2O_3 (10% wt.) and SiO_2 (15% wt.), with additional 2% wt. of Al_2O_3 added to avoid crystallization. The softening temperature of this glass was shown to be around 460°C. After milling, the glass powder presented an average grain size of about 3 μm. The characteristics of the four series of TFRs are combinations of two different RuO_2 grain sizes and two firing temperatures T_f and are presented in table 3.1. Those experimental results are taken from Ref. [5], where more details can be found about the sample preparation. The simple power law of equation 1.1 was

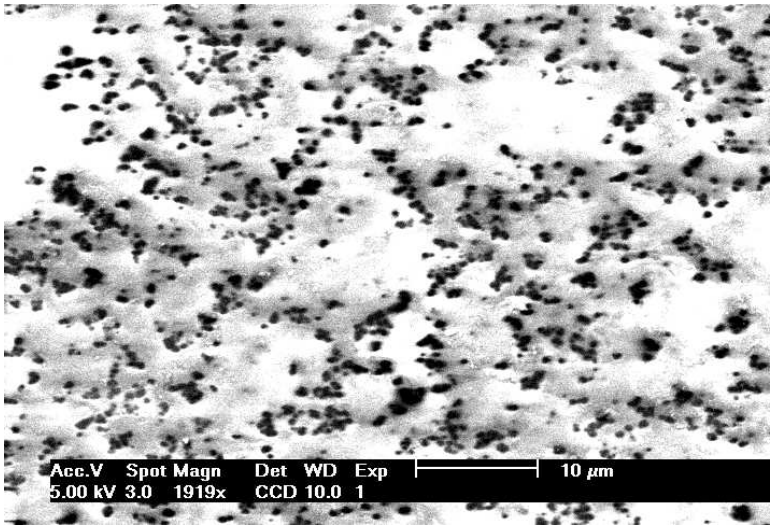

Figure 3.2: SEM image of the surface of a RuO_2-based TFR, with conductor volume fraction $x \simeq 0.08$, conducting grain size of 40 nm and average glass grain size of 3 μm after milling. This image is taken from the work of Vionnet [5]. The conducting phase appears dark, whereas the insulating regions are light-coloured

fitted to the conductivity data of figure figure 3.3(a) and the resulting fits are then shown as black lines in figure 3.3(b) in double logarithmic scale. It is clear from this figure that the conductivity of TFRs is well described by equation 1.1. For comparison the universal behaviour is shown as a black dashed line, evidencing that only the $A1$ series has a universal behaviour, whereas the three others have transport exponents $t > t_0$. The so extracted transport exponents t and critical volume fractions x_c are reported in table 3.1. We see from this table that the critical volume fraction of those TFRs is typically around 6%. This is far below the percolation threshold of a dispersion of spheres with conduction through contacts, which is $x_c \simeq 0.64$ (random close packing of hard spheres [39]). This difference is mainly due to the segregation of the conducting phase, and probably to a non-contact conduction mechanism such as tunnelling.

The piezoresistive factor Γ, of the same series of samples, is shown in figure 3.4(a), where we see the strong enhancement of Γ as the percolation threshold is approached, at least for three of the four series (the $A1$ series presenting a a constant Γ). Now in panel (b) of this figure, we show that Γ has in fact a logarithmic divergence for the three non-universal sample series, whereas it is constant for the last one, having a universal transport exponent. The fits to equation 2.34 are shown as straight lines in this panel, confirming the good agreement with a logarithmic divergence. $-dt/d\varepsilon$, given in table 3.1 is the slope of the logarithmic divergence. This feature, meaning a logarith-

Table 3.1: Characteristics of the various samples studied in Ref. [5] with fitting parameters of Eqs.(1.1) and (2.34)

Label	**A1**	**A2**	**B1**	**B2**
$\mathbf{RuO_2}$ **grain size**	400 nm	400 nm	40 nm	40 nm
$\mathbf{T_f}$	525°C	600°C	525°C	600°C
$\mathbf{x_c}$	0.0745	0.0670	0.626	0.525
$\ln(\mathbf{\Sigma_0}[\mathbf{Sm^{-1}}])$	11.1 ± 0.3	14.2 ± 0.2	14.3 ± 0.5	13.7 ± 0.7
$\mathbf{t}$	2.15 ± 0.06	3.84 ± 0.06	3.17 ± 0.16	3.15 ± 0.17
$\mathbf{\Gamma_0}$	16.5 ± 4.5	-26.4 ± 4.8	-45.9 ± 9	-57.9 ± 7.2
$\mathbf{d}t/\mathbf{d}\varepsilon$	-0.6 ± 1.2	16.2 ± 1.5	26.1 ± 2.7	33.0 ± 2.1

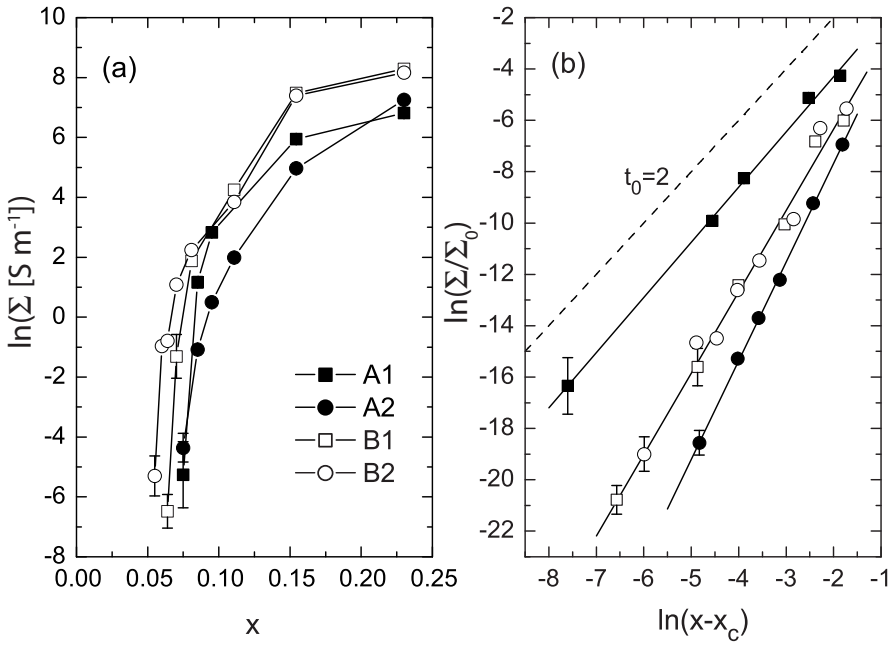

Figure 3.3: (a) Conductivity Σ as a function of RuO_2 volume fraction x for four different series of TFRs. (b) ln-ln plot of the same data of (a) with fits to equation 1.1 shown by solid lines. The dashed line has slope $t_0 = 2$ corresponding to universal behaviour of transport. The prefactor Σ_0, critical concentration x_c and transport exponent t values, obtained from the fits, are reported in Table 3.1. This figure is taken from Ref. [5].

mic divergence for non-universal systems, and a piezoresistance independent of the concentration for universal series, is one of the main experimental results supporting tunnelling-percolation origin of non-universality, and will be repeatedly verified in the models developed in this thesis.

The representation of Γ as a function of $\ln(x - x_c)$ is not very practical, as it is dependent on the determination of the percolation threshold x_c. From

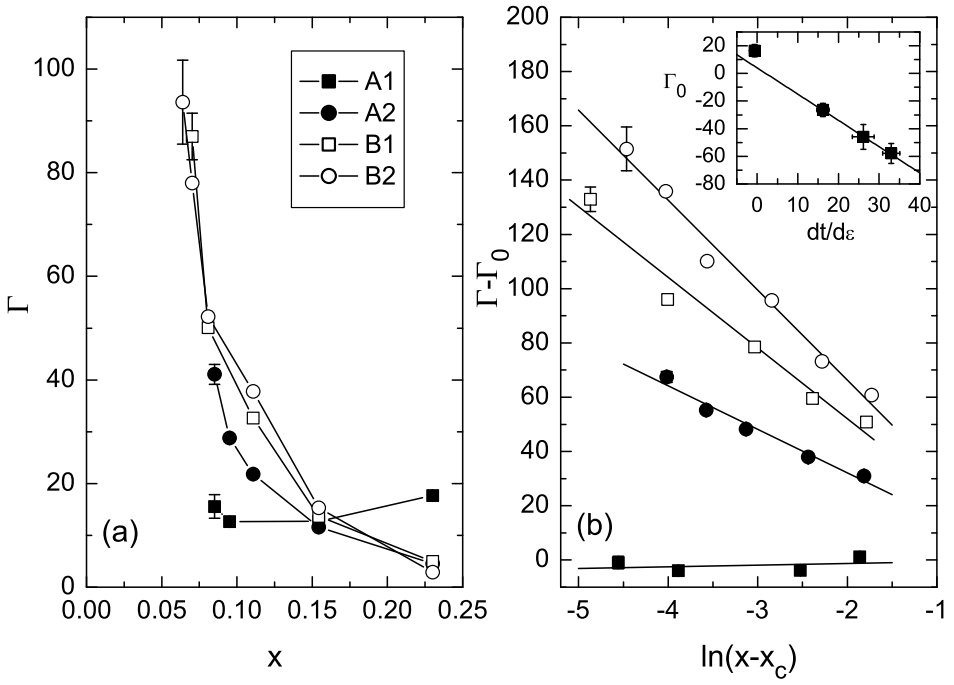

Figure 3.4: Piezoresistive factor $\Gamma = \Gamma_{\parallel} + 2\Gamma_{\perp}$ of the same TFRs of figure 3.3, plotted as a function of RuO_2 volume concentration x in panel (a) and as a function of $\ln(x - x_c)$ in panel (b) together with fits (solid lines) to Eq. (2.34). The fit parameters $dt/d\varepsilon$ and Γ_0 are reported in table 3.1. The inset shows the fitting parameter Γ_0, together with $\Gamma_0 = -1.9dt/d\varepsilon$ (solid line), which is of the form predicted by the TP model. This figure is taken from Ref. [5].

equation 2.34 and 1.1, it is clear that Γ does not only present a logarithmic divergence as a function of $x - x_c$, but also as a function of the conductivity Σ. We can rewrite Eq. (2.34) as

$$\Gamma = \begin{cases} \Gamma_0, & t = t_0 \\ \Gamma_0 + \frac{1}{t}\frac{dt}{d\epsilon}\ln(\Sigma_0/\Sigma), & t > t_0 \end{cases} \tag{3.1}$$

The results of figure 3.4 are shown as a function of Σ in figure 3.5, together with the fits to the above equation 3.1. This is how the piezoresistivity will be mostly studied in the remainder of this work, as it is a representation that is completely independent from any model and from the fit of the conductivity to equation 1.1. Those experimental results will be examined and compared to the theoretical work of this thesis in later chapters.

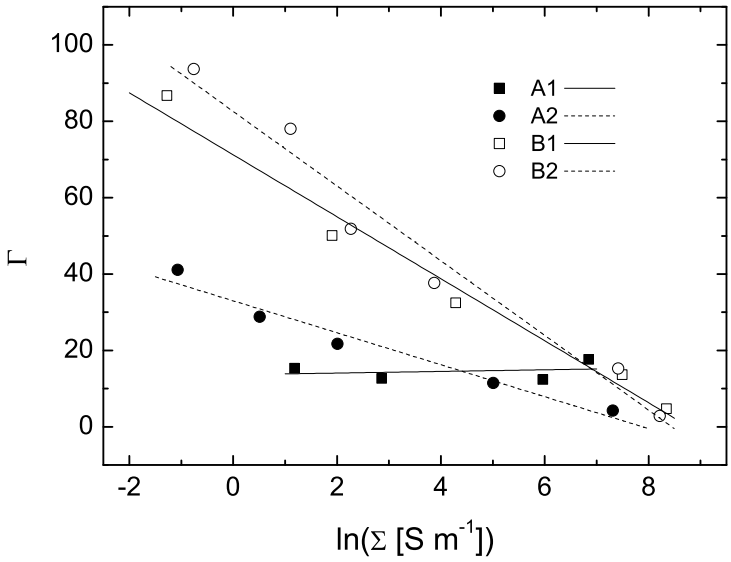

Figure 3.5: Piezoresistive factor $\Gamma = \Gamma_{\parallel} + 2\Gamma_{\perp}$ plotted as a function of the logarithm of the conductivity $\ln(\Sigma)$, where Σ is expressed in $[\mathrm{Sm}^{-1}]$, for the same samples as in figures 3.4 and 3.3. The lines are fits to equation 3.1

3.4 High-voltage trimming

Another interesting property of TFRs is their sensitivity to high voltage pulses. TFRs, when subjected to high-voltage pulses, undergo microstructural changes, altering the value of their resistance. This is of course not desired for electronic applications, as an undesired voltage pulse, due for example to a static electricity discharge, can permanently change the values of the resistances and damage the circuit. On the other hand this sensitivity to voltage pulses can be used to precisely adjust a resistor to a desired value. Indeed, in thick-film technology the production of a resistor with a precise value is very difficult. The variability of a resistor compared to its design value is as large as $20-30\%$ [40], and it usually has to be adjusted in order to fit the requirements for the production of reliable electronic devices. In industrial applications, this is usually done by laser trimming, though it damages the resistor, lowering its stability and causing a post-trim drift [41]. Pulse voltage trimming has several advantages compared to laser trimming. It is a cheap and effective method (it was shown to allow adjustments to less than 1% for RuO_2 based TFRs [40]), allowing trimming of buried or very small resistors. It was shown to be reversible [42, 43] and to make the trimmed resistors less sensitive to voltage pulses. Nevertheless this technique is not used in industrial applications because it causes a shift of the thermal

coefficient of resistance and has the disadvantage to make the resistors more sensitive to temperature, limiting its application to fields where the resistors aren't exposed to temperatures higher than 100°C [44].

3.4.1 Description of experiments

We present here an experimental study of high-voltage trimming of a series of TFRs, with the same compositions as the samples presented in section 3.3. Samples with different volume concentrations x of RuO_2, with 40 and 400 nm grain sizes, are considered, and the samples were fired at $T_f = 625$°C. More details about this study can be found in Refs [45, 46].

The setup used for the voltage trimming is rather simple. A capacitor is charged to the desired high voltage and then discharged through the resistance being trimmed. Our setup allows charging the capacitor up to 1500 V and its capacity can be changed between 0.1 and 10 nF. The value of the resistance is measured between two voltage pulses, or less often as the number of pulses gets high.

3.4.2 Experimental results

In this study we decided to set the same trim voltage and capacity for all measurements. We used respectively 500 V and 0.33 nF, and the trimmed resistors have a length of 0.8 mm, which gives an electrical field of 625 V/mm. Typical trimming results are shown in figure 3.6 where the conductance Σ of the sample relative to its conductance before trimming Σ_I is shown as a function of the number of pulses applied to the sample. The first pulses usually lead to important changes in the resistivity of the sample, which then tends toward an asymptotic final value after trimming Σ_T. We can already see from this figure that the conducting phase volume fraction has a strong influence on the sensitivity of the resistors to voltage pulses and that the conductivity of the most sensitive samples can be trimmed up almost an order of magnitude, as shown by the results for the sample with $x = 0.064$.

In what follows all samples were subjected to 2300 voltage pulses, so that the conductivity of the trimmed samples Σ_T corresponds to the conductivity after 2300 pulses. In the left panel (a) of Fig. 3.7 we show the inverse of the relative variation of the conductivity (Σ_I/Σ_T) as a function of the RuO_2 volume fraction, for the two particle sizes. If we define the sensitivity to trimming as

$$TS = 1 - \Sigma_I/\Sigma_T \tag{3.2}$$

one can notice that it increases monotonically as the volume fraction of the conducting phase is diminished. Tobita et al. had observed [40, 47] that the sensitivity to trimming was greater for larger conducting particles. This

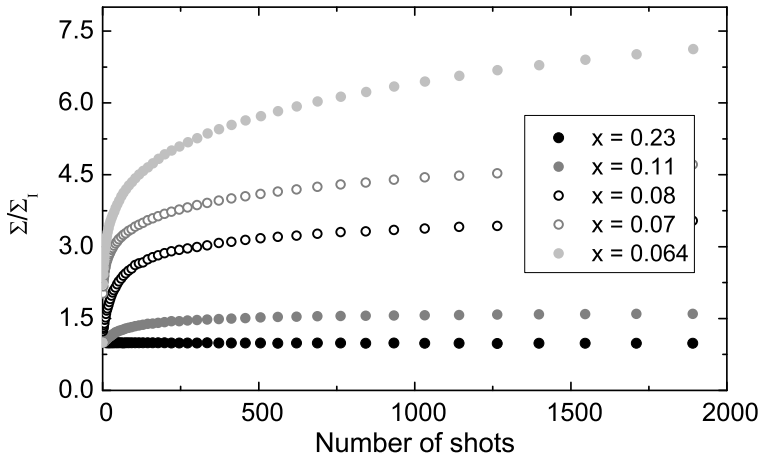

Figure 3.6: Evolution of the normalized conductivity $\Sigma/\Sigma_{\mathrm{I}}$ during trimming, for samples with 40 nm RuO_2 particles and for different volume fractions.

tendency is also observed here though it seems that the most important parameter governing this sensitivity is the volume fraction of the conducting phase. There seems to be a critical behaviour of the TS as a certain critical RuO_2 volume fraction is attained. The first intuition is of course that this volume fraction is the same critical concentration at which the conductor-insulator transition takes place. We calculated this critical concentration from conductivity measurements for 8 different volume fractions for both RuO_2 particle sizes and found

$$\begin{aligned} x_c &= 0.036 \pm 0.008 \quad \text{for 40 nm} \\ x_c &= 0.059 \pm 0.002 \quad \text{for 400 nm} \end{aligned}$$

If we now look at the conductivity change $\Sigma_{\mathrm{I}}/\Sigma_{\mathrm{T}}$ as a function of relative distance to x_c, shown in Fig. 3.7(b), we see that for both particle sizes, 40 nm and 400 nm, $\Sigma_{\mathrm{I}}/\Sigma_{\mathrm{T}}$ seems to vanish at the percolation threshold. This shows that the effectiveness of voltage trimming is somehow governed by the underlying current-carrying percolation network. More details about these results can be found in Ref. [45]

3.4.3 Post trim stability

Let us discuss now the stability of the TFRs after trimming. As already pointed out, the values of the resistors are expected to drift after trimming, especially if exposed to temperatures higher than 100°C. The post-trim stability was assessed by placing the trimmed samples in an oven for 80 hours at 100°C, followed by 85 hours at 250°C. Their characteristics were periodically

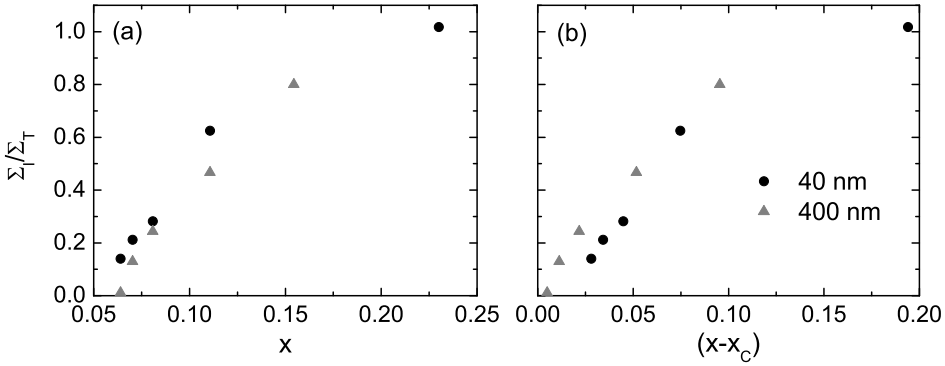

Figure 3.7: Relative change of the conductivity during trimming Σ_I/Σ_T, as a function of RuO_2 volume fraction x (panel (a)) and $x - x_c$ (panel (b)), for samples with 40 (black circles) and 400 nm (grey triangles) RuO_2 mean grain size.

measured during this period of time.

Fig. 3.8 shows the evolution of the conductivity of the 400 nm RuO_2 grain size series during trimming and their thermal stability as a function of RuO_2 volume fraction. It shows the initial conductivity, the conductivity after trimming, the conductivity at the end of the thermal treatment at 100°C and finally the conductivity after the 85 hours at 250°C. As already noticed in figure 3.7, samples with lower filler content are more sensitive to trimming. We notice that for all samples studied here, the trimming leads to an increase in conductivity. More interestingly we can see that for all samples except for the one closest to the percolation threshold, the thermal treatment also leads to an increase in conductivity, and not to a recovery of the initial value of the conductivity. The drift goes in the same direction as the change induced by trimming.

In Fig. 3.9 we show the evolution of the normalized conductivity Σ/Σ_T during the thermal treatment. We can see that the change in resistivity occurs mostly during the first hours in the furnace, followed by a slower drift. Notice that the lines are just a guide for the eye, but that the slopes of the true evolutions of the conductance are probably even larger during the first moments at 100°C and at 250°C than it seems on this graph. We also see that samples with lower conductive filler content have a larger post trim drift for the 40 nm grain size series, but we obtained the opposite result for the 400 nm series (this is not shown here, but this result can be found in Ref. [46]). Intuitively we would think that the larger the effect of trimming, the larger the post trim drift, which is only the case in our results for the set of sample with 40 nm grain sizes. For the other set of sample this is not the case, and no clear relation could be established between the post trim drift and the relative change of conductivity during trimming.

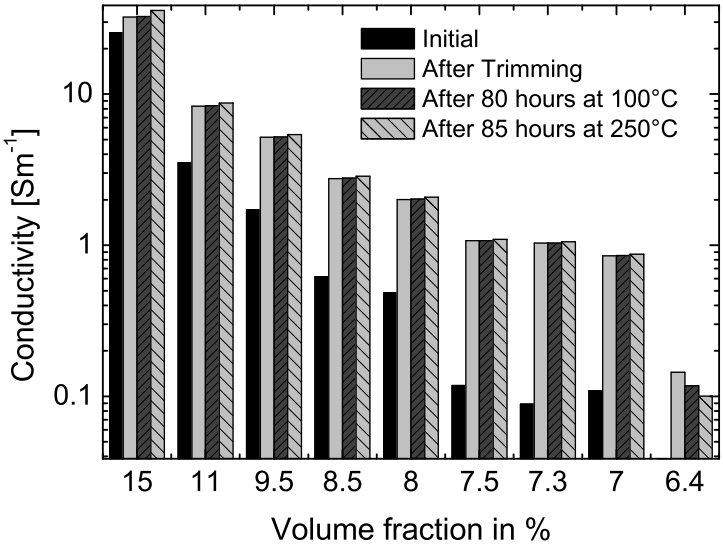

Figure 3.8: Change of conductivity induced by trimming and its thermal stability, as a function of conducting filler volume fraction for the sample set with 400 nm RuO_2 grain size.

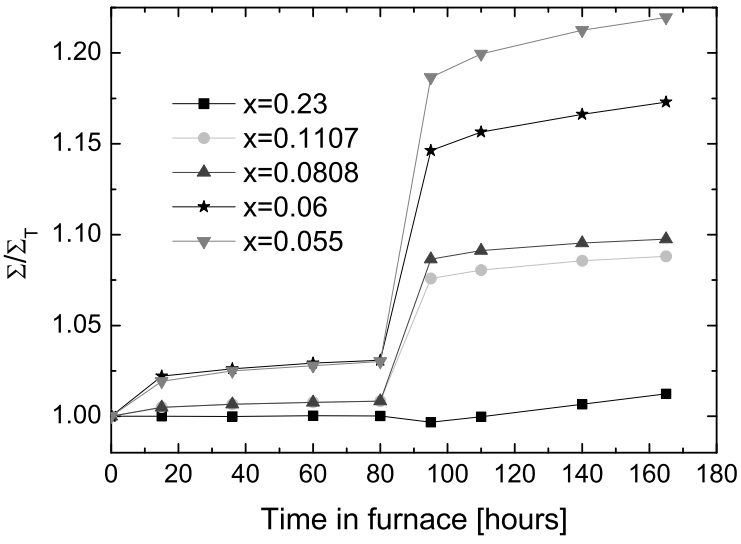

Figure 3.9: Evolution of the normalized post-trim conductivity of several samples from the 40 nm series during thermal treatment. The first 80 hours were at 100°C and then at 250°C.

We also studied the thermal coefficient of resistance (TCR) of the two sets of samples. The TCR was shifted upwards by the voltage trimming for all samples, as shown in Fig. 3.10. But contrary to what is observed for the conductivity, the shift is maximal for values of the volume fraction x in the middle of the range studied here. It decreases for very small and large values of x. Moreover we see that the TCR evolves towards its original value during thermal treatment, contrary to what is observed for the conductivity (this is also the case for almost all samples of the 40 nm series).

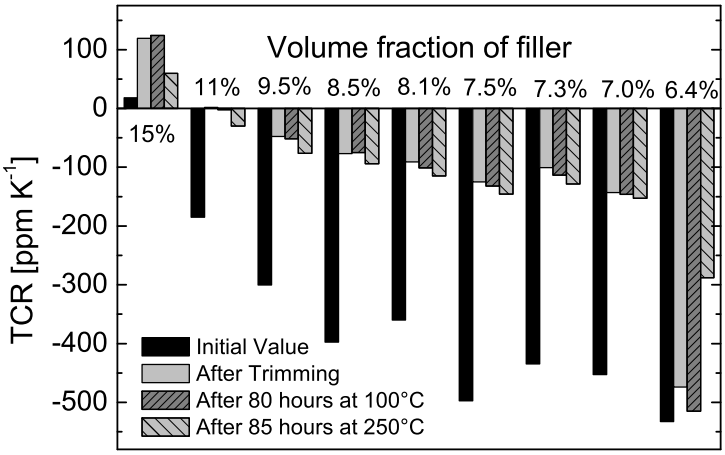

Figure 3.10: Shift of the thermal coefficient of resistance during trimming and its thermal stability for the 400 nm TFR series.

3.4.4 Conclusion

We see from this study that TFRs can be very sensitive to voltage pulses, especially for concentrations close to the percolation threshold. The post-trim drift remains quite low, as long as the resistors are not subjected to high temperatures. We have seen here that the drift remained unimportant after 80 hours at 100°C. On the contrary, when subjected to a thermal treatment at 250°C the drift becomes very important, especially during the first hours at this temperature. These results will be analysed in more detail in chapter 4 of this thesis.

3.5 Why TFRs as model composites

Though presenting results of broad interest for the understanding of the transport properties of conductor-insulator composites, this thesis is mainly

focused on TFRs. This is because, as seen above, TFRs are particularly interesting from a theoretical point of view, presenting non-universality of transport, large piezoresistive effect and a complex microstructure, and from a practical point of view because of their widespread use in industrial applications. Now it is also important to discuss whether TFRs are well-suited as model composites, to check the theoretical results obtained in this work. We will therefore discuss now the use of TFRs as ideal model composites, compared to other composite materials such as carbon-based conducting polymers.

3.5.1 Microstructural properties

All models developed and presented in this thesis rely on a hypothesis of homogeneous mixtures of its constituents, so that the system of spheres is in an equilibrium state. The lattice model of chapter 4 considers hard-core conducting particles randomly placed in one dimensional channels, the continuum models of chapters 5 and 6 equilibrium dispersions of spheres in a three-dimensional space, limited, or not, to regions left over by a segregating insulating phase. This equilibrium state might not always be achieved in conductor-insulator composites. For example, the results presented for the conductivity and piezoresistivity of TFRs in figures 3.3 and 3.4 stem from pastes prepared by our group, homogenized in a three roll mill (Exakt 50), with homogeneous mixture guaranteed down to 20 μm according to the manufacturer's specifications, though our pastes contain glassy grains of ~ 3 μm in diameter and conducting powders with sizes of the order of 40 nm. Good dispersion is therefore not guaranteed, and aggregates of conducting particles might remain after the homogenization step, mainly leading to an increase of the percolation threshold. Now during the firing step, sintering favours the splitting of such aggregates and the homogenization of the composite. Interactions between the conducting particles or between the conducting and insulating phase can also hinder the good homogenization of the composite. In our sense, those problems are of minor importance in TFRs, perhaps influencing somewhat the percolation threshold, but not affecting much the general interpretation of transport properties given in this work. They might change the precise form of the interparticle distance distribution function, but its main features, governing the transport exponents, should not be altered too much. Moreover this problem is not specific to TFRs, on the contrary it seems to be of greater importance in polymer based conductor-insulator composites. Indeed in TFRs, segregation and TP allows to explain the low critical volume fractions observed, whereas a close look at the percolation thresholds obtained for polymer-based composites shows that they are too low to be explained by a TP model with a homogeneous dispersion of the conducting particles [48], which suggests that interactions or unexpected segregation are important in those composites. It

was shown that Coulomb and London-Van der Waals interactions leaded to aggregation of carbon-black particles dispersed in epoxy resin [49]. This phenomenon drastically changes the percolation threshold and microstructure of the composite, leading to the formation of a segregated structure.

A clear advantage of TFRs over other classes of composites stems from the good control over the sizes and shapes of the constituents, allowing also to tune segregation. The approaches used to prepare metal-oxides powders include precipitation, spray pyrolysis, solid state reactions, sol-gel *etc.* and selected methods have been employed to narrow the size distribution of the conducing particles [50]. For the glass particles, besides the common milling operations, sol-gel techniques permit to prepare mono-dispersed glassy grains. These fabrication procedures offer the capability of controlling the relative sizes of the metallic and insulating grains, and so of tuning the segregation of the conducting phase in a controlled way, at least in the pre-firing stage [50]. In comparison, the carbon-black/polymer system, which is maybe the most studied conductor-insulator composite, has a much less ideal microstructure. The carbon black particles have very complex and irregular shapes [51], increasing their excluded volume, diminishing the percolation threshold and making them very different from dispersions of spheres or other simple geometrical objects.

3.5.2 Chemical properties and stability

Another advantage of TFRs compared to other composites is their long-term stability. The glassy phase of TFRs makes them hermetic to external degrading agents such as humidity, and the aluminum oxide substrates are also very stable. It was shown that the resistivity of common RuO_2-based TFRs showed drifts of less than 1% after more than one month storage at 250°C [38].

Now during the firing process, chemical reactions between the glassy and the conductive phase and with the substrate can take place. This can nevertheless be quite well controlled. For the low-firing (*i.e.* 600°C) composites prepared in our laboratory, little reaction between the composite and the substrate takes place at firing temperatures below 700°C. Above this temperature, the surface of the alumina substrate desaggregates, mainly due to reactions between the glassy phases of the aluminum oxide and of the composite [38]. This reaction can also be well controlled by the choice of the glass composition. Low firing temperature TFRs were developed in which no glass-RuO_2 chemical reactions were detected, the composite remaining a two-phase compound with no formation of a new phase during firing [38].

3.5.3 Mechanical and thermal Properties

Also from the mechanical point of view, TFRs are closer to our idealized model system than polymer-based composites. Indeed, in contrast to polymer-based composites, the glassy phase of TFRs is typically not prone to creep and relaxation phenomena in ambient conditions, providing therefore high mechanical stability to the composite. As we will see later, we idealize the composites as having uniform mechanical properties, *i.e.* that the conducting and insulating phases have the same elastic constants, so that the strain is homogeneous in the composite. This is not the case in TFRs, as RuO_2 has bulk modulus $K \simeq 270$ GPa whereas the glassy phase has typically $K \simeq 40 - 80$ GPa, depending on composition [52]. The authors of Ref. [52] showed that this heterogeneity could be treated separately from the percolation problem and leads to an enhancement of the piezoresistivity. Again it is worth noting that the mechanical heterogeneity, indeed present in TFRs, is a lot worse in polymer-based composites, in which the difference of bulk modulus between the polymer and the filler can be of two or more orders of magnitude.

Let us now discuss the thermal properties of TFRs. The overall thermal mismatch between the composite and the substrate is quite low. Indeed the lead-borosilicate glass has a thermal coefficient of expansion (TCE) around 8 ppm/K, the RuO_2 an average value of 5 ppm/K and the aluminum oxide substrate of 7 ppm/K [38]. However the local thermal mismatches are much higher in the case of RuO_2-based TFRs. Indeed, rutile RuO_2 has anisotropic TCE values of $+9$ ppm/K in two axes and -2 ppm/K in the third one [53]. This local thermal mismatch is one of the possible causes of drift at 250°C, together with more global mismatch between the resistor and the substrate.

3.6 Conclusion

The work in this thesis is mainly theoretical, but it was guided all along by just one goal: explaining the special characteristics of TFRs. In that sense this thesis is really focused on TFRs. Nevertheless, this work is also quite general because most results are also applicable to the other classes of compounds presenting transport non-universality, such as carbon based conducting polymers and granular metals. TFRs are maybe the most complex and interesting class of conductor/insulator composites, presenting several unusual properties: transport non-universality, large piezoresistance, high sensitivity to voltage pulses and low percolation thresholds due to segregation. We have also seen in this chapter, that compared to other composite conductor-insulator materials, TFRs have several advantages and represent an ideal model system. They present good long term, chemical and thermal stability and their microstructure can be well controlled. Mechanically,

though there is a clear mechanical heterogeneity between the glassy phase and the filler, they have the advantage of presenting no creep and relaxation phenomena at ambient temperature, contrary to polymer based composites, providing a high mechanical stability to the composite. All this makes TFRs an ideal choice for studies of the transport properties in segregated disordered conductor-insulator composites.

Chapter 4

Electrical conduction in tunnelling-percolation lattice models

From now on, we will be mostly concerned with the description of the electrical transport in composite materials made of a dispersion of conducting particles in an insulating matrix. In this chapter, I will first present in more detail the classical tunnelling-percolation (TP) model already presented in section 2.5, discuss how non-universality is obtained in the classical TP framework and point out the key ingredients needed for the appearance of non-universality. We will see that one-dimensionality is essential in that framework and we will show, by introducing a generalization of the classical lattice TP model, that non-universality is not obtained anymore for this more general model. Nevertheless, a careful study of the transport properties of this model will lead to the introduction of the concept of *apparent non-universality*, which is from our point of view, sufficient to explain the experimentally observed non-universal transport exponents. Apparent non-universality will be a key feature in this thesis.

In the second part of the chapter we will study the piezoresistivity Γ of the generalized lattice TP model. We will again first present the results for the classical TP model, leading to a logarithmic divergence of the piezoresistive factor as the percolation threshold is approached for systems presenting a non-universal transport exponent and a constant piezoresistivity for universal systems. We will then show that in the generalized model, apparent non-universality leads to a crossover between these two behaviours, namely a logarithmic increase of Γ followed by a saturation for values of p close enough to the percolation threshold p_c.

We end this chapter by an interpretation of high-voltage trimming, based on the models presented in this chapter. We show here that trimming drives the transport exponent towards its universal value, which can be explained

by our simple model.

4.1 Origin of non-universality in tunnelling-percolation models

In this section, I present a discussion from a paper of Grimaldi and coauthors [37], about the interplay between the spatial distribution of the conducting grains, within the insulating matrix, and the transport properties. This discussion also makes clear which ingredients are needed to obtain non-universality, and therefore points at the key assumption behind the classical tunnelling-percolation model. This article is of fundamental importance for this chapter, as it presents a microscopic derivation of the classical tunnelling-percolation model, which I then generalize and analyse in the rest of the chapter.

Now let us first recall the results on which the upcoming discussion will be based. As stated in section 2.3, the conductivity Σ of a random resistor network, with a fraction p of conducting bonds and a fraction $(1-p)$ of insulating ones, follows a power-law

$$\Sigma = \Sigma_0 (p - p_c)^t, \tag{4.1}$$

where Σ_0 is a constant prefactor and t is the D.C. critical exponent, having a universal value, depending solely on the dimensionality d of the system. Non-universality can arise if the distribution of the local conductances, g, of a random resistor network has a strong enough divergence for small g. More precisely, if the conducting bonds are chosen from a distribution function $h(g)$, then if

$$\lim_{g \to 0} h(g) \propto g^{-\alpha}, \tag{4.2}$$

the transport exponent t is given by [21, 22]:

$$t = \begin{cases} t_0 & \text{if} \quad (d-2)\nu + \frac{1}{1-\alpha} < t_0 \\ (d-2)\nu + \frac{1}{1-\alpha} & \text{if} \quad (d-2)\nu + \frac{1}{1-\alpha} > t_0 \end{cases} \tag{4.3}$$

Therefore non-universality arises for $\alpha > \alpha_c$, with $\alpha_c = 0.107$ in three dimensions (easily obtained from the above equation, by using $t_0 = 2$ and $\nu = 0.88$) and $\alpha_c = 0.231$ in $d = 2$. The whole question is now to show what the key assumptions are, that lead to the appearance of an $h(g)$ of the form of equation 4.2.

Let us consider a generic conductor-insulator compound where the conducting grains are embedded in an insulating host. As discussed in the end of chapter 2, we consider that the dominant transport mechanism, in this situation, is tunnelling between neighbouring conducting particles. Electron

tunnelling between small grains imply charging energies and a Coulomb interaction between charged grains, affecting the overall transport properties, especially regarding behaviour in temperature. Here we focus on high enough temperatures and large enough conducting particles to neglect those two effects, so that the electron transfer is dominated by simple tunnelling [54, 55, 56, 57, 58]. With the conducting particles approximated by impenetrable spheres of diameter σ_1, this leads to inter-grain conductivities of the form [37]

$$g(r) = g_0 e^{-2(r-\sigma_1)/\xi}, \tag{4.4}$$

where g_0 is a prefactor, that can be set to unity without any loss of generality, ξ is the tunnelling decay factor and r the distance between the centers of the two spheres. Due to the exponential decrease of the tunnelling conduction with the distance r, contributions from far away spheres can be neglected so that we consider that only nearest-neighbour tunnelling contributes significantly to the overall conductivity of the system. Thus, the distribution function of the tunnelling distances is approximated by the nearest-neighbour distance distribution function $P(r)$ ($P(r)dr$ = probability that the particle nearest to a reference particle is at distance between r and $r+dr$). It is clear that in fact at least nearest and next-nearest neighbours are needed in order to obtain a connected network, but this simplification is nevertheless useful, as the distribution function $P(r)$ is known, contrary to the distribution function for next-nearest neighbours, and as it captures the essential physics of the problem. $h(g)$ can be easily obtained from $P(r)$ as follows:

$$h(g) = \int dr P(r) \delta\big(g - g(r)\big). \tag{4.5}$$

Of course, in real composites, $P(r)$ might depend on the particular microstructure of the composite, which could itself depend on processing methods, interactions between the insulating and conducting phase and interactions between the conducting particles, among others. Now in order to get a general and simple model, we imagine that the interactions can be neglected, so that the conducting spheres can be assumed to be distributed completely randomly in space (Poisson distribution). It can be shown that for a random d-dimensional distribution of points, the nearest-neighbour distance distribution function is given by [28]

$$P(r) = \rho s_D(r) e^{-\rho v_D(r)}, \tag{4.6}$$

where $s_D(r)$ and $v_D(r)$ are respectively the surface and volume of a D-dimensional sphere of radius r. ρ is the number density defined for a system of linear size L containing N conducting particles as $\rho = N/L^D$.

Now as we are interested only in studying the appearance of non-universality, which is driven by the behaviour of $h(g)$ for $g \ll 1$, we can, for simplicity,

keep only the leading term of $P(r)$ for $r \gg 1$, behaving as

$$P(r) \propto e^{-(r/a_D)^D}, \tag{4.7}$$

where a_D is a constant related to the mean-nearest neighbour distance. We should note here that this asymptotic expression 4.7 is also valid for a dispersion of D-dimensional impenetrable spheres in the limit $r \to \infty$ [28]. Using equation 4.5 we can now derive the distribution function $h(g)$. The integration is done using

$$\delta\big[g - g(r)\big] = \frac{\xi}{2g}\delta(r - r_g) \quad \text{with} \quad r_g = -\frac{\xi}{2}\ln(g) \tag{4.8}$$

Now inserting 4.8 and 4.7 in equation 4.5 we obtain:

$$h(g) \propto \frac{\xi}{2g}P(r_g) = \frac{\xi}{2g}\exp\left[-\Big(\frac{\xi}{2a_D}\ln(g^{-1})\Big)^D\right]. \tag{4.9}$$

We can rewrite this expression as

$$h(g) \propto \frac{\xi}{2a_D}g^{\left\{(\xi/a_D)^D\left[\ln(g^{-1})\right]^{D-1}-1\right\}}, \tag{4.10}$$

so that it gets clear that, for $D = 2$ and $D = 3$, the above expression for $h(g)$ goes to zero in the $g \to 0$ limit, irrespective of the value of $\xi/2a_D$. Therefore, no power-law divergence of $h(g)$ is encountered for a three- or two-dimensional random dispersion of conducting spheres, and transport is governed by the universal critical exponent $t = t_0$. On the other hand, in the one-dimensional case, equation 4.10 becomes

$$h(g) \propto \frac{\xi}{2a_1}g^{\left[(\xi/2a_1)-1\right]} \tag{4.11}$$

which is exactly of the form of equation 4.2 if we identify α with $1 - \xi/2a_1$. We have therefore arrived at the result that, if the spheres are Poisson distributed along a one-dimensional line, then $h(g)$ displays a power-law divergence for small conductances, and transport becomes non-universal for sufficiently small values of $1 - \xi/2a_1$.

The difference between the $D = 2$ and 3 and the $D = 1$ cases stems from the decay of $P(r)$, which is, for $D > 1$, much faster than the simple exponential decay of $g(r)$. In fact, one can show, from equation 4.5, that as long as $\lim_{r\to\infty} P(r)/g(r) = 0$, then $\lim_{g\to 0} h(g) = 0$, irrespective of the precise form of $P(r)$, so that transport remains universal. Consequently, to obtain non-universality, the decay of $P(r)$ has to be sufficiently slow, and the above result suggest that one-dimensionality is an important ingredient in that scope, at least as long as interactions between conducting and insulating phases can be neglected. This feature will guide us, in the following section, in the microscopic formulation of the tunnelling-percolation model.

4.2 Lattice tunnelling-percolation model

4.2.1 Introduction

In its original formulation [27], the tunnelling-percolation model was a phenomenological description based on an assumed distribution function of the inter-particle distances. A one-dimensional form of the distribution function $P(r)$ was used, arguing that it captured the essential physics of the problem. Now, as we have seen above, one-dimensionality is in fact a key ingredient to obtain non-universality in a tunnelling-percolation model, and therefore needs to be justified. A fully microscopic derivation has been proposed recently for a particular network construction where the bonds on a cubic lattice have probability p of being occupied by a string of non-overlapping conducting spheres placed randomly along the length σ_2 of the bond [37]. In the limit in which σ_2 is much larger than the diameter σ_1 of the conducting spheres, so that finite bond length effects are negligible, the distribution function of the resulting bond conductances reduces exactly to Eq. 4.2 where $\alpha = \alpha_N = 1 - \frac{\xi/2}{a_N - \sigma_1}$ and a_N is the mean inter-sphere distance for a bond occupied by N particles [37].

In addition to provide a fully microscopic model for the tunnelling-percolation non-universality, the network construction of Ref. [37] is also a possible description, though quite crude, of the main microsctructural properties of RuO_2-based cermets where the glassy grains are surrounded by much smaller RuO_2 particles. Such microscopic phase segregation leads, in a first approximation, to long chains formed by RuO_2 particles separated by thin glass barriers through which tunnelling occurs [59]. A scanning electron microscopy image of a RuO_2-based thick-film resistor was shown in figure 3.2, where this segregated microstructure is clearly seen. Usually the large glassy grains have linear sizes of the order of 1-5 μm and the RuO_2 particles range from 40 nm up to about 500 nm. Hence the assumption $\sigma_2/\sigma_1 \gg 1$ used in Ref. [37] is not always valid *a priori* and finite bond length effects should be taken into consideration for a more correct description of the microstructure.

In this section, we re-formulate the segregated tunnelling-percolation model of Ref. [37] without the restriction $\sigma_2/\sigma_1 \to \infty$ and study the finite bond length effects on the transport critical behaviour. We show that, as long as σ_2/σ_1 is finite, the resulting bond distribution function $h_{\sigma_2}(g)$ is not strictly of the form of equation 4.2, *i.e.*, $h_{\sigma_2}(g)$ is not power law divergent as $g \to 0$. As a consequence, transport is expected to be universal with $t = t_0$. However, depending on the model parameters, $h_{\sigma_2}(g)$ may be a strongly peaked function at small g values, so that the conductivity is well fitted by equation 4.1 with $t > t_0$ within a rather broad range of $p - p_c$ values. In this case the accessible transport phenomenology appears to be non-universal because the region in which $t = t_0$ is restricted to very small $p - p_c$ values [60].

4.2.2 The model

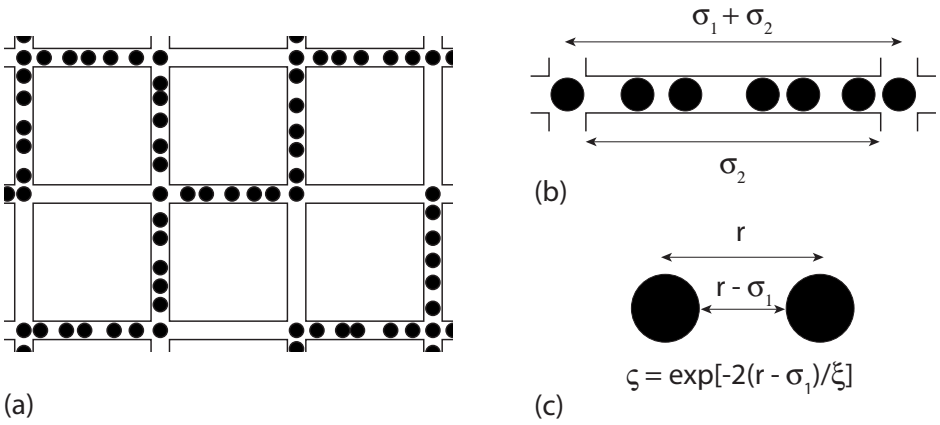

Figure 4.1: (a): square lattice bond percolation model used in this section. The filled circles denote conducting impenetrable particles of diameter σ_1. One particle is assigned to each intersection between the channels (nodes) and each bond has probability p of being occupied by N particles. (b) channel containing $N = 5$ impenetrable particles randomly placed within a length σ_2. (c) tunnelling process between two adjacent particles whose centers are separated by a distance r.

The segregated tunnelling-percolation model studied in this section is illustrated in Fig. 4.1 for a two dimensional lattice. In Fig. 4.1(a) the full circles denote impenetrable conducting particles of diameter σ_1 constrained to occupy the channels between neighbouring insulating squares of length σ_2 (representing the diameter of the insulating grains) [Fig. 4.1(b)]. These channels form a square lattice and each channel has probability p of being occupied by N conducting particles and probability $1 - p$ of being empty. Furthermore it is assumed that the conducting particles are placed randomly inside the occupied channels and that electrons can tunnel between adjacent particles leading to channel conductances g, depending on the values of the tunnelling distances between the particles [Fig. 4.1(c)]. In order to ensure electrical connectivity between two occupied channels, each intersection between channels is assumed to be occupied by a particle. The system, as a whole, defines therefore a square-lattice bond percolation model where a fraction p of bonds (occupied channels) has variable conductances distributed according to $h_{\sigma_2}(g)$ and a fraction $1-p$ has zero conductance. Therefore the bond conductances are taken from the distribution function

$$\Psi(g) = p h_{\sigma_2}(g) + (1-p)\delta(g) \tag{4.12}$$

The model, as defined here, contains the model of reference [37] as limiting case, for $\sigma_2/\sigma_1 \to \infty$. It was shown [37] that, in that limit, the bond

conductivity distribution function is of the form of equation 4.2, leading to possible non-universal critical transport exponent t. The results for the transport exponent t extracted from the numerical simulations of Ref. [37] are shown in figure 4.2 as a function of the parameter α_N, the parameter governing the divergence of $h(g)$. It is clear from this figure that the transport exponent is controlled by the parameters of the model (ξ, σ_2, σ_1 and N) and follows exactly the theoretical prediction of equation 4.3. Here we have $t_0 = 2$, as a cubic lattice was considered in Ref. [37]. In what follows we will have $t_0 = 1.3$, because we simulate the two-dimensional case. We also note that this model can lead to both universal and non-universal critical behaviour, and that any value $t \geq t_0$ can be obtained. As discussed in the section 4.1, such result stems from the one-dimensionality of the channels of our model. A one dimensional arrangement still continues to characterize the situation for which σ_2/σ_1 is finite, but the existence of an upper cut-off in the tunnelling distances also prevents $h_{\sigma_2}(g)$ to diverge for $g \to 0$, which is a necessary condition for the emergence of non-universality. It is therefore interesting to asses how the critical behaviour of the model is influenced by $\sigma_2/\sigma_1 < \infty$. Such problem requires the evaluation of the distribution function of the nearest-neighbour inter-particle distances for N impenetrable particles placed along a distance σ_2, which is calculated in the following section.

4.2.3 Distribution of adjacent particles distances

In this section we derive the distribution function of the distance between two adjacent particles in a system of N impenetrable particles placed randomly inside a channel of length σ_2. In the following, we shall partly follow the procedure of Ref. [61]. Let us consider $N+1$ particles, in a channel of length $\sigma_2 + \sigma_1$, with one particle fixed at $r = 0$ and periodic boundary conditions. Then N particles are distributed in the remaining length σ_2 of the channel with density $\rho = N/\sigma_2$. Let $P_{\sigma_2}(r)dr$ be the probability of finding in the interval $[r, r + dr]$ the center of a particle adjacent to the particle centered at $r = 0$. Since the boundary conditions are periodic, $P_{\sigma_2}(r)$ is also the distribution function of the inter-particle distance of any pair of adjacent particles in the channel. As the particles are impenetrable and the problem one-dimensional, this situation is identical to the one in which N point-particles are randomly placed in a length $\sigma_2 - N\sigma_1$, which is easier to treat. Let us define two events:

$$A = \text{There is no particle center between 0 and } r$$
$$B = \text{There is a particle center between } r \text{ and } r + dr$$

Then we have from elementary probability theory:

$$P_{\sigma_2}(r)dr = P(B \cap A) = P(B \mid A)P(A), \tag{4.13}$$

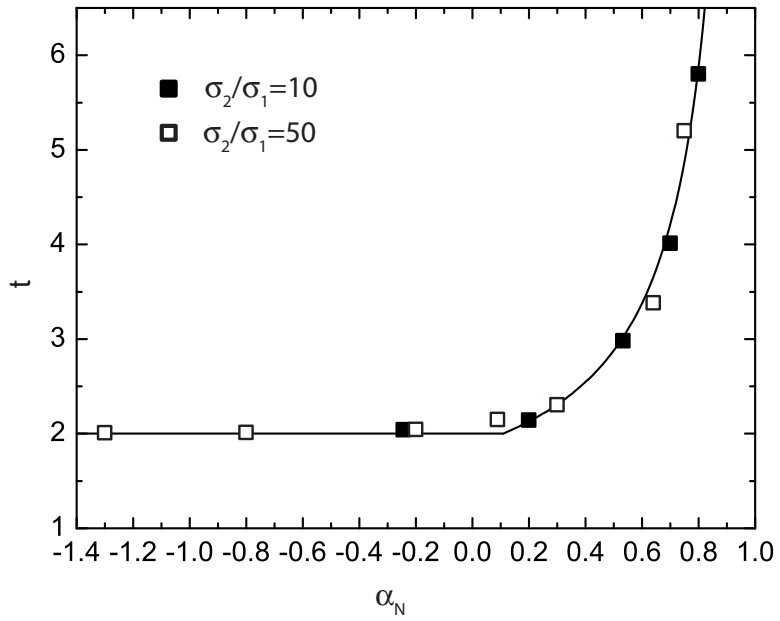

Figure 4.2: Critical exponent t of a three-dimensional lattice TP model, as a function of the tunnelling exponent $\alpha_N = 1 - \frac{\xi}{2(a_N - \sigma_1)}$ for $\xi/\sigma_1 = 0.2$ and different values of σ_2/σ_1 and of the number N of inter-sphere tunnelling junctions accommodated within the occupied channels of a cubic random-resistor network. From left to right: $N = 9, 8, \ldots, 5$ for $\sigma_2/\sigma_1 = 10$ (filled squares) and $N = 46$, 45, 43, 41, 39, 33, 27 for $\sigma_2/\sigma_1 = 50$ (open squares). The solid curve is the theoretical result $t = t_0 \simeq 2.0$ for $\alpha_N < \alpha_c \simeq 0.107$ and $t = \nu + 1/(1 - \alpha_N)$ for $\alpha_N > \alpha_c$.This figure is taken from the article of Grimaldi et al. [37].

where $P(B|A)$ is the conditional probability of B knowing A, *i.e.*, the probability of finding a particle center at a distance between $r > 0$ and $r + dr$ *provided that there are no particles in the inner radius* r. The conditional probability $P(B|A)$ is then found by considering that if in $[0, r]$ there are no particles, then the N particles must be distributed in the remaining space $\sigma_2 - N\sigma_1 - r$, which leads to:

$$P(B|A) = \frac{\rho}{1 - \rho\sigma_1 - (r - \sigma_1)/\sigma_2}\Theta(r - \sigma_1)\Theta(r_{\max} - r)dr, \tag{4.14}$$

where the unit-step function $\Theta(r - \sigma_1)$ arises because the particles are impenetrable and $\Theta(r_{\max} - r)$ prevents the distance between adjacent particles from being larger than $r_{\max} = \sigma_2 - (N - 1)\sigma_1$. Furthermore, from the definition of the event A:

$$P(A) = 1 - \int_0^r P_{\sigma_2}(r')dr'. \tag{4.15}$$

Finally, equations (4.13),(4.14) and (4.15) define an integral equation for $P_{\sigma_2}(r)$,

$$P_{\sigma_2}(r) = \frac{\rho\Theta(r-\sigma_1)\Theta(r_{\max}-r)}{1-\rho\sigma_1-(r-\sigma_1)/\sigma_2}\left[1-\int_0^r P_{\sigma_2}(r')dr'\right] \tag{4.16}$$

which can be solved by taking its derivative d/dr, leading to a differential equation for $P_{\sigma_2}(r)$, which solution has to be of the form:

$$P_{\sigma_2}(r) = P_0\left[A+r\right]^C\Theta(r-\sigma_1)\Theta(r_{\max}-\sigma_1) \tag{4.17}$$

The coefficients of equation 4.17 are found by inserting this solution in the differential equation obtained for $P_{\sigma_2}(r)$ and by using the normalization

$$\int_0^\infty P_{\sigma_2}(r)dr = 1, \tag{4.18}$$

finally holding the solution

$$P_{\sigma_2}(r) = \frac{\rho}{1-\rho\sigma_1}\left[1-\frac{r-\sigma_1}{\sigma_2(1-\rho\sigma_1)}\right]^{\rho\sigma_2-1}\Theta(r-\sigma_1)\Theta(r_{\max}-r). \tag{4.19}$$

From this we can now obtain the mean adjacent inter-particle distance a_{σ_2}

$$a_{\sigma_2} = \int_0^\infty dr\, rP_{\sigma_2}(r) = \frac{\sigma_1+\sigma_2}{\rho\sigma_2+1}. \tag{4.20}$$

By using the above expression for a_{σ_2}, Eq. (4.19) can be re-written as:

$$P_{\sigma_2}(r) = \frac{\rho\sigma_2}{\rho\sigma_2+1}\frac{1}{a_{\sigma_2}-\sigma_1}\left[1-\frac{r-\sigma_1}{(\rho\sigma_2+1)(a_{\sigma_2}-\sigma_1)}\right]^{\rho\sigma_2-1}\Theta(r-\sigma_1)\Theta(r_{\max}-r). \tag{4.21}$$

The maximum possible density ρ_0 corresponds to the close-packing limit $\rho_0 = (\sigma_2/\sigma_1)/\sigma_2 = 1/\sigma_1$, for which $a_{\sigma_2} = \sigma_1$ and Eq. (4.21) reduces to $P_{\sigma_2}(r) = \delta(r-\sigma_1)$, as expected. In the limit $\sigma_2 \to \infty$ but with $\rho = N/\sigma_2 =$ const., equation (4.21) reduces to:

$$P_\infty(r) = \frac{1}{a_\infty-\sigma_1}\exp\left(-\frac{r-\sigma_1}{a_\infty-\sigma_1}\right)\Theta(r-\sigma_1), \tag{4.22}$$

with $a_\infty = 1/\rho$ [see Eq. (4.20)]. Equations (4.21) and (4.22) are plotted in Fig. 4.3 for different values of σ_2/σ_1 and constant density $\rho = 0.3$. The finite channel length effects are most visible for $\sigma_2/\sigma_1 = 10$ and $N = 3$ for which $P_{\sigma_2}(r) = 0$ for $r/\sigma_1 > r_{\max}/\sigma_1 = 8$, while $P_\infty(r)$ becomes zero only asymptotically at $r = \infty$. As we shall see below, such sharp cut-off of $P_{\sigma_2}(r)$ gives rise to a lower bound of the adjacent particle tunnelling conduction,

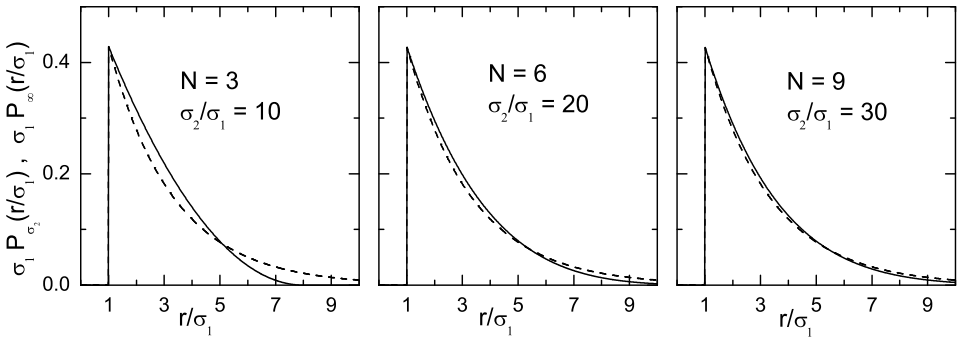

Figure 4.3: Distribution function of the distances between the centers of two adjacent impenetrable particles for $\sigma_2/\sigma_1 \to \infty$ (dashed lines) and for σ_2/σ_1 finite (solid lines). The volume density is fixed at $N\sigma_1/\sigma_2 = 0.3$, and the length of the channel is increased from $\sigma_2/\sigma_1 = 10$ (left panel) to $\sigma_2/\sigma_1 = 30$ (right panel).

preventing the system to display truly non-universal transport behaviour, in contrast with the $\sigma_2 \to \infty$ case for which the lower bound is zero.

Before turning to the problem of finding the network conductance, it is worth to stress that equations 4.19 and 4.20, and equation 4.22 for the $\sigma_2 \to \infty$ case, refer to adjacent particle properties and not to nearest-neighbour ones. If we wanted to find the distribution function of the distance between nearest-neighbour particles $P^{NN}_{\sigma_2}(r)$ (we use here the superscript NN for nearest-neighbour, to differentiate from the case of adjacent particles we have studied in this section), then the corresponding conditional probability $P(B|A)$ would be given by twice the expression reported in Eq. (4.14). This is because, for a given particle, there are two neighbours: one at the left and the other at the right of the reference particle. Hence, by following the same procedure as above $P^{NN}_{\infty}(r)$ is found to be equal to Eq. (4.22) with a_∞ replaced by $a^{NN}_\infty = (1+\rho\sigma_1)/2\rho$, in agreement with the result reported in Ref. [61,28]. This expression is the one that was used in Balberg's paper [27], introducing the original TP model, and derived by Grimaldi [37]. As already discussed (see figure 4.2), this choice of the nearest-neighbour distribution function leads to a transport exponent t dependent on the parameters of the model, or in other words, to non-universality.

4.2.4 Distribution of bond conductances

The transport properties of the network of Fig. 4.1 are governed by the distribution function $h_{\sigma_2}(g)$ of the bond conductivities g, which result from the contribution of the $(N+1)$ inter-particle conductivities ς_i $(i = 1, N+1)$

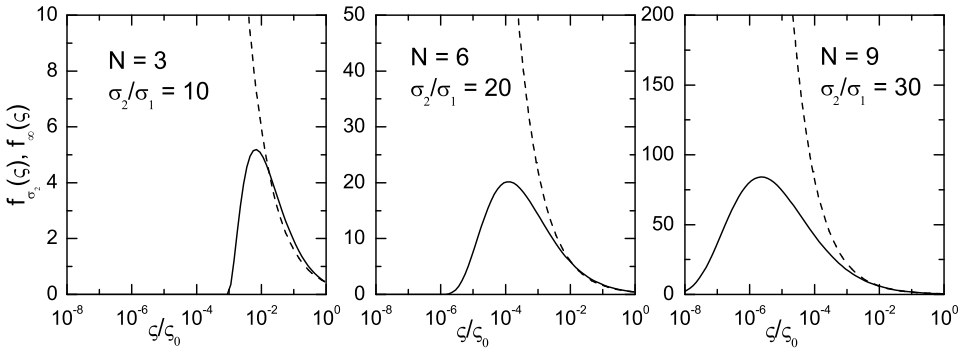

Figure 4.4: Distribution function of the conductivities between two given adjacent particles for $\sigma_2/\sigma_1 \to \infty$ (dashed lines) and σ_2/σ_1 finite (solid lines). The volume density is fixed at $N\sigma_1/\sigma_2 = 0.3$ and $\xi/\sigma_1 = 1$, and the length of the channel is increased from $\sigma_2/\sigma_1 = 10$ (left panel) to $\sigma_2/\sigma_1 = 30$ (right panel).

arranged in series:

$$g = \left(\sum_{i=1}^{N+1} \varsigma_i^{-1} \right)^{-1} . \tag{4.23}$$

Hence $h_{\sigma_2}(g)$ can be obtained from the distribution function $f_{\sigma_2}(\varsigma)$ of the inter-particle conductivities. These are assumed to be due to simple tunnelling processes between adjacent particles so that the conductivity ς between two adjacent particles whose centers are separated by the distance r is approximately of the form:

$$\varsigma(r) = \varsigma_0 e^{-2(r-\sigma_1)/\xi}, \tag{4.24}$$

where ς_0 is a constant that can be set equal to one without loss of generality and ξ is the tunnelling factor. The tunnelling conductance distribution function $f_{\sigma_2}(\varsigma)$ is therefore given by (see equations 4.5 and 4.8):

$$f_{\sigma_2}(\varsigma) = \int_0^\infty dr P_{\sigma_2}(r)\delta[\varsigma - \varsigma(r)] = \frac{\xi}{2\varsigma} P_{\sigma_2}(r_\varsigma), \tag{4.25}$$

where $r_\varsigma = \sigma_1 - \ln(\varsigma)\xi/2$ and $P_{\sigma_2}(r)$ is the distribution function of the adjacent particles distances. By using Eq. (4.21) for $P_{\sigma_2}(r)$, the above expression reduces therefore to:

$$f_{\sigma_2}(\varsigma) = \frac{\rho\sigma_2}{\rho\sigma_2 + 1} \frac{1 - \alpha_{\sigma_2}}{\varsigma} \left[1 + \frac{(1 - \alpha_{\sigma_2}) \ln(\varsigma)}{\rho\sigma_2 + 1} \right]^{\rho\sigma_2 - 1} \Theta(\varsigma - \varsigma_{\min})\Theta(\varsigma_{\max} - \varsigma), \tag{4.26}$$

where $\alpha_{\sigma_2} = 1 - (\xi/2)/(a_{\sigma_2} - \sigma_1)$, $\varsigma_{\max} = \varsigma(\sigma_1) = 1$ and $\varsigma_{\min} = \varsigma\big[\sigma_2 - (N-1)\sigma_1\big] = \exp(\frac{-2[\sigma_2 - N\sigma_1]}{\xi})$. In the limit $\sigma_2/\sigma_1 \to \infty$ ($\rho = \text{const.}$) and by using Eq. (4.22) the above expression reduces to:

$$f_\infty(\varsigma) = (1-\alpha_\infty)\varsigma^{-\alpha_\infty}\Theta(\varsigma_{\max} - \varsigma), \tag{4.27}$$

where $\alpha_\infty = 1 - \frac{\xi/2}{a_\infty - \sigma_1}$, which is exactly of the form of the Kogut-Straley distribution function, needed for the appearance of non-universality (see Eq. (4.45)). It is clear that, in the $\sigma_2/\sigma_1 < \infty$ case, the presence of $\varsigma_{\min} \neq 0$ prevents $f_{\sigma_2}(\varsigma)$ to diverge at $g = 0$, while $f_\infty(\varsigma)$ has a power law divergence at $\varsigma \to 0$. Equation (4.26) is compared with Eq. (4.27) in Fig. 4.4 for the same parameters values of Fig. 4.3 and for $\xi/\sigma_1 = 2$. As σ_2/σ_1 increases, the maximum of $f_{\sigma_2}(\varsigma)$ becomes higher and its position shifts to lower values of ς. For $\sigma_2/\sigma_1 \to \infty$ $f_{\sigma_2}(\varsigma)$ asymptotically reduces to Eq. (4.27) which is reported in Fig. 4.4 by the dashed lines.

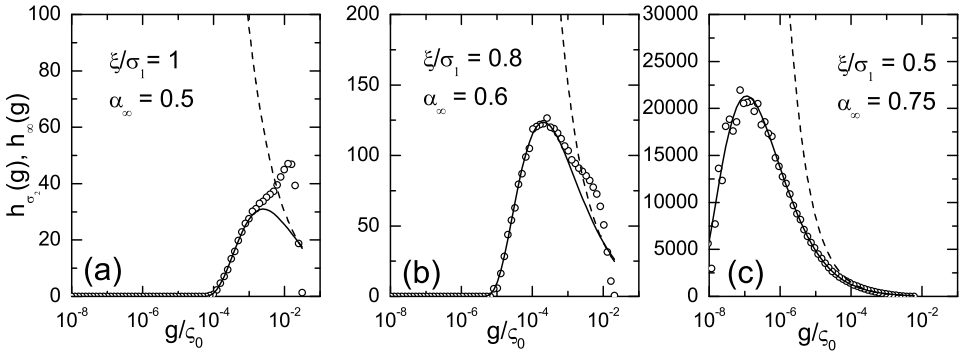

Figure 4.5: Distribution function of the bond conductivities for bonds of length $\sigma_2/\sigma_1 = 10$ containing $N = 5$ particles. Open symbols are numerical calculations obtained as explained in the text and the solid lines are Eq. (4.28). The distribution function h_∞ for $\sigma_2/\sigma_1 \to \infty$ is plotted by a dashed lines for comparison. ξ/σ_1 is varied from $\xi/\sigma_1 = 1$ (left panel) to $\xi/\sigma_1 = 0.5$ (right panel).

At this point, the distribution function $h_{\sigma_2}(g)$ of the total conductance g of a channel of length σ_2 can be easily obtained in the small g limit. From Eq. (4.23) it is in fact clear that g is dominated by the smallest value $\varsigma \simeq \varsigma_{\min}$ among the $N+1$ tunnelling conductances in series. Since there are $N+1$ ways to have $g \simeq \varsigma_{\min}$, the resulting bond conductance distribution function is therefore:

$$h_{\sigma_2}(g) \simeq (N+1) f_{\sigma_2}(g) \quad \text{for} \quad g \simeq \varsigma_{\min}. \tag{4.28}$$

From this equation we can write the definitive result for $h_{\sigma_2}(g)$ and

$h_\infty(g)$:

$$h_{\sigma_2}(g) \approx \rho\sigma_2 \frac{1-\alpha_{\sigma_2}}{g}\left[1+\frac{(1-\alpha_{\sigma_2})\ln(g)}{\rho\sigma_2+1}\right]^{\rho\sigma_2-1}\Theta(g-g_{\min})\Theta(g_{\max}-g) \tag{4.29}$$

$$h_\infty(g) \approx N(1-\alpha_\infty)g^{-\alpha_\infty}\Theta(g_{\max}-g) \tag{4.30}$$

$$\alpha_{\sigma_2} = 1-\frac{\xi/2}{a_{\sigma_2}-\sigma_1} \qquad \text{with} \qquad a_{\sigma_2} = \frac{\sigma_1+\sigma_2}{\rho\sigma_2+1} \tag{4.31}$$

$$\alpha_\infty = 1-\frac{\xi/2}{a_\infty-\sigma_1} \qquad \text{with} \qquad a_\infty = \frac{1}{\rho} \tag{4.32}$$

where, $g_{\max}=1$ and $g_{\min}=\exp[-2(\sigma_2-N\sigma_2)/\xi]$

Equation (4.28) is plotted in Fig. 4.5 for different values of ξ/σ_1 and compared with a numerical calculation of the bond conductance distribution function. This has been obtained by considering 10^6 realizations of channels of length $\sigma_2+\sigma_1$ with two particles fixed at both ends and N impenetrable particles randomly placed inside the remaining length σ_2. The resulting conductance is obtained by recording for each realization the $N+1$ tunnelling lengths and by using equations (4.23) and (4.24). The asymptotic formula (4.28) (solid lines) agrees very well with the numerical results (empty circles) also for g values quite larger than $g=\varsigma_{\min}$. For $\xi/\sigma_1=0.5$ the agreement extends even over the whole $g>\varsigma_{\min}$ region.

Contrary to the $\sigma_2/\sigma_1\to\infty$ case which displays a $g^{-\alpha_\infty}$ divergence for $g\to 0$ (dashed lines in Fig. 4.5), the finite length of the channels forming up the percolation network leads to a maximum of $h_{\sigma_2}(g)$ at g_m, depending on the parameters of the model. g_m is found by setting $dh_{\sigma_2}(g)/dg=0$ in equation 4.29, leading to $g_m=\exp(N-1)g_{\min}$. This has important consequences for the critical behaviour of transport. In fact, in the $\sigma_2/\sigma_1\to\infty$ case, the power-law divergence of $h_\infty(g)$ may lead, via equations (4.2) and (4.3), to transport non-universality for channel occupation probability p close to the critical threshold. This limiting case is the classical TP model, treated in several papers and in full agreement with the theoretical predictions of non-universality given by equation 4.3, as was shown in figure 4.2. On the contrary, when σ_2/σ_1 is finite, the transport exponent should be strictly equal to the universal value t_0, as $h_{\sigma_2}(g)$ is non-divergent. However, a closer look at Fig. 4.5 reveals that the situation is more intricate. In fact, when the position of the peak of $h_{\sigma_2}(g)$ falls at very small values of g [like in the case shown in Fig. 4.5(c)], the region in which Eq. (4.1) displays $t=t_0$ is expected to fall at very small $p-p_c$ values, resulting in a narrowing of the true critical (universal) region. This is due to the fact that not very close to p_c, the percolating cluster is made of several parallel paths, so that the

current flowing through the network can avoid the highest resistive links. In this way $h_{\sigma_2}(g)$ is sampled only for values of g larger than a $p-p_c$ dependent cut-off g^*, which goes to zero only at $p = p_c$. When $p - p_c$ is such that g^* is higher than the peak position of $h_{\sigma_2}(g)$, then the network basically sees an apparent diverging distribution function which may result in an apparent non-universal exponent $t > t_0$ [60].

As it will be shown in the upcoming section, a direct consequence of this situation is that when Σ is plotted for a limited number of p values, and one tries to fit Σ to Eq. (4.1), then an exponent larger than t_0 can be extracted even if the system is strictly universal. In the following section we show how such "apparent" non-universality naturally arises from the tunnelling-percolation model.

4.3 Critical behaviour of transport

4.3.1 Effective medium theory

We start our analysis of the critical behaviour of the conductivity by an effective medium theory (EMT) approach. This is useful, since it allows to get a very good feeling about the global behaviour of the system considered. So let us start with the basic equation for the EMT, already stated in section 2.3.1. Within the effective medium approximation (EMA), the average network conductance G satisfies the integral equation (see for example reference [12]):

$$\int_0^\infty dg\, h_{\sigma_2}(g) \frac{g-G}{g+(k/2-1)G} = \frac{1-p}{p(k/2-1)}, \tag{4.33}$$

where k is the number of neighbours of each node. This can be transformed into a more convenient form:

$$\begin{aligned} \frac{1-p}{p(k/2-1)} &= \int_0^\infty dg\, h_{\sigma_2}(g) \frac{g+(k/2-1)G-k/2G}{g+(k/2-1)G} \\ &= 1 - \frac{k}{2}G \int_0^\infty dg\, \frac{h_{\sigma_2}(g)}{g+(k/2-1)G}, \end{aligned}$$

so that

$$\frac{p-2/k}{Gp(k/2-1)} = \int_0^\infty dg\, \frac{h_{\sigma_2}(g)}{g+(k/2-1)G}. \tag{4.34}$$

Now using $p_c = k/2$ and $k = 4$ for the special case at hand, meaning a two-dimensional square lattice, we obtain the final form of the EMT equation:

$$\frac{p-p_c}{Gp} = \int_0^\infty dg\, \frac{h_{\sigma_2}(g)}{g+G}. \tag{4.35}$$

The numerical solution of equation 4.35, with $h_{\sigma_2}(g)$ as given by its asymptotic form, equation 4.28, is plotted in Fig. 4.6(a) as a function of $(p-p_c)$, for different values of ξ/σ_1. All curves have been calculated for $N = 5$ particles in a channel with a length of $\sigma_2/\sigma_1 = 10$. For $\xi/\sigma_1 = 1$ (dotted line) the EMA conductance G follows apparently a straight line when plotted in the log-log scale, suggesting that Eq. (4.1) applies to the whole range of the considered $p - p_c$ values. A closer look reveals that G actually deviates from a simple power-law behaviour and shows, as a function of $(p-p_c)$, an initially slightly faster decay followed, for sufficiently small values of $(p - p_c)$, by a power-law behaviour with the exponent t corresponding to the EMA universal value of $\bar{t}_0 = 1$. This feature is much more evident for $\xi/\sigma_1 = 0.6$ (dashed lines) and $\xi/\sigma_1 = 0.4$ (solid lines) where the initial decay of G is steeper as ξ/σ_1 is reduced while the universal exponent $\bar{t}_0 = 1$ is recovered only for the relatively small values of $(p - p_c) \lessapprox 10^{-3}$. To quantify the behaviour of G as $(p - p_c) \to 0$ it is useful to introduce the "p-dependent" conductivity exponent that we define "locally" as:

$$t^*(p) = \frac{d\ln(G)}{d\ln(p - p_c)}, \tag{4.36}$$

and shown in Fig. 4.6(b). By reducing the value of ξ/σ_1, it is clearly seen that $t^*(p)$ acquires a stronger $p - p_c$ dependence which would result in an apparent non-universality with $t^*(p) > \bar{t}_0 = 1$. This is apparent if one tries to fit G values according with Eq. (4.1) for the interval of the larger $p - p_c$ values. As $p \to p_c$, the above "local" exponent asymptotically tends to the universal EMA value of $\bar{t}_0 = 1$, independently of the value of the tunnelling factor ξ/σ_1.

The results plotted in Fig. 4.6 stem from the strong dependence of $h_{\sigma_2}(g)$ which, as shown in Fig. 4.5, is non-monotonic with a characteristic maximum at a given value of g. Upon lowering ξ/σ_1, the maximum of $h_{\sigma_2}(g)$ increases in amplitude and shifts to lower values of g. This feature, combined with the factor $1/(g + G)$ in the integrand of Eq. (4.35), which favours the small g region of integration for small G values (i.e. small $(p-p_c)$ values), leads to a change in the "local" exponent as the percolation transition is approached from above. This mechanism is at the origin of the apparent non-universality, which, as shown in the next section, characterizes the tunnelling-percolation model studied in this chapter. This mechanism is also important, because, as discussed in the conclusions of this chapter and in the beginning of the next one, it can also lead to apparent non-universality in systems without invoking the one-dimensionality of the particle distribution.

In the next section we present Monte Carlo simulation results of this TP model and obtain results in qualitative agreement with those obtained in the effective-medium approximation framework.

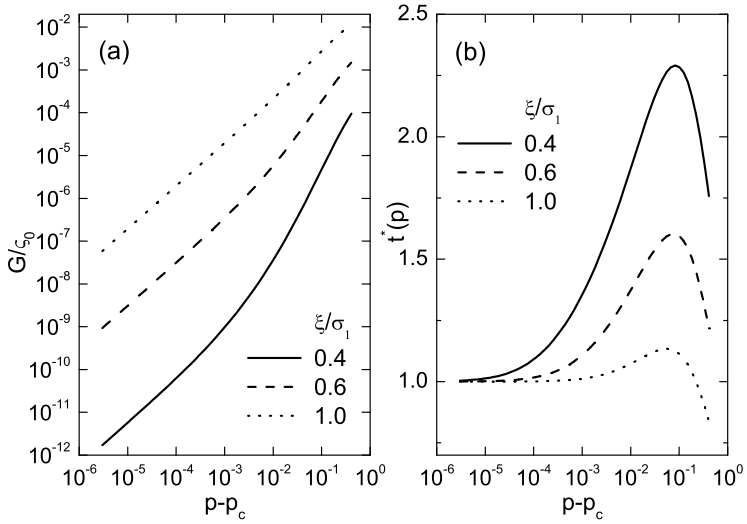

Figure 4.6: (a): the EMA conductance as a function of the proximity to the percolation threshold for the segregated tunnelling-percolation model for different values of ξ/σ_1. Here, $N = 5$ and $\sigma_2/\sigma_1 = 10$. (b): the corresponding p-dependent transport exponent as given by Eq. (4.36).

4.3.2 Monte Carlo results

Let us present now our Monte Carlo results for the conductivity for our tunnelling-percolation model. We construct a $n \times n$ square lattice, with $n = 256$, where each link of length σ_2 has a probability p of being occupied by N impenetrable particles and a probability $1 - p$ of being empty. The calculated distribution function of the occupied link conductance has already been discussed in Sec. 4.2.4 and plotted in Fig. 4.5.

Once the lattice is generated, we calculate the conductivity of the system using a Fourier-accelerated conjugate-gradient algorithm as described in Ref. [62]. For each p value, we average the results over $N_s = 10$ to $N_s = 60$ different realizations of the lattice and use twice the standard deviation of the mean value as the error on the conductivity. We have computed the network conductivity Σ as a function of the bond occupation probability p and for different values of the parameters σ_2/σ_1, N, and ξ. The different values of p have been chosen to range from $p - p_c = 0.1$ down to $p - p_c = 0.001$, where $p_c = 1/2$ is the percolation threshold for the square lattice.

Instead of fitting the so-obtained conductance G with Eq. (4.1), we extract the conductivity exponent t from

$$G = G_0 \left[p - p_c(n)\right]^t, \tag{4.37}$$

where $p_c(n)$ is the percolation threshold for our finite-size systems with $n \times n$

nodes, left free as a fitting parameter. The use of Eq. (4.37) rather than its infinite-size limit Eq. (4.1) is meant to simulate the situation encountered in experiments, where the percolation threshold, in our case $p_c(n)$, is not known a priori and must be obtained by a direct fit to Eq. (4.37). We have checked that, by changing the size of the network, $p_c - p_c(n)$ scales as $n^{-1/\nu}$, where $\nu = 4/3$ is the correlation length exponent in two-dimensions, as expected from finite size scaling [63].

In Fig. 4.7(a) we report the results for a simple binary distribution in which a fraction p of links has conductance $g = 1$ and the remaining fraction $1 - p$ has $g = 0$. Due to the finite size of the network, the conductivity Σ has a critical threshold $p_c(n)$ slightly lower than $p_c = 1/2$ and depending on n. As a function of $p - p_c(n)$, Σ displays a power-law behaviour with exponent $t = 1.3 \pm 0.05$ in full agreement with the universal one $t_0 \simeq 1.3$ [64], indicating that the system size was sufficiently large to make finite size effects negligible for the extraction of t. This is confirmed also by the results reported in Fig. 4.7(b) where Σ is shown for the tunnelling-percolation model with $\sigma_2/\sigma_1 \to \infty$ and for $\alpha_\infty = 1/2$. The extracted exponent is $t = 2.15 \pm 0.11$ in good agreement with the exact result $t = 1/(1 - \alpha_\infty) = 2$ obtained from Eq. (4.3). It should be noticed that the good agreement of the extracted exponents with those expected from theory indicates that the range of p values used in the fits of Figs. 4.7(a) and (b) was well within the critical region. The same p values were then used in all calculations reported in the following. Let us also briefly discuss the origin of the increase of the relative errors on the conductivity as p_c is approached. This phenomenon is mainly due to the divergence of the correlation length as p tends towards p_c, increasing the finite-size effects. As it was stressed in section 2.2.3, the percolating cluster presents inhomogeneities at all length scales for $p = p_c$, so that it is not possible to capture correctly its geometry when looking at a system of finite size. As $p \to p_c$ the variability of the percolation cluster in a system of finite size will increase, leading to a larger intrinsic error on the conductivity of the system. This will be observed for all finite-size systems studied in this thesis.

Results of tunnelling-percolation model for finite σ_2/σ_1 values are reported in Fig. 4.7(c) where Σ is plotted for the same parameter values of Fig. 4.5(a). The extracted exponent $t = 1.39 \pm 0.08$ is in this case close to the universal value $t_0 \sim 1.3$, while the same parameters $N\sigma_1/\sigma_2 = 0.5$ and $\xi/\sigma_1 = 1$ ($\alpha_\infty = 0.5$) have led to $t \simeq 2.15$ for the $\sigma_2/\sigma_1 \to \infty$ case of Fig. 4.7(b). This means that the smallest p values used in the calculation were close enough to $p_c(n)$ to sample the entire distribution function $h_{\sigma_2}(g)$ which, for the case at hand, displays a maximum at not too small values of g. The situation is different for the other cases displayed in Figs. 4.5(b) and (c) where the position of the maximum of $h_{\sigma_2}(g)$ considerably shifts to lower values of g. Indeed, for these cases, the obtained exponents were $t = 1.51 \pm 0.07$ for $\xi/\sigma_1 = 0.8$ [Fig. 4.5(b)] and $t = 2 \pm 0.095$ for $\xi/\sigma_1 = 0.5$

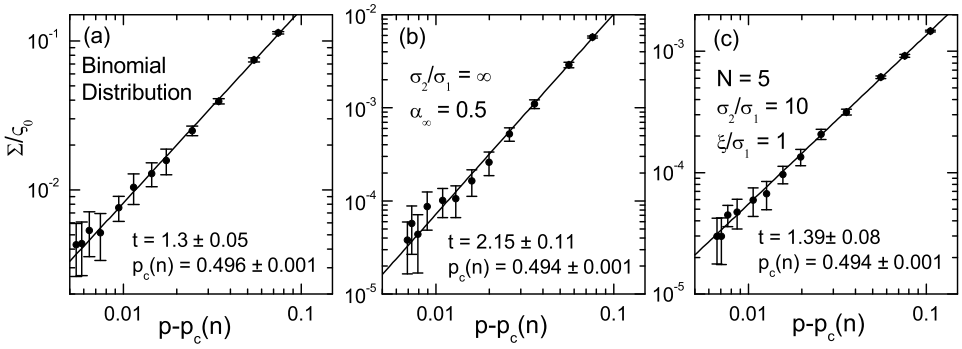

Figure 4.7: Network conductivity Σ for the simple binomial distribution (a), for the tunnelling percolation model with $\sigma_2/\sigma_1 \to \infty$ (b) and for σ_2/σ_1 finite (c). $\xi/\sigma_1 = 1$ and $N\sigma_1/\sigma_2 = 0.5$ for both figures (b) and (c). $p_c(n)$ is the percolation threshold obtained by fitting Σ to Eq. (4.1) for a square lattice of $n \times n$ nodes with $n = 256$.

[Fig. 4.5(c)].

Results for various values of the number of particles per channel N and of the tunnelling factor ξ are summarized in Fig. 4.8 (open triangles). In the left panel, the peak position of $h_{\sigma_2}(g)$ is varied by changing N, while in the right panel N is maintained fixed and ξ is varied. The results for finite σ_2/σ_1 are also compared with the exact formula (4.3) (solid line) and with numerical calculations for $\sigma_2/\sigma_1 \to \infty$ case (open circles). The extracted exponent values for σ_2/σ_1 finite are systematically smaller than those for $\sigma_2/\sigma_1 \to \infty$ and the regime of measured universality is extended to higher values of the control parameter α_∞.

It is important to stress here that the procedure that we followed to obtain the critical exponents t was meant to simulate a typical experimental situation, where a limited number of p values (where p could be the volume fraction of conducting phase) are used, without prior knowledge of the critical threshold value. It is interesting to notice that usually, experiments do not probe values smaller than $(p-p_c)/p_c \simeq 0.1$, whereas in our calculations, we had at least $(p - p_c(n))/p_c(n) \simeq 0.01$. Hence what we have dubbed as "apparent" non-universality of tunnelling-percolating systems could actually be very difficult to distinguish experimentally from the truly non-universal case $\sigma_2/\sigma_1 \to \infty$. As already mentioned in the introduction, disordered RuO_2-glass composites may have σ_2/σ_1 of the order of 10 to 100 but displaying t values clearly larger than the universal one [65]. According to our results, this behaviour could be interpreted as being due to apparent non-universality. However, given the difficulty of preparing samples with p very close to p_c (the critical volume fraction of RuO_2-glass systems is only around 3%), the expected universal regime is practically unreachable, so that the phenomenology remains that characterizing non-universal systems. This is

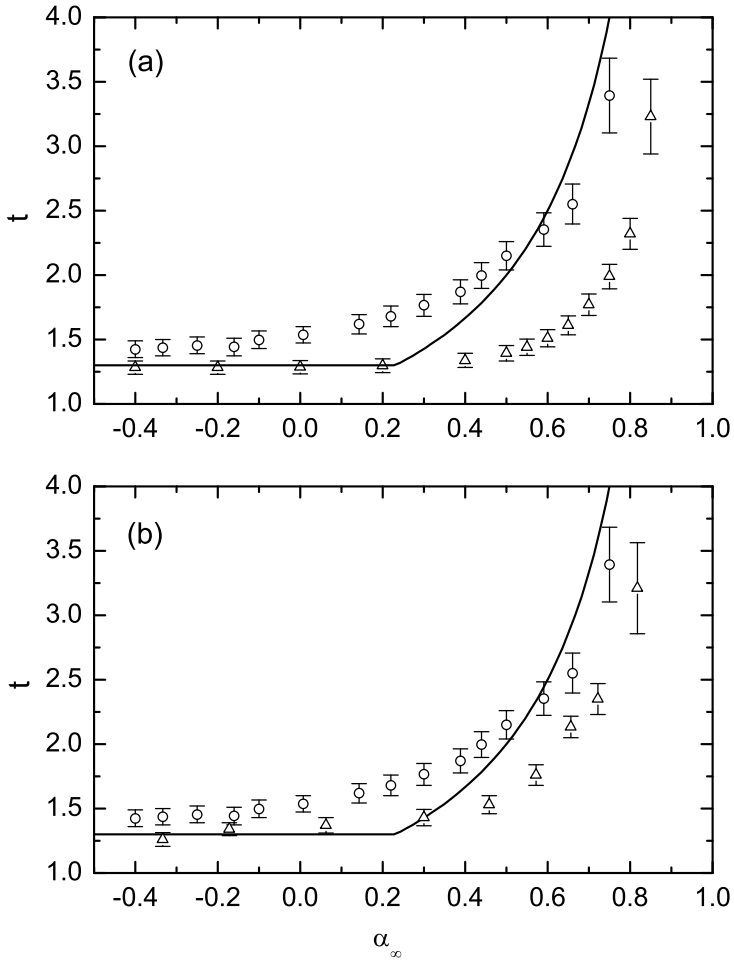

Figure 4.8: Exponent t and corresponding error bars extracted from fits to Eq. (4.1) as a function of $\alpha_\infty = 1 - (\xi/2)/(\sigma_2/N - \sigma_1)$. The solid line is the exact result of Eq. (4.3) for the $\sigma_2/\sigma_1 \to \infty$ case which is compared with the corresponding Monte Carlo results (open circles). The open triangles are the numerical results for finite σ_2/σ_1. Panel (a): $\sigma_2/\sigma_1 = 10$, $N = 5$ and ξ/σ_1 is varied from 2.8 to 0.3. Panel (b): the triangles are for $\sigma_2/\sigma_1 = 19$, $\xi/\sigma_1 = 0.5$ and α_∞ is varied by changing N.

really the key result obtained for transport properties in the framework of this model: non-universality can be explained without invoking a diverging $h(g)$. Indeed we have shown that a highly peaked $h(g)$ was sufficient to obtain apparent non-universality, which can account for the experimental results. This has an important consequence, as it means that the one-dimensionality in the matter distribution, essential for true non-universality

in the TP model, is not be necessary to obtain apparent non-universality. This will be discussed in more detail in the beginning of following chapter.

4.4 Piezoresistivity

In the preceding section, we have seen that the conductivity of our tunnelling-percolation model, though not presenting true non-universality for finite bond length σ_2/σ_1, had an apparent non-universal behaviour. Nevertheless we argued that the transport exponent should cross over to its universal value close enough to the percolation threshold. Unfortunately, it is very difficult to observe this crossover from measurements of the conductivity for limited numbers of $p - p_c$ values. We propose in this section to study the piezoresistivity of tunnelling-percolation systems, which will be shown to be directly linked to the transport exponent and, therefore, to be a very good tool to study this crossover between universal and non-universal regimes.

It is clear that TP systems are expected to display high piezoresistive responses, as the conductivity of a tunnelling junction decreases exponentially with the inter-particle distance, which will change with an applied exterior strain. It is also easy to see why piezoresistivity should be a good tool to study the tunnelling-percolation non-universality. Indeed, as the transport exponent t depends on the mean nearest-neighbour distance a only in the non-universal regime, t is expected to change with the applied strain only for $t > t_0$. This will be shown to give rise to two very different behaviours of the piezoresistivity, which can be used not only to clearly distinguish the universal from the non-universal regime, but also to confirm the tunnelling-percolation origin of non-universality in real composites.

Now, I will first present the piezoresistive response of the original tunnelling-percolation model ($\sigma_2/\sigma_1 \to \infty$), compared with some experimental results, as presented in a series of papers of our group, prior to this thesis [66,67,68,5]. As outlined above, this will give a strong evidence of the applicability of the TP model to real compounds and it will also help us understand the results obtained in systems displaying apparent non-universality, that will be presented towards the end of this chapter.

4.4.1 Theory of piezoresistivity

Before anything else, we shall recall some basic theory of piezoresistivity, mostly taken from Ref. [5].

Let us consider the rather general situation in which a parallelepiped with dimensions L_x, L_y and L_z is subjected to a deformation along its main axes x, y, and z. The initial volume $V = L_x L_y L_z$ changes to $V(1 + \Phi)$ where $\Phi = \varepsilon_x + \varepsilon_y + \varepsilon_z$ is the volume dilatation and $\varepsilon_i = \delta L_i / L_i$ are the principal strains along $i = x, y, z$. In the absence of strain, we assume that

the conductivity Σ of the undeformed parallelepiped is isotropic, so that the conductance G_i measured along the i axis is $G_i = \Sigma L_j L_k / L_i$. For small $\varepsilon_i \neq 0$ $(i = x, y, z)$, the conductance variation δG_i is therefore:

$$\frac{\delta G_i}{G_i} = \frac{\delta \Sigma_i}{\Sigma} - \varepsilon_i + \varepsilon_j + \varepsilon_k, \tag{4.38}$$

where

$$\frac{\delta \Sigma_i}{\Sigma} = -\Gamma_{\parallel} \varepsilon_i - \Gamma_{\perp} (\varepsilon_j + \varepsilon_k) \tag{4.39}$$

are the relative variation of the conductivity along the $i = x, y, z$ directions. The coefficients $\Gamma_{\parallel}$ and $\Gamma_{\perp}$ are the longitudinal and transverse piezoresistive factors defined as:

$$\Gamma_{\parallel} = - \left. \frac{d \ln(\Sigma_i)}{d\varepsilon_i} \right|_{\varepsilon_i = 0} \tag{4.40}$$

$$\Gamma_{\perp} = - \left. \frac{d \ln(\Sigma_j)}{d\varepsilon_i} \right|_{\varepsilon_i = 0} \qquad (i \neq j), \tag{4.41}$$

The distinction between longitudinal, $\Gamma_{\parallel}$, and transverse, $\Gamma_{\perp}$, piezoresistive responses is important whenever the values of the strains ε_i depend on the direction, as it is encountered when the sample is subjected to uniaxial distortions as those induced in cantilever beam experiments (see next section).

In what follows, we are mainly interested in the isotropic (or hydrostatic) piezoresistive factor Γ defined as the resistivity change induced by the isotropic strain field $\varepsilon_i = \varepsilon$ for all $i = x, y, z$:

$$\Gamma = - \left. \frac{d \ln(\Sigma)}{d\varepsilon} \right|_{\varepsilon = 0}, \tag{4.42}$$

which can be obtained by applying an hydrostatic pressure to the parallelepiped. However, Γ can also be obtained by setting $\varepsilon_i = \varepsilon$ in Eq. (4.39) yielding:

$$\Gamma = \Gamma_{\parallel} + 2\Gamma_{\perp}, \tag{4.43}$$

which is a useful relation when the experimental set up does not permit to apply an isotropic strain field. Let us note here that, usually, in experiments, we do not measure directly the piezoresistive factors, but rather the gage factors which are extracted from the conductance (instead of the conductivity) variation. Therefore the strains have to be known in order to extract $\Gamma_{\parallel}$ and $\Gamma_{\perp}$ from the gage factors. The definitions and relations between the gage and piezoresistive factors can be found in Refs. [69, 70].

4.4.2 Piezoresistivity in truly non-universal TP systems

Let us now study how the tunnelling-percolation theory of non-universality affect the piezoresistive factor Γ. For clarity, we recall here the basic equations governing the transport properties of the system. So first of all the conductivity of the percolation network is given by:

$$\Sigma = \Sigma_0 (p - p_c)^t \tag{4.44}$$

As shown in section 4.2.4, the distribution function $h_\infty(g)$ of the bond conductances for $\sigma_2/\sigma_1 \to \infty$ is given by (see equations 4.28 and 4.27)

$$\begin{aligned} h_\infty(g) &\simeq (1-\alpha_\infty) g^{-\alpha_\infty} && (4.45)\\ \alpha_\infty &= 1 - \frac{\xi/2}{a_\infty - \sigma_1} && (4.46)\\ a_\infty &= \rho^{-1}, && (4.47) \end{aligned}$$

Leading to a transport exponent t depending on the parameters of the system as

$$t = \begin{cases} t_0 & \text{if} \quad t_1 < t_0 \\ t_1 = (D-2)\nu + \frac{1}{1-\alpha_\infty} & \text{if} \quad t_1 > t_0 \end{cases} \tag{4.48}$$

We now assume that a cubic bond-percolation network is embedded in a homogeneous elastic medium and that the elastic coefficients of the network and the medium are equal. Under an isotropic strain field $\varepsilon_i = \varepsilon$ $(i = x, y, z)$, the mean tunnelling distance a changes to $a(1+\varepsilon)$ independently of the bond orientation. Hence, by assuming for simplicity that $\sigma_1 \to \sigma_1(1+\varepsilon)$, the tunnelling parameter α_∞, given in equation 4.46, becomes $\alpha_\infty \to \alpha_\infty + (1-\alpha_\infty)\varepsilon$ for $\varepsilon \ll 1$. Now, from the definition of Γ given in equation 4.42 and equation 4.44, we have (for clarity we do not always recall here that the derivative is evaluated at $\varepsilon = 0$)

$$\begin{aligned} \Gamma &= -\frac{d}{d\varepsilon}\left[\ln(\Sigma_0) + t\ln(p-p_c)\right] && (4.49)\\ &= \Gamma_0 - \frac{dt}{d\varepsilon}\ln(p-p_c), && (4.50) \end{aligned}$$

with

$$\Gamma_0 = -\left.\frac{d\ln(\Sigma_0)}{d\varepsilon}\right|_{\varepsilon=0}. \tag{4.51}$$

Looking at equation 4.48, it is clear that $dt/d\varepsilon$ will be non zero only in the non-universal case, so that we finally obtain:

$$\Gamma = \begin{cases} \Gamma_0 & \alpha_\infty \le \alpha_c \\ \Gamma_0 - \frac{dt}{d\varepsilon}\ln(p-p_c) & \alpha_\infty > \alpha_c \end{cases}, \tag{4.52}$$

with

$$\frac{dt}{d\varepsilon} = \frac{1}{1-\alpha_\infty} = 2(a_\infty - \sigma_1)/\xi, \tag{4.53}$$

where we have used $d\alpha_\infty/d\varepsilon = (1-\alpha_\infty)$. The tunnelling distance dependence of the DC transport exponent is therefore reflected in a *logarithmic* divergence of Γ as $p \to p_c$. Instead, when $\alpha_\infty \leq \alpha_c$ (universal regime), the DC exponent remains equal to t_0, also when $\varepsilon \neq 0$, and the resulting piezoresistive factor is simply equal to $\Gamma = \Gamma_0$, independently of the bond probability p.

This shows that the tunnelling-percolation origin of non-universality is characterized by a logarithmic divergence of the piezoresistivity for $p \to p_c$, which is a feature unique to this model. We can now turn back to the interpretation of the experimental results presented in section 3.3. The piezoresistivity of four different sets of samples, was presented in figure 3.4 as a function of the concentration $x - x_c$. Those experimental results are perfectly compatible with the above result for Γ. Indeed the logarithmic divergence of Γ is well verified by this experimental set of data. Moreover, a constant piezoresistivity is found for the A1 series, which was the only one to display an almost universal transport exponent $t = 2.15 \pm 0.06$. Equation 4.52 is an exact result as long as we are concerned with the $(p - p_c)$ dependence close to the percolation threshold. However, in addition to the prefactor of the logarithm, Γ depends also on the tunnelling parameter α_∞ through the term Γ_0. This dependence is far from trivial and it is also shown in this paper [5] that Γ_0 behaves as predicted by the TP model. This strong agreement between TP theory and experiments is really comforting tunnelling as the dominant transport mechanism in TFRs.

4.4.3 Piezoresistivity in apparent non-universal systems

Because of the very good agreement of this piezoresistive response between theory and classical TP theory, it is important to see whether our apparent non-universal systems also display this behaviour. Moreover, as shown in section 4.3, the apparent transport exponent also depends on the mean nearest-neighbour distance and yields the universal value t_0 only for p values very close to p_c. Therefore, the piezoresistivity is expected to yield both behaviours found above: a logarithmic divergence for values of p not too close to p_c and a universal constant behaviour $\Gamma = \Gamma_0$ for $p \to p_c$. So we expect the piezoresistivity to be a much more sensitive tool than the study of the conductivity, to observe this change from apparent non-universal to universal regime. We therefore now study the piezoresistivity of our TP model, first using the effective medium theory, allowing us to understand the behaviour of Γ, and then by means of Monte Carlo simulations, to asses the real behaviour of our model [71].

4.4.3.A Effective medium theory

To quantify the piezoresistive response within EMA, let us first rewrite the basic EMT equation 4.35 in its discrete form:

$$\frac{1}{\mathcal{N}'}\sum_i{}' \frac{1}{g_i+G} = \frac{p-p_c}{pG}, \tag{4.54}$$

where the primed summation is restricted to the occupied channels ($g_i \neq 0$) which are a fraction $p = \mathcal{N}'/\mathcal{N}$ of the total channel number $\mathcal{N}$ forming the square lattice. As done in section 4.4.2, let us assume that the conducting and insulating phases have identical elastic constants so that the system is elastically homogeneous. In this way, the applied strain ϵ is uniform and g_i and G reduce to

$$g_i \rightarrow g_i(\epsilon) \simeq g_i[1-\gamma(g_i)\epsilon], \tag{4.55}$$
$$G \rightarrow G(\epsilon) \simeq G[1-\Gamma\epsilon], \tag{4.56}$$

where, ϵ has been assumed infinitesimal, $\gamma(g_i) = -d\ln g_i(\epsilon)/d\epsilon|_{\epsilon=0}$ is the piezoresistive coefficient for a given channel and

$$\Gamma = -\left.\frac{d\ln(G)}{d\epsilon}\right|_{\epsilon=0} \tag{4.57}$$

is the piezoresistive response coefficient of the whole system. Once the above expressions are substituted into Eq. (4.54), the terms linear in ϵ enable to find the following EMA equation for Γ:

$$\Gamma = \frac{\sum_i{}' \frac{g_i\gamma(g_i)}{(g_i+G)^2}}{\sum_i{}' \frac{g_i}{(g_i+G)^2}} = \frac{\int_0^\infty dg \frac{gh_{\sigma_2}(g)}{(g+G)^2}\gamma(g)}{\int_0^\infty dg \frac{gh_{\sigma_2}(g)}{(g+G)^2}}, \tag{4.58}$$

where in the second equality we have restored the continuum representation by using $h_{\sigma_2}(g) = \frac{1}{\mathcal{N}'}\sum_i{}'\delta(g-g_i)$. Within the approximation scheme derived for equation 4.28 (considering that the conductance of a bong g is dominated only by the worst interparticle conductivity in the bond), for small values of g, the function $\gamma(g)$ in Eq. (4.58) is approximately given by $\ln(1/g)$. The $(p-p_c)$ dependence of the resulting Γ is plotted then in Fig. 4.9(a) for the same parameter values that were used for Fig. 4.6. Two different behaviours are clearly discernible. In the not too close vicinity of p_c, Γ increases approximately as $\ln[1/(p-p_c)]$, and the increases is stronger as ξ/σ_1 is smaller. Upon the approach to p_c, the piezoresistivity response coefficient crosses over to a region where Γ is independent of $(p-p_c)$. The crossover position depends on ξ/σ_1 and moves towards the percolation threshold as ξ/σ_1 is lowered. When

Γ is plotted as a function of the EMA conductance G, as in Fig. 4.9(b), a logarithmic behaviour of the form

$$\Gamma \propto \ln(1/G) \tag{4.59}$$

is obtained for the interval of the larger G values. This interval is broadened towards the smaller G values as the value of ξ/σ_1 is lowered. We can define then a crossover G value, that we denote G^*, that characterizes the transition in the G-dependence of Γ. In Fig. 4.10(a) we illustrate how the value of G^* can be extracted from the fits of Γ to the large, $G > G^*$, and low, $G < G^*$, intervals of the conductance range. The corresponding ξ/σ_1 dependence of the crossover conductance is shown in Fig. 4.10(b) for several values of ξ (filled squares).

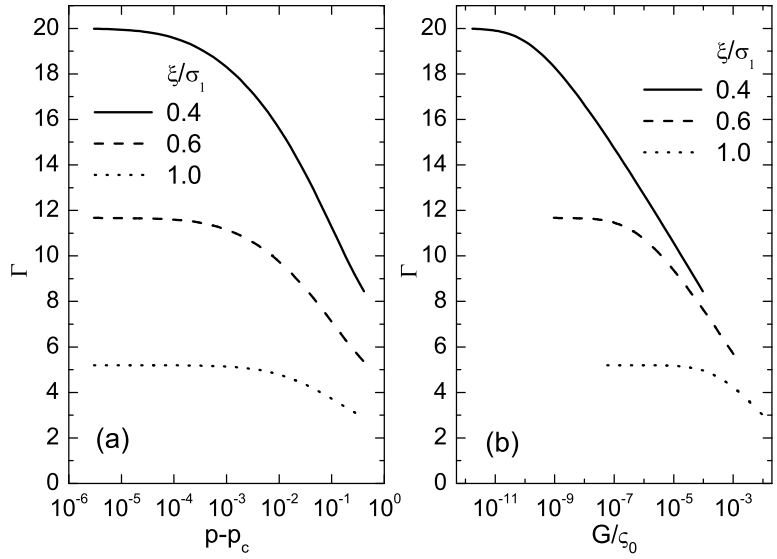

Figure 4.9: (a): the piezoresistive response coefficient as a function of the proximity to the percolation threshold. The results were obtained from the EMA equation for the same parameter values of Fig. 4.6. (b): the same coefficient plotted as a function of the system conductance.

The behaviour of Γ can be understood by assuming that the crossover G^* is given actually by the bond conductance value for which $h_{\sigma_2}(g)$ approaches zero. As shown in Fig. 4.5(c), for small values of ξ/σ_1, $h_{\sigma_2}(g)$ is sharply peaked at $g = g_m = \exp(N-1)g_{\min}$ (for definitions of g_m and $g_{\min}$ refer to section 4.2.4) and then falls rapidly to zero for lower values of g. In this case the estimate $G^* \approx g_m$ can be used. The logarithmic dependence Eq. (4.59) for $G \gtrsim G^* \approx g_m$ can then be derived from Eq. (4.58) by noticing that the function $g/(g+G)^2$ appearing in the integrals is strongly peaked at $g = G$, especially for small G values, so that the main contribution to Γ comes from

$g \simeq G$, and thus Eq. (4.59) follows from the approximation $\gamma(g) \simeq \ln(1/g)$ for small values of g. On the other hand, for $G \lesssim G^* \approx g_m$, Γ is independent of G and can be approximated by the $G \to 0$ limit of Eq. (4.58) which reads:

$$\lim_{G\to 0} \Gamma \equiv \Gamma_0 = \frac{\int_0^\infty dg \frac{h_{\sigma_2}(g)}{g} \gamma(g)}{\int_0^\infty dg \frac{h_{\sigma_2}(g)}{g}}. \tag{4.60}$$

The same reasoning can be followed also when ξ/σ_1 is large, so that the corresponding $h_{\sigma_2}(g)$ has a much weaker dependence, as shown in Fig. 4.5(a), provided that G^* is approximated now by the g-value for which $h_{\sigma_2}(g)$ vanishes, i.e. $G^* \approx g_{\min}$. Hence, we have obtained analytic bounds for the G^* dependence on the value of ξ/σ_1: $G^* \approx g_m$ for small ξ/σ_1 values and $G^* \approx g_{\min}$ for the larger ξ/σ_1 values. These two bounds of G^* are displayed in Fig. 4.10(b). The comparison with the G^* values extracted from the EMA results (solid squares) indicates that the above estimates can be considered as reasonable bounds to the G^* versus ξ/σ_1 behaviour.

4.4.3.B Monte Carlo results

Let us present now our Monte Carlo results on the piezoresistance for the model introduced in Sec.4.2.2. The simulation procedure is the same as the one described in the beginning of section 4.3.2. We again use $n = 256$ for the size of the square lattice, but this time the number of realizations is set to $N_s = 20$ and p has been chosen to range from $p - p_c = 0.5$ down to $p - p_c = 0.003$ (again with $p_c = 0.5$).

The piezoresistive response is obtained by calculating, for a given lattice realization, the conductance G when a homogeneous strain $\epsilon = 0.01$ is applied to the lattice. The difference ΔG with respect to the case without strain is then used to evaluate Γ via $\Gamma = -\Delta G/\epsilon G$. Again twice the standard deviation of the mean value of Γ is used to estimate the error on the piezoresistivity.

In Fig. 4.11 we present then typical results for G and Γ as functions of $p - p_c(n)$ as obtained from our Monte Carlo calculations for $N = 5$ particles and $\xi/\sigma_1 = 1$. The critical exponent extracted from the fit of the conductance shown in Fig. 4.11(a) is $t = 1.42 \pm 0.08$ which is slightly above the universal value $t_0 \simeq 1.3$ for two-dimensional networks. From our discussion of the EMA results in the last section, such relatively large values of ξ/σ_1 are not expected to give rise to a strong p dependence of the transport exponent t, as observed in Fig. 4.11(a), and our Monte Carlo data for G can be reasonably well fitted by an almost universal power-law with constant exponent in a wide range of p-values.

In Fig. 4.11(b) we show our calculated piezoresistive response coefficient as a function of $p - p_c(n)$ for the same parameter values of Fig. 4.11(a)

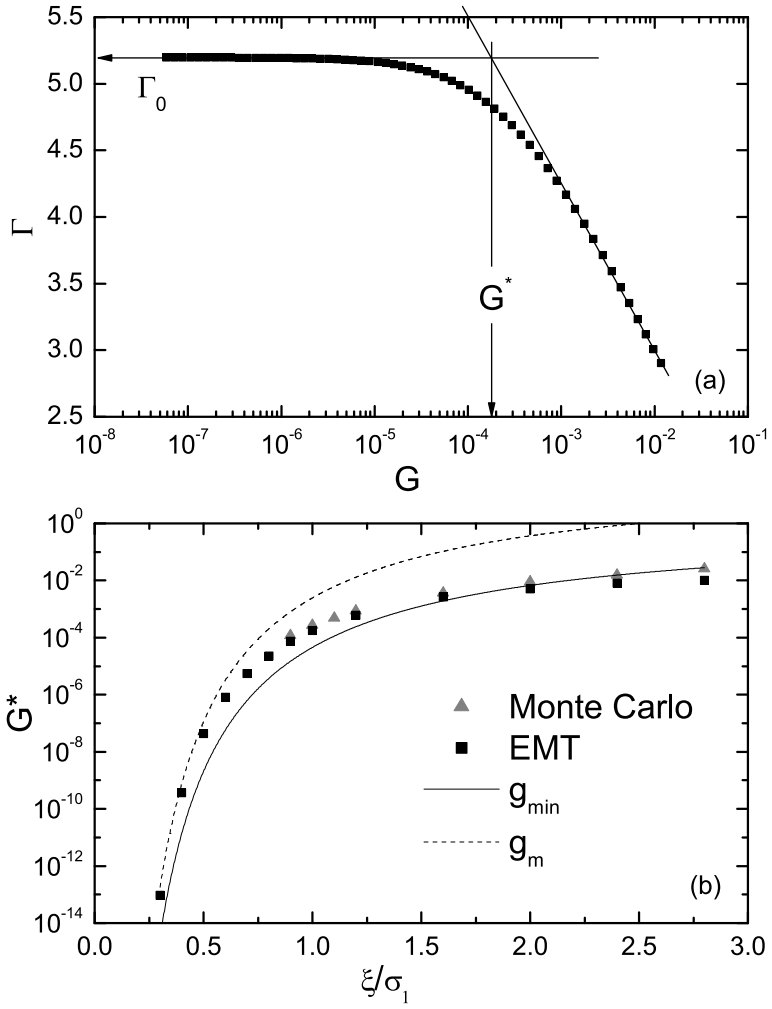

Figure 4.10: (a): the dependence of the piezoresistive response coefficient on the sample conductance, as obtained by the EMA calculation, for $\sigma_2/\sigma_1 = 10$, $N = 5$ and $\xi/\sigma_1 = 1$. The solid lines are linear fits to the low and large conductances and the crossover value G^* is determined by their intersection. (b): the dependence of G^* on ξ/σ_2 for the same σ_2/σ_1 and N. The analytic bounds to the observed behaviour are determined by the channel conductance where the corresponding distribution function Eq. (4.29) vanishes, $g_{\min} = \exp[-2(L-N\sigma_2)/\xi]$, or is maximized, $g_m = \exp(N-1)g_{\min}$ and are shown as a plain and a dashed line respectively.

(where $p_c(n)$ is the critical bond concentration extracted from the fit of the conductivity to the power-law). For bond concentration values larger than $p - p_c(n) \simeq 0.03$, Γ follows approximately a logarithmic behaviour while, for lower concentrations, it saturates at $\Gamma \simeq 4.75$. This trend is very similar to that reported in the last section for our EMA calculations of the piezoresistive response [Fig. 4.9(a)] and suggests a crossover between quasi

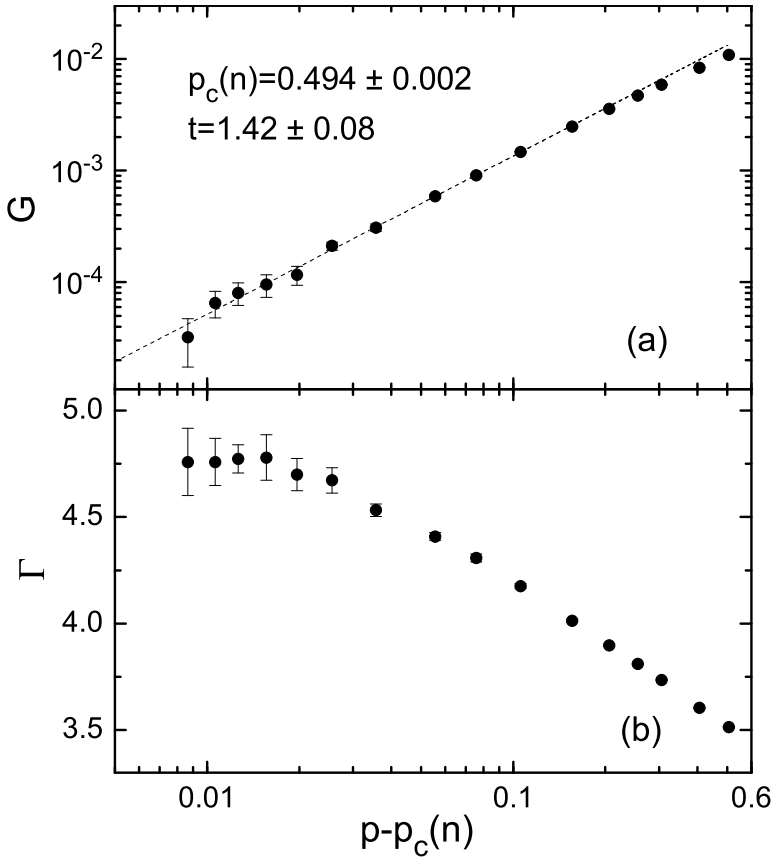

Figure 4.11: (a): Monte Carlo results for the system conductance as a function of the proximity to the percolation threshold (as determined from the fit of the conductivity), for $\sigma_2/\sigma_1 = 10$, $N = 5$, and $\xi/\sigma_1 = 1$. The dashed line is a fit to Eq. (4.37). (b): our Monte Carlo results of the piezoresistive response coefficient for the same parameter values of (a).

non-universality at high p values and universality at lower p, despite of the apparently accurate power-law behaviour displayed by G in Fig. 4.11(a).

The tunnelling-percolation nature of the crossover is verified in Fig. 4.12 where Γ is plotted against G for several values of the tunnelling factor ξ/σ_1 and for the fixed $L/\sigma_1 = 10$ and $N = 5$ values. As ξ/σ_1 is reduced, the point below which Γ saturates moves to lower values of G, in accordance with the EMA results shown in Fig. 4.9(b). By following the interpolation procedure described in Fig. 4.10(a), the values of crossover conductance G^* (grey triangles in Fig. 4.10(b)) match very closely those obtained from our EMA calculations. G^* is also represented in figure 4.12 by the dashed line, crossing $\Gamma(G)$ at G^* for the different values of ξ/σ_1.

The Monte Carlo calculations reported above show clearly that, as we

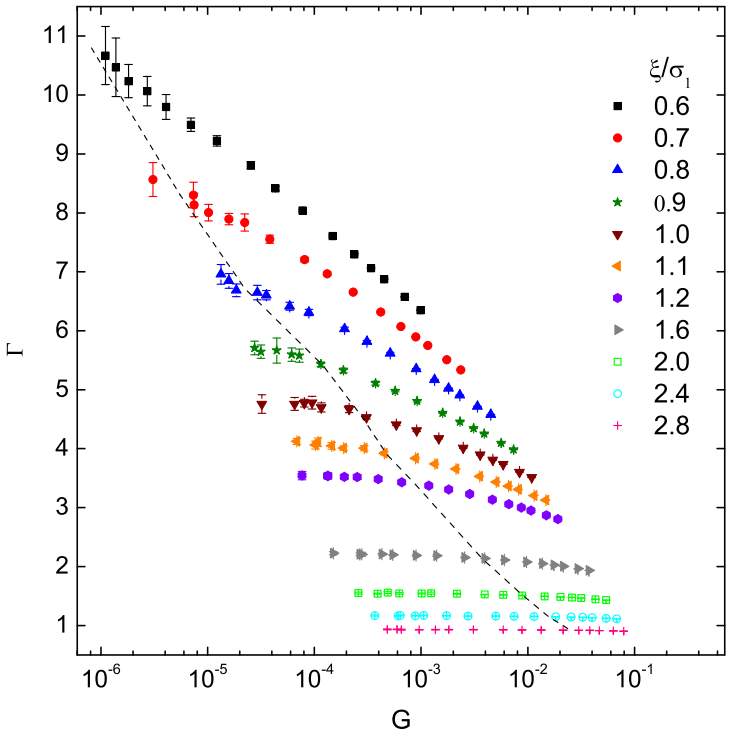

Figure 4.12: Monte Carlo results of the piezoresistive response coefficient as a function of the system conductance for different values of ξ/σ_1. This is for $\sigma_2/\sigma_1 = 10$ and $N = 5$. The dashed line represents the piezoresistance $\Gamma(G^*)$ as a function of the crossover conductance G^* extracted from our Monte Carlo results for $\xi/\sigma_1 \geq 0.9$ and from the EMT results for $\xi/\sigma_1 < 0.9$ (see Fig. 4.10).

suggested, the piezoresistive response is a much more sensitive quantity for the investigation of the TP crossover between non-universality and universality than the conductance itself, whose crossover is masked by the limited number of p values and the increasing fluctuations of G as the percolation threshold is approached from above [71]. From the random-resistor-network point of view, such sensitivity of Γ can also be understood by noticing that, away from the percolation threshold, the current flows through the less resistive links in the network, so that the bond conductance distribution function $h_{\sigma_2}(g)$ is probed, basically, only for the larger g values. On the contrary, close to the percolation threshold, the current is forced to flow through bonds with much lower g values, so that the conductivity of the system is basically dominated by the lowest such conductance and therefore the behaviour of $h_{\sigma_2}(g)$ as $g \to 0$ is directly probed. Since $h_{\sigma_2}(g)$ for our TP model does not diverge as $g \to 0$, the resulting piezoresistance for p close to p_c is expected to be independent of p, as for any universal TP system. This situation is illustrated

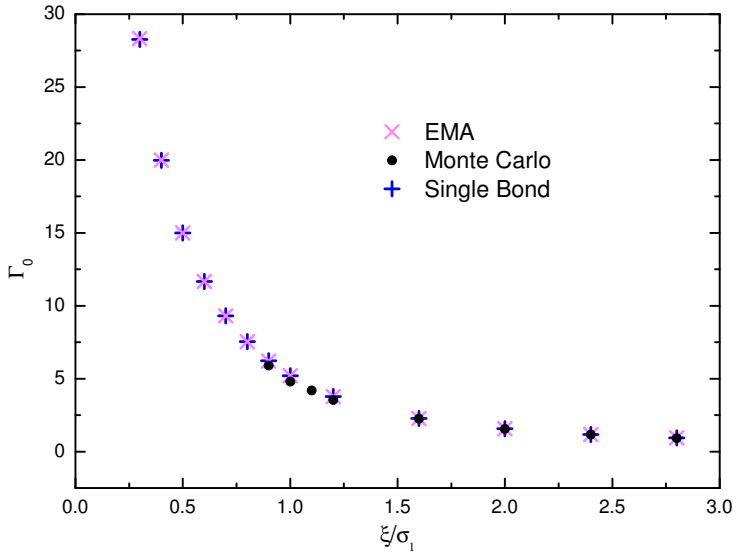

Figure 4.13: Comparison of the ξ/σ_1 dependencies of the asymptotic value of the piezoresistive response coefficient that were obtained from EMA, from Monte Carlo calculations and from the averaged piezoresistive response of a single bond with $\sigma_2/\sigma_1 = 10$ and $N = 5$.

in Fig. 4.13 where we have plotted the asymptotic limit $\Gamma_0 = \lim_{p\to p_c} \Gamma$ extracted from our Monte Carlo results (filled circles) together with the EMA formula Eq. (4.59) (crosses) which is identical to the piezoresistive response of a linear chain of conductances distributed according to $h_{\sigma_2}(g)$. This suggests that, very close to the percolation threshold, Γ is insensitive to the topology of the percolating cluster, as it is also verified by computing the averaged piezoresistive response obtained from a single channel occupied by N impenetrable spheres, that is also shown in Fig. 4.13.

Now coming back to the experimental results shown in figures 3.4 and 3.5, it appears that this crossover between logarithmic divergence and constant peizoresistivity, expected from our model, cannot be observed here. This can be attributed to the fact that, for so high piezoresistivities as measured here for the non-universal systems, the crossover is expected to fall at values of $x - x_c$ smaller than the ones probed in these experiments. For such low values of $x - x_c$, jointly high resistivities, the measurement of Γ is difficult due to noise, surface leakage and finite impedance of the electronics, making our interpretation of non-universality difficult to test. We nevertheless believe that a careful experimental study of the piezoresistivity of conductor-insulator, should allow to observe this crossover.

4.5 High-voltage trimming

We can now use the model developed in this chapter to try to understand the experimental results presenting, in section 3.4, the effect of high-voltage pulses on different characteristics of TFRs. These results can be explained if we consider the mechanisms involved in voltage trimming and the topology of the underlying current carrying network, supporting the existence of a percolation network with a broad distribution of local conductances.

We suppose that the global change of conductivity and other properties, is due to changes in the local intergrain conductances. It was proposed by Feldbaumer [42] that those changes were due to local heating, due to Ohmic dissipation, and that this was effective only if the local temperature exceeded the maximal temperature reached during firing. This assumption is somewhat supported by the results presented in figure 4.14, showing the initial resistivity $1/\Sigma_{\mathrm{I}}$ (panel (a)) and the relative change of conductivity $\Sigma_{\mathrm{I}}/\Sigma_{\mathrm{T}}$ due to trimming (panel (b)), as a function of the firing temperature, T_f, of the samples. We recall here that the samples were subjected to 2300 voltage pulses induced by the discharge of a capacitor of 0.33 nF charged at 500 V. We see in panel (a) that the initial resistivity of the samples depends on the firing temperature T_f. It first increases with increasing firing temperature, reaching a maximum around 600°C, and then decreases with further increasing T_f. This can be explained as follows: for low T_f the glass does not soften enough to break the aggregates of RuO_2, leading to good conduction. Then for higher T_f the glass starts to better wet the conducting grains, disassembling the RuO_2 aggregates, increasing the resistivity of the sample. Finally, for even higher firing temperatures, RuO_2 starts to diffuse into the glass, increasing the global conductivity of the sample. Now, as we had seen, in figure 3.7, the sensitivity to trimming depends largely on the distance to the percolation threshold $x - x_c$, and therefore on the initial conductivity Σ_{I} of the sample. In panel (b) of figure 4.14 we show how sensitive the samples are to trimming, depending on their firing temperature. We see that the relation between firing temperature and sensitivity to voltage pulses is monotonic, and can therefore not be explained solely by the change of the initial resistivity of the samples, which presents a maximum, as shown in panel (a) of this figure. We see in this figure that samples fired at higher temperatures are less sensitive to voltage pulses, supporting the above assumption that the resistance changes are due to local heating, which has to exceed the maximal firing temperature in order to be effective.

As our setup did not allow us to measure the discharge curves, which would have provided a clearer image of the phenomenon, we now assume that local Joule heating is responsible for the change of local resistances. The energy locally deposited in the sample is maximal in singly connected bonds with a large resistance, that will carry the whole current of the voltage pulse together with a large voltage drop. For samples far from the percola-

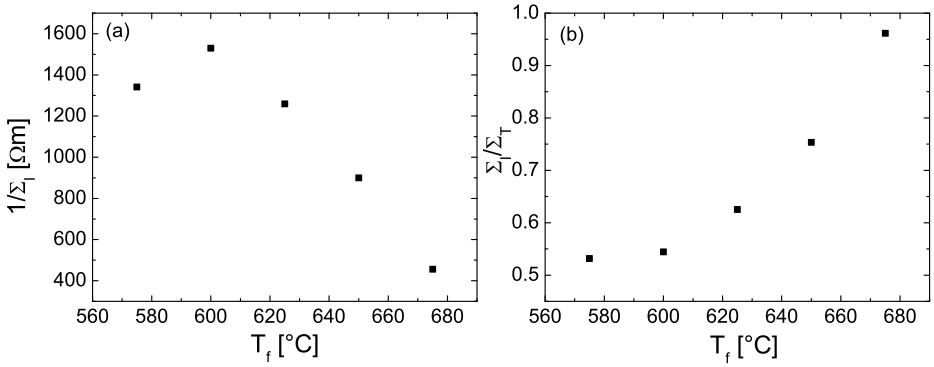

Figure 4.14: Resistance (a) and sensitivity to trimming (b) as a function of the firing temperature T_f for TFRs with RuO_2 grain size of 40 nm and concentration $x = 0.11$.

tion threshold, the current can avoid the large local resistances, because there are several parallel routes and very few singly-connected bonds. Trimming will therefore have little influence on the characteristics of the samples with volume fractions of conductor far above the percolation threshold. As the percolation threshold is approached the probability to have singly-connected bonds with large resistances increases and trimming becomes more effective. Of course, the largest local resistances are the ones that will be most affected by local heating, so that a broad distribution function $h(g)$ of the local conductivities will favour the change of global conductivity of the sample under high-voltage pulses. This local heating seems to lead to the decrease of the high resistances, which could be caused by several phenomena such as diffusion of RuO_2 into the insulating matrix, or diminution of the interparticle distance caused by the attraction due to electric potential difference and enabled through local melting of the insulating matrix. This phenomenon would basically change the distribution function $h(g)$, by cutting its tail for small g. As the number of singly-connected bonds diverges as the percolation threshold is approached, we expect that the relative change of conductivity induced by trimming will diverge as the percolation threshold is approached. This is indeed what was observed in figure 3.7, explaining well the increase of conductivity due to trimming and the dependence of the sensitivity to trimming on the distance to the percolation threshold x_c.

Now, as we have seen in this chapter, in the tunnelling-percolation model the piezoresistivity is even more dominated by the large local resistances than the resistivity of the sample, and should therefore be highly sensitive to the voltage pulses. We therefore now look at the change induced by trimming in the piezoresistivity of the samples. We study here the piezoresistive response coefficient Γ^{H}, for a TFR of resistance R deposited on a substrate

and subjected to hydrostatic pressure, defined by:

$$\Gamma^{\mathrm{H}} = \frac{\partial R}{R\partial\epsilon_z} = \left[\Gamma_\perp - 1 + \frac{\Gamma_\parallel + \Gamma_\perp}{1+\omega}\right] \tag{4.61}$$

$$\omega = \frac{1+\nu_R}{1-\nu_R}\left(\frac{E_S}{E_R}\cdot\frac{1-2\nu_R}{1-2\nu_S} - 1\right), \tag{4.62}$$

where ϵ_z is the strain in the normal direction to the surface of the substrate, E and ν are the elastic modulus and Poisson's coefficient and the subscripts R and S stand respectively for the resistor and the substrate. $\Gamma_\parallel$ and $\Gamma_\perp$ are the longitudinal and transverse piezoresistive coefficients as defined in equations 4.40 and 4.41. To calculate Γ^{H} from our hydrostatic measures we need to know the relation between the strain and the applied hydrostatic pressure P^{H}. This is given by:

$$\epsilon_z = -\frac{1-2\nu_S}{E_S}(1+\omega)P^{\mathrm{H}}. \tag{4.63}$$

Justifications of equations 4.61, 4.62 and 4.63 can be found in Ref. [70].

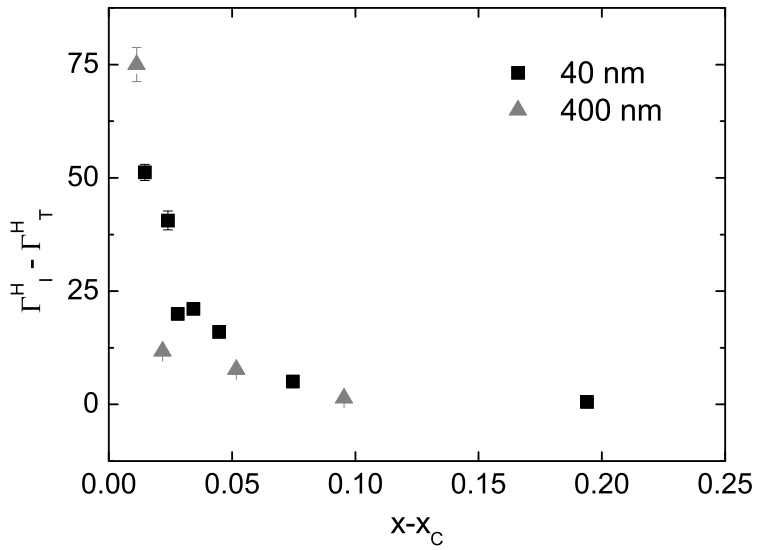

Figure 4.15: Change of piezoresistivity as a function of $x - x_c$ induced by voltage trimming. Γ_I^H and Γ_T^H are respectively the initial piezoresistive response coefficient and the one after trimming

In Fig. 4.15 we show the shift of piezoresistivity due to high-voltage trimming as a function of $x - x_c$. For all samples the piezoresistivity Γ^{H} diminished after trimming and the shift seems to diverge as the percolation threshold is approached. This is again compatible with our interpretation,

as the lowest local conductivities dominate the piezoresistive response. We therefore expect the piezoresistivity to decrease with voltage-trimming, and that this decrease should become very large close to the percolation threshold. This is indeed what we observe in this figure, confirming that the piezoresistivity is very sensitive to high-voltage pulses close to x_c and supporting our above interpretation of high-voltage trimming..

This interpretation, namely that voltage trimming changes $h(g)$, by increasing the lowest conductivities in the system has two more consequences. The first is that sample series presenting universal transport exponents should be less sensitive to voltage pulses, as the distribution of local conductances is less broad, with fewer low local conductances. This could not be verified by our results and is probably very difficult to asses as the sensitivity to voltage pulses also depends on many other factors, so that it remains an open question. The second is that when trimming is applied on a non-universal set of samples, it should drive the transport exponent towards universality, as the lowest conductances in the system are increased, moving the position of the peak of $h(g)$ to higher g values.

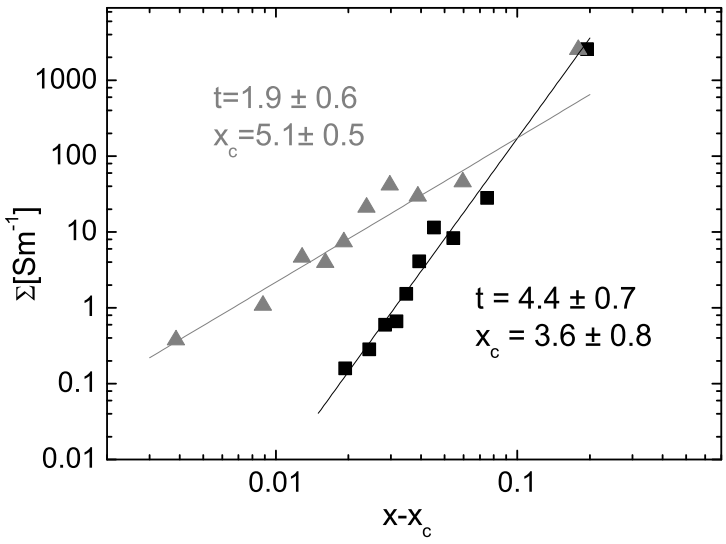

Figure 4.16: Conductivity of the 40 nm RuO_2 grain size series as a function of $x - x_c$. Black squares are the values before trimming and gray triangles after trimming. The critical concentrations and transport exponents obtained from fits to equation 4.1 are also shown.

In Fig. 4.16 we show the conductivity of the 40 nm RuO_2 grain size series, as a function of $x - x_c$ before and after trimming and the fits of equation 4.1 to these data (in fact the logarithm of equation 4.1 was fitted to $\ln(\Sigma)$ which gives better fits). As we can see this set of samples initially

showed a non-universal behaviour, with an exponent $t = 4.4 \pm 0.7$. Now if we look at the gray curve in Fig. 4.16, we see that, after trimming, the critical exponent has become universal, $t = 1.9 \pm 0.6$. It is also interesting to notice that the change in critical exponent t also induces a change of the critical concentration. The diminution of t leads to an increase of x_c, as is observed from our Monte Carlo results for the TP model in the continuum, that will be presented in the next chapter and shown in figure 5.17. For the 400 nm series, the exponent changes from $t = 2.5 \pm 0.2$ to $t = 1.7 \pm 0.13$. In this case the diminution is still present though the change is less significant. These results shed a new light on high-voltage trimming and support the explanations given above. High-voltage trimming changes $h(g)$, cutting off its tail for small g values, driving the DC critical exponent t towards its universal value t_0. The fact that t diminishes explains the divergence of the change of conductivity and piezoresistivity as the percolation threshold is approached. To further verify this fact it would be interesting to perform such a study on a series of samples having a universal behaviour. In that case t should remain constant and no divergence of the relative change of conductivity should be observed.

4.6 Conclusion

In this chapter we have addressed the problem of DC transport properties in a tunnelling-percolation model of segregated (or cellular) systems. Using a fully microscopical description, the exact distribution functions of inter-particle distances and tunnel conductivities for N hard conducting spheres of diameter σ_1 randomly placed in a bond of length σ_2 was obtained. An explicit formula of the bond conductivity distribution function $h_{\sigma_2}(g)$ was also obtained for small g values. It was shown that $\lim_{\sigma_2/\sigma_1 \to \infty} h_{\sigma_2}(g)$ has a power-law divergence at $g = 0$ driving the network towards a non-universal regime of transport criticality, while for σ_2/σ_1 finite $h_{\sigma_2}(g)$ has an upper bound which prevents the onset of non-universality at $p = p_c$ [60].

A closer look at the distribution function $h_{\sigma_2}(g)$ of the channel conductances g shows that it has a non-monotonic behaviour characterized by a strong peak at some low $g = g_m$ value. This feature results in a macroscopic conductance G that does not follow a simple power law, but rather displays a p-dependent transport exponent $t^*(p)$. It was shown, within the EMA, that $t^*(p)$ was higher than the universal t_0 and approaches the universal limit only very close to the percolation threshold p_c, so that an apparent non-universal transport exponent is extracted when fitting the system's conductivity to a simple power-law.

Numerical Monte Carlo calculations showed that for finite σ_2/σ_1 the system displays an apparent non-universality in a quite broad region close to the percolation threshold. This finding implies that the non-universality

observed in composites which are well described by a finite σ_2/σ_1 tunnelling-percolation model is probably due to a sampling of conductivities far away from the true critical region. We have however argued that, depending on the physical parameters, such a critical region may be so narrowed that in practice it may be experimentally inaccessible. In this scenario, the phenomenology is basically indistinguishable from that of a truly non-universal system.

This result is also important because it shows that a truly diverging $h(g)$ is not needed to explain the experimentally observed non-universal t values. Indeed, apparent non-universality might be observed in two- or three-dimensional tunnelling percolation models, without invoking a one-dimensional particle distribution. A similar situation has been recently described in Ref. [36] for the case of the three-dimensional homogeneous distribution of conducting spherical particles, which displays indeed a microscopic conductance behaviour qualitatively similar to the one presented in Fig. 4.5. This issue will be addressed in the following chapter of this thesis, while dealing with tunnelling-percolation in continuum systems (off-lattice).

Finally, we noted that the study of the p-dependent transport exponent $t^*(p)$ was very inefficient to characterize the crossover from non-universal to universal behaviour and to experimentally verify the existence of apparent non-universality, as it requires the measurement of the conductance G at many concentrations very close to the percolation threshold, which is experimentally very difficult. We therefore proposed the study of the piezoresistivity Γ as an efficient tool to study this crossover. Indeed, we have shown that Γ displayed two very different behaviours when t is p-dependent and when not. In the first case, Γ has a logarithmic divergence, and in the second, when $t^*(p)$ reaches its asymptotic value t_0, Γ has a constant value Γ_0.

We have also carried out Monte Carlo simulations of the piezoresistivity of our TP model, which allowed us to show that, although the conductivity could be fitted by a simple power law with a non-universal exponent, the piezoresistivity clearly allowed to observe the crossover between the apparent non-universal and the universal regime. We interpreted those observations as due to the fact that Γ is much more sensitive to the tunnelling-percolation features than the values of G [71]. We therefore conclude that, at least in principle, this result could be used in tunnelling-percolation materials to experimentally investigate the origin of their non-universal exponents, by measuring Γ as a function of $p - p_c$ or G.

Finally we concluded this chapter by interpreting the high-voltage trimming results of section 3.4 in the light of the tunnelling-percolation model. We show that a simple explanation of voltage trimming can be given in terms of changes in the distribution function $h(g)$ of the local conductances. This explanation is sufficient to explain our experimental results and is further supported by our experimental observation that the transport exponent t is driven towards universality by high-voltage trimming.

Chapter 5

Electrical conduction in continuum tunnelling-percolation systems

In this chapter, we study the tunnelling-percolation mechanism of conduction in disordered conductor-insulator composites, for a realistic continuum model, where conducting and impenetrable spherical particles are dispersed in a three-dimensional continuum insulating material. Conduction between particles occurs via tunnelling processes and a maximum tunnelling distance d is introduced. We determine the percolation critical concentration for several values of d. By so doing, we relax the restrictions applied in the previous studies of the problem, i.e. the considerations of the underlying lattice and the contribution of only the nearest neighbours. The tunnelling percolation transport is then analysed by studying the conductance of the composite at and near the percolation threshold, using a decimation procedure and a conjugate gradient algorithm. We show that at the critical concentration, and independently of the tunnelling parameters, the critical transport exponent t reduces to the universal value $t_0 \simeq 2$, while moving away from the percolation threshold, the conductance exponent becomes larger than t_0, acquiring a strong concentration dependence [72]. We interpret this feature as arising from the peculiar form of the distribution function for the local tunnelling conductances. Consequently, apparent non-universality of transport appears when the conductance of the composite is fitted by forcing the exponent to be independent of the concentration. This leads us to believe that our tunnelling-percolation theory is sufficient to explain the non-universal transport exponents observed in real disordered conductor-insulator compounds.

Before presenting our results, I briefly summarize an EMA calculation of

the transport properties in three-dimensional tunnelling-percolation systems, presented in a paper by C. Grimaldi and I. Balberg [36].

5.1 Effective medium approximation of 3D tunnelling-percolation transport

As we have seen in the preceding chapter, in section 4.1, the nearest neighbour distribution function $P(r)$ has to decrease slower than the inter-particle conductivity with the distance r, in order to obtain a diverging $h(g)$ leading to non-universality. We have seen that in a random distribution of spherical particles, one-dimensionality is essential in this respect. But as pointed out in the conclusion of chapter 4, a diverging $h(g)$ is not necessary to obtain apparent non-universality, sufficient to explain the observed experimental non-universal transport exponents. It is therefore interesting to check whether apparent non-universality is also obtained in TP models with realistic matter distributions, with $P(r)$ decreasing faster than the tunnelling conductivity. To this end we consider an effective medium approximation of electrical transport in a three-dimensional tunnelling percolation system. We use the effective medium theory, for lattice bond percolation, but using a realistic distribution function $P(r)$ for a homogenous dispersion of spheres in the continuum. To this end, let us consider a bond percolation model of a cubic lattice . The corresponding EMA equation is (see equation 4.34 or Refs. [12, 19]):

$$2G\int_0^1 dg\frac{h(g)}{g+2G}=\frac{p-p_c}{p}, \tag{5.1}$$

where $p_c = 1/3$ is the EMA bond percolation threshold. Following Ref. [36], we assume that $h(g)$ is given by tunnelling processes between nearest-neighbour particles, so that $h(g)$ is given by

$$h(g)=\int_0^\infty dr\,P(r)\delta\Big(g-g(r)\Big) \tag{5.2}$$

and Eq. (5.1) reduces to

$$2G\int_0^\infty dr\frac{P(r)}{g(r)+2G}=\frac{p-p_c}{p}, \tag{5.3}$$

where $g(r)$ is the tunnelling conductance given in Eq. (5.24) and $P(r)$ is the distribution function of the distance r between two nearest-neighbours. The authors of reference [36] studied this model, using

$$P(y) = \frac{24x(\gamma_1 y^2 + \gamma_2 y + \gamma_3)}{\sigma_1} \exp\left[-8x\gamma_1(y^3-1) - 12x\gamma_2(y^2-1) - 24x\gamma_3(y-1)\right]\Theta(y-1), \quad (5.4)$$

with $y = r/\sigma_1$ for the nearest-neighbour inter-particle distance [28]. The authors solved equation 5.3 numerically and obtained a transport behaviour very similar to our results on lattice percolation, presented in chapter 4. The local transport exponent they obtained, $t^*(p)$, as defined in equation 4.36, is shown in figure 5.1 for different values of the control parameter α (for a definition of α refer to equation 5.34) and for point-particles in the left panel ($\sigma_1 = 0$) and hard core particles in panel (b) ($\sigma_1 > 0$). It is clear from that figure that apparent non-universality is also obtained in that framework, with $t^*(p) > \bar{t}_0 = 1$, not too close to p_c and for large enough values of α, and with $t^*(p)$ reaching asymptotically $\bar{t}_0$ only very close to p_c. Again in this situation, a mean value $\bar{t}^* > t_0$ of $t^*(p)$ would be obtained if fitting the conductance of the system with a simple power law, for a limited number of p values, leading to apparent non-universality.

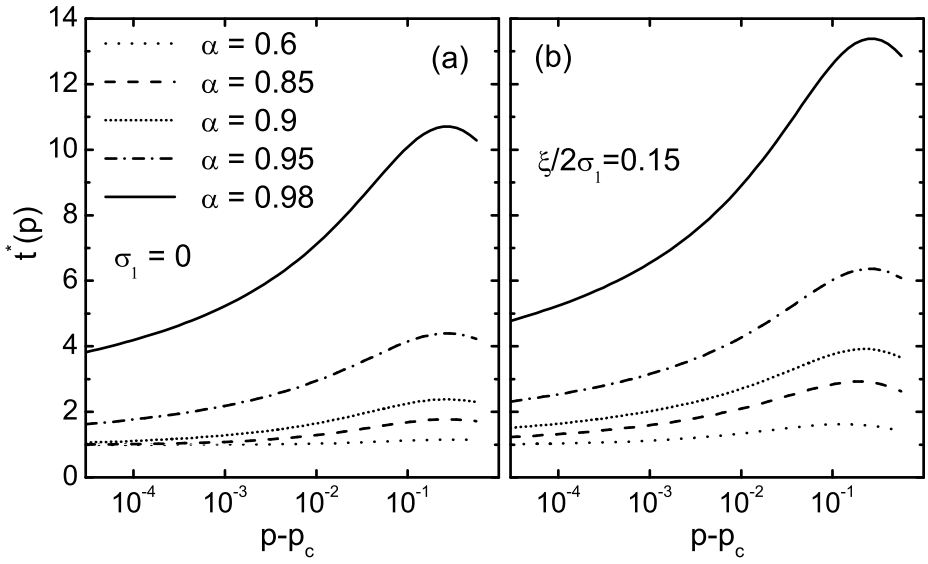

Figure 5.1: The local transport exponent $t^*(p)$, defined in equation 4.36 and derived from the calculated EMA conductance G as a function of $p - p_c$. The different cases refer to different values of the parameter $\alpha = 1 - \xi/2(a - \sigma_1)$. Results in the left panel are for point-particles ($\sigma_1 = 0$) and in the right one for spheres with diameter $\sigma_1 > 0$. This figure is taken from reference [36]

5.1.1 Effective Medium approximation for the conductance

We will now further develop this effective medium theory to obtain an analytical expression for the conductivity G of the system and for the p-dependent transport exponent. For simplicity, we consider the limiting case of point-like particles ($\sigma_1 = 0$), for which $P(r)$ is given by the Hertz distribution:

$$P(r) = \frac{3r^2}{a^3} \exp\left(-\frac{r^3}{a^3}\right), \tag{5.5}$$

where a is the mean nearest-neighbour distance. We rewrite Eq. (5.3), using Eq. (5.5) and introducing an upper cut-off d in the bounds of integration. This bound is introduced in view to better fit the continuum model we will introduce in the following section. Basically, d sets a limit to the tunnelling range, beyond which two neighbouring particles are considered electrically disconnected. By introducing the dimensionless variable $z = r/a$, we obtain:

$$\int_0^{d/a} dz \, \frac{2G\, 3z^2 e^{-z^3}}{e^{-2az/\xi} + 2G} = \frac{p - p_c}{p}. \tag{5.6}$$

We will now develop solely the left hand term of equation (5.6). Introducing $W(z) = 2G/\left[2G + \exp(-2az/\xi)\right]$ and integrating by parts, we obtain

$$\frac{2G}{1+2G} - \frac{2G\, e^{-(d/a)^3}}{e^{-2d/\xi} + 2G} + \int_0^{d/a} dz \, W'(z) e^{-z^3}. \tag{5.7}$$

We can rewrite W as

$$W(z) = \frac{1}{e^{-\frac{2a}{\xi}(z-z^*)} + 1} \quad \text{with} \quad z^* = \frac{\xi}{2a} \ln\left(\frac{1}{2G}\right) \tag{5.8}$$

So that

$$W'(z) = \frac{2a}{\xi} \frac{e^{-\frac{2a}{\xi}(z-z^*)}}{\left[e^{-\frac{2a}{\xi}(z-z^*)} + 1\right]^2} \tag{5.9}$$

is strongly peaked at $z = z^*$ for small ξ/a. In particular, for $\xi/a \to 0$, we have $\lim_{\xi\to 0} W(z) = \Theta(z - z^*)$, where Θ is the Heaviside step function, so that

$$\lim_{\xi\to 0} W'(z) = \delta(z - z^*). \tag{5.10}$$

For small ξ/a values, two cases have to be considered: z^* inside the interval of integration, meaning $z^* < d/a$, or z^* outside the interval of integration ($z^* > d/a$). We start with this second case, when $z > d/a$ or equivalently

$2G < \exp(-2d/\xi)$, corresponding to the situation close to the percolation threshold. As $2G < \exp(-2d/\xi) \ll 1$ equation 5.7 becomes

$$2G - 2Ge^{2d/\xi-(d/a)^3} + 2G\int_0^{d/a} dz\,\frac{2a}{\xi}e^{2az/\xi-z^3}. \tag{5.11}$$

As ξ is small, the exponential term in the integral is growing with increasing z and is dominated by $z = d/a$. We therefore develop the argument of the exponential around $z = d/a$ and equation 5.11 reads

$$2G - 2Ge^{2d/\xi-(d/a)^3} + 2G\frac{2a}{\xi}\int_0^{d/a} dz\,e^{2d/\xi-(d/a)^3+[2a/\xi-3(d/a)^2](z-d/a)} \tag{5.12}$$

$$= 2G - 2Ge^{2d/\xi-(d/a)^3} + 2G\frac{e^{2d/\xi-(d/a)^3}}{1-3(d/a)^2\xi/2a}\left[1-e^{3(d/a)^3-d/\xi}\right]. \tag{5.13}$$

We now eliminate the unimportant second term in the square brackets and develop the fraction at first order of ξ, giving

$$2G + 6G\left(\frac{d}{a}\right)^2\frac{\xi}{2a}e^{2d/\xi-(d/a)^3} \simeq 6G\left(\frac{d}{a}\right)^2\frac{\xi}{2a}e^{2d/\xi} \tag{5.14}$$

Reintroducing the left-hand term of equation 5.6 we finally obtain for G:

$$G = \frac{1}{6}\left(\frac{a}{d}\right)^2\frac{2a}{\xi}e^{-2d/\xi}\left(\frac{p-p_c}{p}\right), \tag{5.15}$$

corresponding to $G \approx (p - p_c)$, *i.e.*, the conductance is universal with EMA exponent $\bar{t}_0 = 1$, as long as we are "close enough" to p_c. How close to p_c we have to be in order to observe universality depends on the parameters of the model, notably ξ, through the condition $2G < \exp(-2d/\xi)$.

Let us now look at the second case, for $z^* < d/a$, or equivalently for $2G > \exp(-2d/\xi)$. In that case, and for small ξ, we can evaluate the integral of equation 5.7 by using Eq. (5.10), obtaining

$$\frac{p-p_c}{p} = \frac{2G}{1+2G} - \frac{2G\,e^{-(d/a)^3}}{e^{-2d/\xi}+2G} + e^{-\left[\frac{\xi}{2a}\ln\left(\frac{1}{2G}\right)\right]^3}. \tag{5.16}$$

Now as $G \ll 1$ and $2G > \exp(-2d/\xi)$ this expression can be simplified into

$$\begin{aligned}\frac{p-p_c}{p} &= 2G - e^{-(d/a)^3} + e^{-(\xi/2a\ln(1/2G))^3} \\ &\simeq \exp\left\{-\left[\frac{\xi}{2a}\ln\left(\frac{1}{2G}\right)\right]^3\right\},\end{aligned} \tag{5.17}$$

so that the resulting conductance is given by

$$G \approx \exp\left[-\frac{2a}{\xi}\left(\ln\frac{p}{p-p_c}\right)^{1/3}\right] = \left(\frac{p-p_c}{p}\right)^{\frac{2a}{\xi}\left(\ln\frac{p}{p-p_c}\right)^{-2/3}}, \quad (5.18)$$

where in the second equality we have made explicit that in this regime the conductance is governed by a p-dependent exponent. From the above results we obtain that the conductance reduces to the universal EMA power-law $G \approx (p-p_c)$ only if $p-p_c$ is so small that $G \ll \exp(-2d/\xi)$. Conversely, when $G \gtrsim \exp(-2d/\xi)$, the conductance takes a more complicated form with a p-dependent transport exponent. In the whole $p-p_c$ region, the solution to Eq. (5.6) may be expressed conveniently as a conductance of the form

$$G \approx \left(\frac{p-p_c}{p}\right)^{t(p)}, \quad (5.19)$$

with p-dependent exponent

$$t(p) = t_0 + \frac{2a}{\xi}\left(\ln\frac{p}{p-p_c}\right)^{-2/3}, \quad (5.20)$$

which contains the limiting behaviours discussed above (Eqs. (5.15) and (5.18)).

5.1.2 Test of the analytical solution

The validity of Eqs. (5.19) and (5.20) can be tested using the results of Ref. [36] presented in section 5.1. We use the results of the panel (a) of figure 5.1, as it is for dot particles, which is the case treated here. This figure shows $t^*(p)$ obtained from $t^*(p) = d\ln(G)/d\ln(p-p_c)$ as a function of $p-p_c$. We have to be careful here because we have indeed that

$$t^*(p) = \frac{d\ln(G)}{d\ln(p-p_c)} = t(p)\frac{p_c}{p} + \frac{dt(p)}{dp}(p-p_c)\ln\left(\frac{p-p_c}{p}\right) \neq t(p). \quad (5.21)$$

Therefore in figure 5.2 we compare $t^*(p) \equiv d\ln(G)/d\ln(p-p_c)$ obtained from equations 5.19 and 5.20,

$$t^*(p) = \frac{d\ln(G)}{d\ln(p-p_c)} = \frac{p_c}{p}\left[t_0 + \frac{1}{3}\frac{1}{1-\alpha}\ln\left(\frac{p}{p-p_c}\right)^{-2/3}\right] \quad (5.22)$$

with the results for $t^*(p)$ of Ref. [36]. In panel (a) of this figure, equation 5.22 is shown, whereas in panel (b), it is this same equation, but in the limit of

small ξ/a, namely without the term t_0. We see a good overall agreement of our analytical result with the numerical solution of equation 5.3, as the two limiting bounds are well reproduced. Indeed in panel (b) of this figure we see that the solution obtained for $2G > \exp(-2d/\xi)$ is in very good accord with the results shown for larger α, whereas in panel (a) with see that the other bound $t(p) = t_0$ holds for smaller values of α, as expected. We can also note that the simple Ansatz made in equation 5.20 to combine the two solutions leads to an overestimation of $t(p)$ for the larger values of α and p close to p_c. Nevertheless, this Ansatz is sufficient and convenient to describe the general situation encountered in this system and holds well in the limiting cases.

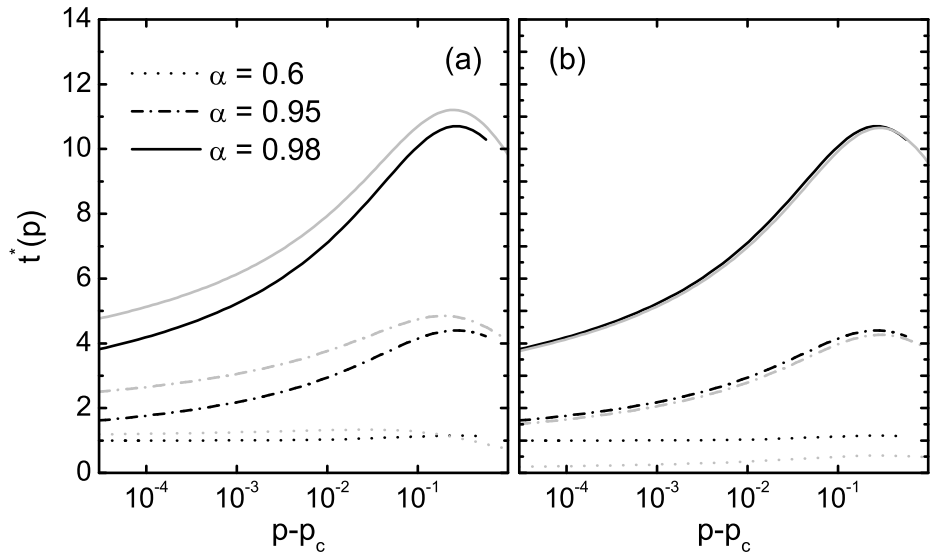

Figure 5.2: Comparison of the analytical result 5.22 with the numerical solution of equation 5.3 taken from Ref. [36]. Three cases for different values of the control parameter α are shown. In the left panel we show the analytical result obtained for $t^*(p)$ as given in equation 5.20, whereas in panel (b) we use the result obtained for small ξ/a values. The black curves are the numerical results and the grey ones the analytical solution.

An extension of the EMA analysis presented above is briefly described in appendix A for the case of impenetrable particles with a hard-core diameter $\sigma_1 \neq 0$. The interesting feature is that both results show that the ratio of the distance between particle surfaces, $a - \sigma_1$, to the tunnelling decay length ξ is the basic parameter that governs the non-universal behaviour, as is the case in one-dimensional systems, but in three dimensions this dependence is weakened, reaching universality, as the percolation threshold is approached.

The result obtained in equations 5.19 and 5.20 can also be tested directly for the conductivity G. A good way to rewrite this result is as follows:

$$\ln\left(\frac{p}{p-p_c}\right)^{-2/3} = \frac{\xi}{2a}\left[\frac{\ln(G)}{\ln\left(\frac{p-p_c}{p}\right)} - t_0\right] = (1-\alpha)\left[t(p) - t_0\right] \tag{5.23}$$

So that if we plot the quantity $(\xi/2a)[t(p) - t_0]$ as a function of $(p - p_c)/p$, we should obtain a data collapse, meaning that all results, for different α, should approximately lie on the same master curve. This is shown in Fig. 5.3 where this quantity, obtained by solving Eq. (5.6) by numerical integration and iteration, is plotted as a function of $(p - p_c)/p$ for different values of $\alpha = 1 - \xi/2a$. In agreement with the above results, the curves are nearly independent of α and approximately follow $[\ln(p/(p - p_c)]^{-2/3}$ (solid black line) in the whole range of $(p - p_c)/p$, verifying therefore the validity of Eq. (5.20).

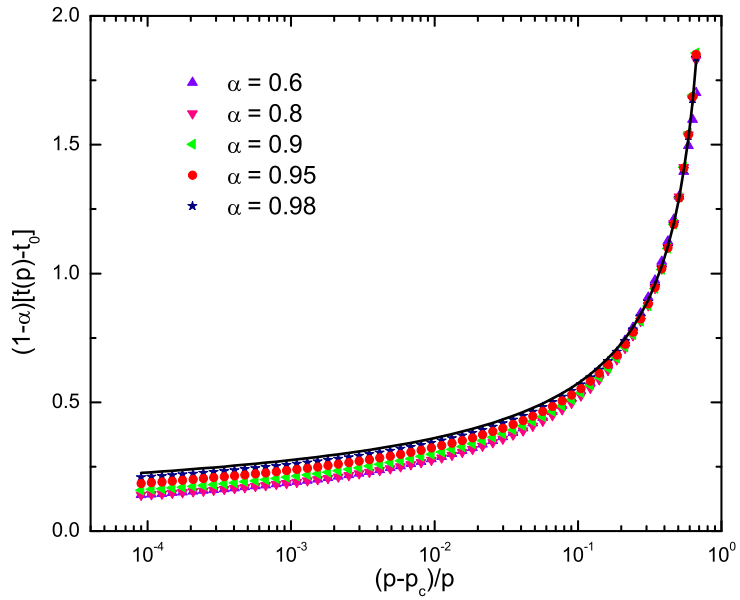

Figure 5.3: Concentration dependence of the local transport exponent of the EMA of the continuum TP model, as calculated from a numerical solution of Eq. (5.6) for different values of $\alpha = 1 - \xi/2/(a - \sigma_1)$ for point-like particles ($\sigma_1 = 0$). The solid line describes the $[\ln(p/(p - p_c))]^{-2/3}$ dependence.

It is worth to stress here that this result is of importance for the TP origin of non-universality. It shows indeed that the constraint on the one-dimensional distribution of the conducting particles can be released, without hindering the appearance of apparent non-universality. We should, nevertheless, keep in mind that this result is again a lattice result, though using

a nearest neighbour distance distribution function of a homogeneous dispersion of particles, and that it is treated only in the approximate framework of effective medium theory. In what follows we study a continuum tunnelling-percolation model, relaxing the lattice restriction of the above results.

5.2 Continuum tunnelling-percolation model

As stated above, all previous studies of the TP origin of non-universality were based on mappings of the continuum percolation on a regular lattice. Moreover, the model of the pioneering work [27] and the study on apparent non-universality in three-dimensional dispersions of spheres discussed above [36], consider the inter-particle distances to be distributed according to the nearest neighbour distance distribution function. It is clear that at least nearest and next-nearest neighbour tunnelling is needed to assure connectivity of the percolating cluster. In this chapter we relax these restrictions by considering an off-lattice model where the conducting (impenetrable) particles are given by equally sized spheres dispersed in an insulating continuum, and tunnelling between particles is allowed to extend also beyond the nearest-neighbour distances. By using exact numerical renormalization techniques and relaxation methods, we demonstrate that, right at the percolation threshold, the system is universal with the electrical transport exponent t_0, while away from x_c the conductance follows a power-law with an x-dependent exponent $t(x)$, leading therefore to the appearance of apparent non-universality in this continuum TP model [72]. Furthermore, we show that $t(x)$ depends on the tunnelling decay factor ξ and on the mean distance between nearest-neighbouring particles a, verifying therefore the effective medium results of Ref. [36] and the on-lattice calculations of the preceding chapter

5.2.1 The Model

Let us consider equal size conducting spheres of diameter σ_1 dispersed in a continuous three-dimensional insulating medium. Furthermore, let us assume that the spheres are impenetrable and that the conductance between two spheres whose centers are separated by r (with $r \geq \sigma_1$) is given by:

$$g(r) = g_0 \exp\left(-\frac{2(r-\sigma_1)}{\xi}\right) \tag{5.24}$$

where ξ is the characteristic tunnelling distance and g_0 a constant prefactor. In principle, Eq. (5.24) applies to all pairs of particles regardless of their relative distances. However, in practice, particles which are set apart by a distance much larger than $\xi/2$, can actually be considered as electrically disconnected. In order to deal with this situation, we introduce an upper

distance cutoff d beyond which the tunnelling conductance between two particles is set equal to zero. This cutoff has several physical justifications. For example, if the continuous medium has an intrinsic conductivity $\Sigma_2 \neq 0$, then all tunnelling processes with conductances smaller than the contribution of the matrix ($g(r) \lesssim \Sigma_2$) do not contribute (or contribute very little) to the macroscopic conductivity of the system. This defines a maximum tunnelling distance which can be estimated through

$$d \approx \frac{\xi}{2} \ln\left(\frac{g_0 d}{\Sigma_2 {\sigma_1}^2}\right), \tag{5.25}$$

where the term $d/{\sigma_1}^2$ comes from geometrical considerations (in fact we compare the tunnelling-conductance with the conductance of the cylindrical volume of matrix located in between the conducting particles). Of course, as $\Sigma_2/g_0 \to 0$, the maximum distance d cannot grow indefinitely, because when d is several times larger than the tunnelling decay factor ξ, any small perturbation in the potential of the continuous medium would cause the collapse of the wave function, so that two particles a distance $d \gg \xi$ apart are electrically disconnected.

Whatever is the origin of the cutoff distance d, its presence is an important physical parameter of the problem, which gives rise to a percolation behaviour of transport. Its introduction leads to the composite particle model shown in Fig. 5.4(a), where the black disk is the impenetrable metallic sphere, while the attached concentric shell has a thickness $d/2$. From the structural point of view, our model is a penetrable-concentric-shell model (known also as cherry-pit model or semi-permeable particles model). As shown in Fig. 5.4(b), the composite particles define a spatially correlated continuum percolation system, where two hard-core particles are considered linked, and the corresponding inter-particle conductance is given by Eq. (5.24), if and only if the separation between their closest surfaces is less than the cut-off distance d.

Due to the composite nature of the particle system, hard-core spheres of diameter σ_1 and semi-permeable spheres of diameter $\sigma_1 + d$, the definitions of the particle concentration and the percolation threshold depend on which aspect of the composite particles is relevant for the problem. For the electrical transport properties, it is of course the whole composite sphere which must be considered, since the electrical connectivity is governed by the overlap of the permeable shells of two or more composite particles. Hence, given N spheres in a volume V, for the determination of the conductor-insulator transition of the system, we shall use as a density variable the following dimensionless quantity:

$$\eta = \rho \frac{\pi}{6} (\sigma_1 + d)^3 \tag{5.26}$$

where $\rho = N/V$ is the number density. The corresponding critical concen-

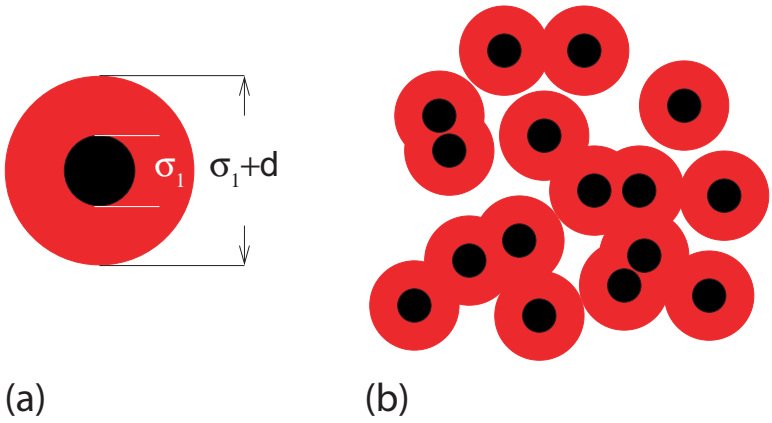

Figure 5.4: Two-dimensional representation of the composite-particle model used in the present chapter. (a): The filled circle denotes a conducting impenetrable sphere of diameter σ_1, while the concentric shell of thickness $d/2$ defines the upper cutoff for the conductance. (b) When several particles are arranged together, their microstructure is that of impenetrable spheres with penetrable shells. When the separation between the closest surfaces of two (black) spheres is larger than d, the inter-particle conductance is set equal to zero, otherwise it follows Eq. (5.24).

tration for the onset of electrical conduction, η_c, determines the conductor-insulator percolation threshold of the system. Instead, the volume concentration of hard-core particles $x = \rho\pi\sigma_1^3/6$ has the direct significance of volume percentage of the conducting phase dispersed in the whole conductor-insulator composite. The concentration x is related to Eq. (5.26) through the relation

$$x = \lambda^3 \eta \tag{5.27}$$

where

$$\lambda = \frac{\sigma_1}{\sigma_1 + d} \tag{5.28}$$

is the penetrability coefficient which has limiting value $\lambda = 0$ ($\lambda = 1$) for completely penetrable (impenetrable) spheres.

5.2.2 Percolation threshold

Since the electrical connectivity is established only if the overlaps of the particle shells span the entire sample, it is essential for the evaluation of the composite conductance to estimate the percolation threshold η_c and its dependence on the penetrable shell thickness (and hence on λ). Here, we obtain η_c as a function of λ by first computing the spanning probability, $\Pi(\eta)$ for finite systems with linear size L/σ_1, *i.e.*, the probability of having a percolating cluster which spans the system from one side to the opposite

one, and then by extrapolating the results to the $L/\sigma_1 \to \infty$ limit [73]. In practice, we consider a box with edges of length L where N spheres of diameter σ_1 are placed randomly but with no overlaps. A simple Metropolis algorithm is used to attain equilibrium [74, 75]. The use of the equilibrium state here, with no other interaction than the hard-core repulsion between the conducting spheres, implies that we neglect, in our model, the influence of any other interaction between the conducting spheres (such as electrostatic forces) and between the conducting spheres and the matrix. Such interactions would of course influence the morphology and the distribution of conducting spheres in the system. This can drastically change the percolation threshold of real composites, as was for example observed in Ref. [49], where electrostatic interactions spontaneously lead to a segregated structure in a carbon-black/polymer composite. This particular microstructure, which is one possible morphology induced by interactions between the matrix and the conducting particles, is studied in the next chapter of this work.

Let us turn back to our Monte Carlo simulation procedure. After the equilibrium state is reached, for a given value of d/σ_1 (hence of λ), we use a modified Hoshen-Kopelman algorithm to extract, if it exists, the percolating cluster for a given realization [76, 77]. Finally $\Pi(\eta)$ is obtained by recording the number of times that a percolating cluster appears for several realizations (for more details about the simulation procedures, refer to appendix B). In Fig. 5.5 we show the so-obtained spanning probability for $L/\sigma_1 = 15$, 20, 30, 50 and for $d/\sigma_1 = 1$ ($\lambda = 0.5$), calculated by imposing open boundary conditions. The calculations have been performed for number of particles N ranging from $N = 200$ (with $N_s = 2000$ realizations) up to $N = 10000$ ($N_s = 250$). According to the finite-size scaling method described for example in Ref. [73], the critical density $\eta_c(L)$, for finite L, can be extracted by imposing $\Pi(\eta_c(L)) = 1/2$. This can be evaluated by fitting the discrete data with some suitable function. Here we use [73]:

$$\Pi(\eta, L) = \frac{1}{2}\left(1 + \tanh\left[\frac{\eta - \eta_c(L)}{\Delta(L)}\right]\right) \tag{5.29}$$

where $\Delta(L)$ is the width of the percolation transition. Equation (5.29) is presented by the solid lines in Fig. 5.5, and the resulting best fitting values of $\eta_c(L)$ and $\Delta(L)$ are reported in Fig. 5.6. Using scaling arguments [4] (or see equation 2.11 in the state of the art of this thesis), it can be shown that the functions $\Delta(L)$ and $\eta_c(L)$ follow the scaling relations

$$\Delta(L) \propto L^{-1/\nu} \tag{5.30}$$

$$\eta_c(L) - \eta_c \propto L^{-1/\nu} \tag{5.31}$$

where ν is the correlation length exponent. Hence, the exponent ν can be extracted from Eq. (5.30) and used in Eq. (5.31) to evaluate the critical

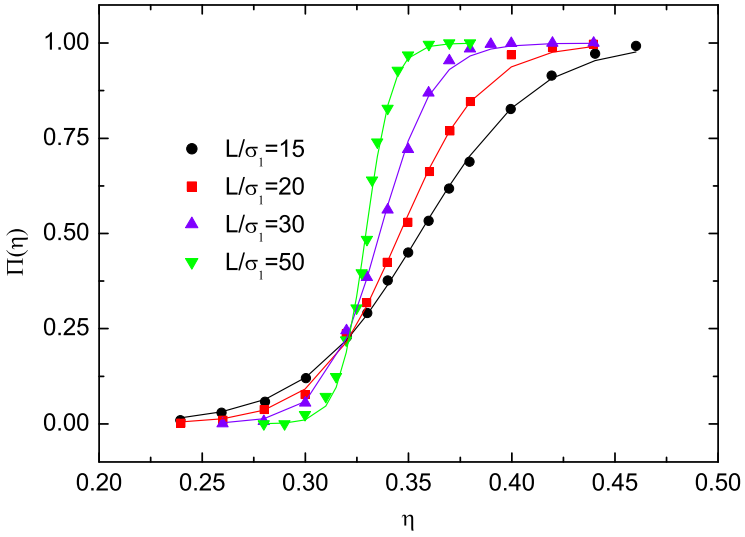

Figure 5.5: Spanning probability Π as a function of the density η for different system sizes L/σ_1 and for the penetrability coefficient value $\lambda = 1/2$. The solid lines are fits to Eq. (5.29).

density η_c for an infinite system. The results we obtained by this procedure are shown in Fig. 5.6 for $\lambda = 1/2$. From the relation 5.30 we have obtained (inset of Fig. 5.6) $\nu = 0.87 \pm 0.02$, which is in excellent agreement with other estimations yielding $\nu \simeq 0.88$, [73, 78] while from Eq. (5.31) we have deduced (main frame of Fig. 5.6) $\eta_c = 0.3203 \pm 0.0003$ by using the commonly admitted value for ν. By using Eq. (5.27) we also find the corresponding value in terms of the volume fraction of impenetrable spheres. This value, $x_c \approx 0.04$, is of course much lower than the geometrical percolation threshold for direct contact between hard-core spheres ($x_c \approx 0.64$ for random close packing [79]).

The behaviour of η_c for different values of the penetrability coefficient λ is plotted in Fig. 5.7 (crosses) together with the results of Ref. [78] (empty circles) and of Ref. [39]. For $\lambda = 0$ we obtain $\eta_c = 0.3423 \pm 0.0003$ which is in very good accord with the most accurate value to date ($\eta_c = 0.341889 \pm 0.000003$) reported in Ref. [80] (open square in Fig. 5.7). Such agreement holds true also for $\lambda > 0$, for which our results are perfectly compatible with the original work of Balberg and Binenbaum in 1987 [81], and with the more recent results of Lee and Yoon [78] and of Heyes [39].

Having established the behaviour of η_c as a function of the penetrability coefficient, let us now consider the problem of choosing some representative values of the cut-off parameter for the evaluation of the system conductance. From the results of Fig. 5.7, and by using Eq. (5.27), it is straightforward to

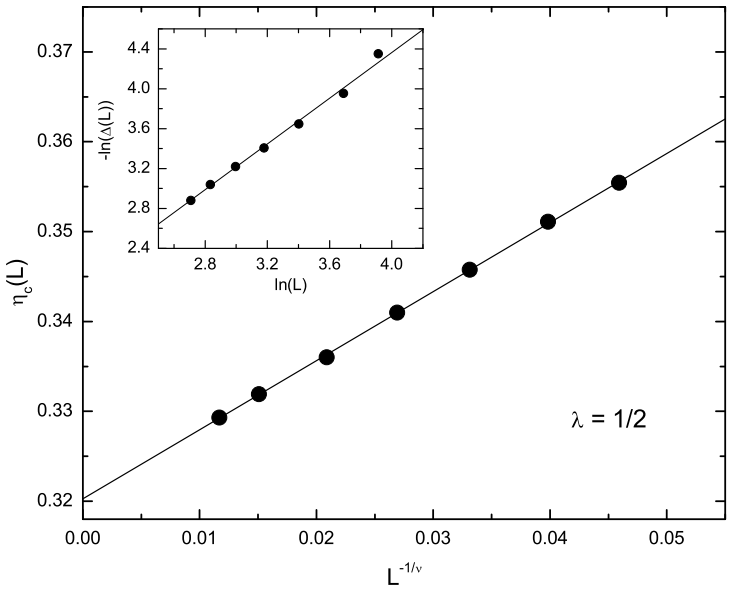

Figure 5.6: Evaluation of the critical density as a function of L/σ_1 for $\lambda = 1/2$. The solid line follows Eq. (5.31) and η_c is given by the intercept at $L^{-1/\nu} = 0$. The value of the correlation length exponent ν is extracted from Eq. (5.30) by fitting the data of $\Delta(L)$ as derived from Fig. 5.5 and Eq. (5.29) (inset).

obtain the critical concentration x_c of the conducting particles as a function of the cut-off parameter d/σ_1. This dependence is shown in Fig. 5.8(a), from which one infers that the electrical connectivity of the system is established for concentration values that are rapidly decreasing as d/σ_1 increases. Hence, for an efficient numerical evaluation of the system conductance, it is certainly preferable to consider large enough values of d/σ_1 so that not too many particles ought to be considered in the calculation of the conductance. Yet, large values of d/σ_1 may lead to important finite size effects and/or poor statistics. Hence, intermediate values of d/σ_1 should represent the best compromise. We have chosen then for our work the values of $d/\sigma_1 = 1$ and $d/\sigma_1 = 2$ which, according to Fig. 5.8(a), amount to describe a system with a relatively low critical particle concentration. Such values of the cut-off length, however, do not limit the validity of the subsequent calculations, since the ratio between the cut-off length d and the typical inter-particle separation, $(a_c - \sigma_1)$, where a_c is the mean nearest-neighbour particle distance at percolation, changes little with d/σ_1. This is demonstrated in Fig. 5.8(b), where the plotted $d/(a_c - \sigma_1)$ values have been obtained from the data of Fig. 5.8(a) and by using $a_c = \int dr\, r P(x_c, r)$, where $P(x_c, r)$ is the distribution function for the distance between two neighbouring impenetrable spheres at concentration x_c as given in Ref. [28]. From the results in the figure, it is seen that

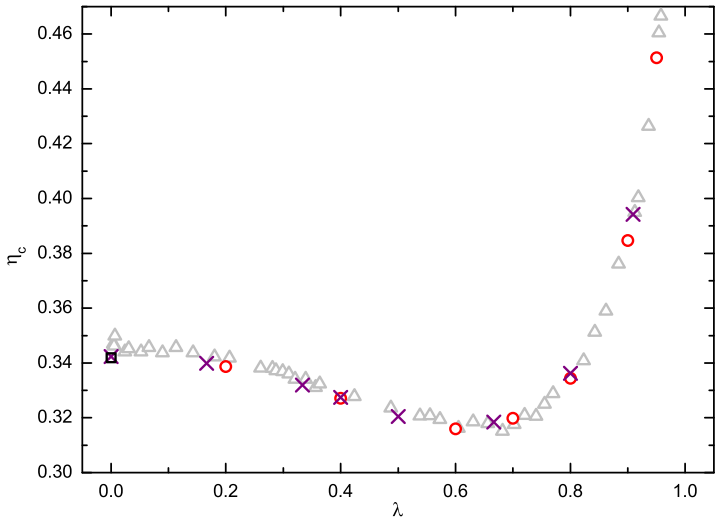

Figure 5.7: The percolation critical density η_c as a function of the penetrability coefficient λ. Crosses: our results. Circles: results from Ref. [78]. Triangles: results from Ref. [39]. Open square: (at $\lambda = 0$) from Ref. [80].

$d/(a_c - \sigma_1)$ is comprised between 1.7 and 2.1 for a two-orders of magnitude change of d/σ_1. In the limit of point-like particles ($d/\sigma_1 = \infty$) it is found that $d/a_c = 2\eta_c^{1/3}/\Gamma(4/3)$ [28], where Γ is the Gamma function, so that for $\eta_c \approx 0.342$ one finds $d/a_c \approx 1.6$. The weak dependence of $d/(a_c - \sigma_1)$ on the cut-off length points out therefore that the above values of d/σ_1, that we have chosen for the conductance simulations, below, not only have a computational convenience, but are actually representative of quite a general situation.

We can also note here the difference of behaviour between x_c and η_c. Indeed x_c monotonically decreases when d/σ_1 is increased. This is of course due to the fact that the hard-core volume of the composite particles compared to its total volume participating to the connectivity decreases with increasing d/σ_1, so that x_c tends to zero as σ_1/d vanishes. On the other hand η_c has a non monotonic behaviour. As λ increases (decreasing d/σ_1), η_c first diminishes, as the hard-cores diminish the mean overlap between the conducting particles, and then starts increasing for higher values of λ, because the penetrable shell becomes so thin that the conducting particles have to be almost in contact in order to obtain connectivity. Finally for $\lambda = 1$ close packing is needed for the conducting phase to percolate through the system ($x_c \simeq 0.64$).

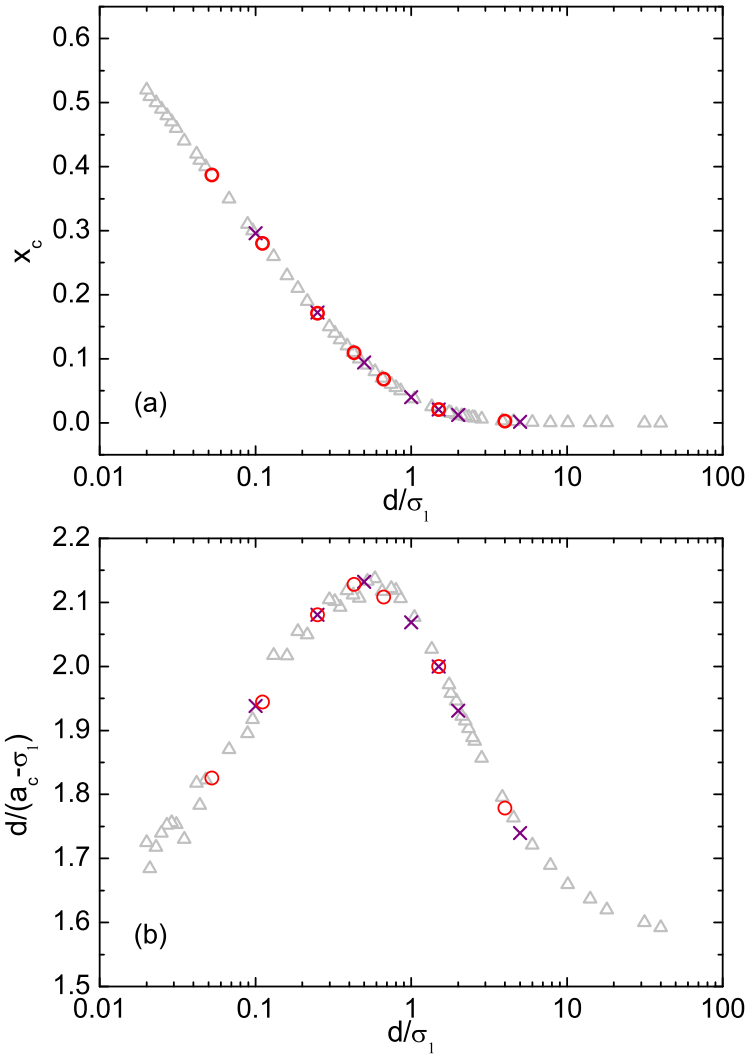

Figure 5.8: (a): The percolation critical concentration x_c as a function of the cut-off length d/σ_1. (b): The corresponding values of $d/(a_c - \sigma_1)$, where $a_c - \sigma_1$ is the mean distance between the closest surfaces of two nearest neighbour conducting spheres. Crosses: our results. Circles: results from Ref. [78]. Triangles: results from Ref. [39].

5.2.3 Transport exponent from finite-size scaling

We are now in the position to evaluate the behaviour of the conductivity at the percolation threshold η_c and the value that the transport exponent t acquires at η_c. To this end we have used, as outlined below, a finite scaling analysis of systems of linear size L. In general, the conductivity Σ is a

function which depends on both the concentration η and the size L. For η sufficiently close to the percolation threshold $\eta_c(L)$ for a finite system of size L one expects, in view of the above:

$$\Sigma(\eta, L) = \Sigma_0(L)\big[\eta - \eta_c(L)\big]^t \tag{5.32}$$

where $\Sigma_0(L)$ is a size-dependent pre-factor. By setting $\eta = \eta_c$, where η_c is the percolation threshold for $L \to \infty$, and by using Eq. (5.31) and Eq. (5.32) one sees that the main dependence of $\Sigma(\eta_c, L)$ upon L is of the form $L^{-t/\nu}$, so that the transport exponent t (as the exponents of other properties, see Ref. [4] or equation 2.11 in chapter 1), can be extracted from the linear dependence of $\ln[\Sigma(\eta_c, L)]$ on $\ln(L)$. However, rather generally, fluctuations at finite L may result to be important and, furthermore, the pre-factor $\Sigma_0(L)$ provides some, although weaker, dependence on L. These finite-size contributions can be taken into account by considering the following, more general, scaling relation

$$\Sigma(\eta_c, L) = \beta_1 L^{-t/\nu}(1 + \beta_2 L^{-\omega}) \tag{5.33}$$

where the quantity within brackets is an Ansatz aimed to capture the main L dependence of the finite-size corrections. The evaluation of t goes then as follows. The conductivity at η_c is calculated for several values of L, and the resulting values of $\Sigma(\eta_c, L)$ are fitted by varying t/ν and the parameters β_1, β_2, and ω of Eq. (5.33). Since ν is known, the best fit provides then the resulting value for t.

In our work we have extracted the conductivity of a system of size L, by isolating first the percolating cluster as described in the previous section. Then we implemented a numerical decimation procedure which replaces, by applying iterative exact transformations, the initial set of conductances (belonging to the percolating cluster) by a single conductance [82, 83]. Since the iterative transformation is exact, the final single conductance value coincides with $\Sigma(\eta_c, L)$. The transformation simply proceeds by successively eliminating each node in the cluster and replacing the adjacent conductances by following Kirchoff's laws. More details for the numerical simulation procedures can be found in appendix B.

A collection of t/ν exponents obtained for different σ_1/ξ values is plotted in Fig. 5.9 for $d/\sigma_1 = 1$ (full circles) and $d/\sigma_1 = 2$ (open squares). Within the error bars, determined from the statistics and the error fits to Eq. (5.33), the calculated t/ν exponents for $d/\sigma_1 = 1$ practically coincides with the universal value $t_0/\nu \simeq 2.0/0.88 \simeq 2.27$ (horizontal dashed line) independently of the tunnelling factor value. For $d/\sigma_1 = 2$ the mean value of t/ν lies slightly above 2.27 for σ_1/ξ larger than about 6, but universality is still confirmed within the error bars in the whole range of σ_1/ξ. The results reported in Fig. 5.9 confirm therefore our previous suggestion (Ref. [36]) that, at the percolation threshold η_c of the composite system, the transport exponent is

universal, independently of the tunnelling characteristic distance and of the value of the cut-off parameter d.

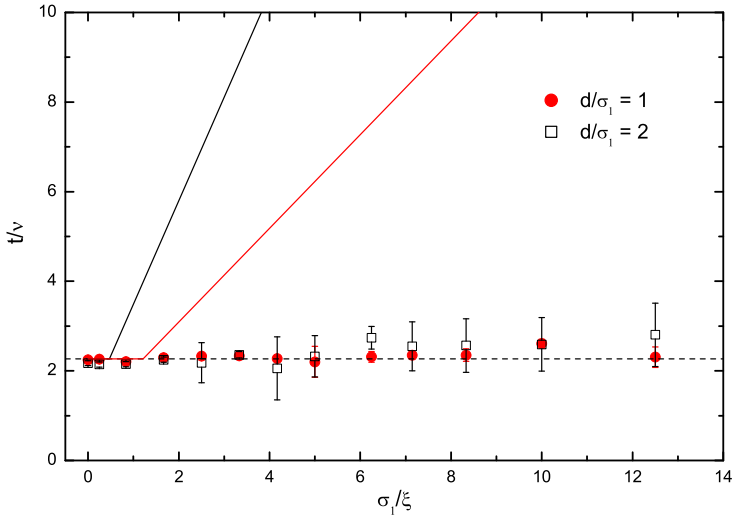

Figure 5.9: The calculated values of the DC transport exponent from fits to Eq. (5.33) for different values of the tunnelling decay factor ξ and for $d/\sigma_1 = 1$ (filled circles) and $d/\sigma_1 = 2$ (open squares) and the corresponding error bars as obtained from the fits. The horizontal dashed line is the universal value $t/\nu = 2.27$, while the solid lines refer to the corresponding Kogut-Straley exponent of Eq. (4.48) with α given by Eq. (5.34).

The significance of this result with respect to the classical tunnelling-percolation (one dimensional-like [27]) theory of non-universality is best appreciated by looking at the corresponding values of the Kogut-Straley exponent which, by taking into account the fact that the particles are impenetrable, reduces to

$$\alpha = 1 - \frac{\xi/2}{a - \sigma_1}. \tag{5.34}$$

α is the control parameter in the classical tunnelling-percolation model. Therefore, comparing the transport exponents we obtain in our model with the ones obtained in the classical TP model for the same values of α, allows to asses how this more realistic model behaves for the same model parameters. For $d/\sigma_1 = 1$ the percolation threshold value used in Fig. 5.9 is $\eta_c \approx 0.32$, which corresponds to a hard-core sphere density of $x_c \approx 0.04$. The corresponding value of the mean nearest neighbour distance a can be obtained either from Fig. 5.8 or, more transparently, by identifying a with the radius of a sphere containing, on average, only one particle at its center [27, 36]. Since for $x \approx 0.04$ the system is well within the low concentration regime,

a simple estimate of a is obtained by assuming that the particles are implanted randomly with a concentration ρ, so that a can be extracted from $(4\pi/3)\rho a^3 = 1$, leading to $a/\sigma_1 \simeq (1/x)^{1/3}/2 \approx 1.46$. By using Eq. (5.34), the resulting Kogut-Straley exponent reduces therefore to $\alpha \simeq 1 - 1.087\xi/\sigma_1$ which, according to Eq. (4.48), would predict non-universality as soon as $\sigma_1/\xi > 1.217$. The resulting σ_1/ξ dependence of t/ν as obtained by using Eq. (4.48) is plotted in Fig. 5.9 by the solid black curve. According to the original tunnelling-percolation theory, therefore, t/ν would exceed 10 already at $\sigma_2/\xi \simeq 8.6$, while our continuum model gives $t/\nu \simeq 2.27$ for even larger values of σ_1/ξ. By repeating the same analysis for $d/\sigma_1 = 2$ (for which $\eta_c \simeq 0.332$ and $x_c \simeq 0.012$) one would expect non-universality for $\sigma_1/\xi > 0.473$, with an even steeper enhancement of t/ν (grey curve in Fig. 5.9) compared to the $d/\sigma_1 = 1$ case.

5.2.4 Transport exponent from the concentration dependence

The universality of the transport exponent for the tunnelling-percolation continuum model, established in the previous section, poses the problem of how to account for the observed non-universality in real systems within the same theoretical framework. Experimentally, deviations of the transport exponent t from the universal value t_0, when observed, are obtained by measuring the conductivity as a function of the (estimated) distance from the percolation threshold. To examine whether our model also displays similar features, we have calculated the conductivity Σ as a function of the concentration x of the conducting particles. For values of x in the vicinity of x_c we have used the same numerical decimation algorithm that was described in the previous section, while for larger values of x we have implemented a preconditioned conjugate gradient algorithm [62,84], which provides a faster computational technique when x is far above x_c. We have in fact used a combination of those two algorithms, as explained in more details in appendix B. The results are plotted in Fig. 5.10(a) for $d/\sigma_1 = 1$ and in Fig. 5.10(b) for $d/\sigma_1 = 2$. To mitigate the effects of the finite size ($L/\sigma_1 = 40$ in this case) in Fig. 5.10 we have plotted the quantity $\tilde{\Sigma}(x) = \big[\Sigma(x) - \Sigma(x_c)\big]/\Sigma(x_c)$, where $\Sigma(x_c)$ is the conductivity at the critical concentration x_c for $L/\sigma_1 = \infty$. Note in particular that this normalization is unimportant for $\tilde{\Sigma}(x) \gtrsim 10$ and that it was introduced to emphasize the similarity of behaviour for all curves close to the percolation threshold x_c. As it is apparent from the figure, independently of σ_1/ξ and of the cut-off parameter, all the calculated conductivitys follow the same power-law behaviour as $x - x_c \to 0$, not deviating much from $(x - x_c)^2$ (solid line). We have therefore re-obtained the result of the previous section: transport is universal at, or very close to x_c, the percolation threshold. However, away from x_c, the results of Fig. 5.10 clearly indicate also

that different behaviours arise depending on the value of σ_1/ξ. Indeed for $\sigma_1/\xi = 0$ (solid circles) the conductivity matches approximately the $(x-x_c)^2$ behaviour in the whole concentration range. This is of course due to the fact that for $\sigma_1/\xi = 0$ the inter-particle conductance (equation 5.24) becomes a constant regardless of the tunnelling distance, giving rise to universal transport. On the contrary, for larger values of σ_1/ξ, Σ displays a steeper increase as one moves away from x_c and the deviation from the $(x - x_c)^2$ behaviour is stronger for larger σ_1/ξ values and for the $d/\sigma_1 = 2$ case compared to $d/\sigma_1 = 1$.

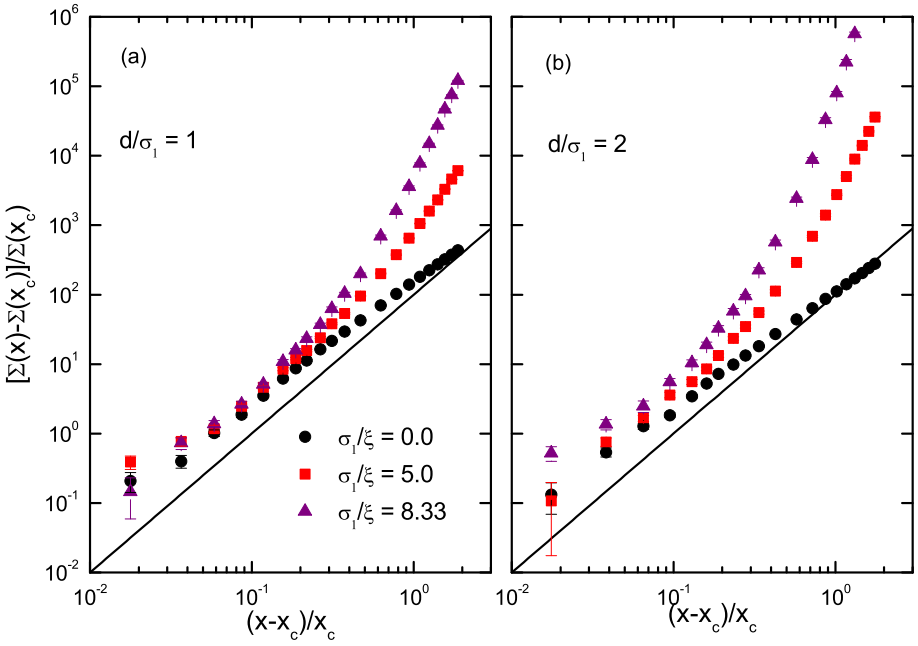

Figure 5.10: The calculated conductivity as a function of the proximity $(x-x_c)/x_c$ to the percolation threshold for different values of σ_1/ξ for $L/\sigma_1 = 40$. This is for $d/\sigma_1 = 1$ (a) and $d/\sigma_1 = 2$ (b). The solid lines represent the universal dependence $(x - x_c)^2$.

5.2.4.A Comparison of EMA-lattice results with off-lattice model results

The behaviour shown in Fig. 5.10 is qualitatively similar to that obtained in the calculations of Ref. [36], based on a lattice tunnelling-percolation model, where it was shown that the transport exponent acquires a concentration dependence, recovering the universal value t_0 only for $x \to x_c$ (see section 5.1). The off-lattice results of Fig. 5.10 can therefore be interpreted in the light of the EMA approach presented in section 5.1. We can now assume that, also for the off-lattice case, the main contribution to Σ comes from the tun-

nelling processes between nearest-neighbouring particles. Furthermore, since now the relevant quantity is the volume fraction x of the conducting phase, we make use of the site percolation formulation of the EMA equations as described in Ref. [19]. This amounts to replace, in Eq. (5.6), $(p - p_c)/p$ by $(x^2 - x_c^2)/x^2$, where, in order to approximately map the off-lattice case to the EMA formulation, x_c is now regarded as the percolation threshold determined by d. Finally, since the tunnelling length is limited by the cut-off d, the upper limit of integration of Eq. (5.6) is set equal to d/a. As noticed in Sec.III, d/a is approximately $1.6a_c/a$, where a_c is the nearest-neighbour mean distance at percolation, so that for large $2a/\xi$ the upper limit of integration can actually be safely set to infinity because the peak of $W'(z)$ is at $z^* \ll 1.6a_c/a < 1.6$. Therefore, by following the same steps which led to Eqs. (5.19) and (5.20) and for finite conducting particle diameters σ_1 (see appendix), the conductivity of the tunnelling-percolation model in the continuum can be argued to be well described by a generalized power-law behaviour with a concentration dependent exponent of the form

$$\Sigma \approx \left(\frac{x^2 - x_c^2}{x^2}\right)^{t(x)} \tag{5.35}$$

$$t(x) = t_0 + \frac{a - \sigma_1}{\xi/2} f\left(\frac{x^2 - x_c^2}{x^2}\right) \tag{5.36}$$

where the mean distance a depends implicitly on x, $t_0 \simeq 2$ is the universal transport exponent for three dimensions, and $f(y)$ is a generic function which should go to zero when $y \to 0$, in order to recover universality very close to the percolation threshold (as was obtained in the finite size analysis of the model, in section 5.2.3). We first check whether the conductivity of our model, which was shown, in figure 5.10, to be well described by the simple power law of Eq. 5.44, agrees with equation 5.35. To this end, we replot in figure 5.11 the results of figure 5.10, but as a function of $(x^2 - x_c^2)/x^2$. By comparing the two figures, we see that in fact, the conductivity close to the percolation threshold seems to be better described by equation 5.35, than by the commonly admitted simple power law.

We will now try to extract $f(y)$ from our Monte Carlo results, with $y = (x^2 - x_c^2)/x^2$. Let us denote by $\Sigma(x, \xi)$ the conductivity of the system with characteristic tunnelling distance ξ, and $\Sigma(x, \infty)$ for a system with $\sigma_1/\xi = 0$, which is obtained by setting the conductance between two adjacent particles equal to 1. This second case should give universal results, following

$$\Sigma(x, \infty) \simeq \left(\frac{x^2 - x_c^2}{x^2}\right)^{t_0}, \tag{5.37}$$

which is indeed verified in figure 5.11. So finally, $f(y)$ can be obtained from

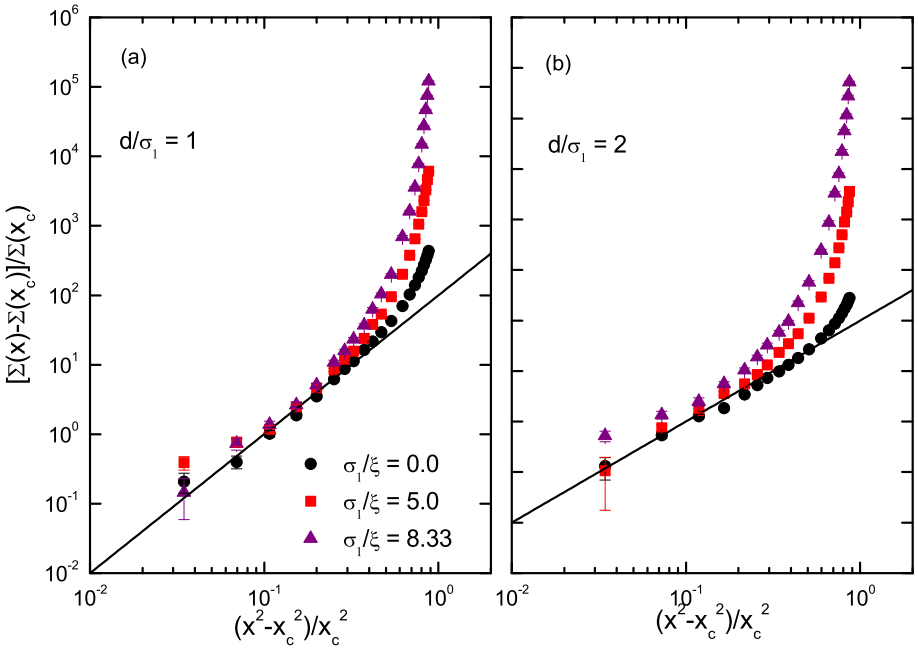

Figure 5.11: The calculated conductivity as a function of the proximity $(x^2 - x_c^2)/x_c^2$ to the percolation threshold for different values of σ_1/ξ for $L/\sigma_1 = 40$. This is for $d/\sigma_1 = 1$ (a) and $d/\sigma_1 = 2$ (b). The solid lines represent the universal dependence $\left[(x^2 - x_c^2)/x^2\right]^2$.

the following quantity:

$$\ln\left(\frac{\Sigma(x,\xi)}{\Sigma(x,\infty)}\right)\frac{1}{\ln(y)}\frac{\xi}{2(a-\sigma_1)} = \Big(t(x) - t_0\Big)\frac{\xi}{2(a-\sigma_1)} = f(y). \qquad (5.38)$$

We can now try the same form for $f(y)$ than obtained in the lattice EMA, namely we take

$$f(y) = f_0\left[\ln\left(\frac{1}{y}\right)\right]^{-b}. \qquad (5.39)$$

so that, by using Eq. (5.39) in Eq. (5.38) and taking the logarithm, we have

$$\ln\left[\Big(t(x) - t_0\Big)\frac{\xi}{2(a-\sigma_1)}\right] = \ln(f_0) - b\ln\left[\ln\left(\frac{1}{y}\right)\right]. \qquad (5.40)$$

This is the final form we test in figure 5.12, where we plot the left hand side of equation 5.40 as a function of $\ln[\ln(1/y)]$, for $d/\sigma_1 = 1$ and $\sigma_1/\xi = 5$. The advantage of this representation is that it allows to verify the form chosen for $f(y)$, as it should lead to a straight line. It is clear from that figure that,

in the case considered, our numerical Monte Carlo results follow very closely equation 5.40, with $f_0 = 1.9$ and $b = 1.18$, obtained by fitting the right-hand side of equation 5.40 to our data.

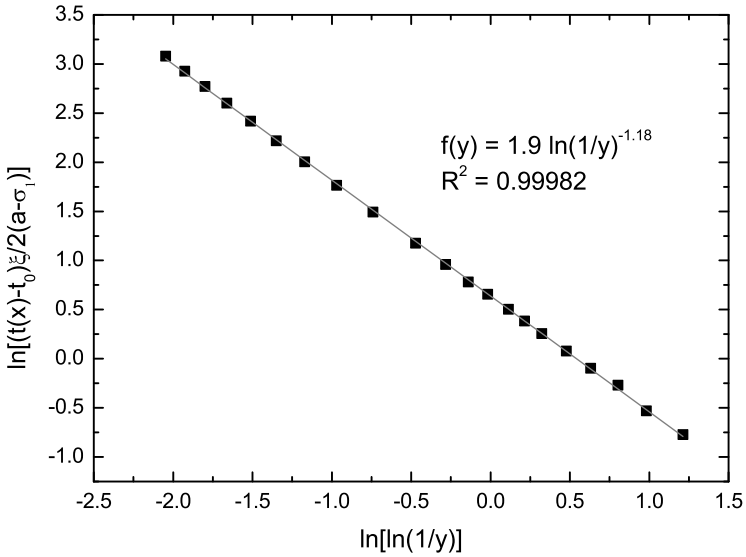

Figure 5.12: Plot of the Monte Carlo results for the conductivity Σ for $\sigma_1/\xi = 5$ and $d/\sigma_1 = 1$, plotted, as explained in the text, following equation 5.40. The solid line is a fit of Eq. (5.39) with the fitting parameters given in the figure.

The agreement between equation 5.40 and our Monte Carlo data is also very impressive for all other cases studied (all values of σ_1/ξ and for $d/\sigma_1 = 1$ and $d/\sigma_1 = 2$) and the fitting parameters obtained for f_0 and b are not varying much from one case to another. f_0 is found to vary between $f_0 = 1.59$ and $f_0 = 2$, whereas b varies between 1.09 and 1.33. This small variation of the fitting parameters allows us to represent all data obtained by a single function. In figure 5.13 we show again the lefthand side of equation 5.40 as in figure 5.12, but for all values of σ_1/ξ and d/σ_1 studied. The black line is $\ln[f(y)]$ with the parameters set to their mean values of $\bar{f}_0 = 1.83$ and $\bar{b} = 1.175$ obtained from the fits for the different cases. We see in this figure that the conductivity follows almost perfectly a single master curve for all cases considered. It is quite surprising that the conductivity of this complex continuum model can be described by this simple EMA result

$$\Sigma(x,\xi) = \Sigma(x,\infty)\left(\frac{x^2 - x_c^2}{x^2}\right)^{\frac{2(a-\sigma_1)}{\xi} f_0 \left[\ln\left(\frac{x^2}{x^2-x_c^2}\right)\right]^{-b}}, \qquad (5.41)$$

with only the exponent $-2/3$, of the EMA calculation, replaced by $-b = -1.17$ and an additional multiplicative constant $f_0 = 1.83$. We note here

that in those two figures we did not use Σ as obtained directly from the Monte Carlo simulations, but rather used $\bar{\Sigma}(x) = \Sigma(x) - \Sigma(x_c)$ to minimize the finite size effects.

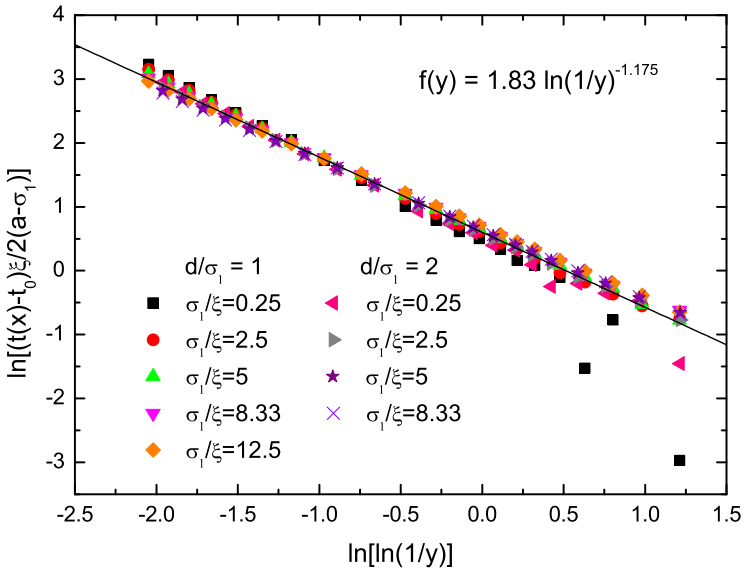

Figure 5.13: Plot of the Monte Carlo results for the conductivity Σ for different parameters, plotted, as explained in the text, following equation 5.40. The solid line is Eq. (5.39) with the mean values of the fits as parameters, as given in the figure.

Now taking a closer look at the fitting parameters b and f_0 obtained for the different ξ/σ_1 and d values, shown in figure 5.14, we see that these parameters have a weak dependence on ξ. In fact f_0 is better represented as a function of $2(a_c - \sigma_1)/\xi$ and f_0 as a function of σ_1/ξ, so that the results for the $d = 1$ and $d = 2$ cases lie approximately on a single curve. We can asses from this figure that $\lim_{\xi\to\infty} b = 1$ and $\lim_{\xi\to\infty} f_0 = 2$, so that, in the limit of small ξ, equation 5.41 reduces to the very simple form:

$$\Sigma(x,\xi) = \Sigma_0 e^{-\frac{4(a-\sigma_1)}{\xi}} \left(\frac{x^2 - x_c^2}{x^2}\right)^2 \tag{5.42}$$

So basically we show that for both asymptotic cases, $\xi \to 0$ and $\xi \to \infty$, the expression for the conductivity of the system is very simple. In the first case it is governed by the universal exponent t_0, and in the second we simply have an additional dependence on the typical nearest-neighbour conductance $g(a)$, where all the dependence on x stems from the dependence of the nearest-neighbour mean distance a on the volume fraction x.

In fact, it is clear from equation 5.42 that the behaviour of Σ, for small

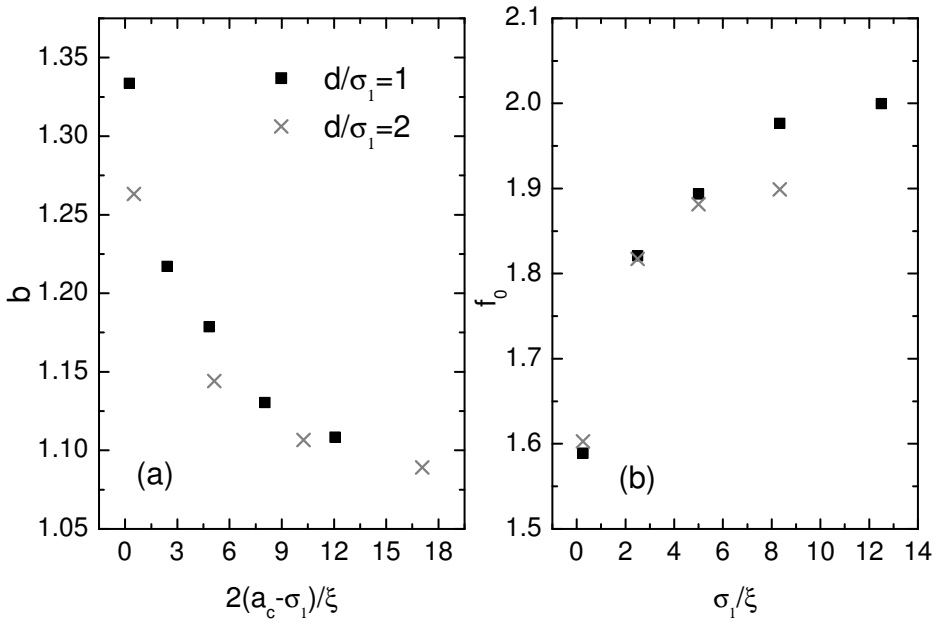

Figure 5.14: Fitting parameters obtained by fitting equation 5.40 to our Monte Carlo data. (a): the exponent b of equation 5.39 as a function of $2(a_c - \sigma_1)/\xi$. (b): the multiplicative constant f_0 of equation 5.39 as a function of σ_1/ξ

ξ and x not too close to x_c, is dominated by the exponential term. We therefore recover a result of Seager and Pike [85] obtained from a critical path analysis [58] of the same problem studied here and in this special limit. They showed that, for small ξ and not too close to x_c, the conductivity is given by

$$\Sigma \propto e^{-\frac{2d_c}{\xi}}, \tag{5.43}$$

where d_c is the critical shell thickness, for which a conducting cluster first appears in the system if the penetrable shell thickness d is increased. d_c can be easily linked to the mean nearest-neighbour distance a using panel (b) of figure 5.8, where we see that $d_c \simeq c(a - \sigma_1)$ and $1.9 \lesssim c \lesssim 2.1$ in the range of volume fractions x studied. In fact the value of c should be compared with the limiting values obtained for f_0 in figure 5.14 (b) for small σ_1/ξ, which shows very good agreement between our results and the result of Ref [85]. We can also stress here that this comparison shows us that the use of the mean nearest-neighbour distance a in equations 5.41 and 5.42 is not the only parametrization possible, as any representative distance of the conductivity in the system such as a, d_c, the mean next-nearest-neighbour distance or the simply the mean tunnelling distance will have the same dependance on the concentration, namely they will be proportional to $x^{-1/3}$. From this per-

spective it seems clear that the use of the mean-nearest neighbour distance a is just a parametrization but that it is probably not the correct parameter governing the conductivity of the system.

5.2.4.B Discussion

Following the above results, it is interesting at this point to discuss what a strongly varying local exponent $t(x)$ would imply when the x-dependence of the conductivity is forced to be of the form

$$\Sigma = \Sigma_0 (x - x_c)^t, \tag{5.44}$$

with an x-independent exponent, albeit not necessarily equal to t_0. This issue is fundamental in establishing a connection with experiments in real composites, where indeed Eq. (5.44), with t independent of x, is used to fit the concentration dependence of the measured conductivity, without an a priory knowledge of the percolation threshold x_c. We have fitted then the data of Fig. 5.10, and few more cases for different values of σ_1/ξ, by using Eq. (5.44) with the prefactor Σ_0, the exponent t, the critical concentration x_c and an additive constant (to take into account the finite size of the system) as fitting parameters. An example of such a fit is shown in figure 5.15, for $d/\sigma_1 = 1$ and $\sigma_1/\xi = 6.25$. We see on this example that we obtained a transport exponent $t = 2.8 \pm 0.3$ larger than $t_0 = 2$. For each set of parameters d/σ_1 and σ_1/ξ, we have done four such fits to different simulation data of the conductivity and averaged the extracted transport exponents in order to get better estimates and diminish the uncertainty on t. The so-obtained transport exponents, and corresponding error bars, are plotted by filled squares in Figs. 5.16(a) and 5.16(b) for $d/\sigma_1 = 1$ and $d/\sigma_1 = 2$, respectively, as a function of σ_1/ξ. Also, shown are the corresponding finite size results of Fig. 5.9 (filled circles) and the Kogut-Straley exponent Eq. (5.34) (solid lines). From the plots in Fig. 5.16 it is clear that forcing the exponent t to be independent of the concentration leads to a sort of average, say t^*, of the local one $t(x)$. Consequently, the fitted exponent results are confined between the universal value obtained from the finite size analysis and the non-universal Kogut-Straley exponent. Hence, by reducing σ_1/ξ, the mean value t^* of the fitted, or apparent, exponent decreases from a large value at large σ_1/ξ towards the universal limit $t_0 \simeq 2$ as $\sigma_1/\xi \to 0$. Furthermore, since the local exponent $t(x)$ has a stronger x dependence for larger σ_1/ξ values, the error bars resulting from the fitting procedure get reduced as well when $\sigma_1/\xi \to 0$. Finally, for fixed σ_1/ξ, the error bars increase by going from $d/\sigma_1 = 1$ to $d/\sigma_1 = 2$, partially because of the stronger $t(x)$ variation, and partially because of the increased finite size effects.

A last interesting feature is given by the σ_1/ξ dependence of the "apparent" critical concentration x_c^* resulting from the fits to Eq. (5.44). In Fig. 5.17, the "apparent" exponent t^* of Fig. 5.16 is plotted as a function of

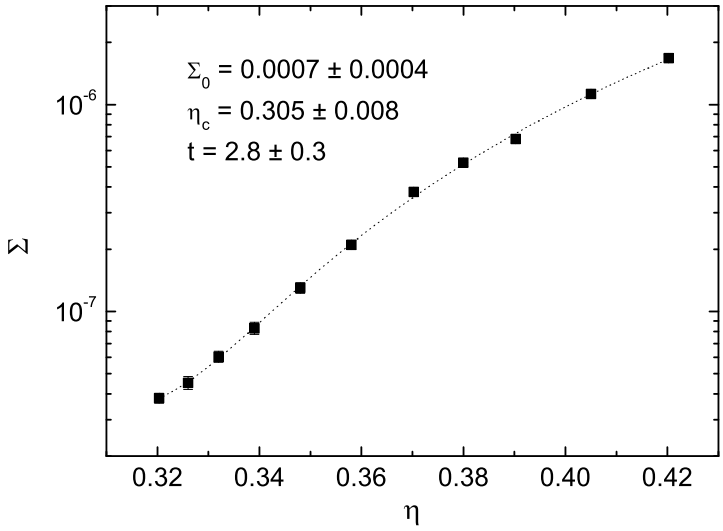

Figure 5.15: Example of a fit of equation 5.44 to Monte Carlo conductivity data for $d/\sigma_1 = 1$, $\xi/\sigma_1 = 6.25$ and the system size $L/\sigma_1 = 40$. The best fitting parameters are shown on the figure.

the corresponding x_c^* values. This result shows a clear correlation between the increase of t^*, resulting from the decrease of σ_1/ξ, and the (apparently counter intuitive) reduction of x_c^*. This feature can be understood by noticing that, in order to maintain $(x - x_c^*)^{t^*}$ approximately constant, as long as $x - x_c^* \ll 1$, an increase of t^* would require an increase of $x - x_c^*$, and so lead to a decrease of x_c^* for fixed x. What makes this feature interesting is that, when collecting the measured exponents and the corresponding critical concentrations in real disordered composites, a trend similar to the one of Fig. 5.17 is observed: namely, for the same type of particles (say, spheres in cellular composites [37]) lower percolation thresholds are accompanied by larger and more dispersed values of the measured exponent (as can be seen in figure 1.1). This is of course not the case when other reasons (such as when the conductance distribution changes with the particles shape [27, 86, 87]) modify the percolation threshold.

5.3 Comparison with an experimental result

In this section we seek to verify the applicability of our model to real composites. To this end we want to compare our formulas 5.36 and 5.35 for the conductivity Σ of our model, with experimental measurements. As our model is applicable only for homogeneous dispersions of spheres, which should have

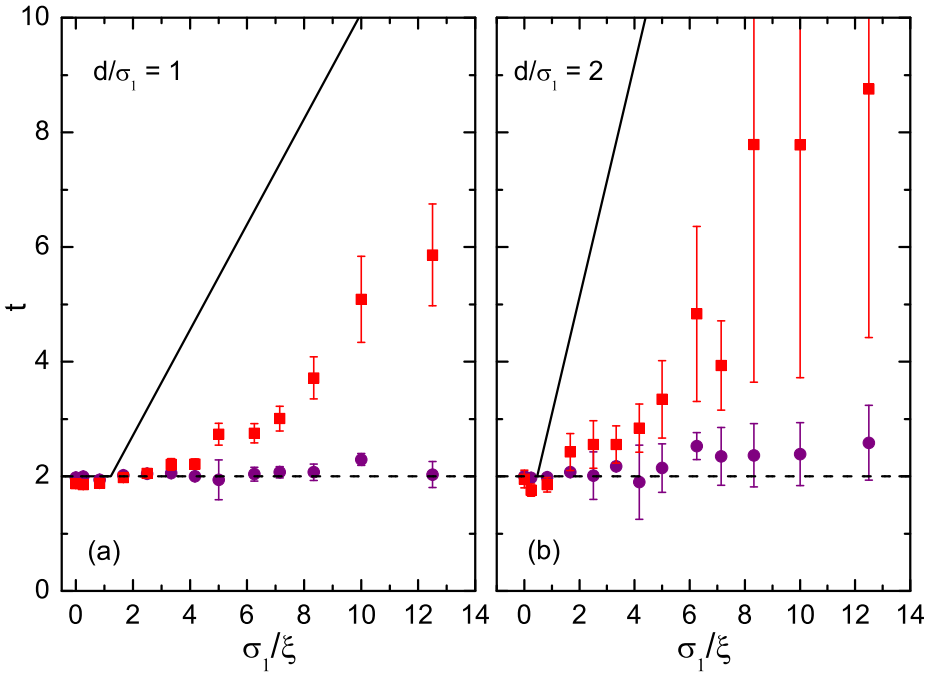

Figure 5.16: Comparison between the Kogut-Straley exponent (solid lines), and the exponents obtained from the finite size analysis (filled circles) and the apparent exponent t^* (filled squares) obtained by using Eq. (5.44). The horizontal dashed line is the universal value $t_0 = 2$. (a): $d/\sigma_1 = 1$, (b): $d/\sigma_1 = 2$.

quite high percolation thresholds of the order of 30 to 60% (lower percolation thresholds can be obtained for very small conducting particles with which it is usually difficult to obtain a homogeneous dispersion, particles with high excluded volume or in segregated structures), and as we wanted to fit our model to a system that was dubbed as non-universal, we chose to fit our formulas to the results of Rubin et al. [87], presenting the conductivity of a set of low-structure carbon-black/polymer composites.

We show in figure 5.18 the fits to the conductivity data of equations 5.44, 5.41 and 5.42, in panels (a), (b) and (c) respectively. All three equations seem to fit the data equally well. The fit of the classical power law, gives a non-universal exponent $t = 6.8 \pm 0.9$ and a prefactor for the conductivity $\Sigma_0 \simeq 7000\,\Omega^{-1}\mathrm{cm}^{-1}$ with a very large uncertainty (Σ_0 between 300 and 13000 $\Omega^{-1}\mathrm{cm}^{-1}$) . In the article [87], Rubin and coauthors measure the conductivity of the CB filler and find $\Sigma \approx 100\,\Omega^{-1}\mathrm{cm}^{-1}$, so that we expect the prefactor Σ_0 rather of the order of $10\,\Omega^{-1}\mathrm{cm}^{-1}$, so that the prefactor obtained by fitting the simple power-law is not very satisfactory. Now in order to use equations 5.41 and 5.42 to fit the conductivity data, we need

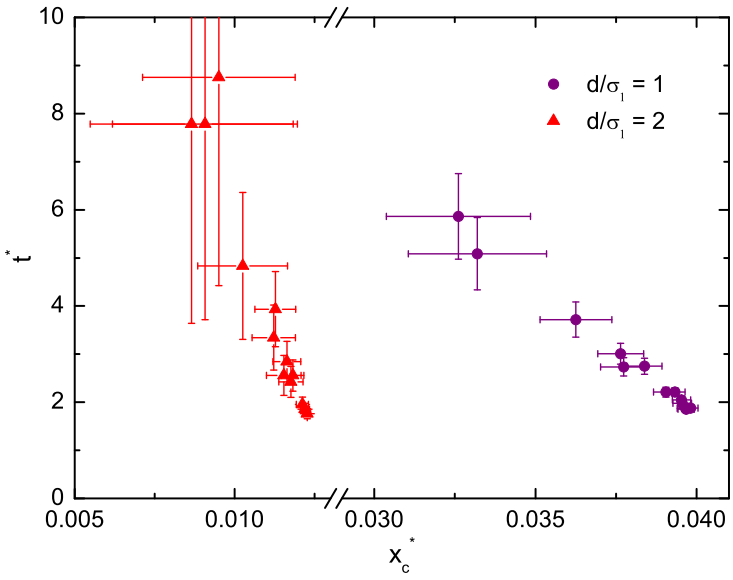

Figure 5.17: The apparent DC transport exponent t^* as a function of the corresponding apparent critical concentrations x_c^* for $d/\sigma_1 = 1$ and $d/\sigma_1 = 2$.

an expression for the mean nearest-neighbour distance a for relatively high densities of conducting particles, which can be found in [28] and takes the form:

$$a/\sigma_1 = 1 + \frac{(1-x)^3}{12x(2-x)}. \tag{5.45}$$

This expression gives satisfactory estimations of a for $x \gtrsim 0.15$. We also use for σ_1 the mean CB grain size, as given in the article, $\sigma_1 = 320\,\mathrm{nm}$. Finally the fits of equation 5.41 and its limiting case equation 5.42 give fitting $\Sigma_0 = 20 \pm 3\,\Omega^{-1}\mathrm{cm}^{-1}$ and $\xi = 2.3 \pm 0.1\,\mathrm{nm}$ in the first case and $\Sigma_0 = 8 \pm 1\,\Omega^{-1}\mathrm{cm}^{-1}$ and $\xi = 2.4 \pm 0.1\,\mathrm{nm}$ in the second case. As ξ is typically expected to be of the order of $1-3\,\mathrm{nm}$ [87,86], the fitting parameters obtained from equations 5.41 and 5.42 are perfectly compatible with the theoretical values.

To give a better idea of how apparent non-universality arises, we show in figure 5.19 the local transport exponent $t(x)$ obtained from the fit of Eq. (5.41) to the conductivity data, corresponding to panel (b) of figure 5.18. In this figure, $t(x)$ is shown as a plain line in the range of x in which the fit to equation 5.41 was done. We see that the apparent transport exponent obtained from the fit to the classical power law, $t = 6.8$ (see figure 5.18(a)) corresponds more or less to the average of $t(x)$ over the fitting range. We also show in figure 5.19 $t(x)$ for values outside the fitting range, closer to

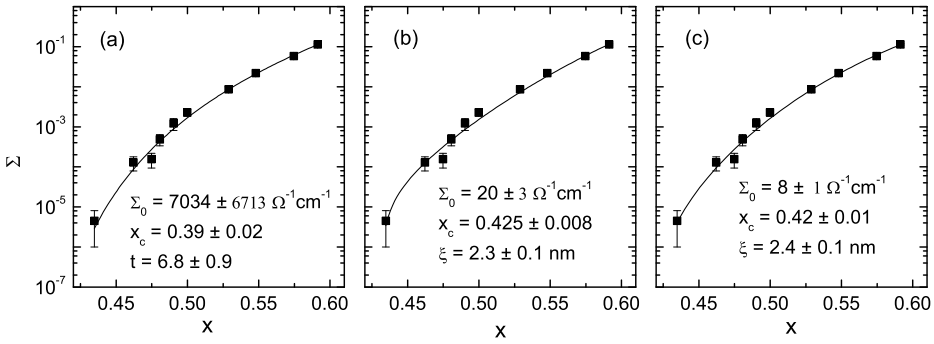

Figure 5.18: Experimental results for a low-structure carbon-black/polymer composite, taken from Ref. [87]. In panel (a) we show the fit of the classical power-law of equation 5.44, in panel (b) of equation 5.41 and in (c) of equation 5.42.

x_c, as a dotted line. x_c is shown in this figure as a vertical dashed line, and we can see how $t(x)$ falls asymptotically towards the universal values for x-values only very close to x_c. It is in fact clear from this figure that the range of x-values where the real universal behaviour could be observed seems experimentally unreachable. We should recall here that the expression used for $t(x)$ was obtained by simply conciliating the limiting cases obtained for x far from x_c and for x very close to x_c, so that it might not represent exactly the transition between those two limiting behaviours.

5.4 Piezoresistivity in the continuum TP model

As we have seen in section 3.3, the piezoresistive response is one of the main experimental result supporting the tunnelling-percolation models of conductivity in TFRs. Indeed it was seen in figure 3.4 that the piezoresistivity presents a logarithmic divergence as the percolation threshold is approached, for samples presenting non-universal transport exponents, and a constant piezoresistivity in the universal case. It is essential to asses whether our continuum TP model also leads to this behaviour, we therefore study in this section the piezoresistivity Γ of our model.

5.4.1 Monte Carlo results

The piezoresistivity was obtained from our Monte Carlo simulations, as described in appendix B.5. Namely, we calculated the conductivity Σ for a given set of parameters twice, only changing ξ to $\xi/(1+\epsilon)$, with $\epsilon = 0.01$,

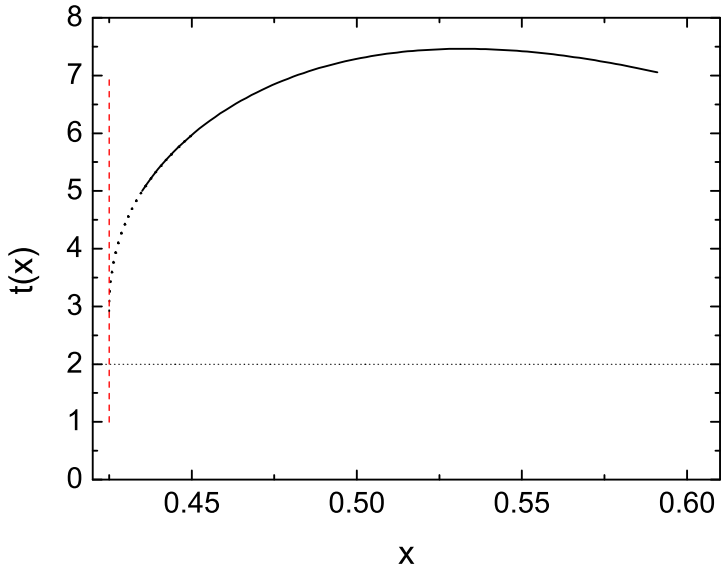

Figure 5.19: Local transport exponent $t(x)$ obtained from the fit of panel (b) of figure 5.18. $t(x)$ is shown as a plain line in the fitting interval of the conductivity data, and as dotted line outside this interval. x_c is also shown as a vertical dashed line and $t_0 = 2$ as a horizontal dashed line.

and obtained Γ from the difference $\Delta\Sigma$ between the two conductivities:

$$\Gamma_s = \frac{\Delta\Sigma}{\Sigma\epsilon}, \tag{5.46}$$

and

$$\Gamma = \Gamma_s + \frac{\epsilon}{2}\Gamma_s^2. \tag{5.47}$$

Our Monte Carlo results for Γ are shown in figure 5.20 for the same parameters of figure 5.16(a). We shall notice here that the fits giving the transport exponents of figure 5.16(a) were done using ten values of the concentration x, corresponding for each σ_1/ξ to the 10 smallest conductivity values of figure 5.20. We see that systems with large ξ present a universal behaviour, *i.e* a constant piezoresistivity $\Gamma = \Gamma_0$ in the whole range of concentrations studied, whereas for smaller ξ, the range of universality is reduced to a region very close to the percolation threshold x_c, with a logarithmic behaviour of the piezoresistiviy further away from x_c: $\Gamma \propto \ln(1/\Sigma)$.

Now as we have seen, the conductivity Σ of systems of finite sizes does not go to 0 at x_c but rather to a finite value $\Sigma(x_c)$. As Γ is shown in figure 5.20 as a function of Σ it is important to check whether the finite-size effects are of importance here or not. This is done in panel (a) of figure 5.21, where we show $\Gamma(\Sigma)$ for $d/\sigma_1 = 1$ and $\sigma_1/\xi = 6.25$ and for three different system

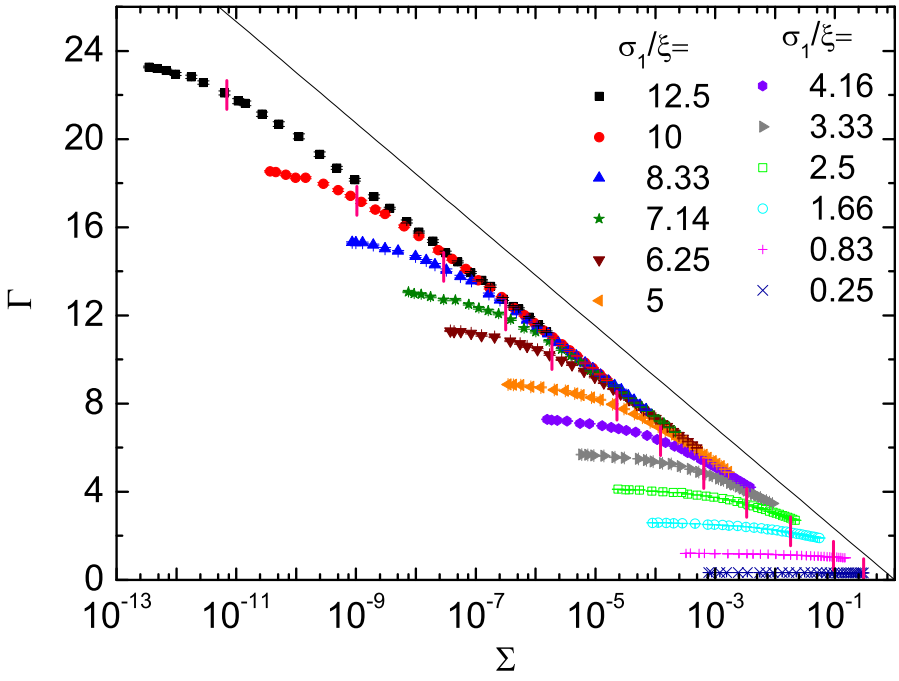

Figure 5.20: Monte Carlo results for the piezoresistivity Γ as a function of the conductivity of the system Σ for $d/\sigma_1 = 1$ and different values of σ_1/ξ. The black line is $\ln(1/\Sigma)$ and the short vertical lines are the estimation for the crossover between non-universal and universal behaviour obtained from the EMA equation 5.49.

sizes. We see that the system size has little influence on Γ, except that larger L/σ_1 allow to explore the behaviour of Γ for smaller conductivities, which would correspond to being closer to the percolation threshold for an infinite system. At least it is clear that the plateau observed for small Σ is not a finite size effect, it is on the contrary rather masked by the finite size of the system, forbidding to asses the behaviour for $\Sigma = 0$.

5.4.2 Comparison with the EMA

We now extract an analytical expression for the piezoresistivity of our system from our EMA result for the conductivity Σ. We obtain Γ from equations 5.15 and 5.18 and from the relation (see appendix B.5).

$$\Gamma = \frac{d\ln(\Sigma)}{d\ln(\xi)} \tag{5.48}$$

so that we obtain

$$\Gamma = \begin{cases} \Gamma_0 = \frac{2d}{\xi} - 1 & \text{if} \quad \Sigma < 1/2e^{-2d/\xi} \\ \ln(1/\Sigma) & \text{if} \quad \Sigma > 1/2e^{-2d/\xi} \end{cases} \tag{5.49}$$

There is no need here to change from the lattice representation to the continuum one by replacing p with x^2 as was done for the conductivity, as the results are independent of x. The $\ln(1/\Sigma)$ behaviour is plotted as a black line in figure 5.20, satisfactorily describing the limit for small σ_1/ξ and not to close to x_c. Also plotted in this figure as vertical short lines is $1/2\exp(-2d/\xi)$, representing the value of Σ where the crossover between non-universal and universal behaviour takes place. The values obtained are in good agreement with our Monte Carlo results.

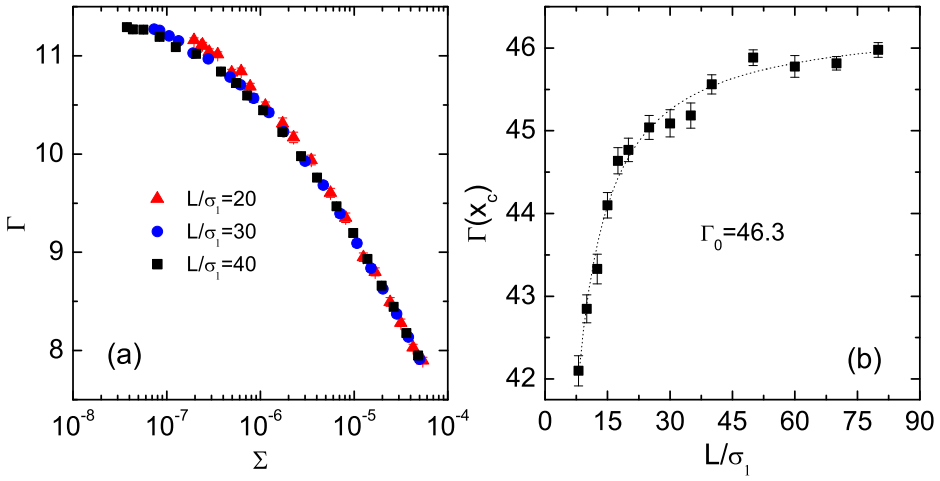

Figure 5.21: For $d/\sigma_1 = 1$: (a) Γ as a function of Σ for different system sizes L/σ_1 and for $\sigma_1/\xi = 6.25$. (b) $\Gamma(x_c)$ as a function of the system size L/σ_1 for $\sigma_1/\xi = 25$. The dotted line is the fit with equation 5.50.

Now to test the behaviour close to the percolation threshold, given by $\Gamma = \Gamma_0$, we extract Γ_0 from our Monte Carlo results. In order to limit the finite size effects, we extract Γ_0 for the infinite system, by fitting $\Gamma(x_c, L)$ for different system sizes with an appropriate function. Here we use

$$\Gamma = \Gamma_0 - A\left(\frac{L}{\sigma_1}\right)^{-\omega} \tag{5.50}$$

with Γ_0, A and ω as fitting parameters. An example of such a fit is shown in figure 5.21(b), for $d/\sigma_1 = 1$ and $\sigma_1/\xi = 25$. The best fit is shown as dotted line and the extracted value for Γ_0 is $\Gamma_0 = 46.3$ and is also shown in the figure. In figure 5.22 the so-obtained Γ_0 are shown for different values

of σ_1/ξ and for $d/\sigma_1 = 1$ and for for $d/\sigma_1 = 2$ as a function of $2d/\xi$. The black line is $\Gamma_0 = 2d/\xi - 1$ as obtained in equation 5.49. The EMA result of equation 5.49 maps very closely our Monte Carlo results.

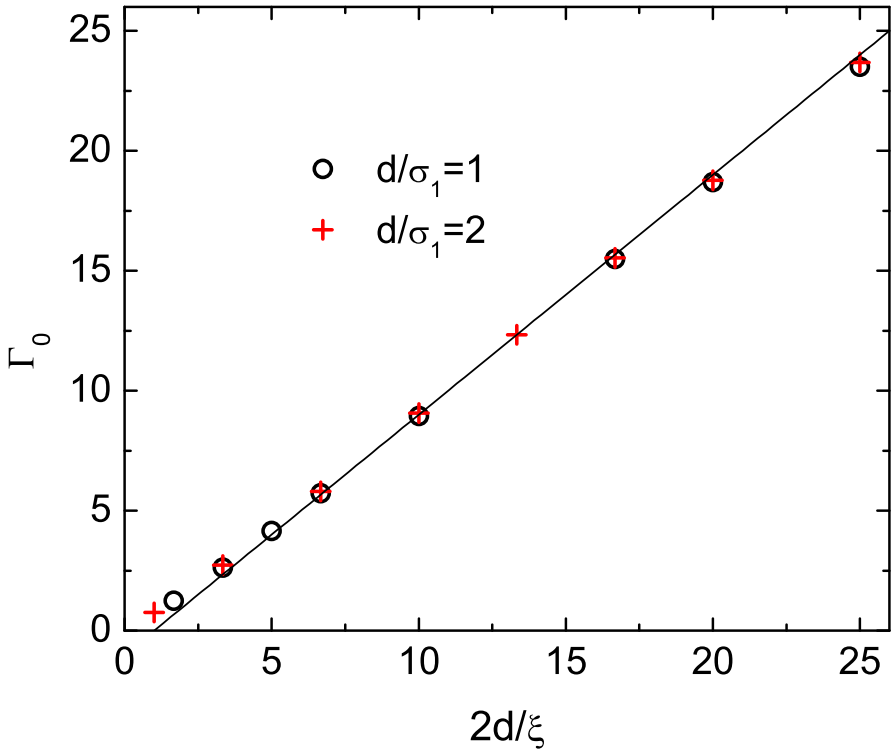

Figure 5.22: Γ_0 as a function of $2d/\xi$. Empty circles are Monte Carlo results for $d/\sigma_1 = 1$ and crosses for $d/\sigma_1 = 2$. The black line is $\Gamma_0 = 2d/\xi - 1$ as given in equation 5.49.

5.4.3 Discussion

The main difference between our continuum tunnelling-percolation model and the classical TP model stems from the absence, for any σ_1/ξ, of a true divergence of the piezoresistivity Γ as $x \to x_c$. Instead we have seen that Γ tends towards a maximal value Γ_0 as the percolation threshold is approached. In this regard, our model can lead to both, universal (constant) and non-universal (diverging) behaviours for the piezoresistivity, depending on the parameters of the model, but also on $x - x_c$. In fact the system undergoes, as for the lattice model studied in chapter 4, a crossover from non-universal to universal behaviour as the percolation threshold is approached. It seems

that our model is sufficient in describing the existing experimental measurement of the piezoresisitve response of conductor-insulator composites, and especially TFRs. Indeed, even though we do not have truly universal and non-universal systems, we still observe that, for a fixed $x-x_c$ range, if a non-universal transport exponent is extracted from the fit of the conductivity to equation 5.44, then a logarithmically increasing Γ will be obtained. On the other hand, a universal transport exponent will lead to a constant $\Gamma = \Gamma_0$. This can be seen by comparing our results for Γ, shown in figure 5.20 and those for the transport exponent of figure 5.17(a), keeping in mind that only the ten points for Γ with the smallest Σ correspond to the fitting range that lead to the transport exponent of figure 5.17(a).

Let us stress here that, if observed experimentally, the crossover between the universal and non-universal regime, would be a clear signature of tunnelling-percolation origin of non-universality, and would confirm our interpretation of the non-universal transport exponents as being due to apparent non-universality. Nevertheless this has, to our knowledge, not been observed yet. The issue here is the difficulty of obtaining precise values of the piezoresistivity very close to the percolation threshold. Nevertheless, the fact that this can be observed in a plot of Γ as a function of Σ instead of $x - x_c$, lifts the constraint of precisely knowing the concentration of the samples studied, making it experimentally easier to observe.

5.5 Conclusion

In the present chapter, we have considered an off-lattice model of the tunnelling percolation mechanism of electrical conduction in disordered composites. We have shown that, by using a numerically exact decimation procedure and a finite size analysis, at the percolation threshold, the conductivity critical exponent is universal and close to the value $t_0 \simeq 2$. Conversely, by moving away from the percolation threshold, we have demonstrated that, depending on the value of the characteristic tunnelling distance, the exponent acquires a strong concentration dependence, attaining values larger, or much larger, than t_0 [72]. We have interpreted this feature in terms of the strongly varying distribution of the local tunnelling conductivities, which leads to a shrinking of the (universal) critical region to concentrations very close to the percolation threshold. In particular we have shown the similarity of the results obtained from the lattice and off-lattice models, indicating that the first nearest neighbours dominate the values derived for the conductivity exponent in the tunnelling percolation problem. This is not a trivial conclusion since there is a clear competition between the decrease of the particle-to-particle conductance and the increase of the possible number of routes with the increase of the particle-to particle distance. These results therefore confirm similar findings for a realistic continuum model and the

lattice models of tunnelling-percolation. In fact, for the lattice, we were able to derive (in an asymptotic case) an analytic expression for the conductivity exponent in the three dimensional system, noting that such an expression was given previously only for the much simpler one dimensional system. It was also shown that this result for lattice percolation could be transposed to our continuum TP model, giving a surprisingly good evaluation of the conductivity Σ of the system. Furthermore, we have evaluated the apparent exponent arising from a fit of our numerical results by forcing the conductivity exponent to be independent of the concentration. This enables us to show that such apparent exponent has a non-universal behaviour, despite the fact that the system is strictly universal, confirming that apparent non-universality can arise in realistic models of granular materials, leading to a possible explanation of many experimental results.

We have then explored the piezoresistive response of such systems and found that it showed a crossover from a logarithmically diverging to a constant behaviour as x_c is approached. Contrary to the study of the conductivity Σ, Γ allows to directly follow the change from non-universal to universal regime. Although this feature has, to our knowledge, never been observed in real composite materials, it would give a direct confirmation of our interpretation of transport non-universality. Careful experimental studies of the piezoresistivity of conductor insulator compounds, should allow to verify this theoretical result.

Chapter 6

Segregation

In this chapter we study the effect of segregation on the percolation threshold of our tunnelling-percolation model. To this aim we reformulate the continuum percolation model, presented in chapter 5, by adding inhomogeneities to the microstructure, represented by spherical inclusions forbidding the percolating conducting spheres to occupy large regions of the composite. We show that, by varying the degree of segregation of the system, the percolation threshold is generally not a monotonic decreasing function of segregation, as suggested by earlier studies [88, 89, 90, 91, 92, 93, 51], but rather it exhibits a minimum shortly before maximum segregation is reached. Hence, the optimal percolation threshold does not necessarily coincide with the most segregated structure, leading to a more complex phenomenology than previously thought [94]. We then study the transport properties of this model, and find that they remain basically unchanged compared to the non-segregated systems. We are indeed able to map the conductivity of the segregated systems onto that of non-segregated ones, simply by shifting the critical concentration x_c and using an appropriate renormalization of the conductivity. This allows us to apply the theoretical results of the preceding chapter to obtain a simple expression for the conductivity in segregated tunnelling-percolation systems. This expression is applied to experimental measurements of the conductivity of TFRs, leading to values of the parameters of the model completely consistent with the theoretical expectations.

6.1 Lowering the percolation threshold

Unlike the universal (or quasi-universal) behaviour of the critical exponents characterizing the percolative transition, the value of the percolation threshold is a function of several variables such as the shape of the percolating objects, their orientation and size dispersion, their possible interactions and the microstructure in general [95].

Of fundamental importance for several technological applications is the

possibility of exploiting such a multi-variable dependence to tailor the percolation threshold. In particular, an issue of great interest concerns the problem of lowering the percolation threshold, so to have long range connectivity of the percolating phase with the minimum possible overall critical concentration. This is the case when, for objects dispersed in a continuous medium, one wishes to exploit the properties of the percolating elements, but still preserving those of the host medium. For example, low conducting filler amounts in a conductor-insulator composite permit to obtain an adequate level of electrical conductivity with mechanical properties of the composite being basically unaltered with respect to those of the pristine insulating phase.

Now, there exist two main strategies to lower the percolation threshold through the manipulation of the microstructure of heterogeneous composites. In one of such methods, one exploits the large excluded volume $v_{\rm ex}$ of particle fillers with large aspect-ratios, such as rods and/or disks dispersed in a three-dimensional continuum medium [96], whose critical concentrations, being proportional to $1/v_{\rm ex}$, can be made extremely small for sufficiently large aspect-ratios [97]. Such percolation threshold lowering has been studied in detail for several particle shapes and inter-particle interactions, and is now well documented [98, 81, 99, 100].

For example, the authors of Ref. [101] considered the percolation of oblate ellipsoids of revolution, with major axis a_m, minor axis b and aspect ratios a/b between 1 (spheres) and 100. Those objects are mainly meant to represent graphite fillers, which have typically the form of platelets. The connectivity criterion is the same as in our tunnelling-percolation model, *i.e.* each hard-core ellipsoid is surrounded by a penetrable shell of constant thickness $d/2$ (representing for example the tunnelling conductivity range), and two particles are considered connected if their shells overlap. Using simulation procedures similar to the ones I present in appendix B, the authors evaluate the hard-core critical concentration x_c as a function of the aspect ratio and shell thickness. This result is shown in figure 6.1. x_c is shown to decrease with increasing a_m/b, especially for thin penetrable layers. For the thinnest layer considered here, $d/a_m = 0.0526$, x_c can be reduced by about one order of magnitude by increasing the aspect ratio from $a_m/b = 1$ to $a_m/b = 100$.

We have seen in figure 6.1 that the reduction of x_c with increasing aspect ratio was especially important for thin penetrable layers d. The reason for this gets clear from figure 6.2, where η_c, the concentration obtained by using the total volume (hard-core plus penetrable shell), is shown as a function of the penetrable shell thickness d. For $d > a_m$ the form of the percolating object (hard-core plus penetrable shell) tends towards that of a sphere, so that $\eta_c \simeq 0.34$, as for fully penetrable spheres, independently of the aspect ratio.

Let us turn now to discuss the second strategy to lower the percolation threshold. It is obtained by forbidding the percolating objects to occupy

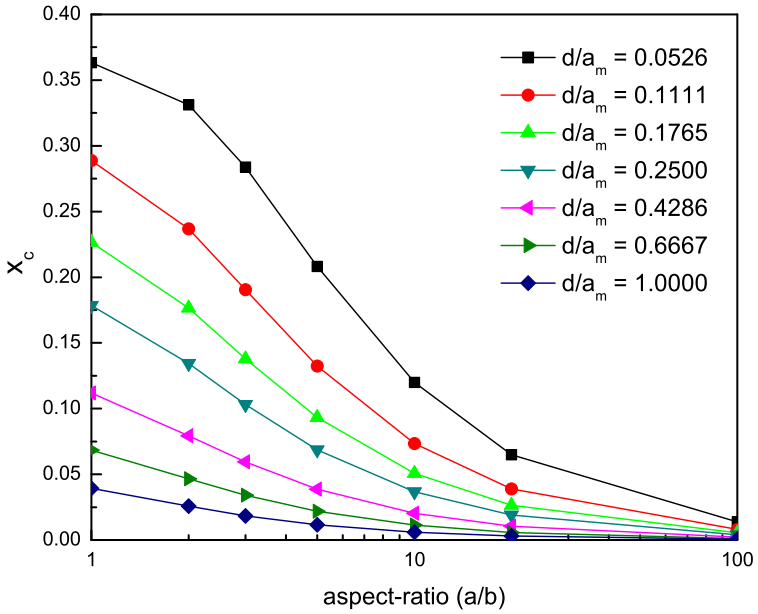

Figure 6.1: Percolation threshold x_c variation as a function of the aspect-ratio for different shell thicknesses. This figure is taken from Ref. [101]

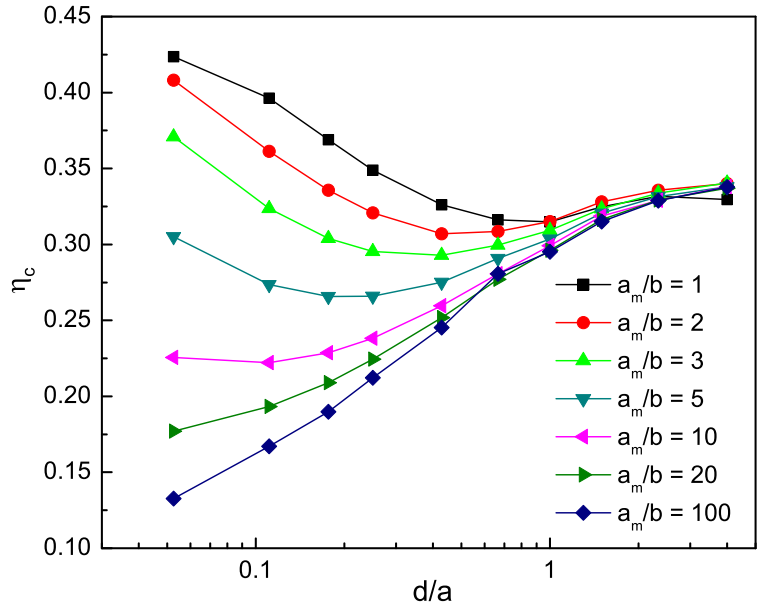

Figure 6.2: η_c as a function of the shell thickness for different aspect-ratios. This figure is taken from Ref. [101]

large (compared to the particle size) volumes inside the material, so to give rise to a segregated structure like the one shown in Fig. 6.4(b). In practice, this can be achieved when elements of two (mutually impenetrable) species have different sizes and percolation is established by the smaller elements. Typical examples of segregated systems are conductor-insulator composites, such as TFRs, where the size of the conducting particles is much smaller than that of the insulating regions [49, 102, 103], which display critical concentrations of a few percent or lower.

Despite the fact that such low percolation thresholds are qualitatively understood by the reduced available volume for arranging the conducting particles, very few studies exist on segregated percolation in the continuum [90, 91], while the vast majority of studies are limited to lattice representations of the segregated structure [88, 89, 92, 93, 51], which provide only a partial understanding of the percolation properties of segregated systems.

We will now introduce a realistic continuum model of segregated percolation, primarily aimed at describing the microstructure of segregated conductor-insulator composites, but general enough to represent also other structurally similar systems such as particle-laden foams [104] or filled hydrocarbon matrices [105].

6.2 The model

The model of segregated percolation is an extension of the continuum TP model introduced in chapter 5, where a dispersion of hard core conducting particles of diameter σ_1 was considered. We model the segregation by introducing a second kind of spherical particles. Those particles are insulating, have diameter $\sigma_2 \geq \sigma_1$ and are allowed to penetrate each other. Furthermore, to generate segregation, we assume that the two species of particles are mutually impenetrable, and that the voids left over from the two kind of particles are filled by the second (*i.e.* insulating) phase. Finally, the connectivity criterion for the conducting phase is defined by introducing a penetrable shell of thickness $d/2$ surrounding each conducting sphere, so that two given particles are connected if their penetrable shells overlap, as in the TP model of the preceding chapter. A two-dimensional representation of this model is shown in figure 6.3, where it is made clear that the hard core of the conducting particles cannot penetrate the insulating spheres, whereas the penetrable shell, of thickness $d/2$, can.

This model represents a rather faithful description of real segregated composites, such as the RuO_2-glass systems [88, 89, 106, 5], where thermal treatments on mixtures of RuO_2 and glassy grains lead to composites made of conducting RuO_2 particles dispersed in a continuum insulating glassy phase. Segregation is induced by the larger size of the original glassy grains compared to that of the conducting particles. Moreover, during the firing

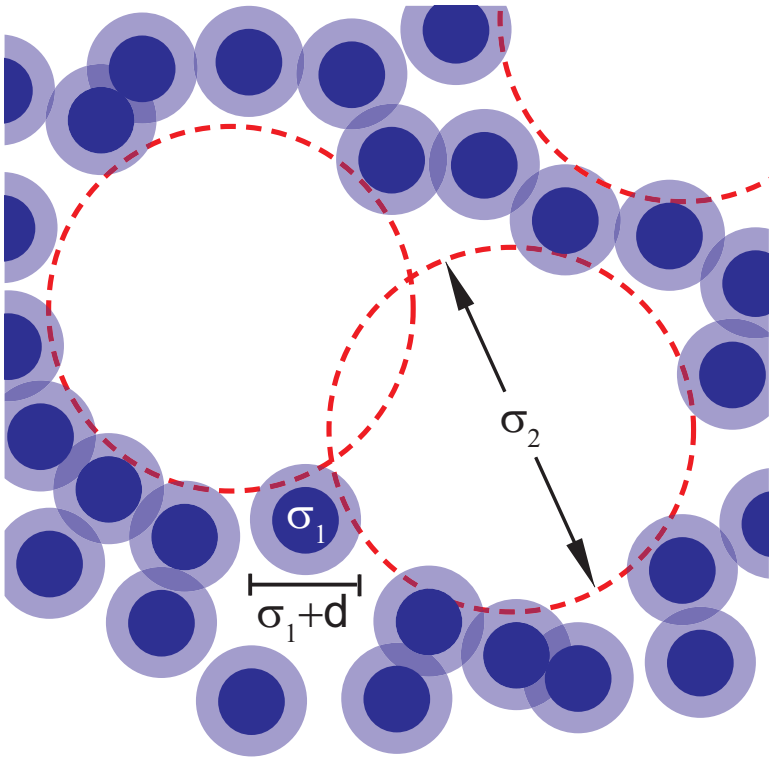

Figure 6.3: Schematic representation of our model of segregated tunnelling-percolation. The insulating spheres are shown as dashed circles, whereas the conducting spheres are shown as dark disks, together with their concentric shell (light coloured).

step of TFRs, the glassy grains soften and merge, which explains our choice of penetrable insulating particles. Furthermore, in this and other similar classes of composites, electrical transport is given by direct tunnelling or hopping processes, defining a characteristic length, represented by d in our model, below which two conducting particles are electrically connected. It is worth to mention that the model introduced here is relevant also for studying transport of macromolecules in disordered porous media [102], where d represents in this case the size of a test macromolecule and σ_2/σ_1 the pore size ratio in a bi-dispersed porous medium.

6.3 Simulation procedure

In our numerical simulations, the system described above is generated by first placing randomly the insulating spheres in a cube of edge length L with a given number density $\rho_2 = N_2/L^3$, where N_2 is the number of spheres.

The corresponding volume fraction for $L \to \infty$ is $\phi_2 = 1 - \exp(-v_2\rho_2)$, where $v_2 = \pi\sigma_2^3/6$ is the volume of a single insulating sphere. In a second step, N_1 conducting (and impenetrable) particles of diameter σ_1 and number density $\rho_1 = N_1/L^3$ are added in the remaining void space and a Metropolis algorithm is used to attain equilibrium. In the following, for the conducting phase, we use the reduced concentration variable $\eta_1 = \rho_1\pi/6(\sigma_1+d)^3$ and the hard-core volume fraction $x = \rho_1\pi/6\sigma_1^3$. Examples of the resulting spatial distributions of the conducting particles are shown in Fig. 6.4(a) for the homogeneous case ($\phi_2 = 0$) and in Fig. 6.4(b) for a segregated one ($\sigma_2/\sigma_1 = 12$ with $\phi_2 = 0.89$) for η_1 values close to their respective percolation thresholds (see below).

The rest of the procedure is the same as for the homogeneous case $\phi_2 = 0$ described in section 5.2.2: a Hoshen-Kopelman algorithm is used to extract the percolating cluster, if present, and the spanning probability $\Pi(\eta_1)$ is obtained from the statistic of appearance of such a spanning cluster. The conductivity of the system, that will be considered in the end of this chapter, is obtained exactly as in the homogeneous case. For more details about the simulation procedures, refer to appendix B

It is maybe important to specify here how this model relates with real TFRs. ϕ_2 is not a measure of the glassy phase volume fraction, as $x + \phi_2 < 1$ in our model. ϕ_2 is only a measure of the degree of segregation, but the insulating phase also fills the void regions in between the conducting particles. In real composites, the glassy grains soften during firing and fill the interstices between the conducting grains and only a part of the initial glassy grains remains unaccessible to the conducting phase and induces segregation. This is the volume represented by ϕ_2 in our model. We can also add here that, actually, in some commercial compositions, the TFRs are made with two different glasses, one becoming very fluid during firing and the second solely soft. In that case ϕ_2 would represent the volume fraction of the second type of glass, whereas the first one would be the phase simply filling the remaining void regions.

6.3.1 Extraction procedure for the critical concentration

To obtain the critical density η_1^c for infinitely large system sizes we follow a standard finite-size scaling method, as presented in section 5.2.2. Namely, for given values of σ_2/σ_1, d, and ρ_2, we calculate, as a function of η_1 and L, the probability $\Pi(\eta_1, L)$ that a cluster of phase 1 spans the system in a given direction, with periodic boundary conditions in the other two directions. As in the homogeneous case, the critical density $\eta_1^c(L)$ for finite L is then extracted by fitting an appropriate function to the discrete simulation data. However we do not use here the same function of equation 5.29 for this fit, as the spanning probability has a somewhat more complicated form in the segregated case. Indeed, depending on the system size L and on ϕ_2, the

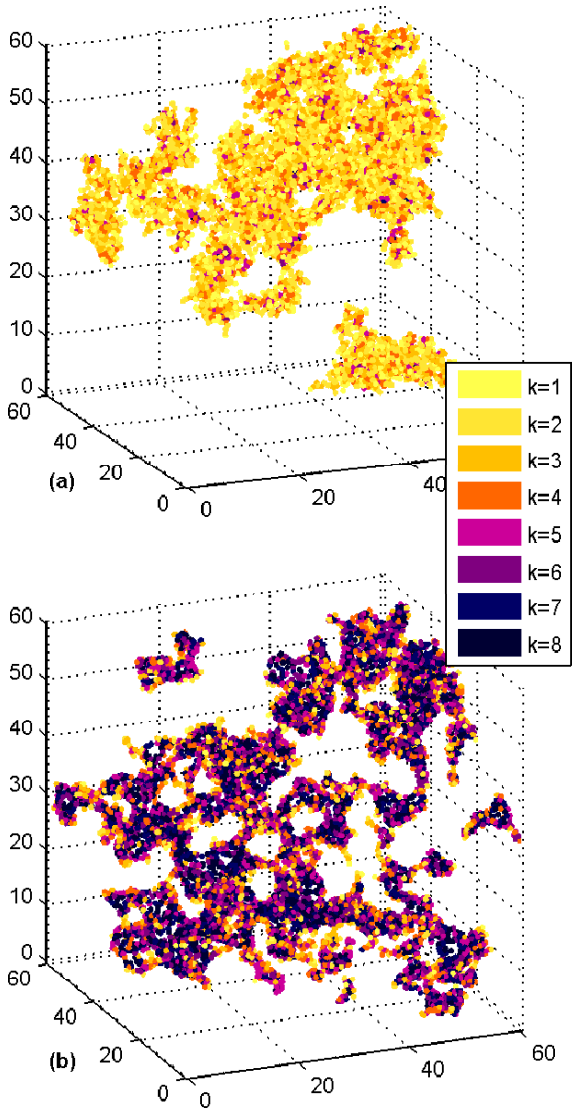

Figure 6.4: Percolating cluster of the conducting phase for (a) the homogeneous case $\phi_2 = 0$ and for (b) the segregated regime with $\sigma_2/\sigma_1 = 12$ and $\phi_2 = 0.89$. The conducting particles are plotted together with their penetrable shells with $d = \sigma_1$. The colour map defines the values of the connectivity number k for each particle (see text).

insulating phase can make it impossible for the conducting one to percolate. There is in fact a maximal value of ϕ_2, ϕ_2^*, beyond which percolation of the conducting phase becomes impossible. ϕ_2^* obviously depends on σ_2, σ_1 and d. We have in fact a percolation transition of the volume available to the conducting particles, so that there is a non-zero probability that the

conducting phase is hindered to percolate by the insulating one. This effect is of course more visible for large ϕ_2, close to ϕ_2^*, and small L, so that the spanning probability $\Pi(\eta_1, L)$ will not tend asymptotically towards 1 anymore but towards a smaller value $A < 1$. An example of this effect is shown in figure 6.5, where the spanning probability of a highly segregated system ($\phi_2 \simeq 0.94$) is shown for different system sizes. In this example the conducting particles have no hard-core, *i.e.* $\sigma_1 = 0$, so that just their center is forbidden to penetrate the insulating spheres. We see on this figure how A changes with the system size, increasing from $A = 0.46$ for the smallest system size ($L = 10$) to $A = 0.95$ for $L = 40$. Let us also notice that the approach of $\Pi(\eta_1, L)$ toward A becomes very slow for small L and large ϕ_2, making the transition asymmetric. We used the logistic function

$$f(\eta_1) = A - \frac{A}{1 + (\eta_1/\eta_1^c)^q} \tag{6.1}$$

fitting very well our simulation data. The fits of Eq (6.1) to the $\Pi(\eta_1, L)$ data of figure 6.5, are shown as dashed lines in this figure. The values for A indicated there stem from these fits. Of course, the case shown in that figure is an extremely bad one; in most cases we obtain values of $A \simeq 1$, so that a true percolation transition is observed for the conducting phase and the results would not change much if we simply used $A = 1$. We nevertheless introduced this parameter to obtain better overall fits, also for the extreme cases.

From the definition of equation 6.1, we see that we have chosen $\eta_1^c(L)$ as defined by $f(\eta_1^c(L)) = A/2$. The critical concentration η_1^c for an infinite system is then obtained following the same procedure as in section 5.2.2, *i.e.* from the scaling relation [107, 73]

$$\eta_1^c(L) - \eta_1^c \propto L^{-1/\nu}, \tag{6.2}$$

with $\nu \simeq 0.88$ the correlation length exponent. ν can be obtained from the width of the percolation transition $\Delta(L)$, following [73]

$$\Delta(L) \propto L^{-1/\nu}. \tag{6.3}$$

Finally, $\Delta(L)$ is obtained by imposing that 80% of the transition is comprised in this width:

$$\Delta = \eta_1^2 - \eta_1^1 \tag{6.4}$$

where η_1^1 and η_1^2 are such that

$$f(\eta_1^2) = 0.9A \quad \text{and} \quad f(\eta_1^1) = 0.1A. \tag{6.5}$$

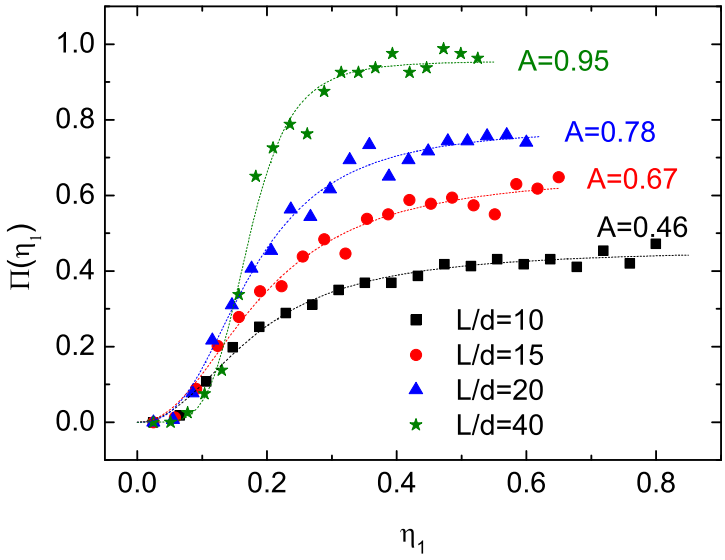

Figure 6.5: Spanning probability as a function of η_1 for a few values of the system linear size L/d and for penetrable conducting particles ($\sigma_1 = 0$), $\sigma_2/d = 6$ and $\phi_2 = 0.936$. The asymptotic values A of $\Pi(\eta_1)$ and the fits to equation 6.1 (dotted lines) are also shown.

6.3.2 Simulation parameters and correlation length exponent

Let us start here with the case of penetrable conducting particles, with $\sigma_1 = 0$ and $d = 1$. We extracted $\eta_1^c(\sigma_2, \phi_2)$, for each value of σ_2 and ϕ_2, from 8 different system sizes. For each size, 20 different concentrations η_1 were typically used to fit the spanning probability $\Pi(\eta_1, L)$. We considered here four different values of the insulating particles diameter, ranging from $\sigma_2/d = 2$ to $\sigma_2/d = 11$. As, in order to obtain satisfactory statistics, L has to be larger than σ_2, the system sizes considered depended on σ_2. Moreover, as seen in the preceding section, small system sizes with large ϕ_2 also become difficult to treat, so that the system sizes chosen also depended on the insulating sphere volume fraction. Finally the system size L and the number of realizations N_s ranged from $L/d = 10$ with $N_s = 1500$ to $L/d = 30$ with $N_s = 50$ for $\sigma_2/d = 2$ and from $L/d = 17.5$ ($N_s = 700$) to $L/d = 60$ ($N_s = 50$) for $\sigma_2/d = 11$.

Examples of the spanning probabilities and their fits to equation 6.1 have been shown in figure 6.5. We show in figure 6.6 the correlation length exponents, extracted from the widths of the spanning probabilities using equations 6.3, 6.4 and 6.5. The values obtained for small ϕ_2 are in reason-

able accord with the admitted value $\nu = 0.88$ [108], shown in the figure as the black dashed line, though in mean a little too high. For large ϕ_2 the scatter and the errors become more important and the values of ν seem to increase, mostly for large σ_2/d. Considering that no finite size corrections were applied to equation 6.3, this is probably due to finite size effects, being more important for large ϕ_2 and σ_2/d. We tried to verify this by adding a correction term for the finite size to equation 6.3, giving

$$\Delta(L) = BL^{-1/\nu}\left(1 + \frac{b}{L^c}\right). \tag{6.6}$$

It was usually not possible to obtain a fit when leaving all parameters of equation 6.6 free, so that we fixed the value of the exponent $c = 1$. With this we could obtain fits for almost all cases studied, leading to lower ν-values. For the cases of figure 6.6 where we had obtained too large ν-values, we obtained values in accord with $\nu = 0.88$, though with quite large error bars. For the rest of the cases, the tendency was to obtain values of ν in accord or below $\nu = 0.88$. This might be due to the correction with $c = 1$ being too important in those cases. We cannot draw a final conclusion here, but I nevertheless think that the discrepancies between our extracted values for ν and the admitted $\nu = 0.88$ stem from finite size effects and insufficient number of points to obtain a good fit of equation 6.6 with the finite size corrections.

Now let us turn to the case of segregated systems with conducting particles having a hard core diameter $\sigma_1 \neq 0$. We considered here larger system sizes than for the penetrable case. It ranged from $L/\sigma_1 = 16$ with $N_s = 1500$ realizations to $L/\sigma_1 = 60$ ($N_s = 100$) for $\sigma_2/\sigma_1 = 1$ and from $L/\sigma_1 = 60$ ($N_s = 200$) to $L/\sigma_1 = 140$ ($N_s = 100$) for $\sigma_2/\sigma_1 = 12$. The calculated ν values were very similar to those presented in figure 6.6, and are not shown here.

6.4 Critical concentration

Let us now come to the study of the critical concentrations in segregated systems. Typical spanning probability results are reported in Fig. 6.7, where we plot $\Pi(\eta_1, L)$ for $\sigma_2/\sigma_1 = 4$, $d = \sigma_1$, and for two values of ϕ_2 with few different system sizes. As it is clear from the figure, compared to the homogeneous case $\phi_2 = 0$, the spanning probability transition for $\phi_2 \neq 0$ gets shifted to lower values of η_1, indicating that the percolation threshold is reduced by segregation. This is confirmed by the scaling analysis described above, which gives $\eta_1^c = 0.3203 \pm 0.0003$ for $\phi_2 = 0$, which is in very good accord with Ref. [39, 72], and $\eta_1^c = 0.1821 \pm 0.0004$ for $\phi_2 = 0.65$.

Although the reduction of η_1^c shown in Fig. 6.7 has to be expected on the basis of reduced available volume arguments, we find that, actually, this

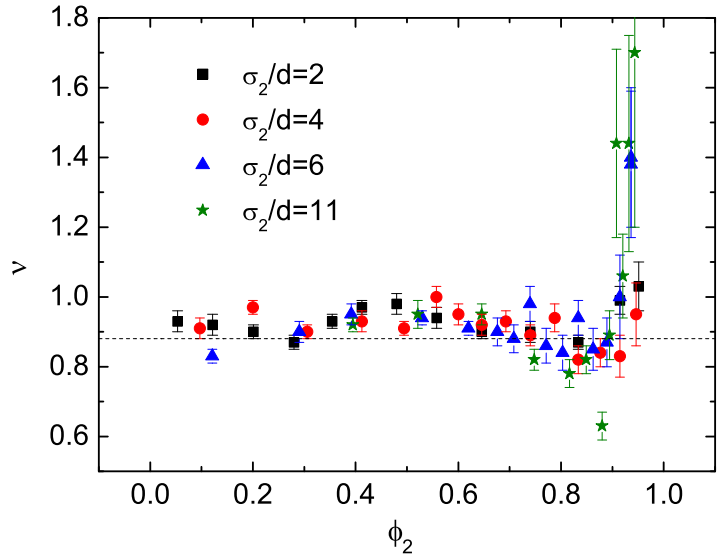

Figure 6.6: Collection of correlation length exponents obtained from the width of the percolation transitions, as described in the text. Here we consider the case $\sigma_1 = 0$ and $d = 1$, for four different σ_2/σ_1 and several volume fractions ϕ_2. The admitted value $\nu = 0.88$ is shown as a black dashed line.

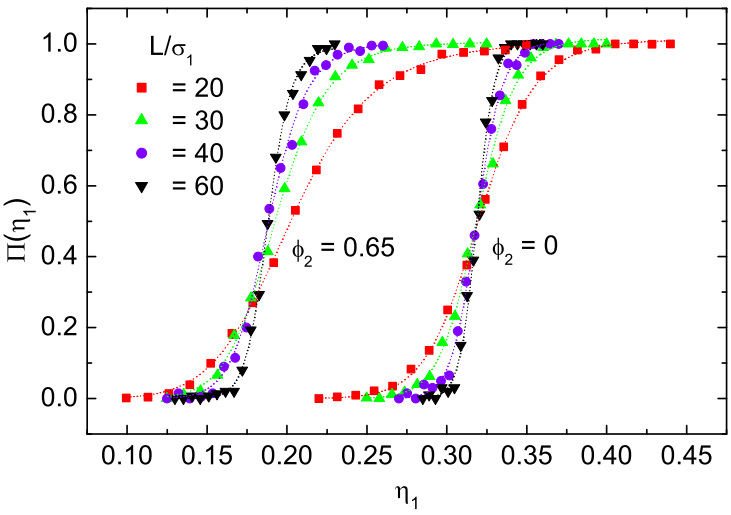

Figure 6.7: Spanning probability as a function of η_1 for few values of the system linear size L/σ_1 and for two different values of insulating phase volume fraction ϕ_2. The penetrability length is $d = \sigma_1$ and $\sigma_2/\sigma_1 = 4$.

is not always the case, and that η_1^c is generally a non-monotonic function of ϕ_2 for fixed σ_2/σ_1 (for $\sigma_1 \neq 0$), or σ_2/d (for $\sigma_1 = 0$). This is first shown for fully penetrable conducting particles in figure 6.8(a), where η_1^c is plotted for different values of σ_2/d and ϕ_2. For partially impenetrable particles, this is shown in Fig. 6.9(a) where η_1^c is plotted as a function of ϕ_2 for $d = \sigma_1$ and for several values of σ_2/σ_1, and in Fig. 6.9(b) where $\sigma_2/\sigma_1 = 4$ and d is varied. For all cases studied, on enhancing ϕ_2 from the homogeneous case $\phi_2 = 0$, the behaviour of the percolation threshold is characterized by an initial linear decrease of η_1^c, followed by a minimum at a particular value of ϕ_2 which depends upon σ_2, σ_1 and d, and a final increase well before maximum segregation is reached at ϕ_2^*. Lower bounds of ϕ_2^* are plotted in figures 6.8 and 6.9 by vertical dashed lines. For the case of penetrable conducting particles, as just the center of the conducting particles is forbidden to penetrate the insulating spheres, it is clear that a good estimate for ϕ_2^* is obtained when the voids left over between the insulating spheres just percolate. This is known as the void percolation threshold and is given by $\eta_1 = \phi^c_{\text{void}} \simeq 0.03$ [109,110] and $\phi_2^* = 1 - \phi^c_{\text{void}} \simeq 0.97$. Now a lower bound for ϕ_2^* can also be obtained for semi permeable conducting particles ($\sigma_1 \neq 0$). In that case we have to consider, not the volume left over by the insulating spheres, but the volume available for arranging the centers of the conducting ones, $\phi_{\text{avail.}}$. This volume can be easily obtained by noticing that $\phi_{\text{avail.}} = \exp(-v_{\text{excl.}}\rho_2)$, where $v_{\text{excl.}} = \pi(\sigma_2 + \sigma_1)^3/6$ is the excluded volume of an insulating sphere (volume from which the centers of the conducting particles are excluded), and by using the definition of ϕ_2 given above, so that we obtain

$$\phi_{\text{avail.}} = (1 - \phi_2)^{(1+\sigma_1/\sigma_2)^3}. \tag{6.7}$$

Now the lower bound ϕ_2^* is obtained by requiring that $\phi_{\text{avail.}}$ coincides with ϕ^c_{void}, so that the volume available to the centers of the conducting particles, with hard-core diameter σ_1, barely percolates through the system.

For completely penetrable conducting particles and $d/\sigma_2 \to \infty$, the conducting phase can be considered as continuum. We therefore expect that η_1^c will decrease linearly in the whole range of possible ϕ_2, and tend to $\eta_1^c = \phi^c_{\text{void}}$ as $\phi_2 \to \phi_2^*$. This limiting case is shown in the figure 6.8 as an open circle, and we see that η_1^c seems to tend to this limit for $d/\sigma_2 \to 0$ and $\phi_2 \to \phi_2^*$ as expected.

As shown in Figs. 6.8(a) and 6.9(a), the slope of the initial decrease of η_1^c is steeper for larger σ_2/d, respectively σ_2/σ_1, and the position of the minimum gets shifted to higher values of ϕ_2. A similar effect is found by decreasing the penetrable shell thickness d for fixed σ_2/σ_1, Fig. 6.9(b), leading to infer that for $d/\sigma_2 \to 0$ the minimum disappears and η_1^c decreases monotonically all the way up to ϕ_2^* for all cases. These features, and in particular the appearance of a minimum (i.e. optimal) value of the percolation threshold for finite penetrable shells, represent the main finding of this section and

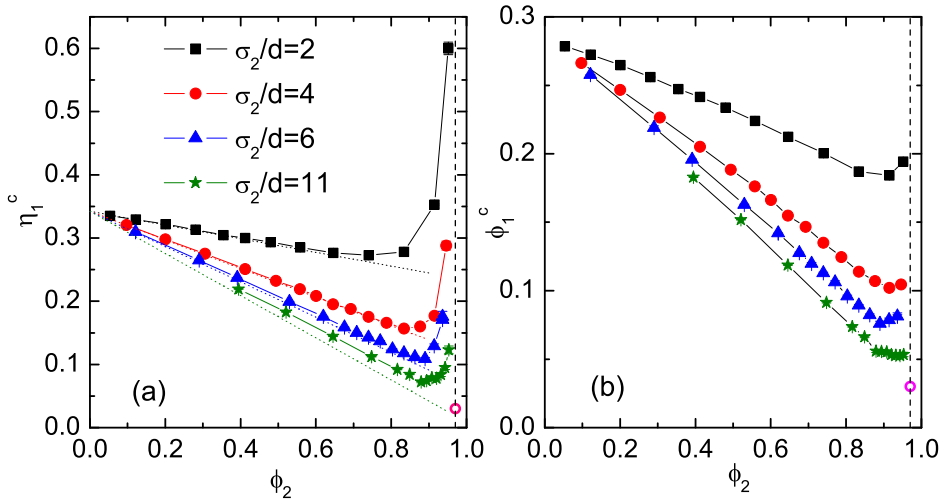

Figure 6.8: Percolation threshold values η_1^c (a), or ϕ_1^c (b), as a function of the volume fraction ϕ_2 of the insulating spheres for $d = 1$, $\sigma_1 = 0$ and several value of σ_2/d. The dotted lines are from Eq. (6.9) and the empty circle is the limiting case $(1-\phi^c_{\rm void};\, \phi^c_{\rm void})$, corresponding to the maximally segregated system with $d/\sigma_2 = 0$, where $\phi^c_{\rm void}$ is the void percolation threshold. The vertical dashed line corresponds to the maximal segregation possible $\phi_2^* = 1 - \phi^c_{\rm void}$.

provide a previously unnoticed scenario for segregated percolation [94].

Let us discuss now the physical origin of the non-monotonic behaviour of the percolation threshold. The initial decrease of η_1^c can be fairly well reproduced by assuming that, for low values of ϕ_2, the volume fraction ϕ_1^c of the composite conducting particles (hard-core plus penetrable shell) is reduced by the volume occupied by the insulating spheres. The assumption here is that the conducting phase will percolate if we have the critical concentration for a homogeneous system ($\phi_1^c(\phi_2 = 0)$) in the volume left over by the insulating phase. This is obviously the case if σ_2 is very large compared to d and σ_1, but not necessarily for smaller σ_2. Indeed, since the penetrable shells of the conducting particles may actually overlap the insulating spheres, the latter may be treated as having effectively a smaller volume, $v_{\rm eff} \leq v_2$, leading to

$$\phi_1^c(\phi_2) \simeq \phi_1^c(0)(1 - \phi_2 v_{\rm eff}/v_2). \tag{6.8}$$

Taking into account that insulating particles with $\sigma_2 \lesssim a$, where a is the mean distance between the closest surfaces of nearest neighbour conducting particles, should be ineffective in reducing ϕ_1^c, we approximate $v_{\rm eff}$ by a sphere of diameter $\sigma_2 - a$. Finally, by expanding $\phi_1^c(\phi_2)$ in powers of $\eta_1^c(\phi_2) -$

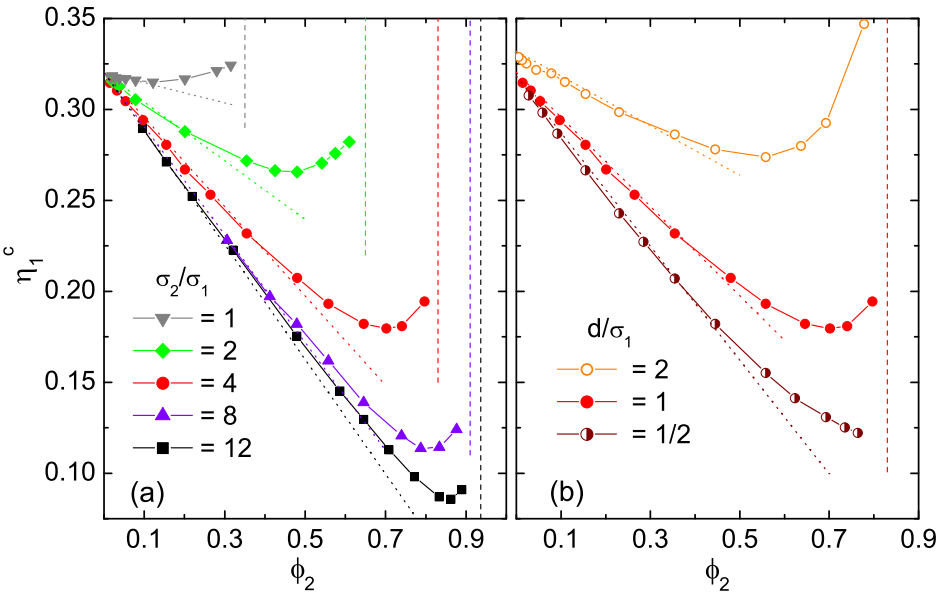

Figure 6.9: Percolation threshold values η_1^c as a function of the volume fraction ϕ_2 of the insulating spheres for (a) $d = \sigma_1$ and several value of σ_2/σ_1 and (b) $\sigma_2/\sigma_1 = 4$ and few values of d. The vertical dashed lines are lower bounds of the maximum segregation obtained from Eq. (6.7), while the dotted lines are from Eq. (6.9).

$\eta_1^c(0)$, at the lowest order in ϕ_2 we find

$$\eta_1^c(\phi_2) \simeq \eta_1^c(0) - \frac{\phi_1^c(0)}{\phi_1^c(0)'} \left(\frac{\sigma_2 - a}{\sigma_2}\right)^3 \phi_2, \tag{6.9}$$

where $\phi_1^c(0)' = \lim_{\phi_2 \to 0} d\phi_1^c(\phi_2)/d\eta_1$ and can be obtained from [95, 111]:

$$\phi_1(0) = 1 - (1 - \eta_1\lambda^3) \exp\left[-\frac{(1-\lambda^3\eta_1)}{(1-\eta_1\lambda^3)^3}\right] A(\eta_1, \lambda) \tag{6.10}$$

where

$$\begin{aligned} A(\eta_1, \lambda) \quad = \quad & \exp\left\{-\frac{{\eta_1}^2\lambda^3(\lambda-1)}{2(1-\eta_1\lambda^3)^3}\Big[(7\lambda^2+7\lambda-2)\right. \\ & \left. -2\eta_1\lambda^3(7\lambda^2-5\lambda+1) + {\eta_1}^2\lambda^6(5\lambda^2-7\lambda+2)\Big]\right\}. \end{aligned} \tag{6.11}$$

As it is seen in panel (a) of figure 6.8 and in figure 6.9, where Eq. (6.9) (dotted lines) is plotted by using $a = (\sigma_1 + d)/2\eta_1^c(0)^{1/3} - \sigma_1$ [72], the low ϕ_2 behaviour of η_1^c is rather well reproduced by equation 6.9 for all cases considered.

Now the more unexpected and interesting result of figures 6.8 and 6.9 is the non-monotonic behaviour η_1^c, presenting a minimum and an increase

as $\phi_2 \to \phi_2^*$. First of all, we verify that this increase is not simply an effect of our choice of using η_1 as concentration variable, which takes into account the overlaps between conducting particles, and can therefore diverge in the completely penetrable case, whereas ϕ_1 represents the volume fraction occupied by the composite particles, therefore remaining bounded between 0 and 1. We replot the results of figure 6.8(a) in figure 6.8(b), but using the volume fraction ϕ_1^c instead of η_1^c. ϕ_1^c was obtained here from the simulations by simply dividing the system in small cubes and counting the fraction of cubes having their center inside the diameter d of any conducting particle. We see from this figure that, though less pronounced, the minimum is still present when considering the volume fraction ϕ_1. Moreover, for the $\sigma_1 \neq 0$ case, using η_1 or x is identical for a same d, as $x = \lambda^3 \eta_1$. Therefore, panel (a) of figure 6.9 would look the same if x_c was plotted instead of η_1, except that the y-axis would be rescaled by a factor 1/8. But as x can be directly interpreted as the volume fraction of conducting particles in a real composite, it is clear that this minimum is not an artefact, but that it has a physical origin.

This behaviour can be understood by taking a closer look at the structure of the system. Actually, as it is shown in Fig. 6.4 where the colour map defines the connectivity number (degree) k, *i.e.* the number of conducting particles directly connected to a given one, for each particle in the percolating cluster, the microstructure of the system strongly changes with segregation. In the homogeneous case (Fig. 6.4(a)), mostly all particles have between 1 and 4 neighbours and the cluster seems quite compact, whereas in the highly segregated regime of Fig. 6.4(b), clusters of highly connected particles (k large) are bound together by "chains" of particles having low k values. This change can be better appreciated in figure 6.10(a), where the distribution function of the connectivity number, $P(k)$, is shown for $\sigma_2/\sigma_1 = 12$ and for different ϕ_2. We see in this figure that $P(k)$, which is a rather narrow distribution for the homogeneous case, peaked around the mean value $\langle k \rangle \simeq 2.25$ [39, 81], broadens with segregation, with its maximum shifting towards higher k-values. In the highly segregated regime, with $\phi_2 = 0.89$, corresponding to the structure presented in figure 6.4(b), the mean degree is as high as $\langle k \rangle \simeq 7.75$ and there are particles with $k > 15$, in strong contrast with the homogeneous case.

Now, by construction, the above argument (Eq. (6.9)) to explain the linear decrease of η_1^c, neglects possible effects of $\phi_2 \neq 0$ on the connectivity number k. The change observed in the distribution of k values is due to the fact that, in the vicinity of ϕ_2^*, the structure of the void space available for arranging the centers of the conducting particles is characterized by many narrow (quasi-one dimensional) necks connecting more extended void regions [25]. Percolation is possible only if such necks are populated by connected conducting particles, and since for $\phi_2 \to \phi_2^*$ the necks become narrower, and so have less probability of being populated, more particles

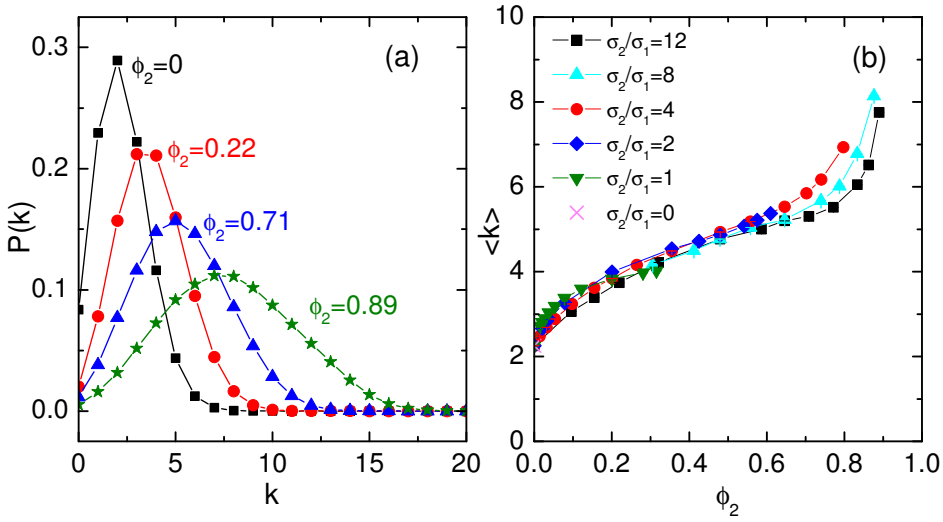

Figure 6.10: (a) Distribution function $P(k)$ of the degree k of the particles in the percolating cluster for $\sigma_2/\sigma_1 = 12$, $d = \sigma_1$ and for different ϕ_2. (b) Mean connectivity number $\langle k \rangle$ as a function of ϕ_2, for the same cases of Fig. 6.9(a).

are needed to ensure connectivity, thereby "overcrowding" the many void regions between the necks. The net effect of such mechanism, not captured by Eq. (6.9), is the enhancement of η_1^c as $\phi_2 \to \phi_2^*$. This is demonstrated in Fig. 6.10(b), where $\langle k \rangle$, plotted for the same cases of Fig. 6.9(a), displays a sudden enhancement (more marked for σ_2/σ_1 larger) at values of ϕ_2 corresponding to the points of upturn of η_1^c of Fig. 6.9(a). The competition between the effect of reduced available volume, which lowers η_1^c [Eq. (6.9)], and the enhanced connectivity at high segregation, which increases η_1^c, is therefore at the origin of the minimum percolation threshold observed by us [94].

6.4.1 Discussion

Let us now discuss the possibility of observing the features presented here in real segregated materials. The central point here is that the minimum vanishes if $d \ll \sigma_1$ and if $\sigma_2 \gg \sigma_1$, so that it is interesting to assess in what compound this could be observed. In conductor-insulator composites where transport is driven by tunnelling, d represents the maximum tunnelling distance between the conducting particles. A realistic estimate of d can be obtained by comparing the tunnelling conductivity with the intrinsic conductivity of the matrix, so that the tunnelling will be effective only if it gives higher conductivity than the cylinder of matrix between the two adjacent particles, so that, using equation (5.24) for the tunnel conductivity, d can be

extracted from

$$\frac{2d}{\xi} \simeq \ln\left(\frac{g_0 d}{\Sigma_2 {\sigma_1}^2}\right), \tag{6.12}$$

where Σ_2 is the conductivity of the matrix and g_0 the prefactor of the tunnelling conductivity. Typically the insulating matrix has a conductivity of around 10^{-15} to 10^{-17} Sm^{-1}, the tunnelling factor is around $\xi = 2$ nm and g_0 is around 0.01 S [112]. For conducting particles with $\sigma_1 = 50$ nm, we obtain $d \simeq 20$ nm. Because of the logarithmic dependencies of the above equation, d is not very sensitive to the precise values used for the different parameters and is always found to be of the order of $d \simeq 10\xi$. For such values of d, the results of Fig. 6.9 would therefore apply to nano-composites with $\sigma_1 \approx d = 20$ nm and σ_2 not exceeding a few hundreds of nanometers. Model conducting films with particles with even smaller diameters (4 nm diameter) and typical inter-particle distances of the order of the nanometer were prepared and studied for example in Ref. [113]. Now in RuO_2-glass composites, much larger values of d are possible, where a reactive layer of thickness 0.2-0.4 μm (or even more) surrounding the RuO_2 particles presents modified chemical and structural properties [114], most probably favouring hopping processes [115]. In this case, the parameters used in our work would easily account for composites with σ_1 in the range 50-500 nm and σ_2 of few microns, so that this minimum should be experimentally observable, even in TFRs.

6.5 Electrical transport in the segregated TP model

We now turn to the last part of this work: the study of the conductivity in the segregated tunnelling-percolation model. For this study we considered only the $d/\sigma_1 = 1$ case, three different insulating particle diameters $\sigma_2/\sigma_1 = 1$, 4 and 12, four different tunnelling factors $\xi/\sigma_1 = 1$, 0.16, 0.12 and 0.08 and several values of the insulating phase volume fraction ϕ_2. The system sizes considered were $L/\sigma_1 = 60$ for $\sigma_2/\sigma_1 = 1$ and 4 and $L = 80$ for $\sigma_2/\sigma_1 = 12$. The range of $x - x_c$ values that can be studied depends largely on the volume available to the conducting phase, $\phi_{\text{avail.}}$ defined in equation 6.7. To have comparable results for all cases studied, we fixed the range of $(x - x_c)/x_c$ values to the interval $[0, 0.3]$, so that, for large σ_2 and ϕ_2, as x_c becomes very small, the interval of x studied is very narrow.

If we first look at the case $\sigma_2/\sigma_1 = 1$, shown in figure 6.11 for $\xi/\sigma_1 = 0.12$, we see that the presence of the insulating spheres has almost no effect in that case. The conductivity Σ, shown in panel (a) as a function of x, is almost independent of the volume fraction ϕ_2 of insulating spheres. As the

percolation threshold x_c also depends only very weakly on ϕ_2, the curves for the conductivity superpose when plotted as a function of x. In panel (b) we show $\widehat{\Sigma}(x) = \Sigma(x) - \Sigma(x_c)$, a quantity used to minimize the finite size effects leading to a non-zero conductivity at the percolation threshold, as a function of $x - x_c$. We see that again all our results for different volume fractions ϕ_2 fall on a single curve. This is shown here only for the $\xi/\sigma_1 = 0.12$ case, but is also true for the other cases studied. This result is not very surprising as the insulating particles are of approximately the same size as the mean nearest neighbour distance, so that the presence of the insulating phase has no real effect on the system.

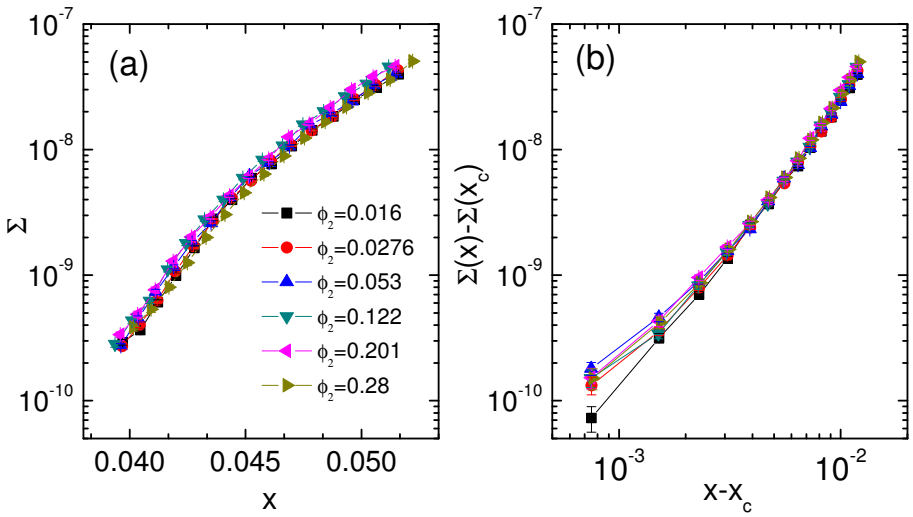

Figure 6.11: Conductivity of a segregated system with $\sigma_2/\sigma_1 = 1$ and $\xi/\sigma_1 = 0.12$. In panel (a) Σ is shown as a function of x and in panel (b), $\Sigma(x) - \Sigma(x_c)$ is shown as a function of $x - x_c$

Now if we turn to the case $\sigma_2/\sigma_1 = 4$, shown in figure 6.12, we see from panel (a) that, as expected from our above results for the critical concentration, increasing ϕ_2 allows to obtain conducting systems with lower concentrations x, until optimal segregation is reached, then further increasing ϕ_2 shifts x_c back to higher values. Here, due to segregation, the conductivities of the systems with different ϕ_2 of course do not fall on a single curve. But when we look at $\widehat{\Sigma}(x)$ as a function of $x - x_c$, as shown in panel (b) of this figure, we see that the conductivities nicely collapse on a single master curve. The same results are obtained for the $\sigma_2/\sigma_1 = 12$ case. Unfortunately, for smaller ξ this is not the case anymore. We show in figure 6.13(a) $\widehat{\Sigma}(x)$ as a function of $x - x_c$, still for $\sigma_2/\sigma_1 = 4$, but this time for $\xi = 0.12$. It is clear from that figure that $\widehat{\Sigma}(x)$ seem to have the same behaviour, regardless of ϕ_2, but that they are shifted by a multiplicative constant. We therefore

further normalize this data, using this time $[\Sigma(x) - \Sigma(x_c)]/\Sigma(x_c)$ and plot it as a function of $x - x_c$ in panel (b) of figure 6.13, obtaining again a collapse of our numerical simulation data on a single curve. The same results are obtained for $\xi/\sigma_1 = 0.08$ and for $\sigma_2/\sigma_1 = 12$. The fact that the curves collapse for the different values of ϕ_2 means that segregation, does not basically alter the behaviour of the conductivity of the system, which gets only shifted to lower x values and multiplied by a constant value, depending on ξ/σ_1, σ_2 and ϕ_2. This is an important result, as it will allow us to basically map the segregated system on the non-segregated one, and use the analytical expression obtained for the conductivity in chapter 5, provided that we can obtain an expression for the multiplicative constant. This will be tackled later in this section, but let us first look at the transport exponent of the segregated systems.

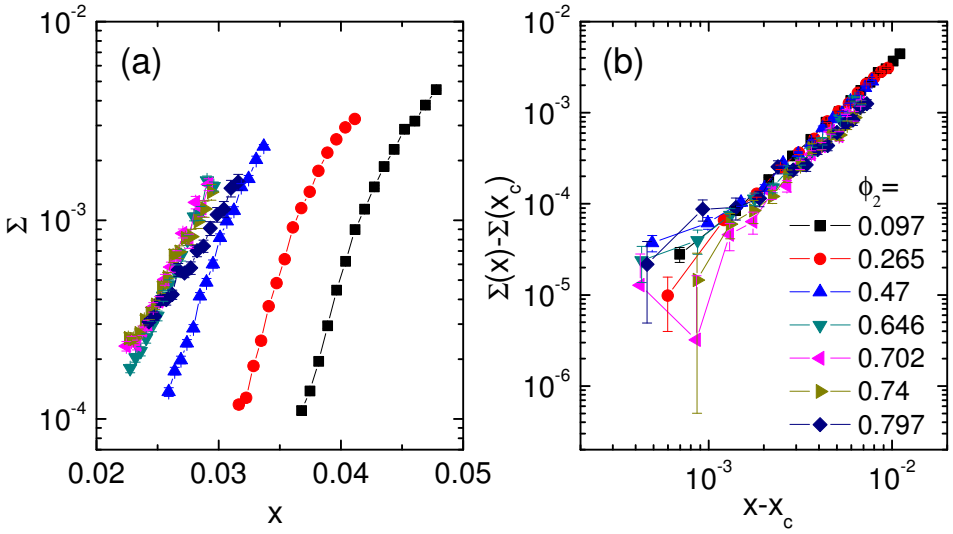

Figure 6.12: Conductivity of a segregated system with $\sigma_2/\sigma_1 = 4$ and $\xi/\sigma_1 = 1$. In panel (a) Σ is shown as a function of x and in panel (b), $\Sigma(x) - \Sigma(x_c)$ is shown as a function of $x - x_c$

We obtained the transport exponent by fitting $\widehat{\Sigma}(x)$ with a simple power law, as follows:

$$\widehat{\Sigma}(x) = \Sigma_0(x - x_c)^t. \tag{6.13}$$

We show in figure 6.14 the transport exponents we obtained for $\sigma_2/\sigma_1 = 12$ and different values of ξ/σ_1 and ϕ_2. For large ϕ_2 it is sometimes not possible to obtain a best fit to equation 6.13, or the obtained transport exponent has very large error bars. This is due, as mentioned in the beginning of this section, to the fact that the interval of x values studied becomes very narrow

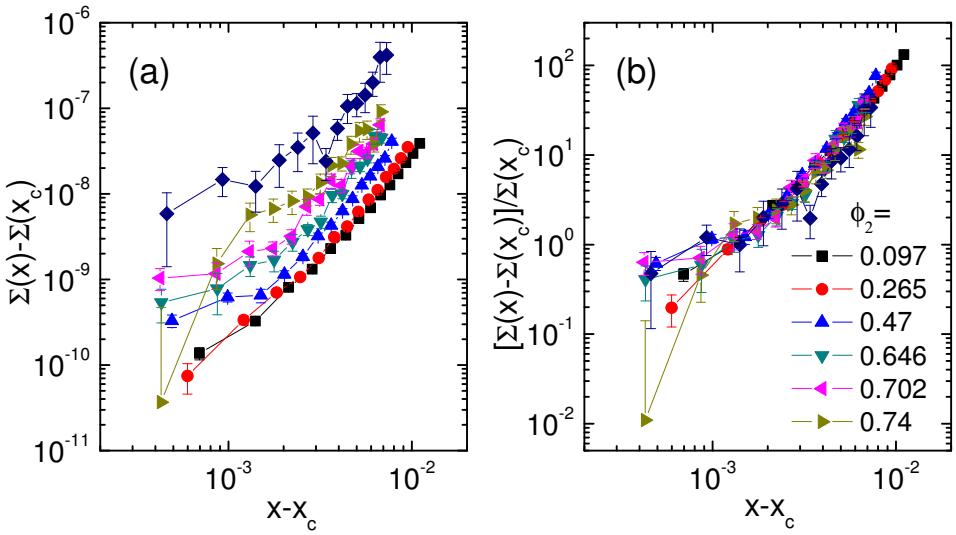

Figure 6.13: Conductivity of a segregated system with $\sigma_2/\sigma_1 = 4$ and $\xi/\sigma_1 = 0.12$. In panel (a) $\Sigma(x) - \Sigma(x_c)$ and in panel (b) $\big[\Sigma(x) - \Sigma(x_c)\big]/\Sigma(x_c)$ are shown as a function of $x - x_c$

for very segregated systems. Despite this, the transport exponent seems to increase a little with increasing ϕ_2 before falling to the universal transport exponent as the the maximal segregation is reached. This can be qualitatively understood, as at the maximal segregation, the conducting phase is already densely packed at the percolation threshold, so that the mean nearest neighbour distance a is small already at the percolation threshold. And as apparent non-universality is driven by the factor $2a/\xi$, a small a tends to drive the system towards universality. The same behaviour was obtained for $\sigma_2/\sigma_1 = 4$, whereas for $\sigma_2/\sigma_1 = 1$ the transport exponent seems quite unsensitive to segregation.

6.5.1 Discussion

As we have seen above, for small ξ/σ_1, which is the situation of interest to us, the conductivity $\widehat{\Sigma}$ of the segregated system, coincides with that of the non segregated one for a same $x - x_c$, only if it is normalized by $\Sigma(x_c)$. In order to be able to map the results of the segregated case on the non segregated ones, it is therefore important to obtain an expression for $\Sigma(x_c)$. Making use of our analytical result obtained for the conductivity with small ξ/σ_1 for non-segregated systems (Eq. (5.42)), we can write for the conductivity of a system of finite size L at the percolation threshold:

$$\Sigma(x_c, \xi, L) = \Sigma(x_c, \infty, L) e^{-4(a_c - \sigma_1)/\xi}, \tag{6.14}$$

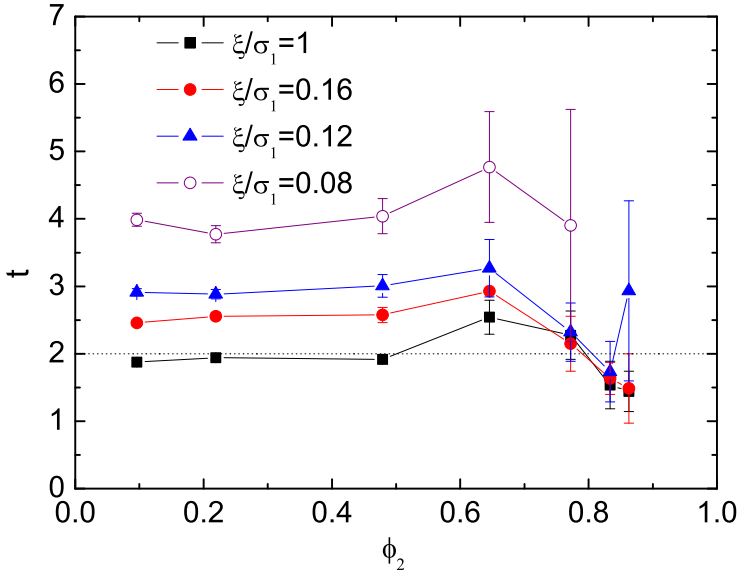

Figure 6.14: Critical transport exponents for $\sigma_2/\sigma_1 = 12$ and for different ϕ_2 and ξ/σ_1 obtained as explained in the text.

where a_c is the mean nearest neighbour distance at the percolation threshold, and $\Sigma(x_c, \infty, L)$ is the conductivity at the percolation threshold of a non-segregated system, with $\sigma_1/\xi = 0$. Now we make the assumption that, for a segregated system, only the mean nearest neighbour distance at the percolation threshold changes compared to the homogeneous case (apart from the shift introduced in the percolation threshold), so that, if a_c' is the mean nearest neighbour distance in the segregated system and a_c that in the non-segregated one, and using Eq. (6.14), we obtain

$$\Sigma(x_c^s, \xi, \phi_2, L) = \Sigma(x_c, \xi, 0, L) e^{-4(a_c' - a_c)/\xi}, \tag{6.15}$$

where $\Sigma(x_c^s, \xi, \phi_2, L)$ is the conductivity of the segregated system at its percolation threshold x_c^s (whereas x_c is the percolation threshold of the non-segregated one). The problem reduces now to finding an expression for a_c'. Similarly to the approach used to evaluate the percolation threshold of segregated systems, we consider here that the conducting phase is restricted by the segregation to occupy a smaller volume, limited by the presence of the insulating spheres, with effective volume v_{eff}. As in section 6.4, this effective volume is approximated by a sphere of reduced diameter $\sigma_2 - a_c$. Under these assumptions, the effective volume available, ϕ_{eff}, which is obtained similarly

to equation 6.7, yields

$$\phi_{\text{eff}} = (1 - \phi_2)^{\left[(\sigma_2 - a_c)/\sigma_2\right]^3}, \tag{6.16}$$

with a_c given by the mean nearest neighbour distance of a homogeneous system at the percolation threshold, $a_c = 0.4816$ for $\sigma_1/d = 1$. Now in the space available to the conducting phase, its concentration can be estimated by $x_c' = x_c^s/\phi_{\text{eff}}$. Finally the mean nearest neighbour distance a_c' of the segregated system can be obtained from numerical integration of $a_c' = \int dr\, r P(x_c', r)$, where $P(x_c', r)$ is the distribution function for the distance between two neighbouring impenetrable spheres at concentration x_c' as given in Ref. [28] (for a homogeneous system).

This estimate is compared to our Monte Carlo results in figure 6.15, where we compare $\Sigma(x_c^s, \xi, \phi_2, L)$, the conductivity at the percolation threshold obtained from Monte Carlo simulations, with the right-hand side of equation 6.15. This is done for $\sigma_2/\sigma_1 = 12$ and different values of ξ/σ_1. This estimation, though not perfect, is in relatively good agreement with our simulation data and allows us to map the conductivity of segregated systems directly on that of non-segregated ones, using equation 6.15.

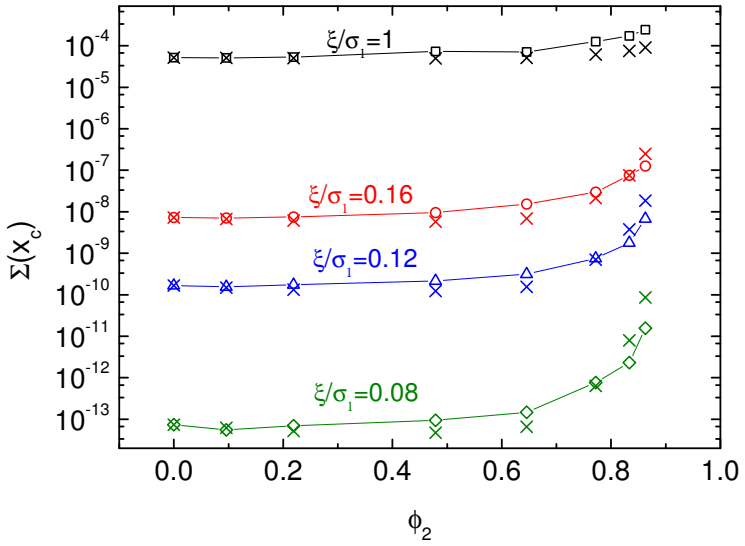

Figure 6.15: Comparison of the Monte Carlo results for $\Sigma(x_c)$ as a function of ϕ_2, shown as empty symbols, and the analytical expression of equation 6.14 shown as crosses, for $\sigma_2/\sigma_1 = 12$ and different ξ/σ_1

Now if we work with the normalized conductivity

$$\widetilde{\Sigma}(x - x_c^s + x_c, \xi, \phi_2) = \Sigma(x, \xi, \phi_2) e^{4(a_c' - a_c)/\xi} \tag{6.17}$$

where x_c^s is the percolation threshold of the segregated system and x_c that of the homogeneous one, we can directly use all our analysis of the non-segregated system, so that we can rewrite equation 5.38 but for the segregated system:

$$\ln\left(\frac{\widetilde{\Sigma}(x,\xi,\phi_2)}{G(x,\infty,0)}\right)\frac{1}{\ln(y)}\frac{\xi}{2(a-\sigma_1)} = \Big(t(x)-t_0\Big)\frac{\xi}{2(a-\sigma_1)} = f(y), \quad (6.18)$$

where $y = (x^2 - x_c^2)/x_c^2$. We can now take the logarithm of this expression

$$\ln\left[\Big(t(x)-t_0\Big)\frac{\xi}{2(a-\sigma_1)}\right] = \ln(f_0) - b\ln\left[\ln\left(\frac{1}{y}\right)\right]. \quad (6.19)$$

which is tested in figure 6.16. We compare in that figure, a non segregated case (black squares) with a few segregated cases with different σ_2/σ_1, ϕ_2 and ξ. We see that, as expected from the normalization of the conductivities, all results nicely fall on the same curve as for the homogeneous case. Panel (a) shows the results for Σ normalized using $\Sigma(x_c^s)$ obtained from the Monte Carlo simulations, whereas panel (b) shows the same results but using the approximate normalization given by the estimate of equation 6.17. Using the $\widetilde{\Sigma}$, as in panel (b), leads to slightly less good agreement between the segregated and non segregated cases, though it remains very good overall.

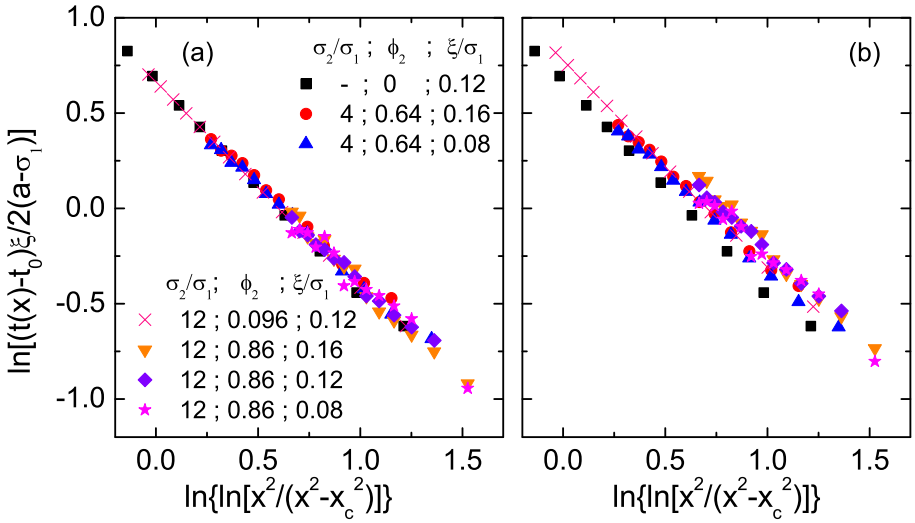

Figure 6.16: Plot of the Monte Carlo results for the conductivity Σ, plotted as explained in the text, following equation 6.19, for a non-segregated system and segregated ones with different ξ/σ_1, σ_2/σ_1 and ϕ_2. In panel (a) Σ was normalized using $\Sigma(x_c)$ whereas in panel (b) using the estimate of equation 6.17.

6.5.2 Comparison with experimental results

As shown in figure 6.16, the conductivity of the segregated systems, if normalized properly, has the same behaviour of the conductivity for the homogeneous case. Therefore $f(y)$ of equation 6.19 is also expected to tend towards $f(y) = 2/\ln(1/y)$, as was assessed for the homogeneous case from figure 5.14, so that we can rewrite the conductivity of the segregated system as

$$\Sigma(x, \xi, \phi_2) = \Sigma_0 e^{-\frac{4(a-\sigma_1)}{\xi}} \left(\frac{\hat{x}^2 - x_c^2}{\hat{x}^2} \right)^2, \tag{6.20}$$

where $\hat{x} = x - x_c^s + x_c$ is the shifted concentration. In this equation, the multiplicative constant we had introduced above to normalize the conductivity has been absorbed in Σ_0. a can be obtained from equation 5.45 which reads

$$a/\sigma_1 = 1 + \frac{(1-\hat{x})^3}{12\hat{x}(2-\hat{x})}. \tag{6.21}$$

The use of the relatively high density approximation for a given above is justified by the relatively high values expected for x_c, so that $\hat{x}$ should not be too small. As already mentioned, this approximation is satisfactory for values of $\hat{x} \gtrsim 0.15$, which will be the case in all experimental data analysed hereafter. Using equation 6.21, equation 6.20 can be fitted to experimental results with only four free parameters: Σ_0, x_c^s, x_c and ξ, as σ_1 can be experimentally measured. We show in figures 6.17, 6.18 and 6.19 some experimental measurements of the conductivity of TFRs, with a comparison of the fits to the classical power law (Eq. (5.44)) shown in panels (a) and to the above expression (6.20) shown in panels (b). Those experimental results are from the same series of TFRs as presented in section 3.3. For figure 6.17 and 6.18, RuO_2 particles with 40 nm average grain size were used, whereas the results of figure 6.19 stem from TFRs made with 400 nm average RuO_2 grain size. The firing temperature was 600°C for the TFRs of first figure and 625°C for the other two. We see that the fit to the classical power law leads to a non-universal transport exponent in all three cases, with $t = 6.5 \pm 0.2$, $t = 4.9 \pm 0.1$ and $t = 6.1 \pm 0.1$ respectively. On the other hand the fits to equation 6.20 are as good, and maybe even better for the measurements of figure 6.17, and present values of ξ in very good agreement with what is expected, namely of the order of the nanometer. Indeed we obtain respectively $\xi = 1.7 \pm 0.5$ nm, $\xi = 2.7 \pm 0.5$ nm and $\xi = 1.4 \pm 0.4$ nm. Now regarding the values of x_c extracted from those fits, we can recall here that, as discussed in section 6.4.1, we expect $d \simeq 10\xi$, which, by using $\xi = 1$ nm would lead $\lambda = \sigma_1/(\sigma_1 + d) \simeq 0.8$ for the 40 nm RuO_2 particles and $\lambda = 0.975$ for the 400 nm case. The critical concentration can then be estimated from figure 5.7 and by recalling that $x = \lambda^3\eta$. We obtain respectively $x_c \simeq 0.17$ and $x_c \simeq 0.59$ for the 40 and 400 nm cases. We can now compare those values

with the ones extracted from the fits. We obtained $x_c = 0.24$ and $x_c = 0.15$ for the 40 nm grain size and $x_c = 0.71$ for the 400 nm case. Again the values obtained from the fits are in fairly good agreement with the theoretical expectations, supporting the interpretation of the conductivity data given by equation 6.20, and the scenario of non-universality being only induced by the fit to the power law for values of x outside the critical region.

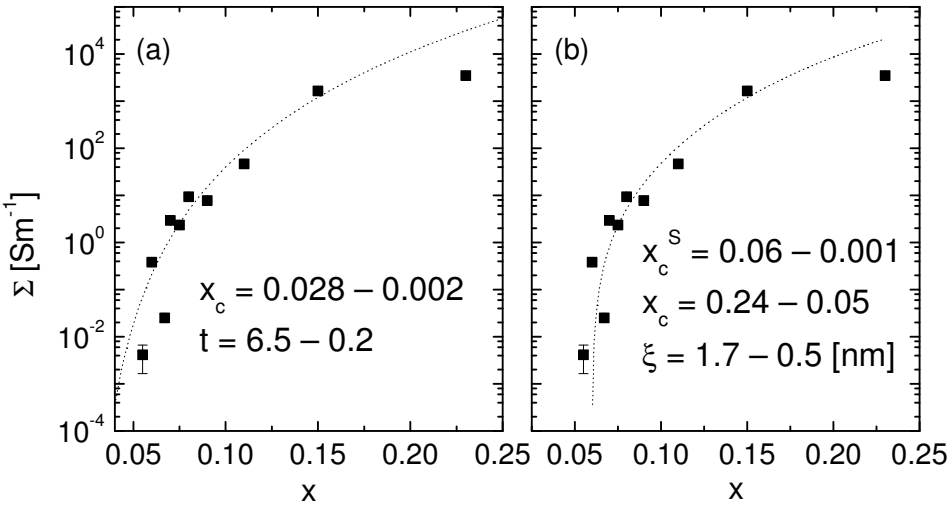

Figure 6.17: Experimental measurements of the conductivity of a RuO_2-based TFR, taken from [38]. The RuO_2 grains have average diameter of 40 nm and average glass grain size before firing of 3 μm. Firing temperature is $T_f = 600°C$. In panel (a) we show the fit (dotted line) of the classical power-law of equation 5.44, in panel (b) of equation 6.20, with the fitting parameters shown in the figure.

6.6 Conclusion

We presented in this chapter a model of segregated tunnelling percolation, aimed at describing TFRs. We modelled the situation by a dispersion of penetrable insulating spheres segregating the smaller conducting spheres in the space left over by the insulating ones. We used this model to make a detailed study of the impact of segregation on the critical concentration x_c. We showed that, contrary to what was expected from earlier studies, x_c is not a monotonically decreasing function of the segregation, rather it displays a minimum before maximal segregation is reached. This result, showing that there is an optimal percolation threshold and that the most segregated structure is not the most effective one to diminish the percolation threshold, might be of great technological interest.

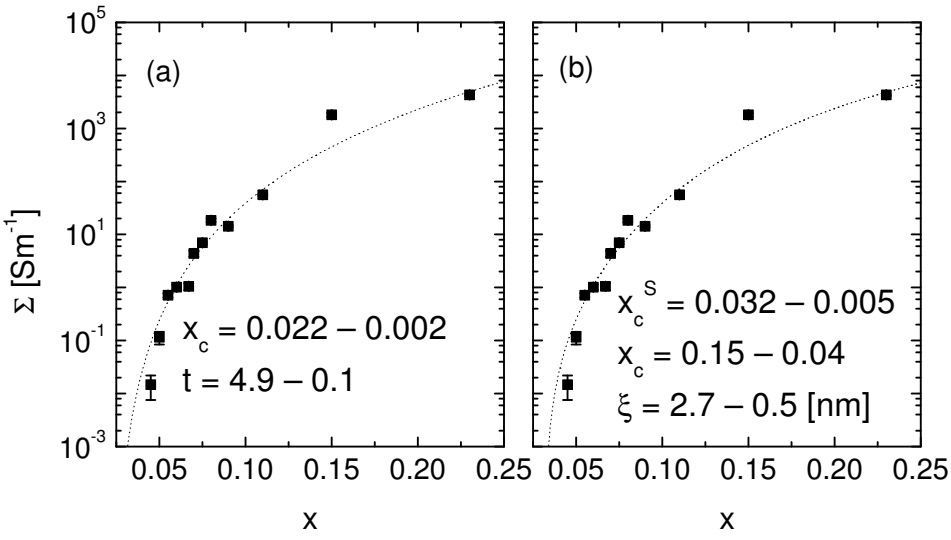

Figure 6.18: As in figure 6.17, but samples prepared with a different firing temperature, $T_f = 625°\mathrm{C}$.

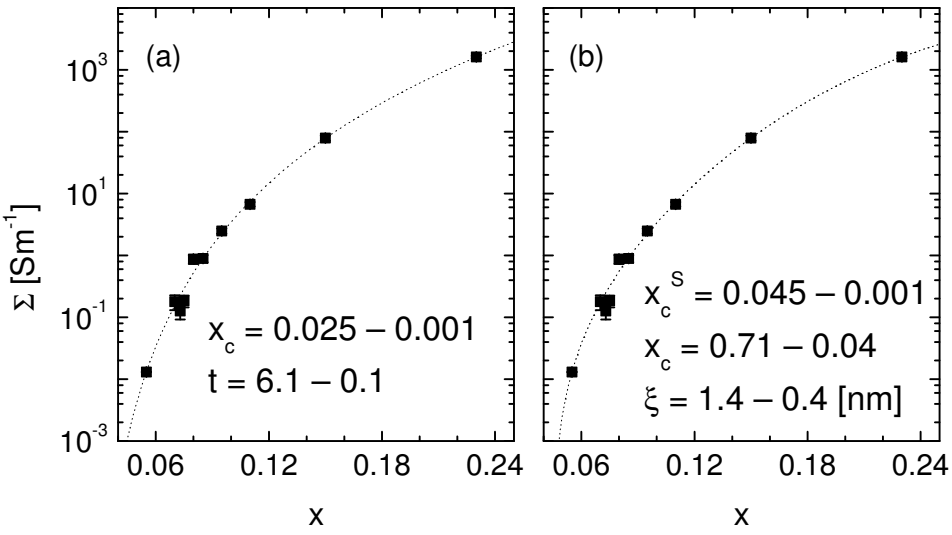

Figure 6.19: As in figure 6.17, but samples prepared with an average RuO_2 grain size of 400 nm and a different firing temperature $T_f = 625°\mathrm{C}$.

In the second part of this chapter, we studied the conductivity of the segregated tunnelling-percolation system. We showed that segregation basically did not alter the behaviour of the conductivity and that it could therefore be mapped on our results for the homogeneous tunnelling-percolation model of the preceding chapter. This allowed us to obtain an analytical expression

for the conductivity of segregated systems which was successfully fitted to experimental measurements of the conductivity of TFRs. Those fits yielded values of ξ in very good agreement with the expected one. This supports our interpretation of the origin of non-universality as stemming from the fits of the conductivity for values of x too far away from x_c.

Let us stress here that this was the main goal of this work, namely to obtain a theory of non-universality consistent with the experimentally observed transport exponents. The expression obtained for the conductivity of segregated and non-segregated systems stems from an effective medium approach using the nearest-neighbour distribution function for the inter-particle distances, so that it is not quite clear why it so nicely fits our Monte Carlo results for the complex continuum tunnelling-percolation systems studied. Nevertheless it allows to interpret the experimental conductivity data from a new perspective, attributing the experimentally measured non-universal transport exponents not to a true universality-breakdown, but to apparent non-universality caused by the fitting of the conductivity outside the true critical region. Our results are completely self-consistent, leading to fitting parameters falling inside the range of expected values, leading to a good understanding of the origin of non-universality in conductor-insulator composites.

Chapter 7

Conclusion

The aim of this work was to study in detail the electrical transport mechanism of disordered conductor-insulator composites, with a particular emphasis on an important class of such composites: thick-film resistors. TFRs were chosen as model composites, as they present most complex behaviours observed in conductor-insulator composites, namely a segregated microstructure, large piezoresistive responses, and both universal and non-universal DC transport exponents. Among those, the origin of transport non-universality was the main issue addressed in this thesis. We tried to develop realistic tunnelling-percolation models describing the conductivity in such composites and use them to study their critical transport behaviours.

We started this study by a generalization of a lattice tunnelling-percolation model, in which the bonds of a square lattice are occupied by chains of hard-core conducting particles and electrical transport in the bonds is dominated by simple tunnelling between adjacent conducting grains. This model is a crude description of the microstructure of segregated conductor-insulator composites, where the conducting particles are forced to occupy one-dimensional channels left over in between large insulating grains. We showed that the finite length of those conducting channels hindered the appearance of a true non-universal transport behaviour. Nevertheless we argued that, depending on the parameters of the model, the distribution function of the channel conductances $h(g)$, can be highly peaked at a very low g-value, leading to a transport exponent strongly depending on the concentration of conducting channels p, and tending to its universal value $t = t_0$ only very close to p_c. The fit of the conductivity Σ of the system as a function of p to the simple power-law, $\Sigma \propto (p - p_c)^t$, intended to mimic the experimental procedure, can therefore lead to non-universal transport exponents. This apparent non-universality was also shown to lead to a logarithmic increase of the piezoresistivity Γ, as observed experimentally, followed by a saturation for p close enough to p_c.

This result could explain the origin of non-universality from a new perspective, but was obtained for a lattice TP model, describing only very

roughly real conductor-insulator composites. This motivated us to study, from the same perspective, the transport properties of a realistic continuum tunnelling-percolation model, where impenetrable conducting particles were dispersed in a homogeneous insulating medium. We again considered simple tunnelling as being the dominating transport mechanism in the system. We introduced an upper cutoff distance d, limiting the range of tunnelling, which was justified by the presence of the insulating matrix and leads to a percolation behaviour of the system. Other interactions between the matrix and the conducting phase, which can have important effects on the morphology of the composite, were neglected in this model. We evaluated the percolation threshold values and transport properties by means of extensive Monte Carlo calculations, providing a detailed description for a wide range of values of the microscopic parameters. We showed that phenomena similar to those observed for the lattice cases were obtained in this framework. In particular, we also obtained apparent non-universality in the continuum tunnelling-percolation model and argued that it could be very difficult to distinguish experimentally from a true non universal transport. Furthermore, we showed that, though barely visible when looking at the conductivity of the system, the transition between non-universal and universal regime could be clearly observed from the study of the piezoresistivity. The observation of this crossover would be a direct proof of our interpretation of the non-universal transport exponents and is, for sure, an interesting direction for future research.

We also obtained an analytical expression for the conductivity of non-segregated conductor-insulator composites, which could be applied to experimental measurements of the conductivity of such systems. This formula was fitted to the experimental results with only two free parameters, a multiplicative constant and the tunnelling length ξ. The best fit provided a value of ξ of the order of 2 nm, in very good agreement with what is expected, strongly supporting our model of transport non-universality.

In the last chapter, in order to better describe the locally inhomogeneous microstructure of TFRs and study one possible effect of the interaction between the insulating matrix and the conductive phase, we formulated a segregated tunnelling-percolation model in the continuum, and evaluated the effect of segregation on the morphological and transport properties. This was, to our knowledge, the first detailed study of the mechanism of segregation using a realistic model to describe the microstructure of conductor-insulator composites and especially of TFRs. This study yielded new and interesting results, providing a previously unnoticed scenario of segregation. We showed indeed that the critical concentration x_c was not a monotonically decreasing function of segregation, but presented a minimum, well before maximal segregation is reached. This implies that the minimization of the percolation threshold is not obtained in the most segregated structure, but that there is an optimal segregation. The lowering of the critical concentration is an

important technological goal, as it allows for example to benefit from the characteristics of the filler without degrading too much the initial characteristics of the matrix, or simply to diminish the costs of the composite when, as in TFRs, the filler is much more expensive than the matrix, so that a more detailed experimental and theoretical investigation of segregation would be of great interest for future research.

Concerning the conductivity, we could show that segregation did not fundamentally change the behaviour of the conductivity, basically only shifting it to lower x-values. We could therefore map those results on the ones obtained for the non-segregated TP model and obtain an analytical expression for the conductivity in segregated TP systems. This expression was used to fit some experimental measurements of the conductivity of thick-film resistors, giving values of the fitting parameters, notably of ξ, completely consistent with the theoretically expected ones, comforting us in our theoretical approach. We thus obtained an expression for the conductivity of segregated and non-segregated conductor insulator composites, replacing the classical power-law and yielding a new interpretation of the experimental data. Non-universal behaviours such as measured transport exponents larger than $t_0 = 2$ and logarithmic increase of the piezoresistivity are inherent to this expression and naturally arise in this theoretical framework.

In summary, our approach was mainly theoretical, making large use of Monte Carlo simulations of conductor-insulator composites, but always keeping in mind the experimental procedures used to extract the transport exponents t. We systematically sought to interpret our numerical results by means of analytical frameworks, mostly by using effective medium approaches, in order to provide a better understanding of the observed behaviours. This original approach led to a new interpretation of the origin of transport non-universality, as originating from a dependence of t on the conducting phase concentration. We showed that, in realistic tunnelling-percolation models, though t was in fact universal, it tended to its true critical value $t = t_0$ only very close to the percolation threshold, taking a value $t \geq t_0$ for larger $x - x_c$ values, and that the region of true criticality could get so narrow as to be experimentally not reachable. The non-universal transport exponents observed experimentally, could therefore be explained as originating from the fit of the conductivity for values of x too far away from the critical concentration x_c, namely outside the range of criticality. This scenario, which we dubbed as "apparent non-universality", is the main contribution of this work to the understanding of the origin of non-universality in conductor-insulator composites, yielding a self consistent theory fitting nicely experimental measurements of the conductivity of some examples of the most common such composites, namely carbon-black/polymer and TFRs. Experimentally it could be very difficult to distinguish apparent non-universality from true non-universal transport. However, based on our Monte Carlo results, we propose that a careful experimental investigation of the piezore-

sistive response, close to the critical concentration, should allow to confirm our interpretation of transport non-universality and would therefore be an interesting direction for future research.

Appendix A

Extension of the EMT to hard core particle distributions

In this appendix, we extend the EMA analysis of section 5.1.1 to the case where the conducting particles are impenetrable with a hard-core diameter σ_1. To this end, it suffices to replace in Eq. (5.3) the Hertz distribution of Eq. (5.5) that is valid for $\sigma_1 = 0$, by the corresponding distribution function for $\sigma_1 \neq 0$. We shall use a simplified version of the function reported in Ref. [28]. This version still describes rather accurately the distribution of nearest-neighbouring particles in the low density regime:

$$P(r) \approx 3\frac{r^2}{(a-\sigma_1)^3}\exp\left[-\frac{r^3-{\sigma_1}^3}{(a-\sigma_1)^3}\right], \tag{A.1}$$

where $r \geq \sigma_1$, and a is approximately the distance between the centers of two nearest-neighbouring spheres. In this way, Eq. (5.6) becomes

$$\begin{aligned}\frac{2G}{1+2G} \quad + \quad & \int_{\frac{\sigma_1}{a-\sigma_1}}^{\infty} dz W'(z)\exp\left[-z^3+\left(\frac{\sigma_1}{a-\sigma_1}\right)^3\right] \\ & = \frac{p-p_c}{p},\end{aligned} \tag{A.2}$$

where $z = r/(a-\sigma_1)$ and $W'(z) = dW(z)/dz$, and

$$W(z) = \frac{2G^*}{2G^* + \exp\left[-2(a-\sigma_1)z/\xi\right]}, \tag{A.3}$$

where $G^* = \exp(-2\sigma_1/\xi)G$. For small G^*, the function $W'(z)$ is well approximated by the Dirac-delta function $\delta(z-z^*)$, where z^* is given now by

$$z^* = \frac{\xi}{2(a-\sigma_1)}\ln\left(\frac{1}{2G^*}\right), \tag{A.4}$$

and, since z^* is always larger than $\sigma_1/(a-\sigma_1)$, for small G^* Eq. (A.2) becomes

$$2G + \exp\left[\left(\frac{\sigma_1}{a-\sigma_1}\right)^3 - (z^*)^3\right] = \frac{p-p_c}{p}. \tag{A.5}$$

Consider now the case for which the second term in the left-hand side is larger than the first one. By using Eq. (A.4) and the definition of G^*, equation A.5 reduces to:

$$\left[\frac{\sigma_1}{a-\sigma_1} + \frac{\xi}{2(a-\sigma_1)}\ln\left(\frac{1}{2G}\right)\right]^3 - \left(\frac{\sigma_1}{a-\sigma_1}\right)^3 = \ln\left(\frac{p}{p-p_c}\right), \tag{A.6}$$

which can be recast in the following form

$$G \approx e^{-2\sigma_1/\xi}\left(\frac{p-p_c}{\gamma p}\right)^{\frac{2(a-\sigma_1)}{\xi}\left(\ln\frac{\gamma p}{p-p_c}\right)^{-2/3}}, \tag{A.7}$$

where $\gamma = \exp\{[\sigma_1/(a-\sigma_1)]^3\}$. We have thus shown that also for the more general case of impenetrable particles, the conductance is governed by a p-dependent exponent, reducing to Eq. (5.18) of section 5.1.1 in the very dilute limit, for which σ_1/a is small ($\gamma \approx 1$). Despite the differences between the above Eq. (A.7) and Eq. (5.18), the dominant contribution to the conductance in the whole $p-p_c$ region is still of the form $(p-p_c)^{t(p)}$, with $t(p)$ given by Eq. (5.20) with a replaced by $a-\sigma_1$. This behaviour is demonstrated in Fig. A.1, where $(1-\alpha)\left[\ln(G)/\ln\left((p-p_c)/p_c\right) - t_0\right]$ (with α given by Eq. (5.34) and G obtained by a numerical solution of Eq. (A.2)) is plotted for $a/\sigma_1 = 2$. This is for several values of σ_1/ξ, Fig. A.1(a), and for fixed σ_1/ξ but different a/σ_1 values, Fig. A.1(b). Despite of nearly one order of magnitude change of σ_1/ξ and a/σ_1, the different curves are only weakly dependent on α, and do not deviate much from the $\left[\ln\left(p/(p-p_c)\right)\right]^{-2/3}$ dependence which is represented by the solid lines.

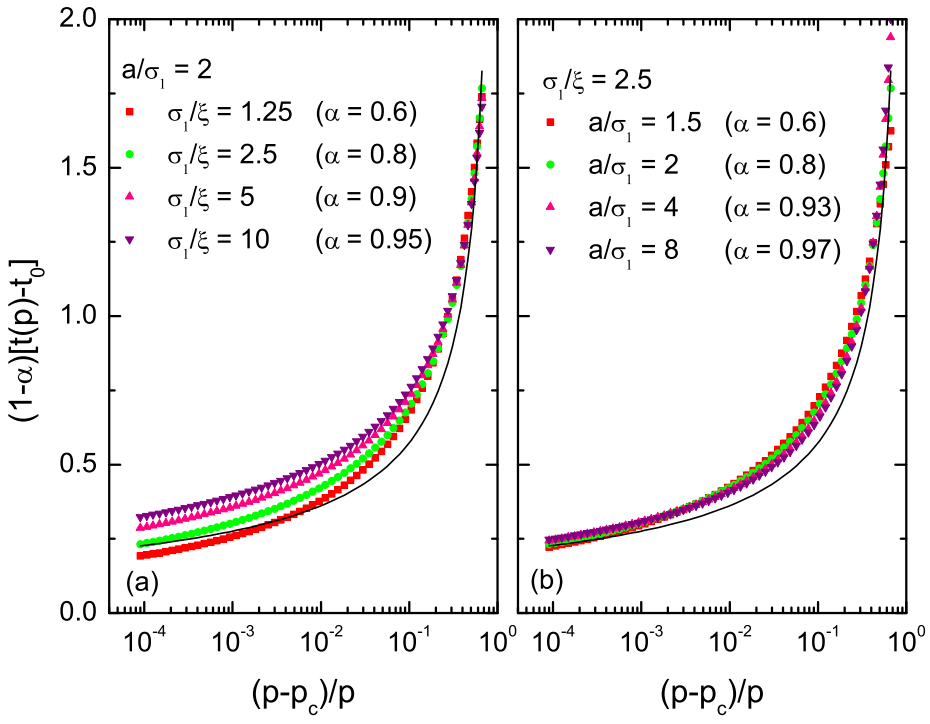

Figure A.1: Concentration dependence of the local transport exponent of the EMA of the continuum TP model for permeable conducting particles, as calculated from a numerical solution of Eq. (A.2) for different values of a/σ_1 (a) and of σ_1/ξ (b). In parenthesis are reported the corresponding values of $\alpha = 1 - \frac{\xi}{2(a-\sigma_1)}$. The solid line describes the $\left[\ln\left(\frac{p}{p-p_c}\right)\right]^{-2/3}$ dependence.

Appendix B

Simulation procedures

In this chapter we give a more extensive description of the simulation procedures used for the Monte Carlo simulations of continuum tunnelling-percolation models. The algorithm is subdivided into several distinct parts: the generation of the dispersion of spheres and the determination of neighbouring particles, the extraction, if present, of the percolating cluster and finally the calculation interparticle conductances and of the global conductivity of the system. We also discuss the generation of the segregated dispersion of spheres and the calculation of the piezoresistivity. The algorithms used for the lattice simulations are not discussed here, as they are very classical. In this chapter we will use *italic* for the names of the variables in the programs, and the following notations to specify elements and operations on the matrices:

- $A[N, M]$ indicates that the matrix A is of size $N \times M$
- *A(i,j)* is the element in row i and column j of matrix A
- *A(i,j : k)* are $k + 1 - j$ elements of row i comprised between column j and column k, so that *A(i,1:3)* are the three first elements of row i in matrix A.
- *A(i,:)* is the whole row i of matrix A.
- $A == B$ represents the attribution of the value of B to A.

B.1 System Generation

Let us now start with the generation of the dispersion of spheres. This step is very simple and uses classical methods. We want to place N_1 particles with hard-core diameter σ_1 in a cubic cell of linear size L with periodic boundary conditions. This is done by sequentially adding randomly placed particles in the system. Each time a new sphere is introduced, we check whether it

intersects any of the earlier placed particles. If yes, it is rejected and a new random position is tried. If not, the particle position is stored and the next one is placed. The position of, say, the i$^{\text{th}}$ particle is stored in *node(i+1,1:3)*, where *node* is a matrix of size $(N_1 + 2) \times 6$. The last three columns are used to speed up the intersection detection algorithm. In fact, we subdivide our simulation cell space in cubes of size slightly larger than $\sigma_1 + d$ (where $d/2$ is the width of the penetrable concentric shell of the composite particle), so that each particle can intersect (and also be neighbour with) only particles in the 26 cubes adjacent of and in the one it is in. Therefore, we check only for intersections with particles belonging to the adjacent cubes and not with all particles in the system. The cubes are designated by three numbers *Nx, Ny* and *Nz*, stored in the three last columns of *Node(i+1,:)* for particle i. For large systems, this greatly improves the speed of the system generation. Let us notice here that the reason why the information about particle i is stored in row $i + 1$ is that *node(1)* and *node(N_1+2)* are reserved for the electrodes, two opposite sides of the simulation cell between which we will look for a connected cluster (this is also the case for some other matrices introduced later in this chapter).

For completely penetrable particles ($\sigma_1 = 0$), this sequential addition procedure suffices to generate an equilibrium state of randomly dispersed particles, but for hard core particles, the dispersion obtained is no an equilibrium state [95]. An additional step is needed to let the system relax towards equilibrium. This is done by a simple Metropolis algorithm [75, 74] which goes as follows: a random small movement is sequentially attempted for each sphere and accepted only if it does not lead to an overlap with any of its neighbours. This loop is repeated until, on average, each particle was moved *Nm* times. To choose a value of *Nm* sufficiently large, the nearest-neighbour distance distribution function was extracted and compared with its analytical formula found in Ref. [28].

Now, for the generation of segregated systems, this algorithm is slightly modified. In that case we first place the N_2 large penetrable insulating spheres (diameter σ_2), by random sequential addition, as described above. No Metropolis algorithm is needed here, as the particles are penetrable. A second subdivision of the system, in cubes of size slightly larger than $\sigma_2 + \sigma_1$, is introduced, so that when we check if a conducting particle intersects an insulating one, we have to check only in the central and in the 26 adjacent cubes. The positions and cube identifier for the insulating spheres are stored in a matrix *NodeGl*$[N_2 \times 6]$. Then the conducting particles are added and moved as explained above, except that after each step overlaps with insulating spheres also have to be checked.

B.2 Network determination

The next step is to identify the neighbours of each particle to create the matrix containing the information about the connectivity of the system. We now remove the periodic boundary conditions in one direction, say the x direction, where we consider that the electrodes are placed, so that the condition for percolation will be the existence of a connected path linking the $x = 0$ and $x = L$ planes, with periodic boundary conditions in the two other directions.

We first check for all particles whether they are in contact with one of the electrodes. A particle is considered to be linked to the electrode if its center is closer than $\sigma_1/2 + d$ from one of the surfaces $x = 0$ or $x = L$. This connectivity information is stored in the matrix $Connect[N_1 \times 2]$. Then, for each particle, we look for all its neighbours (particles with center at distance smaller than $d + \sigma_1$). The j^{th} neighbour of particle i is stored in *NodeNext(i,j)*, so that *node(NodeNext(i,j),1:3)* are the coordinates of this neighbour. *NodeNext* is the adjacency list of the graph, as introduced in section 2.1, which is a very compact representation of the connectivity information of the graph.

B.3 Extraction of the conducting cluster

We can now use the connectivity information stored in *NodeNext* and *Connect* to extract, if there are, the conducting (percolating) clusters in the system. We use here an extension of the Hoshen-Kopelman algorithm [76] as presented in Ref. [77]. In this paper, the algorithm is presented for non-lattice systems, using the adjacency matrix to represent the graph. This algorithm, that I will describe here in just a few words (for more details refer to Ref. [77]), allows the labelling of all clusters in the system, by going just once through the nodes. The core of the method is to use two arrays to label the cluster to which a node belongs, *NodeL* and *NodeLP*, so that the label of the cluster to which node i belongs is *NodeLP(NodeL(i))*. Basically the algorithm is as follows: we scan successively all nodes of the network. For node i, we scan all its neighbours (given in *NodeNext(i+1,:)*) and check whether its neighbours already have a label (*NodeL(NodeNext(i,j))*$\neq 0$). If not, we attribute a new cluster label, *cluster*, to this node, $NodeL(i) == cluster$ and $NodeLP(NodeL(i)) == NodeL(i)$. and increase the cluster counter by one, *cluster==cluster+1*. If yes, look for the smallest cluster label among those of its neighbours and attribute it to particle i and its neighbours. We therefore correct *NodeLP* for all neighbours of particle i. After we have scanned the whole network following this procedure, we have to correct, successively in ascending order, the labels in *NodeLP*: $NodeLP(i) == NodeLP(NodeLP(i))$. Finally we attribute the

correct labels to the nodes: $NodeL(i) == NodeLP(NodeL(i))$.

We are now in position to check whether there are conducting clusters or not. A cluster is conducting if there is at least one particle in the cluster connected to the electrode $x = 0$ and one to the electrode $x = L$. This is easily found from the matrix *Connect* defined in the network determination step.

For the determination of the spanning probability Π, we repeat this whole procedure (from system generation to the extraction of the percolating cluster) N_s times and count the number of times N_0 there is no percolating cluster. The spanning probability is then given by $\Pi = (N_s - N_0)/N_s$. For the calculation of the conductivity or the piezoresistivity, the simulation goes on, considering from now on only the particles in the conducting clusters.

B.4 Calculation of the conductivity

The interparticle conductances are now calculated for all particles belonging to the percolating cluster. The conductance between particle i and j, g_{ij}, is simply obtained using the formula

$$g_{ij} = \exp\left(\frac{-2\big(||r_i - r_j|| - \sigma_1\big)}{\xi}\right) \tag{B.1}$$

where r_i and r_j are the vector positions of particle i and j respectively. The interparticle conductances are stored in a matrix *Cond*, in the elements corresponding to *NodeNext*, so that the conductance between particle i and its neighbour *NodeNext(i,j)* is stored in *Cond(i,j)*.

The calculation of the conductivity of the system can now begin. Here we use two different algorithms for the extraction of the conductivity: a decimation procedure and a conjugate gradient algorithm. Let us start with the decimation algorithm, which is less common than the conjugate gradient.

The decimation basically consists in removing sequentially all nodes from the system, and replacing them by additive resistances. This is an exact transformation, which is easily deduced from Kirchhoff's laws and represented in figure B.1. If node i has n neighbours, then it is replaced by $n(n-1)/2$ conductances between each pair of its neighbours. The conductance that has to be added between neighbour j and k of node i is given by [82, 83]:

$$g_{jk} = \frac{g_{ij}g_{ik}}{\sum_{\{ij\}} g_{ij}}, \tag{B.2}$$

where the sum runs over all neighbours j of node i. Now if there was already a conductance between a pair of neighbours of i, we will have two conductances in parallel, which are replaced by a unique conductance, as shown

in the figure. All nodes except the two nodes representing the electrodes are erased from the system, finally replacing the whole network by just one conductance between the electrodes and holding the conductance of the network. In our program, this is done by scanning successively all nodes in the conducting cluster, updating at each step the information in *NodeNext* and *Cond* following the above equation B.2, until we are left only with node 1 and node $N_1 + 2$. The representation of the connectivity in *NodeNext* and *Cond* makes the algorithm especially simple to implement.

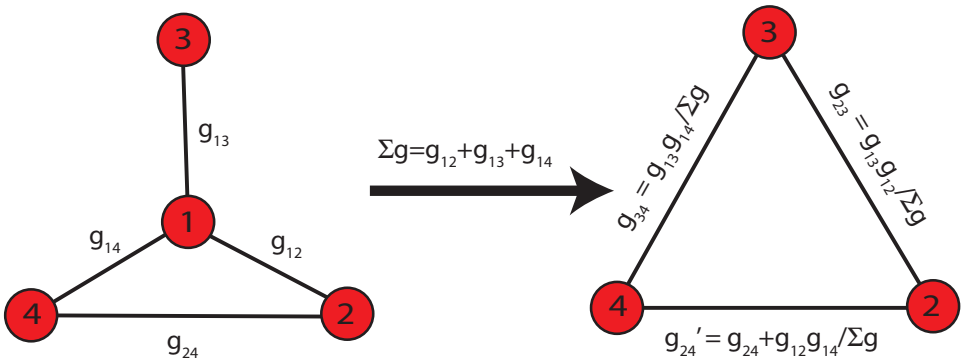

Figure B.1: Illustration of the decimation algorithm. The internal node 1 is removed and replaced by additional conductances between its neighbours. As there was already a link between two of its neighbours (2 and 4), the transformation creates a conductance in parallel with the existing one which are simplified in a unique conductance g'_{24}.

This algorithm has the advantage of being exact and very fast close to the percolation threshold, contrary to the relaxation methods, such as the conjugate gradient method (CGM), which have to converge to the solution of the potential for each node, making them very sensitive to the large fluctuations observed close to p_c. In fact the decimation algorithm is faster close than away from p_c. Indeed if all nodes have several neighbours, at each decimation step we add new neighbours to all neighbours of the decimated node, so that the number of neighbours of the remaining nodes will increase exponentially, considerably slowing down the algorithm. But close to p_c the percolating cluster has a structure with many singly connected bonds, which will hinder the number of neighbours from exploding. In our algorithm we are not eliminating the nodes in a random order; we eliminate them by increasing degree, starting with the nodes having just one neighbour. This considerably increases the speed of the procedure (we gained two orders of magnitude of speed with this ordering of the decimation).

Now, as the decimation is inefficient far away from the percolation threshold, we also implemented a conjugate gradient algorithm. To this end the conduction problem has to be written in matricial form. Starting from the

equation 2.19

$$\sum_j g_{ij}\Big(V(i) - V(j)\Big) = 0 \tag{B.3}$$

which is simply the current conservation at each node i, we can rewrite the conduction problem in matricial form [12]:

$$\sum_{ij} Bonds_{ij}\, V_j = B_i. \tag{B.4}$$

where $Bonds_{ij} = \delta_{ij}\sum_k g_{ik} - g_{ij}$, so that the off-diagonal term $Bonds_{ij} = -g_{ij}$ whereas the diagonal term $Bonds_{ii} = \sum_k g_{ik}$. Except for the diagonal term, this matrix is basically the adjacency matrix of the system as defined in section 2.1. The matrix B, on the righthand side of the above equation, contains the boundary conditions. B_i is zero if i is an internal node, and otherwise contains the conductance linking node i to the electrode multiplied by the voltage of the electrode ($g_{i1}V_1$ or $g_{iN_1+2}V_{N_1+2}$). From equation B.4 it is easy to write the CGM, which is a classical method and will not be discussed in detail here. The procedure can be found in Ref. [62]. To speed up the algorithm, we used an incomplete LU factorization as preconditioner [84].

The difficulty here is that the CGM algorithm is matricial, and that the matrix $Bonds$ is of size $N_1 \times N_1$ becoming rapidly a limitation for large systems (we studied systems containing more than 10^4 particles which leads to a matrix with 10^8 elements). Moreover it is clear that this matrix contains mainly zeros, as each particle has just a few neighbours. It is therefore valuable to implement this algorithm using the sparse matrix representation, which allows to store only the non-zero elements of the matrix. A sparse matrix A of size $N \times N$ with M non-zero elements can be stored using three vectors: $AS[M]$, $AI[N+1]$ and $AC[M]$. AS contains all the non-zero elements of A, in the order of appearance in A if it is read row by row, from left to right. The second vector, AI, contains the indexes of the elements in AS corresponding to the first element of a row of A, so that $AS(AI(i))$ is the first non-zero element of row i of the matrix A. Finally the last vector AC contains the column index corresponding to each element in AS. I give here an example to make things clearer:

$$\begin{aligned} A &= \begin{pmatrix} 2 & 0 & 3 & 0 \\ 0 & 4 & 1 & 0 \\ 5 & 0 & 7 & 9 \end{pmatrix} \\ AS &= (2,\, 3,\, 4,\, 1,\, 5,\, 7,\, 9) \\ AI &= (1,\, 3,\, 5,\, 8) \\ AC &= (1,\, 3,\, 2,\, 3,\, 1,\, 3,\, 4) \end{aligned}$$

In this notation, we have $2M + N + 1$ elements instead of $N^2 + 2N + 1$, which makes of course a huge difference if N is large and $M \ll N$. We therefore implemented both the CGM and the incomplete LU factorization in this sparse matrix formalism.

As already mentioned, the CGM algorithm works very well if the fluctuations in the system are not too large. This is the case not too close to p_c, and for large values of ξ/d. When $\xi/d \ll 1$, the local conductances have a very broad distribution, inducing large local voltage fluctuations, which can considerably slow down the CGM, even when preconditioned. As it is not always easy to predict which algorithm (the CGM or the decimation) will be faster, we used a combination of them. We start with the decimation procedure, eliminating the nodes with few neighbours. The decimation is very fast at the beginning, for the nodes with few neighbours, and then starts to slow down as the number of neighbours per node increases. If the decimation becomes slower than one second per node (this limit was fixed somewhat arbitrarily), we switch to the CGM. The advantage here is that the decimation rapidly reduces the number of nodes in the system, removing the dead ends with just one neighbour, and the nodes with few neighbours, leaving a more homogeneous and compact network, on which the CGM will perform better than on the original network. This combination of the algorithms is useful, mostly because it is difficult to predict which algorithm will run faster, so it removes this choice from the user but it also speeds up a little the overall performance of the program.

Of course, the conductivity is also calculated from an average of N_s realizations and its error is obtained from the standard deviation.

B.5 Piezoresistivity

The last point discussed here is how we obtain the piezoresistivity Γ of the system. Γ is defined as

$$\Gamma = -\frac{d\,\ln(\Sigma)}{d\,\epsilon}. \tag{B.5}$$

We consider here that the matrix and the conducting spheres have the same elastic coefficients, so that, under an applied strain ϵ, the distance r between neighbouring spheres and the diameter σ_1 of the spheres change as:

$$r \rightarrow r(1+\epsilon) \tag{B.6}$$

$$\sigma_1 \rightarrow \sigma_1(1+\epsilon) \tag{B.7}$$

In practice, this assumption is often not valid, but the mechanical heterogeneity can be treated separately from the percolation problem and basically leads to a simple enhancement of the piezoresistivity [52]. Now as the local

conductances are given by equation B.1, changing r and σ_1 is equivalent to changing the tunnelling length ξ instead, following

$$\xi \to \xi/(1+\epsilon). \tag{B.8}$$

We can now rewrite equation B.5 as

$$\Gamma = \frac{d\ \ln(\Sigma)}{d\ \ln(\xi)}, \tag{B.9}$$

which is more convenient for the simulation procedure, as it allows to obtain Γ from the calculation of the conductivity for the same system (same particles distribution) solely changing the value of ξ, so that Γ is obtained from $\Sigma(\xi)$ and $\Sigma\big(\xi/(1+\epsilon)\big)$:

$$\Gamma_s = -\frac{\Delta\Sigma}{\Sigma\epsilon} = -\frac{\Sigma\big(\xi/(1+\epsilon)\big) - \Sigma(\xi)}{\Sigma(\xi)\epsilon}. \tag{B.10}$$

In the limit $\epsilon \to 0$, equations B.10 and B.5 are equal. In our simulations, we used $\epsilon = 0.01$, calculated the conductivity Σ for the same system with the two different values of ξ and extracted Γ_s from the above equation. As ϵ is finite, when Γ is large a correction has to be applied to Γ_s extracted in this manner. Indeed we have:

$$\begin{aligned}
\Gamma &= \frac{d\ \ln(\Sigma)}{d\ \ln(\xi)} \\
&= -\lim_{\epsilon\to 0} \frac{\ln(1+\Delta\Sigma/\Sigma)}{\epsilon} \\
&= -\lim_{\epsilon\to 0} \left[\frac{\Delta\Sigma}{\Sigma\epsilon} - \frac{1}{2\epsilon}\Big(\frac{\Delta\Sigma}{\Sigma}\Big)^2 + O\Big(\frac{\Delta\Sigma}{\Sigma}\Big)^3\right] \\
&= \lim_{\epsilon\to 0} \left[\Gamma_s + \frac{\epsilon}{2}\Gamma_s^2 + O(\epsilon^2\Gamma_s^3)\right],
\end{aligned}$$

so that, if ϵ is finite and Γ_s large, we have to add $(\epsilon/2)\Gamma_s^2$ in order to obtain a better estimate of Γ.

As for the conductivity, Γ_s is obtained from an average over N_s simulations and the error estimation is given by the standard deviation.

Bibliography

[1] D. D. L. Chung. Electromagnetic interference shielding effectiveness of carbon materials. *Carbon*, 39(2):279–285, 2001.

[2] M. Hindermann-Bischoff and F. Ehrburger-Dolle. Electrical conductivity of carbon black-polyethylene composites - experimental evidence of the change of cluster connectivity in the PTC effect. *Carbon*, 39(3):375–382, 2001.

[3] D. Azulay, M. Eylon, O. Eshkenazi, D. Toker, M. Balberg, N. Shimoni, O. Millo, and I. Balberg. Electrical-thermal switching in carbon-black-polymer composites as a local effect. *Physical Review Letters*, 90(23), 2003.

[4] D. Stauffer and A. Aharony. *Introduction to Percolation Theory*. Taylor & Francis, London, 1992.

[5] S. Vionnet-Menot, C. Grimaldi, T. Maeder, S. Strassler, and P. Ryser. Tunneling-percolation origin of nonuniversality: Theory and experiments. *Physical Review B*, 71(6), 2005.

[6] L. Euler. Solutio problematis ad geometriam situs pertinentis. *Comentarii Academiae Scientiarum Imperialis Petropolitanae*, 8:128–140, 1736.

[7] P. J. Flory. Molecular size distribution in three dimensional polymers. I. gelation. *Journal of the American Chemical Society*, 63:3083–3090, 1941.

[8] F. Peruggi, F. Diliberto, and G. Monroy. Some AB-percolation problems in the antiferromagnetic Potts-model. *Physica A*, 123(1):175–190, 1984.

[9] D. S. Gaunt and Sykes M. F. Series study of random percolation in three dimensions. *Journal of Physics A-Mathematical and General*, 16(4):783–799, 1983.

[10] P. H. L. Martins and J. A. Plascak. Percolation on two- and three-dimensional lattices. *Physical Review E*, 67(4), 2003.

[11] C. Moukarzel. A fast algorithm for backbones. *International Journal of Modern Physics C*, 9(6):887–895, 1998.

[12] S. Kirkpatrick. Percolation and conduction. *Reviews of Modern Physics*, 45(4):574, 1973.

[13] David B. Gingold and C. J. Lobb. Percolative conduction in three dimensions. *Physical Review B*, 42(13):8220, 1990.

[14] B. Derrida, D. Stauffer, H. J. Herrmann, and J. Vannimenus. Transfer-matrix calculation of conductivity in 3-dimensional random resistor networks at percolation-threshold. *Journal de Physique Lettres*, 44(17):L701–L706, 1983.

[15] B. Derrida and J. Vannimenus. A transfer-matrix approach to random resistor networks. *Journal of Physics A-Mathematical and General*, 15(10):L557–L564, 1982.

[16] J. M. Normand, H. J. Herrmann, and M. Hajjar. Precise calculation of the dynamical exponent of two-dimensional percolation. *Journal of Statistical Physics*, 52(1-2):441–446, 1988.

[17] H. J. Herrmann, D. C. Hong, and H. E. Stanley. Backbone and elastic backbone of percolation clusters obtained by the new method of burning. *Journal of Physics A-Mathematical and General*, 17(5):L261–L266, 1984.

[18] M. Porto, S. Havlin, H. E. Roman, and A. Bunde. Probability distribution of the shortest path on the percolation cluster, its backbone, and skeleton. *Physical Review E*, 58(5):R5205–R5208, 1998.

[19] M. Sahimi. *Heterogeneous Materials I.* Springer, New York, 2003.

[20] P. M. Kogut and J. P. Straley. Distribution-induced non-universality of the percolation conductivity exponents. *Journal of Physics C-Solid State Physics*, 12(11):2151–2159, 1979.

[21] J. Machta, R. A. Guyer, and S. M. Moore. Conductivity in percolation networks with broad distributions of resistances. *Physical Review B*, 33(7):4818–4825, 1986.

[22] M. Alava and C. F. Moukarzel. Transport on percolation clusters with power-law distributed bond strengths. *Physical Review E*, 67(5), 2003.

[23] B. J. Last and D. J. Thouless. Percolation theory and electrical conductivity. *Physical Review Letters*, 27(25):1719, 1971.

[24] A. R. Kerstein. Equivalence of the void percolation problem for overlapping spheres and a network problem. *Journal of Physics A-Mathematical and General*, 16(13):3071–3075, 1983.

[25] S. C. Feng, B. I. Halperin, and P. N. Sen. Transport-properties of continuum-systems near the percolation-threshold. *Physical Review B*, 35(1):197–214, 1987.

[26] I. Balberg. Limits on the continuum-percolation transport exponents. *Physical Review B*, 57(21):13351–13354, 1998.

[27] I. Balberg. Tunneling and nonuniversal conductivity in composite-materials. *Physical Review Letters*, 59(12):1305–1308, 1987.

[28] S. Torquato, B. Lu, and J. Rubinstein. Nearest-neighbor distribution-functions in many-body systems. *Physical Review A*, 41(4):2059–2075, 1990.

[29] P. Sheng. Fluctuation-induced tunneling conduction in disordered materials. *Physical Review B*, 21(6):2180–2195, 1980.

[30] E. K. Sichel, J. I. Gittleman, and P. Sheng. Transport properties of the composite-material carbon-poly(vinyl chloride). *Physical Review B*, 18(10):5712–5716, 1978.

[31] E. K. Sichel, Ping Sheng, J. I. Gittleman, and S. Bozowski. Observation of fluctuation modulation of tunnel junctions by applied ac stress in carbon polyvinylchloride composites. *Physical Review B*, 24(10):6131, 1981.

[32] A. Amin. Piezoresistivity in ruthenium-based metal-insulator-metal structures. *Journal of Materials Research*, 16(8):2239–2243, 2001.

[33] A. Celzard, E. McRae, G. Furdin, and J. F. Mareche. Conduction mechanisms in some graphite-polymer composites: The effect of a direct-current electric field. *Journal of Physics-Condensed Matter*, 9(10):2225–2237, 1997.

[34] A. Celzard, E. McRae, J. F. Mareche, G. Furdin, and B. Sundqvist. Conduction mechanisms in some graphite-polymer composites: Effects of temperature and hydrostatic pressure. *Journal of Applied Physics*, 83(3):1410–1419, 1998.

[35] G. E. Pike and C. H. Seager. Electrical-properties and conduction mechanisms of Ru-based thick-film (cermet) resistors. *Journal of Applied Physics*, 48(12):5152–5169, 1977.

[36] C. Grimaldi and I. Balberg. Tunneling and nonuniversality in continuum percolation systems. *Physical Review Letters*, 96(6), 2006.

[37] C. Grimaldi, T. Maeder, P. Ryser, and S. Strassler. Segregated tunneling-percolation model for transport nonuniversality. *Physical Review B*, 68(2), 2003.

[38] S. Vionnet Menot. *Low Firing Temperature Thick-Film Piezoresistive Composites - Properties and conduction mechanism.* PhD thesis, EPFL, 2005.

[39] D. M. Heyes, M. Cass, and A. C. Branka. Percolation threshold of hard-sphere fluids in between the soft-core and hard-core limits. *Molecular Physics*, 104(20-21):3137–3146, 2006.

[40] T. Tobita and H. Takasago. New trimming technology of a thick-film resistor by the pulse voltage method. *Ieee Transactions on Components Hybrids and Manufacturing Technology*, 14(3):613–617, 1991.

[41] J. S. Shah and L. Berrin. Mechanism and control of post-trim drift of laser-trimmed thick-film resistors. *Ieee Transactions on Components Hybrids and Manufacturing Technology*, 1(2):130–136, 1978.

[42] D. W. Feldbaumer, J. A. Babcock, V. M. Mercier, and C. K. Y. Chun. Pulse current trimming of polysilicon resistors. *Ieee Transactions on Electron Devices*, 42(4):689–696, 1995.

[43] J. A. Babcock, P. Francis, R. Bashir, A. E. Kabir, D. K. Schroder, M. S. L. Lee, T. Dhayagude, W. Yindeepol, S. J. Prasad, A. Kalnitsky, M. E. Thomas, H. Haggag, K. Egan, A. Bergemont, and P. Jansen. Precision electrical trimming of very low TCR poly-SiGe resistors. *Ieee Electron Device Letters*, 21(6):283–285, 2000.

[44] A. Dziedzic, A. Kolek, W. Ehrhardt, and H. Thust. Advanced electrical and stability characterization of untrimmed and variously trimmed thick-film and LTCC resistors. *Microelectronics Reliability*, 46(2-4):352–359, 2006.

[45] N. Johner, T. Maeder, C. Grimaldi, A. Kambli, I. Saglini, C. Jacq, and P. Ryser. High-voltage sensitivity studies of model thick-film resistors. In *XXX International Conference of IMAPS Poland Chapter*, pages 24–27, Kraków, 2006.

[46] N. Johner, T. Maeder, C. Jacq, and P. Ryser. Study of the impact of high-voltage trimming on several characteristics of model TFRs and their stability. In *16th European Microelectronics and packaging conference and exhibition*, volume 2, pages 537–541, Oulu, Finland, 2007.

[47] T. Tobita, H. Takasago, and K. Kariya. Investigation of conduction mechanism in thick-film resistors trimmed by the pulse voltage method.

Ieee Transactions on Components Hybrids and Manufacturing Technology, 15(4):583–589, 1992.

[48] G. Ambrosetti, 2009. Unpublished work.

[49] R. Schueler, J. Petermann, K. Schulte, and H. P. Wentzel. Agglomeration and electrical percolation behavior of carbon black dispersed in epoxy resin. *Journal of Applied Polymer Science*, 63(13):1741–1746, 1997.

[50] Maria Prudenziati. *Thick film sensors*, volume 1 of *Handbook of sensors and actuators*. Elsevier, Amsterdam Lausanne etc., 1994.

[51] I. J. Youngs. A geometric percolation model for non-spherical excluded volumes. *Journal of Physics D-Applied Physics*, 36(6):738–747, 2003.

[52] C. Grimaldi, P. Ryser, and S. Strassler. Gauge factor enhancement driven by heterogeneity in thick-film resistors. *Journal of Applied Physics*, 90(1):322–327, 2001.

[53] K. V. K. Rao and L. Iyengar. X-ray studies on thermal expansion of ruthenium dioxide. *Acta Crystallographica Section A-Crystal Physics Diffraction Theoretical and General Crystallography*, A 25:302, 1969.

[54] S. T. Chui. Disappearance of the coulomb charging energy and low-temperature resistivity of granular metals. *Physical Review B*, 43(17):14274–14276, 1991.

[55] P. Sheng, B. Abeles, and Y. Arie. Hopping conductivity in granular metals. *Physical Review Letters*, 31(1):44–47, 1973.

[56] A. L. Efros and B. I. Shklovskii. Coulomb gap and low-temperature conductivity of disordered systems. *Journal of Physics C-Solid State Physics*, 8(4):L49–L51, 1975.

[57] N. F. Mott. Conduction in non-crystalline materials 3. localized states in a pseudogap and near extremities of conduction and valence bands. *Philosophical Magazine*, 19(160):835, 1969.

[58] V. Ambegaokar, B. I. Halperin, and J. S. Langer. Hopping conductivity in disordered systems. *Physical Review B*, 4(8):2612, 1971.

[59] Y. M. Chiang, L. A. Silverman, R. H. French, and R. M. Cannon. Thin glass-film between ultrafine conductor particles in thick-film resistors. *Journal of the American Ceramic Society*, 77(5):1143–1152, 1994.

[60] N. Johner, C. Grimaldi, and P. Ryser. Apparent nonuniversality in finite segregated tunneling-percolation models. *Physica A-Statistical Mechanics and Its Applications*, 374(2):646–654, 2007.

[61] J. R. Macdonald. On the mean separation of particles of finite size in one to three dimensions. *Molecular Physics*, 44(5):1043–1049, 1981.

[62] G. G. Batrouni and A. Hansen. Fourier acceleration of iterative processes in disordered-systems. *Journal of Statistical Physics*, 52(3-4):747–773, 1988.

[63] N. Wagner, I. Balberg, and D. Klein. Monte Carlo results for continuum percolation in low and high dimensions. *Physical Review E*, 74(1), 2006.

[64] D. J. Frank and C. J. Lobb. Highly efficient algorithm for percolative transport studies in 2 dimensions. *Physical Review B*, 37(1):302–307, 1988.

[65] G.E. Pike. Electrical transport and optical properties of inhomogeneous media. page 366, New York, 1978. AIP.

[66] S. Vionnet, C. Grimaldi, T. Maeder, P. Ryser, and S. Strassler. Strain dependence of transport critical exponent in RuO_2-glass systems. *Annalen Der Physik*, 13(1-2):99–100, 2004.

[67] S. Vionnet-Menot, C. Grimaldi, P. Ryser, T. Maeder, and S. Strassler. Strain modulation of transport criticality in RuO_2 based thick-film resistors. *Applied Physics Letters*, 85(23):5619–5621, 2004.

[68] S. Vionnet-Menot, C. Grimaldi, T. Maeder, P. Ryser, and S. Strassler. Study of electrical properties of piezoresistive pastes and determination of the electrical transport. *Journal of the European Ceramic Society*, 25(12):2129–2132, 2005.

[69] C. Grimaldi, P. Ryser, and S. Strassler. Anisotropic random resistor networks: A model for piezoresistive response of thick-film resistors. *Journal of Applied Physics*, 92(4):1981–1986, 2002.

[70] T. Maeder, B. Afra, Y. Fournier, N. Johner, and P. Ryser. LTCC ultra-high isostatic pressure sensors. In *16th European Microelectronics and packaging conference and exhibition*, volume 2, pages 375–380, Oulu, Finland, 2007.

[71] N. Johner, P. Ryser, C. Grimaldi, and I. Balberg. Piezoresistivity and tunneling-percolation transport in apparently nonuniversal systems. *Physical Review B*, 75(10), 2007.

[72] N. Johner, C. Grimaldi, I. Balberg, and P. Ryser. Transport exponent in a three-dimensional continuum tunneling-percolation model. *Physical Review B*, 77(17), 2008.

[73] M. D. Rintoul and S. Torquato. Precise determination of the critical threshold and exponents in a three-dimensional continuum percolation model. *Journal of Physics A-Mathematical and General*, 30(16):L585–L592, 1997.

[74] J. E. Gubernatis. Marshall Rosenbluth and the metropolis algorithm. *Physics of Plasmas*, 12(5), 2005.

[75] N. Metropolis, A. W. Rosenbluth, M. N. Rosenbluth, A. H. Teller, and E. Teller. Equation of state calculations by fast computing machines. *Journal of Chemical Physics*, 21(6):1087–1092, 1953.

[76] J. Hoshen and R. Kopelman. Percolation and cluster distribution 1. cluster multiple labeling technique and critical concentration algorithm. *Physical Review B*, 14(8):3438–3445, 1976.

[77] A. Al-Futaisi and T. W. Patzek. Extension of Hoshen-Kopelman algorithm to non-lattice environments. *Physica A-Statistical Mechanics and Its Applications*, 321(3-4):665–678, 2003.

[78] S. B. Lee and T. J. Yoon. Determination of percolation thresholds for the correlated continuum percolation model. *Journal of the Korean Physical Society*, 33(5):612–616, 1998.

[79] G. D. Scott and D. M. Kilgour. Density of random close packing of spheres. *Journal of Physics D-Applied Physics*, 2(6):863, 1969.

[80] C. D. Lorenz and R. M. Ziff. Precise determination of the critical percolation threshold for the three-dimensional "Swiss cheese" model using a growth algorithm. *Journal of Chemical Physics*, 114(8):3659–3661, 2001.

[81] I. Balberg and N. Binenbaum. Invariant properties of the percolation thresholds in the soft-core hard-core transition. *Physical Review A*, 35(12):5174–5177, 1987.

[82] R. Fogelholm. The conductivity of large percolation network samples. *Journal of Physics C-Solid State Physics*, 13(23):L571–L574, 1980.

[83] Rabbe Fogelholm. Computation for conductance distributions of percolation lattice cells. In *Proceedings of the fourth ACM symposium on Symbolic and algebraic computation*, pages 94–99, Snowbird, Utah, United States, 1981. ACM Press.

[84] M. Benzi. Preconditioning techniques for large linear systems: A survey. *Journal of Computational Physics*, 182(2):418–477, 2002.

[85] C. H. Seager and G. E. Pike. Percolation and conductivity - computer study .2. *Physical Review B*, 10(4):1435–1446, 1974. U0399 Times Cited:190 Cited References Count:30.

[86] I. Balberg, D. Azulay, D. Toker, and O. Millo. Percolation and tunneling in composite materials. *International Journal of Modern Physics B*, 18(15):2091–2121, 2004.

[87] Z. Rubin, S. A. Sunshine, M. B. Heaney, I. Bloom, and I. Balberg. Critical behavior of the electrical transport properties in a tunneling-percolation system. *Physical Review B*, 59(19):12196–12199, 1999.

[88] A. Kubovy. A percolation model of the conduction threshold in thick-film resistors : Segregated structures. *Journal of Physics D-Applied Physics*, 19(11):2171–2183, 1986.

[89] A. Kusy. Classical percolation threshold and resistance versus temperature behaviour of RuO_2-glass films. *Physica B*, 240(3):226–241, 1997.

[90] A. S. Ioselevich and A. A. Kornyshev. Approximate symmetry laws for percolation in complex systems: Percolation in polydisperse composites. *Physical Review E*, 65(2), 2002.

[91] D. He and N. N. Ekere. Effect of particle size ratio on the conducting percolation threshold of granular conductive-insulating composites. *Journal of Physics D-Applied Physics*, 37(13):1848–1852, 2004.

[92] A. Malliaris and D. T. Turner. Influence of particle size on electrical resistivity of compacted mixtures of polymeric and metallic powders. *Journal of Applied Physics*, 42(2):614, 1971.

[93] R. P. Kusy. Influence of particle-size ratio on continuity of aggregates. *Journal of Applied Physics*, 48(12):5301–5305, 1977.

[94] N. Johner, C. Grimaldi, T. Maeder, and P. Ryser. Optimal percolation of disordered segregated composites. *Physical Review E*, 79(2), 2009.

[95] S. Torquato. *Random Heterogeneous Materials: Microstructure and Macroscopic Properties*, volume 16 of *Interdisciplinary applied mathematics*. Springer-Verlag, New York, 2006.

[96] I. Balberg, C. H. Anderson, S. Alexander, and N. Wagner. Excluded volume and its relation to the onset of percolation. *Physical Review B*, 30(7):3933–3943, 1984.

[97] I. Balberg. Excluded-volume explanation of Archie's law. *Physical Review B*, 33(5):3618–3620, 1986.

[98] E. Charlaix. Percolation-threshold of a random array of disks : a numerical-simulation. *Journal of Physics A-Mathematical and General*, 19(9):L533–L536, 1986.

[99] E. J. Garboczi, K. A. Snyder, J. F. Douglas, and M. F. Thorpe. Geometrical percolation-threshold of overlapping ellipsoids. *Physical Review E*, 52(1):819–828, 1995.

[100] T. Schilling, S. Jungblut, and M. A. Miller. Depletion-induced percolation in networks of nanorods. *Physical Review Letters*, 98(10), 2007.

[101] G. Ambrosetti, N. Johner, C. Grimaldi, A. Danani, and P. Ryser. Percolative properties of hard oblate ellipsoids of revolution with a soft shell. *Physical Review E*, 78(6), 2009.

[102] W. J. Kim, M. Taya, K. Yamada, and N. Kamiya. Percolation study on electrical resistivity of SiC/Si_3N_4 composites with segregated distribution. *Journal of Applied Physics*, 83(5):2593–2598, 1998.

[103] C. Chiteme and D. S. McLachlan. AC and DC conductivity, magnetoresistance, and scaling in cellular percolation systems. *Physical Review B*, 67(2):024206, 2003.

[104] S. Cohen-Addad, M. Krzan, R. Hohler, and B. Herzhaft. Rigidity percolation in particle-laden foams. *Physical Review Letters*, 99(16), 2007.

[105] M. W. L. Wilbrink, M. A. J. Michels, W. P. Vellinga, and H. E. H. Meijer. Rigidity percolation in dispersions with a structured viscoelastic matrix. *Physical Review E*, 71(3), 2005.

[106] P. F. Carcia, A. Ferretti, and A. Suna. Particle-size effects in thick-film resistors. *Journal of Applied Physics*, 53(7):5282–5288, 1982.

[107] R. M. Ziff. Spanning probability in 2d percolation. *Physical Review Letters*, 69(18):2670–2673, 1992.

[108] D. Stauffer. Minireview: New results for old percolation. *Physica A*, 242(1-2):1–7, 1997.

[109] J. Kertesz. Percolation of holes between overlapping spheres - Monte-Carlo calculation of the critical volume fraction. *Journal de Physique Lettres*, 42(17):L393–L395, 1981.

[110] W. T. Elam, A. R. Kerstein, and J. J. Rehr. Critical properties of the void percolation problem for spheres. *Physical Review Letters*, 52(17):1516–1519, 1984.

[111] A. R. Kansal, S. Torquato, and F. H. Stillinger. Computer generation of dense polydisperse sphere packings. *Journal of Chemical Physics*, 117(18):8212–8218, 2002.

[112] Y. Zweifel, C. J. G. Plummer, and H. H. Kausch. A microscopic investigation of conducting filled polymers. *Journal of Materials Science*, 33(7):1715–1721, 1998.

[113] K. H. Muller, J. Herrmann, B. Raguse, G. Baxter, and T. Reda. Percolation model for electron conduction in films of metal nanoparticles linked by organic molecules. *Physical Review B*, 66(7), 2002.

[114] K. Adachi, S. Iida, and K. Hayashi. Ruthenium clusters in lead-borosilicate glass in thick-film resistors. *Journal of Materials Research*, 9(7):1866–1878, 1994.

[115] C. Meneghini, S. Mobilio, F. Pivetti, I. Selmi, M. Prudenziati, and B. Morten. RuO_2-based thick film resistors studied by extended x-ray absorption spectroscopy. *Journal of Applied Physics*, 86(7):3590–3593, 1999.

Niklaus JOHNER

Swiss, single, 05.12.1980

Ch. de la Venoge 3
CH-1028 Préverenges
☎ +41 (0)76 302 12 20
✉ niklaus.johner@a3.epfl.ch

Education

2004-2009 **Ph.D. student in physics at the Ecole Polytechnique Fédérale de Lausanne (EPFL)**. Specialization in percolation theory.

1999-2004 **M.Sc. in Physics at the EPFL.** Orientation towards energetics and theoretical physics.

1996-1999 High school at the Gymnase de Morges and obtention of the "**maturité fédérale latin-anglais**" in 1999.

Professional experience

2004-2009 **Research assistant at the Laboratoire de Production Microtechnique (LPM**) at the EPFL. Theoretical study, mostly by Monte Carlos simulations, of the transport properties of segregated conductor-insulator composites.

2004 **Research assistant at the Laboratoire d'Energie Solaire et Physique du Bâtiment (LESO-PB)** at the EPFL for three months, writing of a publication on my M.Sc. diploma work.

2003-2004 **Teaching assistant** for physics classes at EPFL.

2002 **One month internship at Institut Straumann** in Waldenburg, canton Basel (CH).

Languages

Swiss-German	Mother tongue
French	Native Fluency (Moved to the French-speaking part of Switzerland in 1985)
English	Very good skills (three months of high school in Canada)
German	Good

Informatics

Programming	Fortran, Matlab, LaTeX, C
Softwares	Origin Pro, Matlab, Adobe Illustrator and photoshop, MS Office

List of publications

2006 C.-A. Roulet, N. Johner, F. Foradini, P. Bluyssen, C. Cox, E.O. Fernandes, B. Muller and C. Aizlewood, "Perceived health and comfort in relation to energy use and building characteristics", *Building research and Information,* **34**(5), 467-474.

2007 N. Johner, C. Grimaldi and P. Ryser, "Apparent nonuniversality in finite segregated tunneling-percolation models", *Physica A,* **374**(2), 646-654.

2007 N. Johner, P. Ryser, C. Grimaldi and I. Balberg, "Piezoresistivity and tunneling-percolation transport in apparently nonuniversal systems", *Phys. Rev. B*, **75**(10).

2008 N. Johner, C. Grimaldi, I. Balberg and P. Ryser, "Transport exponent in a three-dimensional continuum tunneling-percolation model", *Phys. Rev. B*, **77**(17).

2009 G. Ambrosetti, N. Johner, C. Grimaldi, A. Danani and P. Ryser, “Percolative properties of hard oblate ellipsoids of revolution with a soft shell”, *Phys. Rev. E*, **78**(6).

2009 N. Johner, C. Grimaldi, T. Maeder and P. Ryser, “Optimal percolation of disordered segregated composites”, Phys. Rev. E, **79**(2).

2009 G. Ambrosetti, N. Johner, C. Grimaldi, T. Maeder, A. Danani and P. Ryser, “Electron tunneling in conductor-insulator composites with spherical fillers”, submitted to Journal of applied physics.

Conferences, workshops and conference papers

2006 N. Johner, T. Maeder, C. Grimaldi, A. Kambli, I. Saglini, C. Jacq and P. Ryser, “High-Voltage Sensitivity Studies of Model Thick-Film Resistors”, Proceedings of XXX International Conference of IMAPS Poland Chapter, Krakow, 157-160.

2006 Attended the meeting “Complex networks: analysis, control and applications”, which has been held at the University of Bristol (UK), 3rd-7th July 2006.

2007 N. Johner, T. Maeder, C. Jacq and P. Ryser, “Study of the impact of high-voltage trimming on several characteristics of model TFRs and their stability”, Proceedings of EMPC 2007, Oulu, 537-541.

2007 N. Johner, P. Ryser, C. Grimaldi and I. Balberg, “D.C. criticality of continuum tunneling-percolation systems”, poster presentation, XXIII IUPAP International Conference on Statistical Physics, Genova, 322.

Hobbies

Volley-ball (player, referee and coach JS1), tennis, guitar player